



Sengodan, Anand (2013) *The SIMCA algorithm for processing ground penetrating radar data and its practical applications*. PhD thesis.

<http://theses.gla.ac.uk/4177/>

Copyright and moral rights for this thesis are retained by the author

A copy can be downloaded for personal non-commercial research or study, without prior permission or charge

This thesis cannot be reproduced or quoted extensively from without first obtaining permission in writing from the Author

The content must not be changed in any way or sold commercially in any format or medium without the formal permission of the Author

When referring to this work, full bibliographic details including the author, title, awarding institution and date of the thesis must be given

# **The *SIMCA* Algorithm for processing Ground Penetrating Radar data and its practical applications.**



University  
of Glasgow

Anand Sengodan

Submitted in fulfilment of the requirements for the  
Degree of Doctor of Philosophy  
School of Computing Science  
College of Science and Engineering  
University of Glasgow

May, 2012

©Anand Sengodan



## Abstract

The main objective of this thesis is to present a new image processing technique to improve the detectability of buried objects such as landmines using Ground Penetrating Radar (GPR). The main challenge of GPR based landmine detection is to have an accurate image analysis method that is capable of reducing false alarms. However an accurate image relies on having sufficient spatial resolution in the received signal. An Antipersonnel mine (APM) can have a diameter as little as 2cm, whereas many soils have very high attenuation at frequencies above 450 MHz.

In order to solve the detection problem, a system level analysis of the issues involved with the recognition of landmines using image reconstruction is required. The thesis illustrates the development of a novel technique called the *SIMCA* (“*SIM*ulated *COR*relation *Al*gorithm”) based on area or volume correlation between the trace that would be returned by an ideal point reflector in the soil conditions at the site (obtained using the realistic simulation of Maxwell’s equations) and the actual trace. During an initialization phase, *SIMCA* carries out radar simulation using the system parameters of the radar and the soil properties.

Then *SIMCA* takes the raw data as the radar is scanned over the ground and uses a clutter removal technique to remove various unwanted signals of clutter such as cross talk, initial ground reflection and antenna ringing. The trace which would be returned by a target under these conditions is then used to form a correlation kernel using a GPR simulator. The 2D GPR scan (B scan), formed by abutting successive time-amplitude plots taken from different spatial positions as column vectors, is then correlated with the kernel using the *Pearson correlation coefficient* resulting in a correlated image which is brightest at points most similar to the canonical target. This image is then raised to an odd power  $>2$  to enhance the target/background separation.

The first part of the thesis presents a 2-dimensional technique using the B scans which have been produced as a result of correlating the clutter removed radargram (‘B scan’) with the kernel produced from the simulation. In order to validate the *SIMCA 2D* algorithm, *qualitative evidence* was used where comparison was made between the B scans produced by the *SIMCA* algorithm with B scans from some other techniques which are the best alternative systems reported in the open literature. It was found from this that the *SIMCA* algorithm clearly produces clearer B scans in comparison to the other techniques.

Next *quantitative evidence* was used to validate the *SIMCA* algorithm and demonstrate that it produced clear images. Two methods are used to obtain this quantitative evidence. In the first method an expert GPR user and 4 other general users are used to predict the location of landmines from the correlated B scans and validate the *SIMCA 2D* algorithm. Here human users are asked to indicate the location of targets from a printed sheet of paper which shows the correlated B scans produced by the *SIMCA* algorithm after some training, bearing in mind that it is a blind test. For the second quantitative evidence method, the *AMIRA* software is used to obtain values of the burial depth and position of the target in the  $x$  direction and hence validate the *SIMCA 2D algorithm*. Then the absolute error values for the burial depth along with the absolute error values for the

position in the  $x$  direction obtained from the *SIMCA* algorithm and the Scheers et al's algorithm when compared to the corresponding ground truth values were calculated.

Two-dimensional techniques that use B scans do not give accurate information on the shape and dimensions of the buried target, in comparison to 3D techniques that use 3D data ('C scans'). As a result the next part of the thesis presents a 3-dimensional technique. The equivalent 3D kernel is formed by rotating the 2D kernel produced by the simulation along the polar co-ordinates, whilst the 3D data is the clutter removed C scan. Then volume correlation is performed between the intersecting parts of the kernel and the data. This data is used to create isosurfaces of the slices raised to an odd power  $> 2$ .

To validate the algorithm an objective validation process which compares the actual target volume to that produced by the re-construction process is used. The *SIMCA 3D* technique and the Scheers et al's (the best alternative system reported in the open literature) technique are used to image a variety of landmines using GPR scans. The types of mines included plastic, wooden and glass ones. In all cases clear images were obtained with *SIMCA*. In contrast Scheers' algorithm, the present state-of-the-art, failed to provide clear images of non metallic landmines.

For this thesis, the above algorithms have been tested for landmine data and for locating foundations in demolished buildings and to validate and demonstrate that the *SIMCA* algorithms are better than existing technologies such as the Scheers et al's method and the *REFLEXW* commercial software.

## **Acknowledgements**

Firstly I would like to thank my PhD supervisor, Dr. W. Paul Cockshott for his guidance, support and patience throughout the course of this PhD. It is unlikely I would have come this far without him and the time, advice and encouragement he dedicated to my PhD are gratefully acknowledged. I would also like to thank my second supervisor, Dr. J. Paul Siebert for all his guidance and support.

I would like also to take this opportunity to express my sincere appreciation to all the staff at University of Glasgow for their support and valuable assistance throughout my PhD.

I would like to express my sincere thanks to my external and internal examiners and the convenor for taking the time to study this thesis extensively, agreeing to examine me and also for taking interest in this work.

The author would like to thank Mr. Matt Guy and Mr. Chris Leech of Geomatrix Earth Science Ltd, Dr. George Tuckwell (RSK) and Professor John M. Reynolds (Reynolds International Ltd) for reading my thesis and for their time, effort and suggestions and to the various people in the commercial arena for giving their time to review my work and offer me constructive feedback to help in the success of this PhD.

Furthermore, the author would like to extend his deepest gratitude to Dr. David J. Daniels of Cobham Plc. (formerly ERA Technologies) and for Dr. Erica Utsi for their input into the work completed in this PhD and for Dr. David J. Daniels for giving me the opportunity to undertake a work placement program under him.

Sincere gratitude is expressed to Dr. Dean Goodman of Geophysical Archaeometry Laboratory Inc, for providing me a student version of the GPR-SLICE software, and for answering questions regarding GPR applications.

To Ms. Carmen Cuenca-Garcia, of the Department of Archaeology at the University of Glasgow for her guidance, support and to complete the car park survey which provided the data that enabled me to test my algorithm in the case of locating foundations in demolished buildings.

Also to the European researchers and researchers at the Indian Institute of Technology for providing me with the landmine data.

I would like to acknowledge the Engineering and Physical Sciences Research Council (EPSRC) and the University of Glasgow for funding this PhD.

To the Knowledge Transfer Scotland: Policy and Practice Conference 2010 (Heriot-Watt University), for Thales Group (Thales Scottish Technology Prize 2010), and finally to the School of Computing Science at the University of Glasgow for giving me runner up prizes. To SET for Britain 2012 for short listing my PhD work to be showcased at the UK House of Parliament. To the ICT Pioneers Competition 2012 judges for awarding me the finalist prize in the transforming society category.

Last, but by no means least, to my parents for their unconditional love, support and encouragement over the years. Without their help and support I would not have been able to travel this journey and to complete my PhD. For this I dedicate this PhD to them, because without them, life would

not have any meanings. My hope is also that the successful completion of this PhD will bring good health to my father and mother and that the happiness will make them live much longer.

Finally to the innocent victims of landmines, both civilians and the armed forces. I hope the technology developed by this PhD can be used by civilian mine clearing teams, and also by the armed forces to help address the problem of buried devices.

To my Parents,  
You are always in my heart wherever I am,  
I love you both.

#### Originality Announcement

'I hereby declare that this submission is my own work and to the best of my knowledge it contains no materials previously published or written by another person, or substantial proportions of material which have been accepted for the award of any other degree or diploma at the University of Glasgow or any other educational institution, except where due acknowledgement is made in the thesis. Any contribution made to the research by others, with whom I have worked at the University of Glasgow or elsewhere, is explicitly acknowledged in the thesis.'

*Anand Sengodan*

# Contents

<b>1</b>	<b>Introduction</b>	<b>1</b>
1.1	Context and Motivation . . . . .	1
1.2	Background . . . . .	3
1.2.1	Classification of Mines . . . . .	6
1.2.1.1	Anti-tank Mine (ATM) . . . . .	6
1.2.1.2	Anti-personnel Mine (APM) . . . . .	6
1.2.2	Types of GPRs . . . . .	8
1.3	Hypothesis . . . . .	9
1.4	Thesis Contributions and Publications . . . . .	10
1.4.1	Work published in Conference proceedings . . . . .	12
1.4.2	Work to appear in Journal proceedings . . . . .	12
1.4.3	Prizes won . . . . .	12
1.4.4	PATENT . . . . .	13
1.5	Overview of Thesis . . . . .	13
<b>2</b>	<b>Background and Literature Review</b>	<b>15</b>
2.1	History of Landmines . . . . .	15
2.2	Laying of Landmines . . . . .	17
2.2.1	Introduction . . . . .	17
2.2.2	Laying of Landmines used by the German Army . . . . .	18
2.3	History of demining techniques . . . . .	20
2.3.1	Manual demining and Metal detectors . . . . .	20
2.3.2	Acoustic Sensors . . . . .	21
2.3.3	Infrared Imaging . . . . .	21
2.3.4	Dogs and Rodent detection . . . . .	22
2.3.5	Ground Penetrating Radar . . . . .	23
2.4	Typical protocol used in the clearance of landmines . . . . .	24
2.5	Single array and Multi-array Systems available in the market . . . . .	25
2.5.1	Hand-held single-array system . . . . .	27
2.5.1.1	HSTAMIDS . . . . .	27
2.5.1.2	Vallon MINEHOUND VMR3 . . . . .	28

2.5.1.3	Advanced landmine imaging system (ALIS) - Hand-held GPR Metal detector system . . . . .	28
2.5.2	Vehicle based multi-array system . . . . .	30
2.5.2.1	Vehicle based multi-array robotic system . . . . .	34
2.6	GPR and Global Positioning Systems . . . . .	35
2.7	Soil properties and their effect on GPR performance . . . . .	36
2.8	GPR data processing . . . . .	40
2.8.1	Clutter Removal . . . . .	41
2.8.1.1	Signal identification and analysis . . . . .	47
2.8.2	GPRMAX 2D/3D v1.5 used for forward modelling . . . . .	48
2.9	Migration technique to process GPR data . . . . .	51
2.9.1	Exploding source model . . . . .	52
2.9.2	Different types of migration . . . . .	53
2.9.2.1	Diffraction-summation Migration . . . . .	54
2.9.2.2	Kirchhoff Migration . . . . .	55
2.9.2.3	Finite-Difference Migration . . . . .	56
2.9.2.4	Frequency-Wavenumber Migration . . . . .	56
2.9.2.5	Phase-shift Migration . . . . .	57
2.9.2.6	Migration by deconvolution . . . . .	57
2.10	Commercial software available for GPR data processing. . . . .	61
2.10.1	GPR-SLICE software . . . . .	61
2.10.2	REFLEXW software . . . . .	63
2.11	Summary and Discussions . . . . .	65
<b>3</b>	<b><i>SIMCA 2D</i> and its validation</b>	<b>68</b>
3.1	Introduction . . . . .	68
3.2	Calculating depth and velocity of propagation . . . . .	71
3.3	Scheers et al's migration by deconvolution method . . . . .	72
3.4	Development of the <i>SIMCA 2D</i> technique . . . . .	73
3.4.1	GPR Simulations carried out to develop the kernels . . . . .	75
3.4.2	Removal of clutter from the raw GPR data . . . . .	78
3.4.3	Convolution and Correlation . . . . .	78
3.5	Results using simulated data . . . . .	79
3.6	Experimental data source used in the laboratory to obtain the landmine data used to test the <i>SIMCA 2D</i> algorithm . . . . .	81
<b>I</b>	<b>Results obtained by using the <i>SIMCA 2D</i> algorithm on landmine data obtained from GPR experiments conducted by European researchers.</b>	<b>83</b>
3.7	Introduction . . . . .	84
3.8	Generation of Kernels . . . . .	85



3.8.1	Use of the complete hyperbolic signature as a kernel during correlation. . .	86
3.8.2	Influence of the depth on the kernel and its effects on the final correlated image . . . . .	86
3.9	Obtaining the burial depth and the position of burial in the $x$ direction using <i>AMIRA</i> software . . . . .	90
3.10	Results . . . . .	93
3.11	Validation of Results from the <i>SIMCA 2D</i> algorithm . . . . .	108
3.11.1	Validation of results from the <i>SIMCA 2D</i> algorithm using <i>qualitative evidence</i>	108
3.11.1.1	Al-Nuaimy et al. . . . .	108
3.11.1.2	Potin et. al. . . . .	108
3.11.1.3	Daniels and Allan . . . . .	109
3.11.1.4	Groenenboom and Yarovoy . . . . .	109
3.11.2	Validation of the <i>SIMCA 2D</i> algorithm using <i>quantitative evidence</i> . . . . .	109
3.11.2.1	Use of an expert GPR user and 4 other general users who predict the location of landmines and validate the <i>SIMCA 2D</i> algorithm .	109
3.11.2.2	Use of <i>AMIRA</i> software to obtain values of the burial depth and position of the target in the $x$ direction and hence validate the <i>SIMCA 2D</i> algorithm . . . . .	118
3.12	Summary graphs and statistics . . . . .	129
3.13	Summary and Discussions . . . . .	129
<b>4</b>	<b><i>SIMCA 3D</i> and its validation</b>	<b>137</b>
4.1	Introduction . . . . .	137
4.2	Key relevant prior work . . . . .	141
4.3	Simulation carried out to develop kernels . . . . .	144
4.4	Description of <i>SIMCA 3D</i> Algorithm . . . . .	145
4.5	Experimental data source used in the laboratory to obtain the landmine data used to test the <i>SIMCA 3D</i> algorithm . . . . .	149
<b>II</b>	<b>Results produced by the <i>SIMCA 3D</i> algorithm using landmine data obtained from GPR experiments at the Indian Institute of Technology.</b>	<b>151</b>
4.6	Results and Discussion . . . . .	152
4.6.1	Setup 1 - Wet Sandy Soil . . . . .	154
4.6.1.1	A plastic mine, a metallic mine and a wooden handled Browning pistol . . . . .	154
4.6.1.2	A wooden cased mine, a metallic mine, steel cased mine and metal plate buried in wet sandy soil . . . . .	158
4.6.1.3	A metallic mine, 2 plastic mines and a metallic plate. . . . .	159
4.6.2	Setup 2 - Dry Sandy Soil . . . . .	159

4.6.2.1	A Colombian guerrilla developed glass bottle mine, a metallic mine and a metal plate. . . . .	159
4.6.2.2	A Colombian guerrilla cast ironed mine, tree root and a metallic plate . . . . .	168
4.6.2.3	A plastic mine with a stone . . . . .	169
4.6.2.4	A plastic mine, tree root and a metallic plate . . . . .	174
4.6.2.5	A tiny plastic M14 antipersonnel mine, a plastic mine and a metallic plate . . . . .	174
4.6.2.6	A metallic plate buried in a less compacted layer of sand . . . . .	177
4.6.2.7	A plastic and rubber cased mine, a plastic mine and a metal plate . . . . .	181
4.6.2.8	A steel bullet, a plastic mine and a metallic plate . . . . .	184
4.6.2.9	A stone, steel cased mine and a metallic plate . . . . .	188
4.6.3	Setup 3 - Wet clay conditions . . . . .	193
4.6.3.1	A wooden cased mine, a plastic mine and a metallic plate . . . . .	193
4.6.4	Summary of the results . . . . .	193
4.7	Sensitivity of the algorithm to permittivity and depth changes . . . . .	198
4.8	Summary graphs and statistics . . . . .	221
4.9	Comparison with Scheers's algorithm . . . . .	221
4.10	Effect on using interpolation . . . . .	230
4.11	Isosurfaces in <i>MATLAB</i> . . . . .	230
4.12	The use of an image as opposed to an audible signal . . . . .	233
4.13	Why was validation carried out for the <i>SIMCA</i> using human users rather than an automated testing mechanism? . . . . .	233
4.14	Recommended system for a landmine detection scenario and a non landmine detection scenario . . . . .	234
4.14.1	Vehicle based solution for landmine detection . . . . .	234
4.14.2	Hand held system for a non landmine application . . . . .	235
4.14.3	Comparison of the vehicle based and hand held systems . . . . .	235
4.15	Summary and Discussions . . . . .	235
<b>5</b>	<b>Conclusions and Future Work</b>	<b>239</b>
5.1	Introduction . . . . .	239
5.2	Aim of PhD Research . . . . .	240
5.3	Hypothesis, Research Questions and Objectives Revisited . . . . .	240
5.4	Contributions to Research . . . . .	244
5.5	Future Work . . . . .	245
5.6	Summary & Conclusions . . . . .	254
<b>A</b>	<b>Algorithm listing for <i>SIMCA</i> Algorithm</b>	<b>255</b>
<b>B</b>	<b>Car park case study</b>	<b>262</b>

B.1	Data acquisition procedure used to obtain data for locating foundations in demolished buildings . . . . .	262
B.2	Processing of GPR data using <i>SIMCA 2D</i> and its use in locating foundations in demolished buildings . . . . .	263
B.3	Introduction . . . . .	263
B.4	<i>REFLEXW</i> software . . . . .	267
B.5	Results . . . . .	267
B.6	The processing of GPR data using the <i>SIMCA 3D</i> algorithm and its use in locating foundations in demolished buildings . . . . .	273
B.7	Introduction . . . . .	273
B.8	3D Isosurfaces produced by the <i>SIMCA 3D</i> algorithm . . . . .	274
B.8.1	3D Isosurfaces produced by the Scheers method. . . . .	274
B.8.2	Results using the <i>REFLEXW</i> commercial software. . . . .	274
B.8.3	Comparison of Results . . . . .	274
B.9	Summary and Discussions . . . . .	279
	<b>Bibliography</b>	<b>280</b>

# List of Figures

1.1	Countries around the world affected by mines. . . . .	2
1.2	A diagrammatic representation of a GPR showing the transmitter and the receiver. .	4
1.3	The stages in the location and classification of targets and also a diagram giving the scope of this PhD thesis. . . . .	5
1.4	A Russian TM-46 anti-tank blast mine. . . . .	6
1.5	Typical APMs: [A]: Bounding mine - German S-Mine; [B]: A directional mine - Russian MON-50. . . . .	7
1.6	Types of GPRs. . . . .	8
1.7	Thesis Overview. . . . .	14
2.1	A Fougasse mine. . . . .	16
2.2	First mines used to explode on contact. . . . .	16
2.3	The first pressure mine. . . . .	17
2.4	German mine plan. A map to show how the Germans laid their mines and kept records of minefields. . . . .	19
2.5	A manual demining situation using a metal detector. . . . .	21
2.6	Photograph of Landmine clearance using dogs. . . . .	22
2.7	Landmine clearance using rodents. . . . .	23
2.8	A pictorial representation of a hand-held and vehicle based system. . . . .	26
2.9	<i>HSTAMIDS</i> hand-held detector. . . . .	27
2.10	The <i>MINEHOUND</i> hand-held dual sensor technology. . . . .	28
2.11	The ALIS hand-held detector. [A]: Actual system; [B]: Interpolated GPR vertical slice; [C]: Migrated GPR vertical slice. . . . .	29
2.12	Downward-looking vehicle mounted antenna oriented at $45^0$ with respect to the motion direction. . . . .	30
2.13	PSI developed system - [A]: Downward looking system; [B]: Forward looking system. .	31
2.14	The Wichmann/Niitek GPR system - [A]: actual system; [B] GPR B scan produced by the system. . . . .	32
2.15	3d-Radar multi-channel system. . . . .	33

2.16	Images produced from software integrated in 3d-Radar. [A]: control software used during collection of data; [B]: processed archaeological data with a satellite imagery overlay. . . . .	33
2.17	The teleoperated buggy vehicle used as a robotic landmine detection and clearance system . . . . .	34
2.18	Underground locating is accomplished using a GPR scan overlaid on top of a map using a GPS system. . . . .	35
2.19	Typical GPR data processing flow for 2D bistatic common-offset reflection data. . .	40
2.20	The 3D FDTD Yee Cell . . . . .	50
2.21	Principle of migration: The diffracted energy is collapsed back to its point-source and the incorrect dip is corrected. . . . .	52
2.22	[A]: Configuration of exploding source model; [B]: Exploding Reflector model. . .	53
2.23	GPR data from a plastic landmine. [A]: Raw image; [B]: Migrated image. . . . .	54
2.24	Diffraction summation migration. . . . .	55
2.25	Representation of the co-ordinate system for migration by deconvolution. . . . .	59
2.26	A C scan of the point scatterer at a depth of 6cm below the ground calculated by forward modelling. . . . .	60
2.27	Time slices and recorded hyperbolas on a B scan produced by GPR-SLICE software. . . . .	62
2.28	A 3D isosurface of some tree root data produced by GPR-SLICE . . . . .	62
2.29	Processed GPR 2D profiles by the REFLEXW software. . . . .	64
2.30	Processed 3D data by the REFLEXW software - [A]: Time slices; [B]: Subsurfaces included within a 3D data cube. . . . .	64
3.1	[A]: A scan and [B]: B scan. . . . .	69
3.2	[A]: Raw GPR radargram; [B]: Same GPR radargram having clutter removed. . . .	70
3.3	Hyperbolic formation. . . . .	72
3.4	Simulated results showing the migration of a waveform from a point source. Please note that this simulation is based on data collected in a laboratory setting where a flat surface exists, the soil is homogeneous and a spherical reflector response can be used. . . . .	74
3.5	The flowchart of the <i>SIMCA 2D</i> algorithm. . . . .	76
3.6	Process diagram of the <i>SIMCA 2D</i> algorithm. The diagram also shows the B scan along with the 3D isosurface. Note the 3D isosurface indicates that the plates of the plastic mine are open. . . . .	77
3.7	Results using the <i>SIMCA</i> algorithm and the Scheer's algorithm. Also note that the <i>SIMCA</i> method produces a focused image of the spherical object in comparison to the Scheers' method. . . . .	80

3.8	Photograph showing the SPRScan GPR head used which is mounted in the laboratory setup on a robotic positioning table system. This photograph shows the author carrying out scanning of a field laid with landmines at the Cobham plc (ERA Technologies) training facility. This was done during a work placement at Cobham.	82
3.9	The SPRScan radar shown in Figure 3.8 is mounted on a robotic positioning table system.	82
3.10	Pictorial representation of the kernel. [A]: The kernel derived from the GPR simulator; [B]: The normalised kernel and [C]: 3D representation of the kernel produced using the 'surf' command in <i>MATLAB</i> .	85
3.11	Kernels of various sizes for a dry sandy soil, generated using the GPRMAX simulator.	87
3.12	Kernels of various sizes for a wet sandy soil, generated using the GPRMAX simulator.	88
3.13	Correlated result using the <i>SIMCA</i> algorithm. The correlation using a full hyperbolic signature produces better localisation of the landmine in comparison to using a portion of the hyperbolic signature.	89
3.14	The effect of depth on the shape of the kernel when targets are at the following depths:- [A]: 12.3cm; [B]: 12.0cm; [C]: 11.5cm; [D]: 10.0cm; [E]: 9.5cm; [F]: 8.0cm; [G]: 7.5cm; [H]: 6.9cm. Note in the diagrams the Trace Number is on the horizontal axis and the Time (x0.01 ns) is on the vertical axis. Also the value of X is the trace number and the value of Y is the time (x0.01) ns.	91
3.15	Calculating centroid of object using <i>AMIRA</i> software.	92
3.16	Information about the buried targets.	96
3.17	Results of real targets in a dry sandy soil. The GPR survey was conducted 23 days after the survey in Figure 3.18 - [A]: 3D plot showing probability of occurrence of objects with respect to depth and position on the scan line produced by the Scheers algorithm; [B]: Clutter removed raw B scan; [C]: 3D plot showing probability of occurrence of objects with respect to depth and position on the scan line produced by the <i>SIMCA</i> algorithm; [D]: B scan produced from the <i>SIMCA</i> algorithm with brightness raised to power of 3; [E]: B scan produced by the Scheers algorithm.	97
3.18	Results of real targets in a wet sandy soil - [A]: 3D plot showing probability of occurrence of objects with respect to depth and position on the scan line produced by the Scheers algorithm; [B]: Clutter removed raw B scan; [C]: 3D plot showing probability of occurrence of objects with respect to depth and position on the scan line produced by the <i>SIMCA</i> algorithm; [D]: B scan produced from the <i>SIMCA</i> algorithm with brightness raised to power of 3; [E]: B scan produced by the Scheers algorithm.	98

3.19	Results of real targets in a wet clay soil - [A]: 3D plot showing probability of occurrence of objects with respect to depth and position on the scan line produced by the Scheers algorithm; [B]: Clutter removed raw B scan; [C]: 3D plot showing probability of occurrence of objects with respect to depth and position on the scan line produced by the <i>SIMCA</i> algorithm; [D]: B scan produced from the <i>SIMCA</i> algorithm with brightness raised to power of 3; [E]: B scan produced by the Scheers algorithm. . . . .	99
3.20	Results of real targets in a wet sandy soil - [A]: 3D plot showing probability of occurrence of objects with respect to depth and position on the scan line produced by the Scheers algorithm; [B]: Clutter removed raw B scan; [C]: 3D plot showing probability of occurrence of objects with respect to depth and position on the scan line produced by the <i>SIMCA</i> algorithm; [D]: B scan produced from the <i>SIMCA</i> algorithm with brightness raised to power of 3; [E]: B scan produced by the Scheers algorithm. . . . .	100
3.21	Results of real targets in a dry sandy soil - [A]: 3D plot showing probability of occurrence of objects with respect to depth and position on the scan line produced by the Scheers algorithm; [B]: Clutter removed raw B scan; [C]: 3D plot showing probability of occurrence of objects with respect to depth and position on the scan line produced by the <i>SIMCA</i> algorithm; [D]: B scan produced from the <i>SIMCA</i> algorithm with brightness raised to power of 3; [E]: B scan produced by the Scheers algorithm. . . . .	101
3.22	Results of real targets in a wet clay soil - [A]: 3D plot showing probability of occurrence of objects with respect to depth and position on the scan line produced by the Scheers algorithm; [B]: Clutter removed raw B scan; [C]: 3D plot showing probability of occurrence of objects with respect to depth and position on the scan line produced by the <i>SIMCA</i> algorithm; [D]: B scan produced from the <i>SIMCA</i> algorithm with brightness raised to power of 3; [E]: B scan produced by the Scheers algorithm. . . . .	102
3.23	Results of real targets in a wet clay soil - [A]: 3D plot showing probability of occurrence of objects with respect to depth and position on the scan line produced by the Scheers algorithm; [B]: Clutter removed raw B scan; [C]: 3D plot showing probability of occurrence of objects with respect to depth and position on the scan line produced by the <i>SIMCA</i> algorithm; [D]: B scan produced from the <i>SIMCA</i> algorithm with brightness raised to power of 3; [E]: B scan produced by the Scheers algorithm. . . . .	103

3.24	Results of real targets in a dry sandy soil - [A]: 3D plot showing probability of occurrence of objects with respect to depth and position on the scan line produced by the Scheers algorithm; [B]: Clutter removed raw B scan; [C]: 3D plot showing probability of occurrence of objects with respect to depth and position on the scan line produced by the <i>SIMCA</i> algorithm; [D]: B scan produced from the <i>SIMCA</i> algorithm with brightness raised to power of 3; [E]: B scan produced by the Scheers algorithm. . . . .	104
3.25	Results of real targets in a dry clay soil - [A]: 3D plot showing probability of occurrence of objects with respect to depth and position on the scan line produced by the Scheers algorithm; [B]: Clutter removed raw B scan; [C]: 3D plot showing probability of occurrence of objects with respect to depth and position on the scan line produced by the <i>SIMCA</i> algorithm; [D]: B scan produced from the <i>SIMCA</i> algorithm with brightness raised to power of 3; [E]: B scan produced by the Scheers algorithm. . . . .	105
3.26	Results of real targets in a wet clay soil - [A]: 3D plot showing probability of occurrence of objects with respect to depth and position on the scan line produced by the Scheers algorithm; [B]: Clutter removed raw B scan; [C]: 3D plot showing probability of occurrence of objects with respect to depth and position on the scan line produced by the <i>SIMCA</i> algorithm; [D]: B scan produced from the <i>SIMCA</i> algorithm with brightness raised to power of 3; [E]: B scan produced by the Scheers algorithm. . . . .	106
3.27	Results of real targets in a dry sandy soil - [A]: 3D plot showing probability of occurrence of objects with respect to depth and position on the scan line produced by the Scheers algorithm; [B]: Clutter removed raw B scan; [C]: 3D plot showing probability of occurrence of objects with respect to depth and position on the scan line produced by the <i>SIMCA</i> algorithm; [D]: B scan produced from the <i>SIMCA</i> algorithm with brightness raised to power of 3; [E]: B scan produced by the Scheers algorithm. . . . .	107
3.28	A comparison of the resulting B scans from - [A]: <i>SIMCA</i> algorithm; [B]: Al-Nuaimy et al.; [C]: Daniels and Alan. . . . .	111
3.29	A comparison of the resulting B scans from - [A]: <i>SIMCA</i> algorithm; [B]: Potin et al.; [C]: Groenenboom and Yarovoy. . . . .	112
3.30	Figure comparing the <i>SIMCA</i> algorithm with other techniques illustrated in Figures 3.28 and 3.29. . . . .	113
3.31	Summary graph of ground truth depth vs estimated depth for Tables 3.17 and 3.18. . . . .	132
3.32	Summary graph of ground truth position in $x$ vs estimated position in $x$ for Tables 3.19 and 3.20. . . . .	135
4.1	Examples of [A]: A scan; [B]: B scan; [C]: C scan. Please note in the figure that the $t$ -axis in the C scan is also referred to as the $z$ -axis. . . . .	139



4.2	Actual B scan slice from the GPR after removal of various clutter such as cross talk, initial ground reflection and antenna ringing. . . . .	139
4.3	Simulation of point reflector using a 0.025m radius sphere buried at a depth corresponding to the burial depth of the target in the sandbox. It is to be noted that this simulation is based on data collected in a laboratory condition where a flat surface exists, the soil is homogeneous and a spherical reflector response can be used. Once the algorithm worked in test conditions it can be tuned to work in actual soil conditions using a realistic simulation. . . . .	140
4.4	Clockwise from left: [A]: Hyperbolic signature spread due to a buried object; [B]: Hyperbolic formation as the radar moves from position $p_1$ to position $p_2$ . . . . .	141
4.5	The flowchart of the 3D <i>SIMCA</i> algorithm. Note in the figure that to improve the performance of the processing in <i>MATLAB</i> the B-scans are stacked on top of each other but after processing they are stacked adjacent each other. . . . .	146
4.6	Contrast between the inner product and normalised inner product or cosine measures.	148
4.7	A pictorial representation of data and kernel points. The black filled circles are the data points and the unfilled black circles are the kernel points. . . . .	148
4.8	Diagram showing position and direction of the vertical cross sectional slices shown in this chapter. . . . .	153
4.9	Details of the targets buried in Figure 4.10. . . . .	155
4.10	Reconstruction of volumes of real targets in a wet sandy soil using: [A]: <i>SIMCA</i> system after scanning by a GPR at optimised threshold = 230; [B]: Scheers et al algorithm after scanning by a GPR at optimised threshold=252. Note the clearer rendering of non metal objects and parts using <i>SIMCA</i> algorithm; [C]: Vertical cross-sectional slice showing the plastic MAUS mine. . . . .	156
4.11	The internal structure of the PMD-6 wooden cased mine. . . . .	158
4.12	Details of the targets buried in Figure 4.13. . . . .	160
4.13	Reconstruction of volumes of real targets in a wet sandy soil using: [A]: <i>SIMCA</i> system after scanning by a GPR at optimised threshold = 230; [B]: Scheers et al's algorithm after scanning by a GPR at optimised threshold=252. Note <i>SIMCA</i> algorithm can render the steel-cased PROM-1 mine and even show the trip wire. Same ability for the <i>SIMCA</i> algorithm in case of the wooden cased mine; [C]: Vertical cross-sectional slice showing wooden cased PMD-6 mine. . . . .	161
4.14	Trip Wires of Mines. . . . .	162
4.15	Details of the targets buried in Figure 4.16. . . . .	162
4.16	Reconstruction of volumes of real targets in a wet sandy soil using: [A]: <i>SIMCA</i> system after scanning by a GPR at optimised threshold = 230; [B]: Scheers et al's algorithm after scanning by a GPR at optimised threshold=252. Note plastic mines are rendered more accurately by the <i>SIMCA</i> algorithm; [C]: Vertical cross-sectional slice showing the plastic MAUS mine. . . . .	164

4.17	Reconstruction of volumes of real targets in a dry sandy soil using: [A]: <i>SIMCA</i> system after scanning by a GPR at optimised threshold = 230; [B]: Scheers et al's algorithm after scanning by a GPR at optimised threshold=252. Note <i>SIMCA</i> algorithms improved performance on Glass targets; [C]: Vertical cross-sectional slice showing the Colombian guerrilla glass bottle mine. . . . .	166
4.18	Details of the targets buried in Figure 4.19. . . . .	168
4.20	Details of the targets buried in Figure 4.21. . . . .	169
4.19	Reconstruction of volumes of real targets in a dry sandy soil using: [A]: <i>SIMCA</i> system after scanning by a GPR at optimised threshold = 230; [B]: Scheers et al's algorithm after scanning by a GPR at optimised threshold=252. Note even though there is a metallic mine Scheers' algorithm is not so accurate at displaying the mine; [C]: Vertical cross-sectional slice showing cast ironed OZM-45 mine. . . . .	170
4.21	Reconstruction of volumes of real targets in a dry sandy soil using: [A]: <i>SIMCA</i> system after scanning by a GPR at optimised threshold = 230; [B]: Scheers et al's algorithm after scanning by a GPR at optimised threshold=252. Note plastic mines are rendered more accurately by the <i>SIMCA</i> algorithm; [C]: Vertical cross-sectional slice showing plastic AUS 15/50 mine. . . . .	172
4.22	Details of the targets buried in Figure 4.23. . . . .	174
4.23	Reconstruction of volumes of real targets in a dry sandy soil using: [A]: <i>SIMCA</i> system after scanning by a GPR at optimised threshold = 230; [B]: Scheers et al's algorithm after scanning by a GPR at optimised threshold=252. Note <i>SIMCA</i> 's natural ability at rendering plastic mines; [C]: Vertical cross-sectional slice showing plastic APM 29 mine. . . . .	175
4.24	The internal structure of a M14 antipersonnel mine. . . . .	177
4.25	Details of the targets buried in Figure 4.26. . . . .	178
4.26	Reconstruction of volumes of real targets in a dry sandy soil using: [A]: <i>SIMCA</i> system after scanning by a GPR at optimised threshold = 230; [B]: Scheers et al's algorithm after scanning by a GPR at optimised threshold=252. Note <i>SIMCA</i> is more accurate in displaying plastic mines and their parts; [C]: Vertical cross-sectional slice showing plastic PRB M409. . . . .	179
4.27	Details of the targets buried in Figure 4.28. . . . .	181
4.28	Reconstruction of volumes of real targets in a dry sandy soil using: [A]: <i>SIMCA</i> system after scanning by a GPR at optimised threshold = 230; [B]: Scheers et al's algorithm after scanning by a GPR at optimised threshold=252. Note <i>SIMCA</i> produces better reconstructions for metallic mines; [C]: Vertical cross-sectional slice showing metallic M2 mine. . . . .	182
4.31	Figure showing wires in fuse mechanism. . . . .	184
4.29	Details of the targets buried in Figure 4.30. . . . .	185

4.30	Reconstruction of volumes of real targets in a dry sandy soil using: [A]: <i>SIMCA</i> system after scanning by a GPR at optimised threshold = 230; [B]: Scheers et al's algorithm after scanning by a GPR at optimised threshold=252. Note plastic mines are rendered poorly by the Scheers' algorithm; [C]: Vertical cross-sectional slice showing plastic & rubber cased PMA-3 mine. . . . .	186
4.33	Details of the targets buried in Figure 4.34. . . . .	188
4.32	Reconstruction of volumes of real targets in a dry sandy soil using: [A]: <i>SIMCA</i> system after scanning by a GPR at optimised threshold = 230; [B]: Scheers et al's algorithm after scanning by a GPR at optimised threshold=252. Note <i>SIMCA</i> algorithm can reconstruct plastic mines more accurately; [C]: Vertical cross-sectional slice showing plastic PRB M409 mine. . . . .	189
4.34	Reconstruction of volumes of real targets in a dry sandy soil using: [A]: <i>SIMCA</i> system after scanning by a GPR at optimised threshold = 230; [B]: Scheers et al's algorithm after scanning by a GPR at optimised threshold=252. Note steel cased mines are poorly reconstructed by the Scheers' algorithm.; [C]: Vertical cross-sectional slice showing steel cased PLARM-1A mine. . . . .	191
4.35	Details of the targets buried in Figure 4.36. . . . .	194
4.36	Reconstruction of volumes of real targets in a wet clay soil using: [A]: <i>SIMCA</i> system after scanning by a GPR at optimised threshold = 230; [B]: Scheers et al's algorithm after scanning by a GPR at optimised threshold=252. Note <i>SIMCA</i> algorithm can reconstruct plastic mines more accurately; [C]: Vertical cross-sectional slice showing plastic M14 mine. . . . .	195
4.37	Sensitivity of <i>SIMCA</i> algorithm to depth and permittivity changes when building a kernel. Clockwise from left: [A]: Simulated target depth at 5.1cm and using correct soil parameters; [B]: Simulated target depth at 6cm and using correct soil parameters; [C]: Simulated target depth at 12cm and using correct soil parameters; [D]: correct simulated target depth but wrong soil parameters. . . . .	200
4.38	Sensitivity of <i>SIMCA</i> algorithm to depth and permittivity changes when building a kernel. Clockwise from left: [A]: Simulated target depth at 5.1cm and using correct soil parameters; [B]: Simulated target depth at 6cm and using correct soil parameters; [C]: Simulated target depth at 12cm and using correct soil parameters; [D]: correct simulated target depth but wrong soil parameters. . . . .	202
4.39	Sensitivity of <i>SIMCA</i> algorithm to depth and permittivity changes when building a kernel. Clockwise from left: [A]: Simulated target depth at 5.1cm and using correct soil parameters; [B]: Simulated target depth at 6cm and using correct soil parameters; [C]: Simulated target depth at 12cm and using correct soil parameters; [D]: correct simulated target depth but wrong soil parameters. . . . .	204

4.40	Sensitivity of <i>SIMCA</i> algorithm to depth and permittivity changes when building a kernel. Clockwise from left: [A]: Simulated target depth at 5.1cm and using correct soil parameters; [B]: Simulated target depth at 6cm and using correct soil parameters; [C]: Simulated target depth at 12cm and using correct soil parameters; [D]: correct simulated target depth but wrong soil parameters. . . . .	205
4.41	Sensitivity of <i>SIMCA</i> algorithm to depth and permittivity changes when building a kernel. Clockwise from left: [A]: Simulated target depth at 5.1cm and using correct soil parameters; [B]: Simulated target depth at 6cm and using correct soil parameters; [C]: Simulated target depth at 12cm and using correct soil parameters; [D]: correct simulated target depth but wrong soil parameters. . . . .	206
4.42	Sensitivity of <i>SIMCA</i> algorithm to depth and permittivity changes when building a kernel. Clockwise from left: [A]: Simulated target depth at 5.1cm and using correct soil parameters; [B]: Simulated target depth at 6cm and using correct soil parameters; [C]: Simulated target depth at 12cm and using correct soil parameters; [D]: correct simulated target depth but wrong soil parameters. . . . .	208
4.43	Sensitivity of <i>SIMCA</i> algorithm to depth and permittivity changes when building a kernel. Clockwise from left: [A]: Simulated target depth at 5.1cm and using correct soil parameters; [B]: Simulated target depth at 6cm and using correct soil parameters; [C]: Simulated target depth at 12cm and using correct soil parameters; [D]: correct simulated target depth but wrong soil parameters. . . . .	209
4.44	Sensitivity of <i>SIMCA</i> algorithm to depth and permittivity changes when building a kernel. Clockwise from left: [A]: Simulated target depth at 5.1cm and using correct soil parameters; [B]: Simulated target depth at 6cm and using correct soil parameters; [C]: Simulated target depth at 12cm and using correct soil parameters; [D]: correct simulated target depth but wrong soil parameters. . . . .	210
4.45	Sensitivity of <i>SIMCA</i> algorithm to depth and permittivity changes when building a kernel. Clockwise from left: [A]: Simulated target depth at 5.1cm and using correct soil parameters; [B]: Simulated target depth at 6cm and using correct soil parameters; [C]: Simulated target depth at 12cm and using correct soil parameters; [D]: correct simulated target depth but wrong soil parameters. . . . .	211
4.46	Sensitivity of <i>SIMCA</i> algorithm to depth and permittivity changes when building a kernel. Clockwise from left: [A]: Simulated target depth at 5.1cm and using correct soil parameters; [B]: Simulated target depth at 6cm and using correct soil parameters; [C]: Simulated target depth at 12cm and using correct soil parameters; [D]: correct simulated target depth but wrong soil parameters. . . . .	212
4.47	Sensitivity of <i>SIMCA</i> algorithm to depth and permittivity changes when building a kernel. Clockwise from left: [A]: Simulated target depth at 5.1cm and using correct soil parameters; [B]: Simulated target depth at 6cm and using correct soil parameters; [C]: Simulated target depth at 12cm and using correct soil parameters; [D]: correct simulated target depth but wrong soil parameters. . . . .	213

4.48	Sensitivity of <i>SIMCA</i> algorithm to depth and permittivity changes when building a kernel. Clockwise from left: [A]: Simulated target depth at 5.1cm and using correct soil parameters; [B]: Simulated target depth at 6cm and using correct soil parameters; [C]: Simulated target depth at 12cm and using correct soil parameters; [D]: correct simulated target depth but wrong soil parameters. . . . .	214
4.49	Sensitivity of <i>SIMCA</i> algorithm to depth and permittivity changes when building a kernel. Clockwise from left: [A]: Simulated target depth at 5.1cm and using correct soil parameters; [B]: Simulated target depth at 6cm and using correct soil parameters; [C]: Simulated target depth at 12cm and using correct soil parameters; [D]: correct simulated target depth but wrong soil parameters. . . . .	215
4.50	Summary graph for depth of ground truth versus depth estimated for Tables 4.27 and 4.28. . . . .	224
4.51	Summary graph for volume of ground truth versus volume estimated for Tables 4.29 and 4.30. . . . .	227
4.52	Graph of the error on estimating volume of a target as a function of isosurface threshold for <i>SIMCA</i> algorithm. . . . .	228
4.53	Graph of the error on estimating volume of a target as a function of isosurface threshold for Scheers algorithm. . . . .	229
4.54	Various isosurfaces created to test the effect of interpolation. The isosurfaces have been created with various slices left out and the rest of the slices calculated using interpolation. [A]: The isosurface created without leaving any slices out; [B]: starting at the 1st slice and using all slices but at a spacing of 2cm; [C]: starting at the 1st slice and using all slices but at a spacing of 4cm; [D]: starting at the 2nd slice and using all slices but at a spacing of 2cm; [E]: starting at the 2nd slice and using all slices but at a spacing of 3cm; [F]: starting at the 2nd slice and using all slices but at a spacing of 4cm; [G]: starting at the 3rd slice and using all slices but at a spacing of 2cm; [H]: starting at the 3rd slice and using all slices but at a spacing of 3cm; [I]: starting at the 3rd slice and using all slices but at a spacing of 4cm. . . .	231
4.55	Proposed vehicle based system using the cartesian gantry employed in the laboratory and in a forward looking mode. The system also has a stereo vision camera to allow for automatic scanning and to attain positional information. . . . .	236
4.56	3D reconstruction using the <i>SIMCA</i> algorithm - [A]: Using a full hyperbola for the kernel and [B]: Using half a hyperbola for the kernel. . . . .	237
5.1	2D Laser rangefinder used to attain positional information. . . . .	247
5.2	Views of the SSI test cell, antenna cart and survey grid. . . . .	248
5.3	A positioning table. . . . .	249
5.4	The <i>DETEC-2</i> system with the position-tracking bar. . . . .	251

B.1	[A]: Map showing the plan of the GPR survey in the car park; [B]: Satellite photograph of the same car park plan shown. The red box indicates the actual grid of where the survey took place. . . . .	264
B.2	Photographs showing the method used in the acquisition of data in the car park. Note the tape measures which have been laid out to allow for accurate positioning of the data. Also please note that the above photographs show the survey conducted in the adjoining car park and not in that part of the car park where the results are shown for <i>SIMCA 2D</i> and <i>SIMCA 3D</i> . . . . .	265
B.3	Photograph showing the pulseEKKO 100 control unit, the laptop with the software and the battery source to power the system. . . . .	266
B.4	Photographs showing [A]: Location of the original 19th Century terraced houses; [B]: The existing car park after the houses were demolished and the car park built over the location of the demolished buildings. . . . .	268
B.5	The sources of error in the values of the position in the $x$ direction and the burial depth as obtained from the Architect's drawings. . . . .	270
B.6	Results from [A]: Unprocessed B scan; [B]: <i>REFLEXW</i> processed B scan; [C]: 3D plot showing probability of occurrence of objects with respect to depth and position on the scan line; [D]: Normalised Kernel; [E]: B scan processed using <i>SIMCA</i> algorithm; [F]: B scan processed using Scheers algorithm. . . . .	271
B.7	Photographs showing the cracks in the existing car park [A]: Within the boundary of the survey; [B]: Beyond the boundary of the survey. . . . .	272
B.8	3D isosurface produced using the <i>SIMCA</i> method. Isosurface produced at isosurface level = 0.02. . . . .	275
B.9	3D isosurface produced using the Scheers' method. Isosurface produced at isosurface level = 1e3. . . . .	276
B.10	Isosurface generated using <i>REFLEXW</i> commercial software at threshold of 247. . .	277
B.11	Time slices obtained using <i>REFLEXW</i> software. It is to be noted that the foundation is clearly visible in some of the time slices. . . . .	278

# List of Tables

1.1	Typical Specifications of three different types of mines. . . . .	8
2.1	List of relative permittivity for some typical earth materials. . . . .	36
2.2	Price of annual subscriptions and outright purchase of GPR-SLICE software. . . .	63
2.3	Price of REFLEXW software. . . . .	65
3.1	Actual burial depth, depth obtained from the <i>SIMCA</i> method, depth obtained from the Scheers's method for the Spherical object in centimetres. Calculation of the absolute errors of the two methods when compared with the ground truth is also presented. . . . .	79
3.2	Actual depth from the ground truth, estimated depth for the expert user, Actual position of the buried target in the $x$ direction, Estimated position of the buried target in the $x$ direction, The table also gives the percentage errors. The values of the depth and the position in the $x$ direction are in centimetres. . . . .	115
3.3	Estimated depth and estimated position in the $x$ direction for the 4 general users, mean and standard deviation on the depth and the position in the $x$ direction. The values for the position in the $x$ direction and the depth are in centimetres. . . . .	116
3.4	Estimated depth and estimated position in the $x$ direction for the 4 general users, systematic bias on the depth and the position in the $x$ direction. The values for the position in the $x$ direction and the depth are in centimetres. . . . .	117
3.5	The corrected depth and position in the $x$ direction for the general users. The values for the position in the $x$ direction and the depth are in centimetres. . . . .	119
3.6	[A]: False positive and False negative rates. This validation step had a total of 21 mines and the expert and non expert users were asked to identify the locations of the mines and the results were collated from the validation process.; [B]: Error plot of estimated depth versus actual depth. Series 1 to Series 4 indicates the 4 general users. Also the linear trend line analysis has been included. . . . .	120

3.7	Actual burial depth, depth obtained from the <i>SIMCA</i> method, depth obtained from the Scheers's method for each of the targets, Actual position in the $x$ direction, position in the $x$ direction obtained from the <i>SIMCA</i> method, position in the $x$ direction obtained from the Scheers method. All values of depth and the position in the $x$ direction are in centimetres for Figure 3.17. The table also gives the percentage errors for both the <i>SIMCA</i> and Scheers algorithms and also the processing time for the algorithms in seconds. . . . .	121
3.8	Actual burial depth, depth obtained from the <i>SIMCA</i> method, depth obtained from the Scheers's method for each of the targets, Actual position in the $x$ direction, position in the $x$ direction obtained from the <i>SIMCA</i> method, position in the $x$ direction obtained from the Scheers method. All values of depth and the position in the $x$ direction are in centimetres for Figure 3.18. The table also gives the percentage errors for both the <i>SIMCA</i> and Scheers algorithms and also the processing time for the algorithms in seconds. . . . .	121
3.9	Actual burial depth, depth obtained from the <i>SIMCA</i> method, depth obtained from the Scheers's method for each of the targets, Actual position in the $x$ direction, position in the $x$ direction obtained from the <i>SIMCA</i> method, position in the $x$ direction obtained from the Scheers method. All values of depth and the position in the $x$ direction are in centimetres for Figure 3.19. The table also gives the percentage errors for both the <i>SIMCA</i> and Scheers algorithms and also the processing time for the algorithms in seconds. . . . .	122
3.10	Actual burial depth, depth obtained from the <i>SIMCA</i> method, depth obtained from the Scheers's method for each of the targets, Actual position in the $x$ direction, position in the $x$ direction obtained from the <i>SIMCA</i> method, position in the $x$ direction obtained from the Scheers method. All values of depth and the position in the $x$ direction are in centimetres for Figure 3.20. The table also gives the percentage errors for both the <i>SIMCA</i> and Scheers algorithms and also the processing time for the algorithms in seconds. . . . .	123
3.11	Actual burial depth, depth obtained from the <i>SIMCA</i> method, depth obtained from the Scheers's method for each of the targets, Actual position in the $x$ direction, position in the $x$ direction obtained from the <i>SIMCA</i> method, position in the $x$ direction obtained from the Scheers method. All values of depth and the position in the $x$ direction are in centimetres for Figure 3.21. The table also gives the percentage errors for both the <i>SIMCA</i> and Scheers algorithms and also the processing time for the algorithms in seconds. . . . .	124



- 3.12 Actual burial depth, depth obtained from the *SIMCA* method, depth obtained from the Scheers's method for each of the targets, Actual position in the  $x$  direction, position in the  $x$  direction obtained from the *SIMCA* method, position in the  $x$  direction obtained from the Scheers method. All values of depth and the position in the  $x$  direction are in centimetres for Figure 3.22. The table also gives the percentage errors for both the *SIMCA* and Scheers algorithms and also the processing time for the algorithms in seconds. . . . . 125
- 3.13 Actual burial depth, depth obtained from the *SIMCA* method, depth obtained from the Scheers's method for each of the targets, Actual position in the  $x$  direction, position in the  $x$  direction obtained from the *SIMCA* method, position in the  $x$  direction obtained from the Scheers method. All values of depth and the position in the  $x$  direction are in centimetres for Figure 3.23. The table also gives the percentage errors for both the *SIMCA* and Scheers algorithms and also the processing time for the algorithms in seconds. . . . . 126
- 3.16 Actual burial depth, depth obtained from the *SIMCA* method, depth obtained from the Scheers's method for each of the targets, Actual position in the  $x$  direction, position in the  $x$  direction obtained from the *SIMCA* method, position in the  $x$  direction obtained from the Scheers method. All values of depth and the position in the  $x$  direction are in centimetres for Figure 3.27. The table also gives the percentage errors for both the *SIMCA* and Scheers algorithms and also the processing time for the algorithms in seconds. . . . . 126
- 3.14 Actual burial depth, depth obtained from the *SIMCA* method, depth obtained from the Scheers's method for each of the targets, Actual position in the  $x$  direction, position in the  $x$  direction obtained from the *SIMCA* method, position in the  $x$  direction obtained from the Scheers method. All values of depth and the position in the  $x$  direction are in centimetres. The table also gives the percentage errors for both the *SIMCA* and Scheers algorithms and also the processing time for the algorithms in seconds; [A]: for Figure 3.26; [B]: for Figure 3.24. The table also gives the percentage errors for both the *SIMCA* and Scheers algorithms and also the processing time for the algorithms in seconds. . . . . 127
- 3.15 Actual burial depth, depth obtained from the *SIMCA* method, depth obtained from the Scheers's method for each of the targets, Actual position in the  $x$  direction, position in the  $x$  direction obtained from the *SIMCA* method, position in the  $x$  direction obtained from the Scheers method. All values of depth and the position in the  $x$  direction are in centimetres for Figure 3.25. The table also gives the percentage errors for both the *SIMCA* and Scheers algorithms and also the processing time for the algorithms in seconds. . . . . 128

3.17	Summary statistics for burial depth (1). All values in cm. <i>Difference_SIMCA</i> and <i>Difference_Scheers</i> is the difference between the ground truth value and the estimated value from the <i>SIMCA</i> algorithm and Scheers respectively. <i>Root_mean_square_difference</i> is found using $\sqrt{(d * d / N)}$ where $d$ is the values of the differences between the estimated values and the ground truth and $N$ is the total number of differences. . . . .	130
3.18	Summary statistics for burial depth (2). All values in cm. . . . .	131
3.19	Summary statistics for position in the $x$ direction (1). All values in cm. . . . .	133
3.20	Summary statistics for position in the $x$ direction (2). All values in cm. . . . .	134
4.1	[A]: Actual burial depth, depth obtained from the <i>SIMCA</i> method, depth obtained from the Scheers's method for each of the targets in centimetres for Figure 4.10. The table also gives the percentage errors for both the <i>SIMCA</i> and Scheers algorithms; [B]: Actual Volume, Volume of reconstructed target for <i>SIMCA</i> system, Volume of reconstructed target for Scheers algorithm, and processing time (CPU time) for Figure 4.10. The volumes are in cubic centimetres and the processing time is in seconds. . . . .	157
4.2	[A]: Actual burial depth, depth obtained from the <i>SIMCA</i> method, depth obtained from the Scheers's method for each of the targets in centimetres for Figure 4.13. The table also gives the percentage errors for both the <i>SIMCA</i> and Scheers algorithms. ; [B]: Actual Volume, Volume of reconstructed target for <i>SIMCA</i> system, Volume of reconstructed target for Scheers algorithm, and processing time (CPU time) for Figure 4.13. The volumes are in cubic centimetres and the processing time is in seconds. . . . .	163
4.3	[A]: Actual burial depth, depth obtained from the <i>SIMCA</i> method, depth obtained from the Scheers's method for each of the targets in centimetres for Figure 4.16. The table also gives the percentage errors for both the <i>SIMCA</i> and Scheers algorithms; [B]: Actual Volume, Volume of reconstructed target for <i>SIMCA</i> system, Volume of reconstructed target for Scheers algorithm, and processing time (CPU time) for Figure 4.16. The volumes are in cubic centimetres and the processing time is in seconds. . . . .	165
4.4	[A]: Actual burial depth, depth obtained from the <i>SIMCA</i> method, depth obtained from the Scheers' method for each of the targets in centimetres for Figure 4.17. The table also gives the percentage errors for both the <i>SIMCA</i> and Scheers algorithms; [B]: Actual Volume, Volume of reconstructed target for <i>SIMCA</i> system, Volume of reconstructed target for Scheers' algorithm and processing time (CPU time) for Figure 4.17. The volumes are in cubic centimetres and the processing time is in seconds. The table also gives the percentage errors for both the <i>SIMCA</i> and Scheers algorithms. . . . .	167

4.5	[A]: Actual burial depth, depth obtained from the <i>SIMCA</i> method, depth obtained from the Scheers's method for each of the targets in centimetres for Figure 4.19. The table also gives the percentage errors for both the <i>SIMCA</i> and Scheers algorithms; [B]: Actual Volume, Volume of reconstructed target for <i>SIMCA</i> system, Volume of reconstructed target for Scheers algorithm, and processing time (CPU time) for Figure 4.19. The volumes are in cubic centimetres and the processing time is in seconds. . . . .	171
4.6	[A]: Actual burial depth, depth obtained from the <i>SIMCA</i> method, depth obtained from the Scheers's method for each of the targets in centimetres for Figure 4.21. The table also gives the percentage errors for both the <i>SIMCA</i> and Scheers algorithms; [B]: Actual Volume, Volume of reconstructed target for <i>SIMCA</i> system, Volume of reconstructed target for Scheers algorithm, and processing time (CPU time) for Figure 4.21. The volumes are in cubic centimetres and the processing time is in seconds. . . . .	173
4.7	[A]: Actual burial depth, depth obtained from the <i>SIMCA</i> method, depth obtained from the Scheers's method for each of the targets in centimetres for Figure 4.23. The table also gives the percentage errors for both the <i>SIMCA</i> and Scheers algorithms; [B]: Actual Volume, Volume of reconstructed target for <i>SIMCA</i> system, Volume of reconstructed target for Scheers algorithm, and processing time (CPU time) for Figure 4.23. The volumes are in cubic centimetres and the processing time is in seconds. . . . .	176
4.8	[A]: Actual burial depth, depth obtained from the <i>SIMCA</i> method, depth obtained from the Scheers's method for each of the targets in centimetres for Figure 4.26. The table also gives the percentage errors for both the <i>SIMCA</i> and Scheers algorithms; [B]: Actual Volume, Volume of reconstructed target for <i>SIMCA</i> system, Volume of reconstructed target for Scheers algorithm, and processing time (CPU time) for Figure 4.26. The volumes are in cubic centimetres and the processing time is in seconds. . . . .	180
4.9	[A]: Actual burial depth, depth obtained from the <i>SIMCA</i> method, depth obtained from the Scheers's method for each of the targets in centimetres for Figure 4.28. The table also gives the percentage errors for both the <i>SIMCA</i> and Scheers algorithms; [B]: Actual Volume, Volume of reconstructed target for <i>SIMCA</i> system, Volume of reconstructed target for Scheers algorithm, and processing time (CPU time) for Figure 4.28. The volumes are in cubic centimetres and the processing time is in seconds. . . . .	183

4.10	[A]: Actual burial depth, depth obtained from the <i>SIMCA</i> method, depth obtained from the Scheers's method for each of the targets in centimetres for Figure 4.30. The table also gives the percentage errors for both the <i>SIMCA</i> and Scheers algorithms; [B]: Actual Volume, Volume of reconstructed target for <i>SIMCA</i> system, Volume of reconstructed target for Scheers algorithm, and processing time (CPU time) for Figure 4.30. The volumes are in cubic centimetres and the processing time is in seconds. . . . .	187
4.11	[A]: Actual burial depth, depth obtained from the <i>SIMCA</i> method, depth obtained from the Scheers's method for each of the targets in centimetres for Figure 4.32. The table also gives the percentage errors for both the <i>SIMCA</i> and Scheers algorithms; [B]: Actual Volume, Volume of reconstructed target for <i>SIMCA</i> system, Volume of reconstructed target for Scheers algorithm, and processing time (CPU time) for Figure 4.32. The volumes are in cubic centimetres and the processing time is in seconds. . . . .	190
4.12	[A]: Actual burial depth, depth obtained from the <i>SIMCA</i> method, depth obtained from the Scheers's method for each of the targets in centimetres for Figure 4.34. The table also gives the percentage errors for both the <i>SIMCA</i> and Scheers algorithms; [B]: Actual Volume, Volume of reconstructed target for <i>SIMCA</i> system, Volume of reconstructed target for Scheers algorithm, and processing time (CPU time) for Figure 4.34. The volumes are in cubic centimetres and the processing time is in seconds. . . . .	192
4.13	[A]: Actual burial depth, depth obtained from the <i>SIMCA</i> method, depth obtained from the Scheers's method for each of the targets in centimetres for Figure 4.36. The table also gives the percentage errors for both the <i>SIMCA</i> and Scheers algorithms.; [B]: Actual Volume, Volume of reconstructed target for <i>SIMCA</i> system, Volume of reconstructed target for Scheers algorithm, and processing time (CPU time) for Figure 4.36. The volumes are in cubic centimetres and the processing time is in seconds. . . . .	196
4.19	Actual volume, volume from <i>SIMCA</i> reconstructed isosurface to test the sensitivity of <i>SIMCA</i> algorithm to depth and permittivity changes when building a kernel, Percentage error. For [A]: Simulated target depth at 5.1cm and using correct soil parameters; [B]: Simulated target depth at 6cm and using correct soil parameters; [C]: Simulated target depth at 12cm and using correct soil parameters; [D]: correct simulated target depth but wrong soil parameters for Figure 4.40. All volumes are in cubic centimetres. . . . .	199

4.20	Actual volume, volume from <i>SIMCA</i> reconstructed isosurface to test the sensitivity of <i>SIMCA</i> algorithm to depth and permittivity changes when building a kernel, Percentage error. For [A]: Simulated target depth at 5.1cm and using correct soil parameters; [B]: Simulated target depth at 6cm and using correct soil parameters; [C]: Simulated target depth at 12cm and using correct soil parameters; [D]: correct simulated target depth but wrong soil parameters for Figure 4.42. All volumes are in cubic centimetres. . . . .	199
4.14	Actual volume, volume from <i>SIMCA</i> reconstructed isosurface to test the sensitivity of <i>SIMCA</i> algorithm to depth and permittivity changes when building a kernel, Percentage error. For [A]: Simulated target depth at 5.1cm and using correct soil parameters; [B]: Simulated target depth at 6cm and using correct soil parameters; [C]: Simulated target depth at 12cm and using correct soil parameters; [D]: correct simulated target depth but wrong soil parameters for Figure 4.37. All volumes are in cubic centimetres. . . . .	201
4.15	Actual volume, volume from <i>SIMCA</i> reconstructed isosurface to test the sensitivity of <i>SIMCA</i> algorithm to depth and permittivity changes when building a kernel, Percentage error. For [A]: Simulated target depth at 5.1cm and using correct soil parameters; [B]: Simulated target depth at 6cm and using correct soil parameters; [C]: Simulated target depth at 12cm and using correct soil parameters; [D]: correct simulated target depth but wrong soil parameters for Figure 4.38. All volumes are in cubic centimetres. . . . .	203
4.16	Actual volume, volume from <i>SIMCA</i> reconstructed isosurface to test the sensitivity of <i>SIMCA</i> algorithm to depth and permittivity changes when building a kernel, Percentage error. For [A]: Simulated target depth at 5.1cm and using correct soil parameters; [B]: Simulated target depth at 6cm and using correct soil parameters; [C]: Simulated target depth at 12cm and using correct soil parameters; [D]: correct simulated target depth but wrong soil parameters for Figure 4.41. All volumes are in cubic centimetres. . . . .	207
4.17	Actual volume, volume from <i>SIMCA</i> reconstructed isosurface to test the sensitivity of <i>SIMCA</i> algorithm to depth and permittivity changes when building a kernel, Percentage error. For [A]: Simulated target depth at 5.1cm and using correct soil parameters; [B]: Simulated target depth at 6cm and using correct soil parameters; [C]: Simulated target depth at 12cm and using correct soil parameters; [D]: correct simulated target depth but wrong soil parameters for Figure 4.49. All volumes are in cubic centimetres. . . . .	216

4.18	Actual volume, volume from <i>SIMCA</i> reconstructed isosurface to test the sensitivity of <i>SIMCA</i> algorithm to depth and permittivity changes when building a kernel, Percentage error. For [A]: Simulated target depth at 5.1cm and using correct soil parameters; [B]: Simulated target depth at 6cm and using correct soil parameters; [C]: Simulated target depth at 12cm and using correct soil parameters; [D]: correct simulated target depth but wrong soil parameters for Figure 4.39. All volumes are in cubic centimetres. . . . .	217
4.21	Actual volume, volume from <i>SIMCA</i> reconstructed isosurface to test the sensitivity of <i>SIMCA</i> algorithm to depth and permittivity changes when building a kernel, Percentage error. For [A]: Simulated target depth at 5.1cm and using correct soil parameters; [B]: Simulated target depth at 6cm and using correct soil parameters; [C]: Simulated target depth at 12cm and using correct soil parameters; [D]: correct simulated target depth but wrong soil parameters for Figure 4.43. All volumes are in cubic centimetres. . . . .	217
4.22	Actual volume, volume from <i>SIMCA</i> reconstructed isosurface to test the sensitivity of <i>SIMCA</i> algorithm to depth and permittivity changes when building a kernel, Percentage error. For [A]: Simulated target depth at 5.1cm and using correct soil parameters; [B]: Simulated target depth at 6cm and using correct soil parameters; [C]: Simulated target depth at 12cm and using correct soil parameters; [D]: correct simulated target depth but wrong soil parameters for Figure 4.44. All volumes are in cubic centimetres. . . . .	218
4.23	Actual volume, volume from <i>SIMCA</i> reconstructed isosurface to test the sensitivity of <i>SIMCA</i> algorithm to depth and permittivity changes when building a kernel, Percentage error. For [A]: Simulated target depth at 5.1cm and using correct soil parameters; [B]: Simulated target depth at 6cm and using correct soil parameters; [C]: Simulated target depth at 12cm and using correct soil parameters; [D]: correct simulated target depth but wrong soil parameters for Figure 4.45 . All volumes are in cubic centimetres. . . . .	218
4.24	Actual volume, volume from <i>SIMCA</i> reconstructed isosurface to test the sensitivity of <i>SIMCA</i> algorithm to depth and permittivity changes when building a kernel, Percentage error. For [A]: Simulated target depth at 5.1cm and using correct soil parameters; [B]: Simulated target depth at 6cm and using correct soil parameters; [C]: Simulated target depth at 12cm and using correct soil parameters; [D]: correct simulated target depth but wrong soil parameters for Figure 4.46. All volumes are in cubic centimetres. . . . .	219

4.25	Actual volume, volume from <i>SIMCA</i> reconstructed isosurface to test the sensitivity of <i>SIMCA</i> algorithm to depth and permittivity changes when building a kernel, Percentage error. For [A]: Simulated target depth at 5.1cm and using correct soil parameters; [B]: Simulated target depth at 6cm and using correct soil parameters; [C]: Simulated target depth at 12cm and using correct soil parameters; [D]: correct simulated target depth but wrong soil parameters for Figure 4.47. All volumes are in cubic centimetres. . . . .	219
4.26	Actual volume, volume from <i>SIMCA</i> reconstructed isosurface to test the sensitivity of <i>SIMCA</i> algorithm to depth and permittivity changes when building a kernel, Percentage error. For [A]: Simulated target depth at 5.1cm and using correct soil parameters; [B]: Simulated target depth at 6cm and using correct soil parameters; [C]: Simulated target depth at 12cm and using correct soil parameters; [D]: correct simulated target depth but wrong soil parameters for Figure 4.48. All volumes are in cubic centimetres. . . . .	220
4.27	Summary statistics for burial depth (1). All values in cm. . . . .	222
4.28	Summary statistics for burial depth (2). All values in cm. . . . .	223
4.29	Summary statistics for volume (1). All values in ( $cm^3$ ). . . . .	225
4.30	Summary statistics for volume (2). All values in ( $cm^3$ ). . . . .	226
4.31	Actual volume, volume from the <i>SIMCA</i> reconstructions for leaving slices as detailed from Figure 4.54 and percentage errors. All volumes are in cubic centimetres. . . . .	232
B.1	The processing steps used in the <i>REFLEXW</i> software. . . . .	267
B.2	Position in the $x$ -direction from the Architect drawings, Burial depth from Architect drawings and corresponding values produced by the <i>SIMCA</i> algorithm, Scheers algorithm and the <i>REFLEXW</i> commercial software. The table also gives the percentage error for the three methods when compared to the ground truth. The dimensions are in centimetres for the position in the $x$ direction and centimetres for the depth. . . . .	273
B.3	Actual position in the $x$ -direction, actual position in the $y$ -direction, actual burial depth and corresponding values produced by the <i>SIMCA</i> algorithm, Scheers algorithm and the <i>REFLEXW</i> commercial software. The table also gives the Percentage error for the three methods when compared to the ground truth. The positions in the $x$ and $y$ directions are in centimetres and the depth is in centimetres. . . . .	279

# List of Algorithms

1	<i>SIMCA</i> 3D Algorithm to consider spacing in $x$ , $y$ and $z$ directions. The full version of the <i>SIMCA</i> algorithm can be found in Appendix A and also by going to the following url: <a href="https://sites.google.com/site/3dsimcaalgorithm/">https://sites.google.com/site/3dsimcaalgorithm/</a> . . . . .	149
2	<i>SIMCA</i> 3D Algorithm to consider spacing in $x$ , $y$ and $z$ directions. . . . .	256
3	<i>SIMCA</i> 3D Algorithm to consider spacing in $x$ , $y$ and $z$ directions continued from above. . . . .	257
4	<i>SIMCA</i> 3D Algorithm to consider spacing in $x$ , $y$ and $z$ directions continued from above. . . . .	258
5	Algorithm to specify meshgrid function. . . . .	259
6	Algorithm to specify interpolation function. . . . .	260
7	Algorithm specifying how correlation is carried out. . . . .	261



# Chapter 1

## Introduction

*This chapter provides an introduction to the problem area, then presents the motivation for this work, followed by the hypothesis, the contributions made by this PhD thesis; the publications are then presented. Finally the chapter outlines the overview of the thesis.*

### 1.1 Context and Motivation

Landmines pose a constant threat to humans and are a global problem (International Campaign, 2011). The first reported use of a weapon similar to the landmine was in the fifteenth century at the battlefield of Agincourt in northern France (International Campaign, 2011). After that they were in use during the American Civil war. The first modern antitank mines that had a mechanical fuse were introduced by Imperial Germany in World War I. A further historical overview of landmines is given in Chapter 2, Section 2.1. The details about *antitank mines* (ATMs) is given in Section 1.2.1.1 of this chapter. Section 1.2.1.2 gives information about *antipersonnel mines* (APMs). The details of the actual APMs used in the laboratory setups are outlined in Chapters 3 and 4.

The United Nations estimates that there are currently 85 to 90 million landmines buried in 70 different countries.<sup>1</sup> Figure 1.1 illustrates the global distribution of landmines. These landmines each year claim about 26,000 victims and the sad thing is many of these victims are innocent children.<sup>2</sup> They also have a severe impact on military personnel and there have been the unfortunate deaths of UK military personnel in Afghanistan and Iraq. In 2009 there were 7,288 attacks in Afghanistan, a 120% increase over 2008 and a record for the war. For the UK military this reflected 221 military deaths out of a total of 417 deaths in Afghanistan that were caused by *Improvised Explosive Devices* (IEDs).<sup>3</sup> The production of one APM costs \$1, but their removal once deployed costs more than \$1000 to search, find and then destroy them (United Nations, 2011). Landmines have significant medical, psychological and economic consequences on humans and affected areas.

Here is a quote from a landmine victim which shows the unfortunate consequence of landmines:  
“After the blast I saw smoke ... I was on the ground and didn’t know what had happened. It was

---

<sup>1</sup>International Campaign to ban landmines, 2011 - <http://www.icbl.org>

<sup>2</sup><http://www.mineaction.org>

<sup>3</sup>BBC News Website, 2012. <http://www.bbc.co.uk/news/uk-15188729>.

only when I tried to move that I realized I was bleeding.” Lay Sokhum, 2004.

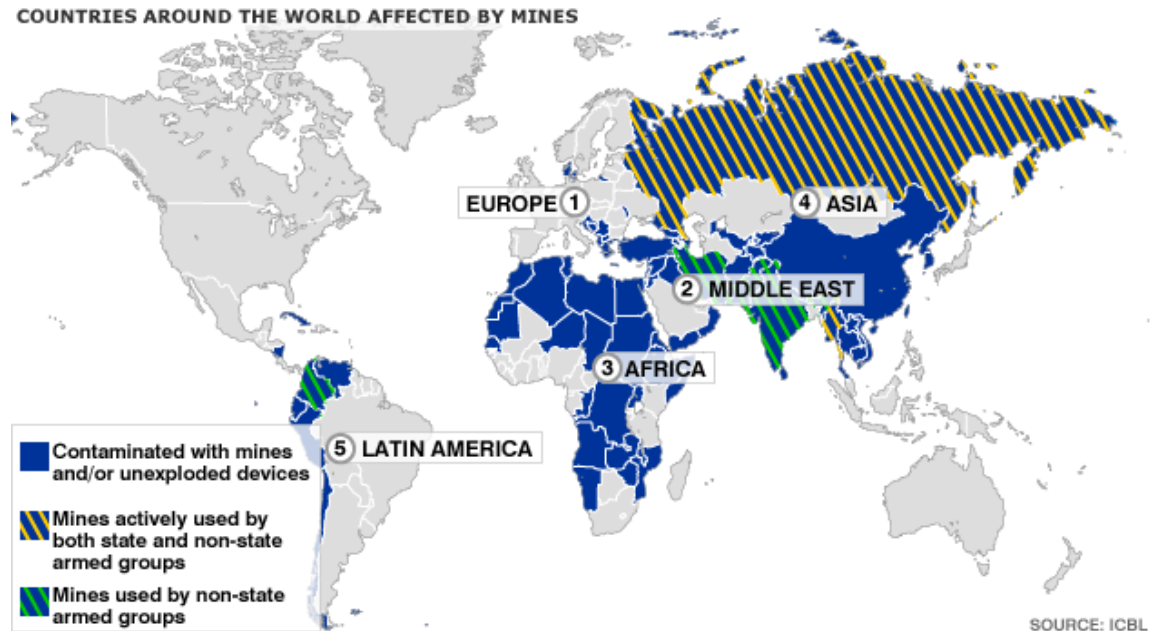


Figure 1.1: Countries around the world affected by mines.  
(BBC news website)

Since the 1980s many countries have worked on the landmine problem. On 1 March 1999, *the Convention on the Prohibition of the Use, Stockpiling, Production and Transfer of APMs and on their Destruction* or the **Ottawa Treaty** came into force. As of September 2011, 158 countries or 80 percent of the world’s nations have joined the 1997 Mine Ban Treaty which seeks to eradicate the use of landmines. An additional two states have signed but not yet ratified whilst 35 UN states are non-signatories (United Nations, 1997). The world’s newest state, South Sudan, and the Pacific island nation of Tuvalu are the most recent countries to join. Whilst the ‘Ottawa Convention’ has been signed by 135 and ratified by 84 states worldwide, out of this 14 EU Member states have signed and 13 have ratified.

Although the ‘Ottawa Convention’ prevents new mines to be laid, the real problem is the clearance of landmine contaminated areas from past wars. This involves the detection, identification and clearance of landmines and is known as *humanitarian demining* (Abujarad, 2007).

Therefore reducing the death caused by these lethal targets is a vital global requirement. The motivation for this thesis was therefore to help demining personnel detect and clear landmines and thus to reduce the unfortunate deaths. Furthermore, during the beginning of this PhD research it was hoped that the development of algorithms to help with landmine clearance could also be used in other settings such as archaeological applications and a further motivation of this PhD research was to try and test the **SIMCA** (“**SIM**ulated **COR**relation **AL**gorithm”) algorithm on other application areas.

## 1.2 Background

The detection and clearance of landmines can be achieved by the development of equipment with in built advanced algorithms such as the *SIMCA* algorithm. The detection of minimum-metal mines buried in sand and soil is not adequately addressed by the state-of-the-art in signal processing algorithms (Daniels, 2004). The clutter background is highly existent and the surface is both lossy and dispersive (Daniels, 2004). The vast literature into the different clutter removal techniques is discussed in Chapter 2. The equipment used for sustainable humanitarian demining has to be portable due to the severe environment the de-miners work in ((Daniels, 2004); (Ackenhusen et al., 2001); (Carin et al., 1999); (Feng and Sato, 2005); (Jol, 1994)). Signal and image processing algorithms used for such a demining task must aid the user in achieving very high levels of detection, which is currently 99.9% (United Nations, 1997). Also it is very important that the false alarm rates be reduced and false-alarm rates in Afghanistan, approach 1,000:1 (Eblagh, 1996).

One of the biggest challenges facing the deminer is the actual detection of the landmine. This is a challenging procedure for the deminer, unless he is equipped with an advanced algorithm. Once the mine has been detected, the deminers can explode, mark or move it to a pit for diffusion or detonation.

The conventional way of detecting land mines using a metal detector is difficult because ((Daniels, 2004); (Jol, 1994)):

1. Mines are now becoming plastic in nature and these minimum to no metal mines are not detected using the metal detector.
2. Mine areas have metal scraps and false targets that create a high false alarm rate (about 99.95%) (Daniels, 2004).

The first successful use of Ground Penetrating Radar (GPR) dates back to the early 1930s and was used as a technique for ice depth probing (Stern, 1930). A further outline of the various demining techniques are outlined in Chapter 2, Section 2.3.

Because of the fact that metal detectors cannot detect minimum metal mines, GPRs are preferred over metal detectors because modern landmines are non metallic in nature ((Abujarad, 2007); (Annan, 1993); (Bruschini et al., 1998); (Carin et al., 1999); (Chen et al., 2001)). The operation of a GPR is that a transmitting antenna emits electromagnetic (EM) waves into the ground and a receiver senses the reflected waves from targets under the ground (Daniels, 2004). The GPR senses reflected EM waves that a target creates and is captured by the receiver (Figure 1.2). The GPR can thus be used as an imaging sensor whereby a focussed 2D or 3D image of the subsurface can be formed from a number of scans measured over a grid (Daniels, 2004). The focussed image can be used to detect and locate targets that lie in the subsurface.

But the unfortunate caveat is the source of error in the GPR data that occurs due to the cluttered reflection from the surface of the ground, antenna coupling, system ringing and soil reflections that prevent the proper detection of the object (Daniels, 2004). Therefore such clutter issues need to be addressed by the application of signal processing techniques that present an image that can be easily understood and interpreted by the demining personnel. (Chen et al. (2000); van der Merwe

and Gupta (2000); Karlsen et al. (2001); Gader et al. (2001a); van Kempen and Sahli (2001)) present some studies carried out in the field of GPR systems.

In addition the beam pattern of the antenna is widely spread and this causes degradation of the spatial resolution of the image, unless it is corrected. This correction is called *migration* and the goal of migration is to focus the reflection footmarks in the recorded data back to their true positions. This is discussed in detail in Chapters 2, 3 and 4.

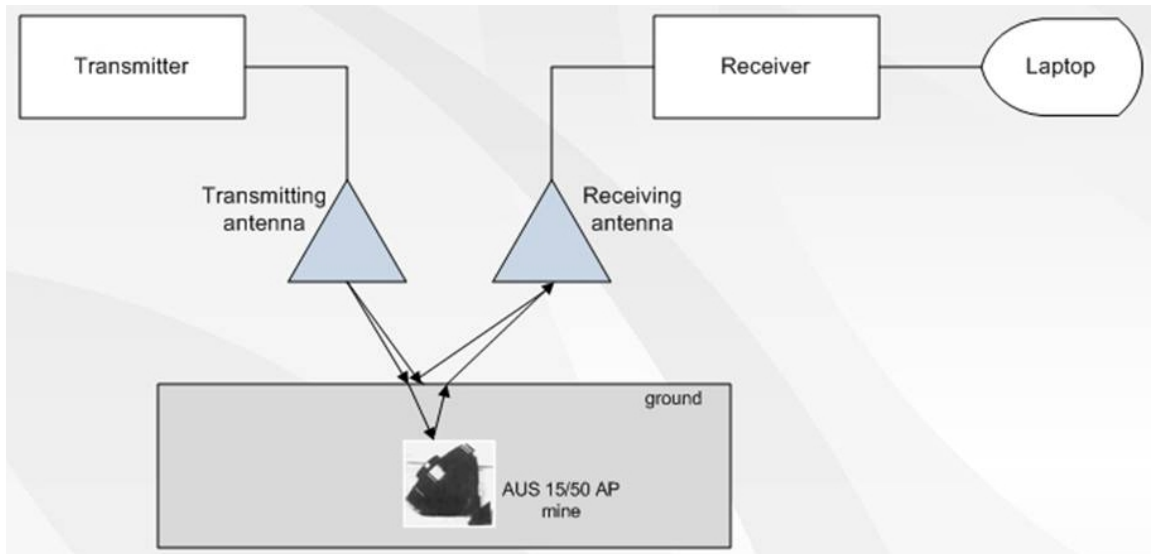


Figure 1.2: A diagrammatic representation of a GPR showing the transmitter and the receiver.  
(Adopted from MacDonald and Lockwood (2003))

The potential benefits of using a GPR in landmine and target detection are ((Daniels, 2004); (Jol, 1994)):

- The reduction of the false alarm rate by target identification<sup>4</sup> on the basis of measured target responses.
- The ability to detect surface laid and buried landmines.
- The ability to detect plastic and metallic cased landmines. This is because GPRs detect changes in the types of materials.
- The ability to determine the depth and horizontal position of an object.
- The possibility of scanning the ground with the antennas at a safe distance from the ground. This is particularly important in landmine clearance because the deminer would not want to place the head of the GPR on the ground for fear of triggering the landmine.

<sup>4</sup>Identification is the process of estimating if a detected object is a landmine and this usage is what is given by the IEEE Standard definition of identification

- The fact that the GPR can be combined with other sensor technology. Other sensor technologies include the integration of the GPR with a Metal detector for example. Other sensor technologies are discussed in detail in Chapter 2.

Three data processing steps are usually used by GPR practitioners to help in the clearance of landmines (MacDonald and Lockwood, 2003) (Figure 1.3):

1. The detection of the landmines - elimination of signals without object information.
2. The identification of the landmines.
3. The classification of the landmines.

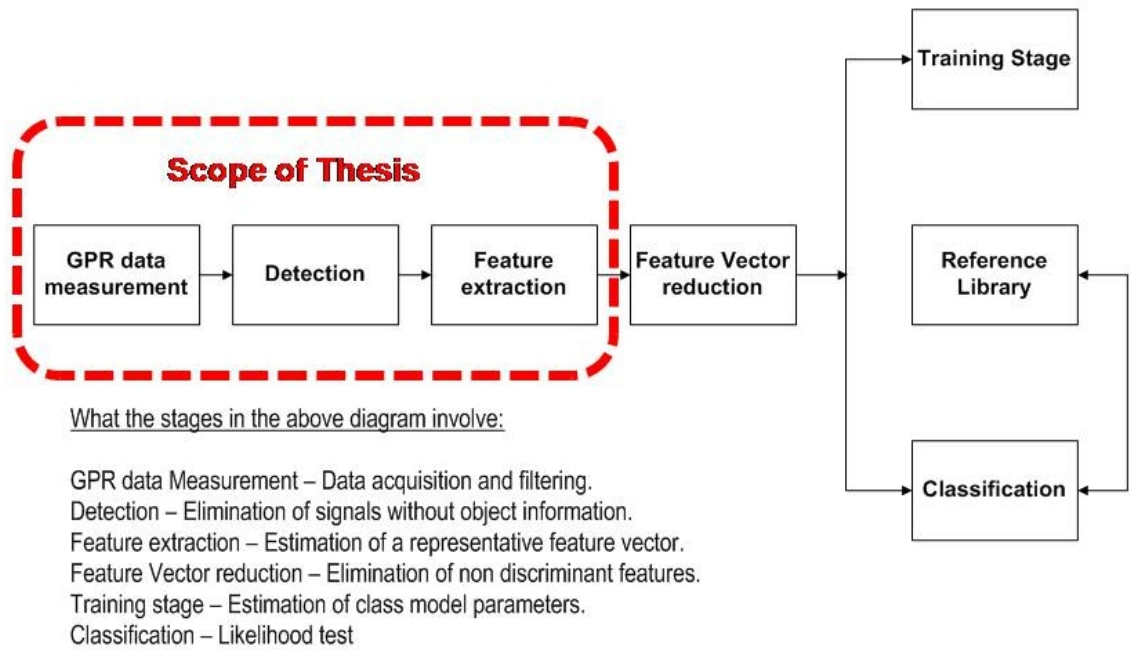


Figure 1.3: The stages in the location and classification of targets and also a diagram giving the scope of this PhD thesis.

*Detection* is the “process of judging whether an object is buried” whereas *identification* is the “process of estimating whether a detected object is a landmine” (Roth, 2004). Figure 1.3 shows the stages in the location and classification of targets and it is important to note that the complete process is an extremely large and vast research field. GPR researchers usually concentrate on either the detection process or the identification process due to the vastness of this research topic. As illustrated in Figure 1.3, the scope of this thesis is restricted to the detection stage and as is shown finally in Chapter 5, the actual identification process can be a future study beyond this PhD research.

Bearing this in mind, through the course of the PhD research and in this PhD thesis *receiver operator characteristic* (ROC) curves are not considered using various thresholds because this is mainly used during the identification or classification stages. Furthermore, as detailed in Chapters 3 and 4, human operators are used to validate the *SIMCA* algorithm and not an automated approach;

therefore removing the need to use ROC curves. The reason as to why human operators are used as opposed to an automated approach is detailed in Chapter 4, Section 4.13.

### 1.2.1 Classification of Mines

There are a vast variety of mines that have been manufactured and laid. According to the potential target, mines can be classified into *ATMs* and *APMs*. Antitank mines are large, generally 20-30cm in diameter whereas antipersonnel mines range from approximately 5-15cm in diameter. The author has received data from colleagues who have conducted research into landmine detection by burying various mines in a laboratory sandbox. A list and details of the various mines buried by researchers acquiring data in the sandbox are given in Chapters 3 and 4. However, a considerable number of landmines are made in an artisan way by various guerrilla forces such as those based in Colombia. Such low cost mines are also called *improvised explosive devices* (IEDs). Table 1.1 gives the typical specification of three different types of mines. It is to be noted that the values given for the detonation pressure in kg is the minimum pressure required to detonate the most sensitive mine in each category. *Unexploded ordnances* (UXO) are explosive weapons that have not exploded when they were buried, but still pose a risk of exploding. A major problem with UXOs are that over the time they were buried in the soil, the detonator and main charge deteriorate and make them more sensitive to disturbance and hence more dangerous to remove.

#### 1.2.1.1 Anti-tank Mine (ATM)

Most ATMs are made of metal and their size is bigger than that of APMs. They are designed mainly to destroy vehicles and hence their detonation pressure is very high and they also produce large metallic splinters after they explode. Figure 1.4 shows an example of an ATM mine.



Figure 1.4: A Russian TM-46 anti-tank blast mine.  
(Cameo Landmine clearance)

#### 1.2.1.2 Anti-personnel Mine (APM)

APMs are the most difficult type of mine to locate and remove, and cause unfortunate deaths to civilians. These mines are made of non-metallic material and are much smaller than ATMs. Their

detonators are so sensitive that less than 10kg of pressure cause them to explode. APMs are divided into three types:

- **Blasting** - These are the most common types of mines encountered during humanitarian demining work. They are much smaller and lighter than the other types of mines. They are also buried underground, although some can be scattered by airplane or floated on a river. Because of their simple mechanism and low cost material, small military groups can easily manufacture such types of mines.
- **Directional fragmentation** - Most of these mines are deployed on the surface and during explosion the fragments spread in a specific direction. The lethal range of some models can reach over 200m. They are detonated by manual operation as well as a trip wire, and hence are considered as an active weapon.
- **Bounding fragmentation** - These are much larger than the blasting types and can destroy a larger area, whilst the blasting type of mines only causes damage to a target within a limited distance. These mines can be either buried under the ground or be deployed on the surface. Direct pressure or a trip wire activates the mines' detonators. They tend to bounce up to a given height and explode with their fragments spreading into an area of up to 30m radius, once their trigger is activated.

Figure 1.5 gives examples of 2 of the 3 above types of APMs.

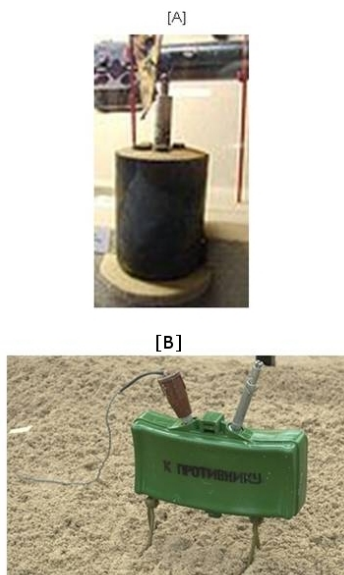


Figure 1.5: Typical APMs: [A]: Bounding mine - German S-Mine; [B]: A directional mine - Russian MON-50.

(Cameo Landmine clearance)

<i>Type</i>	<i>UXO</i>	<i>ATM</i>	<i>APM</i>
<i>Target</i>	Unspecified, general	Vehicle	Human
<i>Weight</i>	Various	Heavy (6 -11 kg)	Light (0.1 - 4kg)
<i>Size (in diameter)</i>	Various	Large (13-40cm)	Small (6-15 cm)
<i>Case material</i>	Mostly metal	Metal, plastic	Metal, plastic
<i>Detonation pressure</i>	Unpredictable	120kg	0.5kg

Table 1.1: Typical Specifications of three different types of mines.  
(Norwegian Aid, 2008)

A hand held landmine detector has to detect Anti-tank mines at depths as great as 30cm and Anti-personnel mines at depths as great as 10cm. Vehicle based systems, on the other hand, require a greater clearance of the ground.

### 1.2.2 Types of GPRs

The types of GPRs can be classified as:

1. **Time domain GPR** with an impulse system - Here the emitted energy pulse possesses a carrier frequency and is usually modulated with a square envelope. The GPR can operate in a limited range of frequency and has a monocycle (Daniels, 2004).
2. The **Ultra Wideband (UWB)** GPR is another time domain system in which the emitting energy is a pulse which does not have a carrier frequency. Therefore the spectral band of the energy is large for such a system (Scheers, 2001).
3. **Frequency domain** GPRs transmit a signal that has a changing carrier frequency. The carrier frequency can be modulated with a variable or linear sweep ((van Kempen, 2006); (Martel, 2001); (van den, 2006)).

Figure 1.6 shows diagrammatically the types of GPRs. The single channel radar used by some equipment manufacturers are based on the impulse radar. Furthermore, designs for multi-channel radar systems can be used on a vehicle. An in depth discussion of the common single channel and multi-channel radar systems are given in Chapter 2, Section 2.5.

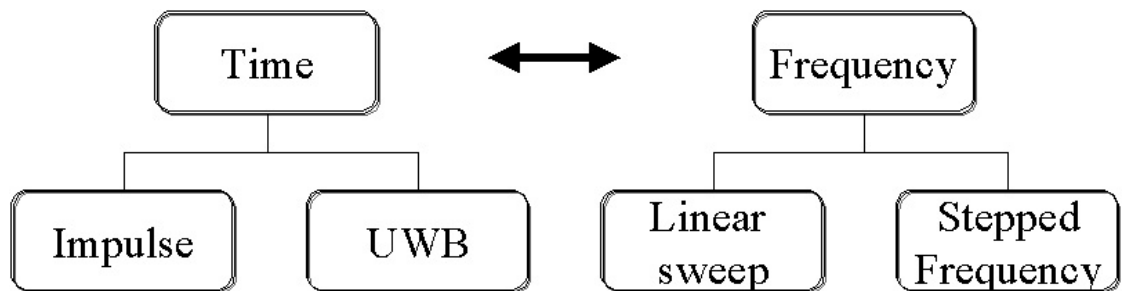


Figure 1.6: Types of GPRs.  
(van Kempen et al., 1999)



## 1.3 Hypothesis

The following hypothesis is established:

*This thesis argues that if the system aspects of the radar as well as the physics of waveguides and the soil properties are taken into consideration, and a kernel<sup>5</sup> developed from these using GPR simulation, then by correlating the kernel against the clutter removed GPR data will produce a much clearer image of the landmines and IEDs than can be obtained by existing techniques.*

Therefore this necessitates the inclusion of system aspects of the GPR such as the waveform of the excitation source, the impulse response of the antennas, the antenna patterns and the characteristics of the ground. Then by using the above properties, the kernel can be generated using the above mentioned properties by the use of a GPR Simulator. The GPR simulator uses the above properties and finds the ideal trace by considering a point reflector placed in the same soil conditions as in the laboratory sandbox. That is during an initialization phase, *SIMCA* carries out radar simulation using the design parameters of the radar and the soil properties; and the trace which would be returned by a target under these conditions is then used to form a kernel. Then a comparison is made between the trace that would be returned by an ideal point reflector in the soil conditions at the site and the actual trace. The system correlates the kernel with the clutter removed data and produces 2D images and 3D images of the surface of subterranean objects detected. Further details are given in Chapters 2, 3 and 4. It can be said that what is being proposed is a mechanism which renders much clearer 2D and 3D GPR profiles that help the demining personnel detect and clear the lethal targets. This thesis is therefore a technique for clearing the cluttered images so that the images are interpretable by human users. The cluttered images are a major problem to the demining personnel in them being able to interpret the images and to successfully clear the landmines.

The above was further refined into a number of questions which had an additional number of objectives each of which is addressed separately in this thesis. The details for each of these will unfold in later chapters of this thesis.

### Research Question 1

A clutter removal technique has to be developed which removes various unwanted signals such as cross talk, initial ground reflection and antenna ringing.

Therefore how to remove the clutter which exists in the raw GPR trace?

#### • Objective 1

Identify the various clutter removal techniques. This is because GPR signals contain not only the response from a potential target, but also undesirable effects from antenna coupling, system ringing and soil reflections.

---

<sup>5</sup>A kernel is an array of coefficients used in filtering. The kernel is set prior to correlation so as to enhance a particular feature in an image.

**Research Question 2**

What technique can be used to re-focus the reflection footmarks in the recorded data back to their true positions?

- **Objective 2**

Identify the different techniques that are available to correct the beam pattern of the antenna which is widely spread and causes degradation of the spatial resolution of the image.

**Research Question 3**

What technique can be used to derive the ideal point reflector trace for a GPR?

- **Objective 3**

Establish how to derive the kernel which has the system aspects of the radar and the characteristics of the ground and how these features can be matched in the clutter removed GPR data.

**Research Question 4**

What 2D technique can be used to produce clearer 2D scans or B scans<sup>6</sup> and also corrects for the issue identified by Research Question 2?

- **Objective 4**

Establish how the techniques identified in Objectives 2 and 3 can be used to present clearer images to the demining personnel when applied to B scans. Also establish how these results can be validated to ensure that clearer images are produced.

**Research Question 5**

What 3D technique can be used to produce clearer 3D reconstructions and also correct the issue identified by Research Question 2?

- **Objective 5**

Establish how the identified techniques in Objectives 2 and 3 can be used to present clearer 3D reconstructions of the targets after scanning by a GPR. Also establish what validation procedure can be used to validate these results and to ensure that clearer images are produced.

## 1.4 Thesis Contributions and Publications

The main contributions of this work are summarised as follows:

---

<sup>6</sup>A B scan is a two dimensional array indexed by spatial distance in the  $x$  direction and time in the  $y$  direction, formed by abutting successive one dimensional arrays of returned energy readings indexed by time. Detailed descriptions of an A scan, a B scan and a C scan are outlined in Chapter 4, Section 4.1 and is shown diagrammatically in Figure 4.1.

- None of the techniques available report on using correlation based on template matching the kernel developed using actual GPR simulations against the clutter removed GPR data; instead they use convolution. A study by Sengodan et al. (2012) revealed correlation is better because it compensates for differences in gain and black level between the kernel and the area of the image being matched (Chapters 2, 3 and 4). Furthermore by using a kernel developed by using a point target buried in the same soil conditions using a GPR simulator, the complete GPR signature (antenna pattern) is obtained rather than part of the signature and this is really important as will be shown in Chapter 4, Section 4.14.1 whereby the use of only half a hyperbola produces in-accurate reconstructions. It is also going to be pointed out in Chapter 3, Section 3.8.1 that using a complete hyperbolic signature produces better localisations in the targets.
- *SIMCA* considers the fact that often the spatial separation between A scans that make up a B scan is typically smaller than, and not always an integer multiple of, the spatial separation between the B scans that make up a C scan (Chapter 4).
- The *SIMCA* algorithm is computationally less intensive than the method proposed by Scheers et al. (2000) because *SIMCA* algorithm only correlates between the intersecting parts of the kernel and the data for the 3D case; thus reducing the data by considering only the relevant sections. Therefore the *SIMCA* algorithm runs much faster than Scheers et al.'s method. (Chapters 3 and 4). For the 2D case the *SIMCA* algorithm is also faster than the Scheers et al. (2001) method.
- Since the *SIMCA* system uses the rendering mechanisms available in the open-source *ParaView*<sup>7</sup> software a flexible 3D isosurface of the targets, along with a flexible approach of rotating the isosurfaces and obtaining slices along a number of planes is produced (Chapters 4).
- The *SIMCA 3D* technique is able to obtain an accurate volume of the rendered mine as shown in the results and validation section (Section 4.6) of Chapter 4; existing techniques do not calculate the volume. Furthermore the estimation of the depth by the *SIMCA* algorithm is more accurate than that produced by Scheers et al. (2000) (Chapters 4).
- The *SIMCA* algorithm produces clearer images both in 2D and in 3D and this will be demonstrated in Chapters 3 and 4.
- Finally, although raising the brightness to an odd power  $>2$  to enhance the target/background separation is not new in image processing, none of the GPR techniques make use of this concept (Chapters 3 and 4).

---

<sup>7</sup>*ParaView* is open source software that runs on multiple platforms and performs the analysis and visualization of scientific data which can be either 2D or 3D (Squillacote, 2008) and <http://www.paraview.org/>.

### 1.4.1 Work published in Conference proceedings

A selection of the work presented in this thesis has been peer-reviewed and published in academic conference proceedings as follows:

- Sengodan, A., and Javadi, A., 2005. Landmine detection using masks on Ground Penetrating Radar images, *IRIS 2005 (Sengodan and Javadi, 2005)*. Chapters 2, 3 and 4 contain extracts from this paper.
- Sengodan, A., Cockshott, W. P., Cuenca-Garcia, C., May 2011. The *SIMCA* algorithm for processing Ground Penetrating Radar data and its use in locating foundations in demolished buildings, *2011 IEEE RadarCon conference*, Kansas City, USA (Sengodan et al., 2011). Appears in *IEEE Xplore*. Appendix B contains material from this paper.
- Sengodan, A., Cockshott, W. P., May 2012a. A 2D processing algorithm for detecting landmines using Ground Penetrating Radar data, *IRIS 2012*, Warsaw, Poland (Sengodan and Cockshott, 2012a). Appears in *IEEE Xplore*. Chapter 3 is partly based on material from this paper.
- Sengodan, A., Cockshott, W. P., July 2012b. The *SIMCA* algorithm for processing Ground Penetrating Radar data and its use in landmine detection, *ISSPA 2012*, Montreal, Canada (Sengodan and Cockshott, 2012b). Appears in *IEEE Xplore*. Chapter 3 covers material from this paper.
- Sengodan, A., Cockshott, W. P., Cuenca-Garcia, C., April 2013. A 3D reconstruction algorithm for the location of foundations in demolished buildings, *EUCAP 2013*, Gothenburg, Sweden (Sengodan et al., 2013). To appear in *IEEE Xplore*. Appendix B contains material from this paper.

### 1.4.2 Work to appear in Journal proceedings

The following journal paper has been submitted for consideration of being published:

- Sengodan, A., Cockshott, W. P., Siebert, J. P., 2012. An algorithm for 3D reconstruction from Ground-Penetrating Radar. *IEEE Trans. Geosci. Remote Sens.* (submitted under review) (Sengodan et al., 2012). Chapter 4 is based on material from this paper.

### 1.4.3 Prizes won

The author has won prizes in the following:

- Runner up prize (£1000) and a trophy - Best runner up poster in the 2009 Knowledge Transfer Conference, Heriot Watt University, Edinburgh.
- Runner up prize (£500) - Thales Scottish Technology Prize 2010, Thales Optronics, Glasgow, Scotland. The initial stages of a vehicle based multi array solution integrated with the *SIMCA*

algorithm was submitted to be developed fully with the help of Thales. But since the Glasgow facility specialized in Optronics solutions; the initial proposal couldn't be taken further.

- Selected and submitted to the judges in the 2010 Converge Challenge competition. But did not make it to the final to commercialize the *SIMCA* algorithm.
- Runner up in the Set for Britain poster competition 2012. A competition to showcase PhD work in the House of Commons, UK parliament.
- Runner up prize (£50) in the School of Computing Science Poster competition 2012, University of Glasgow.
- Won an travel bursary from the British Machine Vision Association and Society for Pattern Recognition (BMVA) to attend *IRIS 2012* in Warsaw, Poland.
- Winner of the UK ICT Pioneers Competition 2012 in the Transforming Society Category. The competition was run by the Engineering and Physical Sciences Research Council (Certificate and £2000).

#### 1.4.4 PATENT

The *SIMCA* algorithm was submitted to the Intellectual Property Manager of the Research and Enterprise team at the university for consideration of patenting the technology. But knowledge gained by the patent attorney who had discussions with the Deputy Director of the Patents Security section at the UK Intellectual Property Office (UKIPO) confirmed that a security order might be placed on the landmine detection invention/application should it be filed with the UKIPO. Therefore for humanitarian reasons to allow the free dissemination of the algorithm being impelled it was decided not to file for patent.

### 1.5 Overview of Thesis

This thesis is organised as follows and is represented as shown in Figure 1.7:

- Chapter 2 gives the background and the literature review for this research project.
- Chapter 3 presents the *SIMCA 2D* algorithm and then validates the *SIMCA 2D* algorithm.
- The *SIMCA 3D* algorithm and its validation are outlined in Chapter 4.
- Chapter 5 details the contributions of this research project and then draws the thesis to a conclusion. Potential future work is also suggested and discussed.
- Finally Appendix A lists the algorithms used in Chapter 4 to produce the 3D reconstruction of volumes of real targets using the *SIMCA 3D* algorithm after scanning by a GPR. The *SIMCA 2D* and *SIMCA 3D* algorithms are also tested on car park data and are conducted in Appendix B.

The next chapter gives the background and the literature review for this research project so that the key relevant studies in the area relevant to this PhD topic can be investigated.

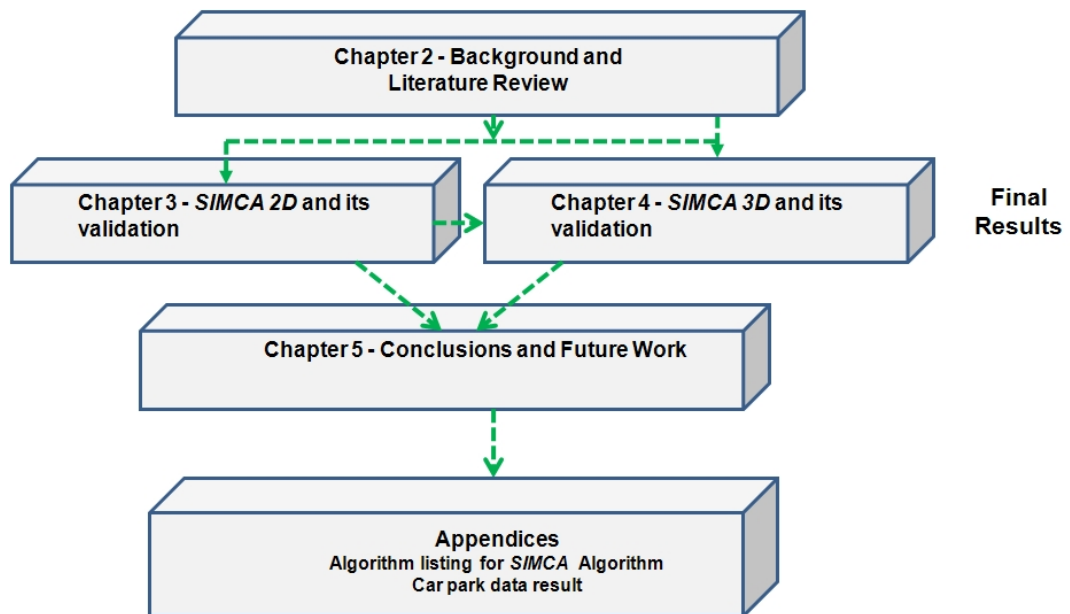


Figure 1.7: Thesis Overview.

## Chapter 2

# Background and Literature Review

*This chapter begins by discussing the history of landmines because the type of landmine material (plastic or metallic) and the characteristics of the target affects the ability of GPR to detect landmines. In the field of landmine detection the actual laying of the landmines is important, so the chapter addresses the laying mechanism used by the German army. These weapons of mass destruction are one of the worst environmental problems that face mankind and therefore the history of the various demining techniques from prodding to GPRs are next outlined. The chapter then goes on to address the important single and multi-array systems in the field. As it is well known that the performance of GPR is influenced mainly by soil dielectric permittivity, a discussion of this topic is vital. Then various existing methodologies in the field of GPR data processing are presented. The author has provided those technologies that are important and relevant to the scope of this thesis; because the area of signal and image processing is so extensive. The view by many of the practitioners in the field of GPR data processing is that signal processing is primarily a means of reducing clutter. GPR is heavily contaminated by clutter, and reduction of this is a key objective. One of the most important weapons in the processing armoury of the GPR user is migration, which is used for improving section resolution and developing more spatially realistic images of the subsurface and migration is discussed in this chapter. REFLEXW, a 2D processing and 2D/3D interpretation software developed by 'Sandmeier Scientific software' and GPR-SLICE, a GPR radar imaging software developed by 'Geophysical Archaeometry Laboratory Inc.' are the two main software programs available to GPR users so this chapter of the thesis presents an overview of the two pieces of software. The advantages and shortfalls of the approaches are discussed and the chapter concludes by suggesting ways to improve existing literature, in order to advance GPR data and image processing.*

### 2.1 History of Landmines

The word 'mine' originates from Latin where it is called *mina* and its meaning was 'vein of ore'. It was initially used to explain the excavation of minerals from the earth. This Latin word was then used by military personnel. In 1530 military forces conducted experiments in the use of landmines in Sicily. These landmines were called *fougasses* and were underground cannons that spat out rocks

and debris over a large area. These weapons were unreliable and the gunpowder they used absorbed water from the air and lost their explosive ability. Figure 2.1 shows a picture of the Fougasse mine.

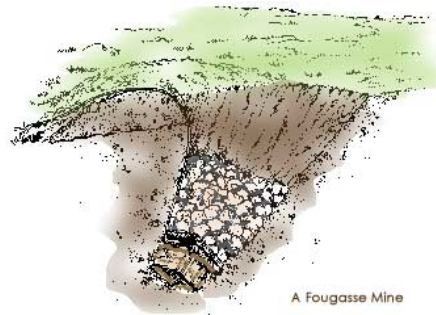


Figure 2.1: A Fougasse mine.

*(International Campaign to Ban Landmines (ICBL))*

The earliest description of a mine operated by pressure was given by the German military historian H. Frieher von Fleming in 1726. In a book he writes what a flying mine looked like. Here is his description: “It consisted of a ceramic container with glass and metal fragments embedded in the clay containing 0.90 kilos (2 lb) of gunpowder, buried at a shallow depth in the glacis of a fortress and actuated by someone stepping on it or touching a low strung wire.”

The first devices to explode on contact were the floating mines used by the US Confederate Navy in 1861 and are shown in Figure 2.2. They were used in a battlefield situation and were used to surprise the Union vanguard. They were made up of a steel tank, 122cm x 91.4cm broad and 25cm deep which contained scrap metal fragment. When a charge exploded the light sides of the case were blown out and the top directed the contents of the tank in a horizontal direction.

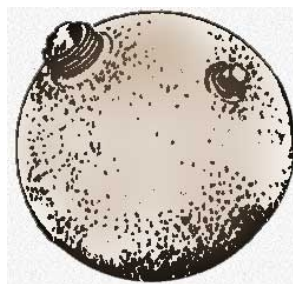


Figure 2.2: First mines used to explode on contact.

*(International Campaign to Ban Landmines (ICBL))*

The Americans were the first nation to develop and use operational antipersonnel mines and in 1862 a Brigadier-General commanded his troops to prepare artillery shells that explode by the pulling of a trigger or by being stepped on. A horse rider scouting along a road leading to Yorktown activated one of these mines and was the first person killed by a landmine operated by pressure. Such a mine is show in Figure 2.3.



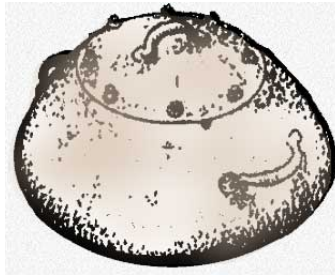


Figure 2.3: The first pressure mine.  
(*International Campaign to Ban Landmines (ICBL)*)

Antipersonnel landmines had been used by the military in all corners of the world until the 90s when the *Ottawa Treaty* banned them as stated in Chapter 1. They were used on a large scale during World War II. After that they found their use in other conflicts like the Vietnam War, first Gulf War and the Korean War. They aimed at maiming rather than killing a soldier. This is because it is more difficult to care for an injured soldier. Then after a while the unfortunate use of these weapons of mass destruction on civilians began. These mines terrorised communities and prevented the use of land.

The mines then appeared on a large scale in 1918, this was to try and combat American tanks. Germans had to design new weapons targeted at the American tanks. In early 1918, the Germans produced an antitank mine which was a wooden box, 45.7cm X 35.5cm X 20.3 cm high and which had 6.3 kilos of guncotton. The triggering was done by depressing a hinged lid that in turn operated a firing lever that was linked to a detonator. They were a defensive weapon that protected borders, camps or bridges and stopped advancing forces. The first modern antitank mines that had a mechanical fuse was introduced by Imperial Germany during World War I.

Initially the practice of marking and mapping mine fields was not followed strictly. It also became obvious that antipersonnel mines caused harm to the soldier of the forces laying the mines if the fields were not properly laid out. The German army took great care in laying and marking these minefields for their own records so as to manage the laying activity better and to protect their own forces. The next section details the laying mechanism used by the German army.

Furthermore, the processing of GPR data and its use in landmine detection is a key area of this thesis, therefore an understanding of the principles used in the laying of landmines is a topic which needs to be addressed. Thus the next section devotes some time to discuss and highlight that the laying of landmines is mostly done in a organized manner.

## 2.2 Laying of Landmines

### 2.2.1 Introduction

Having given the history of landmines and having noted that the first antitank mines were produced by Imperial Germany and also that the German army were careful in the laying of landmines and kept written mapped records of the laid landmines; it would seem natural now to discuss the method

used by the German Army. Information from a US War Department Handbook that was written about the German Military Forces is discussed below. This book was a revised and updated version of a original technical manual titled 'Handbook on German military forces' which was a US war department technical manual written on 15th March 1945 by Ambrose (1990).

### 2.2.2 Laying of Landmines used by the German Army

The German army made wide use of landmines because they felt that they were an effective defensive weapon. They thus took great care in laying minefields and kept confidential records of these minefields using maps. For maximum effect, in areas where they do not go directly and fight the enemy, they dispersed the mines in an irregular pattern. The major antitank mines were laid in a uniform pattern containing antitank mines with a small portion of antipersonnel mines in the front portion of the minefield. These mines were sometimes placed in the intervals between the diagonal wires of a double-apron fence and with trip wires fastened to the diagonals (Ambrose, 1990).

A number of antitank mines were laid in front of the antipersonnel mines to stop any armoured vehicles from triggering the main belt of antipersonnel mines. This is because the antipersonnel mines were meant for soldiers and not the armoured vehicle in some cases. In front of the lanes, the mines were widely spaced or scattered at random (Ambrose, 1990).

Mines were also laid in spacing that run out at  $90^0$  from the forward edge of the minefield, so as to damage vehicles moving along looking for the lanes of mines. To allow for the measurement of distance and spaces, the troops used a mine-measuring tape made from old telephone wire. The wires were usually 24m long, and every metre was marked with a wooden piece. Spaces between mines were determined with reference to the marks on the wires and to offset rows; the four rings on the ends of the wires were used for placing antitank mines. The density of a minefield was determined upon the interval between mines and the number of rows. The Germans usually laid mine belts in sections of 24m x 32m. When hasty withdrawal was necessary the Germans laid a large number of small nuisance minefields which were also difficult to locate and clear (Ambrose, 1990).

In general mines were laid close to or on roads, railways and along telegraph routes; however in a hasty retreat armed forces have been known to lay mines in any strategic location which will hamper the progression of the enemy (Ambrose, 1990). Places containing antitank mines were turnouts (a turn in a road) and sharp bends for example. The Germans took great care to ensure these mines were difficult to detect. They also buried the mines as much as 61cm below the surface where explosions occur only after a number of vehicles have passed and have exposed the fuze. Figure 2.4 shows a map of a typical German mine plan (Ambrose, 1990). S-Mines are also called APMs or Antipersonnel mines and Stock Mines are Antipersonnel mines buried in succession in Figure 2.4. The S-mine called 'Springmine' is also referred as "Bouncing Betty" is a bounding mine. When triggered the mine launches into the air and then triggers at about 0.9m. Shrapnel flies in all directions and inflict casualties.

The stock mine is an anti-personnel stake mine consisting of a cylindrical concrete main body on top of a short wooden stake. The concrete head contained igniting material like TNT and metal



## 2.3 History of demining techniques

The clearance of the landmines is an important part of mine action. Currently most of the humanitarian mine clearance activities are carried out using a combination of metal detectors, manual demining, dog and rodent detection. The widely used approaches for locating mines is metal detection and hand prodding.

Mine clearance was initially carried out using manual techniques and the Rake Excavation and Detection System ('REDS') relied on using rakes. A heavy rake was used to break up the ground and the light rake was used to move the loosened soil back as the excavations commenced. Then the exposed landmine was cleared. Then clearance was carried out using a mixture of manual excavation and metal detector work. They used a long-handled tool for the excavation and kept the users' hands away from close contact of the mines. But these were very dangerous activities and often the soldiers were killed.

Metal detection used by the deminers employs the same principles as those that were used in World War I and refined during World War II (Ackenhusen et al., 2001). Although all metallic objects are detected and identified by a metal detector (MacDonald and Lockwood, 2003), there is a problem when using these technologies to detect and identify the plastic landmines. The poorest performing detector found only 11% of mines in clayey soil and 5% in laterite soil (MacDonald and Lockwood, 2003). 'Laterites are soil layers that are rich in iron oxide and derived from a wide variety of rocks weathering under strongly oxidizing and leaching conditions' (MacDonald et al., 2003b). Furthermore the currently available landmines are made up of plastic parts and would not be detected by such sensors.

Daniels (1996) illustrates that using Ground Penetrating Radar is one of the most useful and innovative technologies for the detection and identification of plastic and low metal buried landmines. The above identified technologies are now going to be detailed.

### 2.3.1 Manual demining and Metal detectors

Here the deminer uses an electromagnetic induction metal detector and a prodding stick to explore every square centimetre of ground and this is illustrated in Figure 2.5. An audible alert is received via the metal detector upon the presence of a metallic object. The deminer then probes the ground using a prodding stick and to feel the side of the mine. This kind of demining can be applied everywhere and is normally reliable. Unfortunately, it is very dangerous, slow and an expensive procedure.

The metal detector operates on the principles of electromagnetic induction. The metal detector has one or more inductor coils that are used to induce a magnetic field. This magnetic field is emitted into the soil and then interacts with metallic elements in the ground. The field then induces an eddy current in the metallic object which induces their own magnetic field. 'If another coil is used to measure the electric field (acting as a magnetometer), the change in the magnetic field due to the metallic object can be detected' (MacDonald and Lockwood, 2003). As stated above also the metal detector can give a lot of false alarms because they are not able to distinguish between

landmines and junk or metal shrapnel's<sup>1</sup>. Metal detectors only identify the presence of an anomaly and do not give any information on whether the object is a landmine or not.

The demining crew initially clear a mined area of vegetation and then divide the area into lanes of about 1m wide. A deminer then slowly but steadily advances down each of these lanes whilst swinging the metal detector close to the ground. When the metal detector points out the presence of an anomaly, a second deminer then probes the area to see whether a mine is really there.



Figure 2.5: A manual demining situation using a metal detector.  
(Lopera, 2008)

### 2.3.2 Acoustic Sensors

An approach of landmine detection using acoustics has been proposed by Brunzell (1998). These sensors send acoustic waves into the ground. These sound waves reflect on the boundaries between materials that have different acoustical properties. The reflected acoustics are used to locate the object. The detection is dependent on the soil density and the bulk modulus.

This detection method is useful in very wet and heavy ground but is less effective in sandy soils. The main problem is the coupling of these waves with the surface without the application of pressure. Also soil inhomogeneities cause the degrading of acoustic measurements.

### 2.3.3 Infrared Imaging

These systems produce infrared images of sufficient temperature and spatial resolution that aid in the detection of anomalies in the ground that are introduced by the presence of landmines. All objects emit infrared radiation that is related to their temperatures. The detection of the targets using such a thermal imaging system is accomplished by the differences in the emitted infrared radiation.

---

<sup>1</sup> shrapnel is a fragment from an exploded artillery shell, mine or bomb.

The differences can be caused by either a temperature difference that occurs between the object and the background or an emittance difference of bodies at the same temperature. For mines, their thermal properties are different to that of the surrounding medium. However for mines laid on the surface a contrast occurs when the environmental and weather conditions are ideal. But for buried mines the contrast occurs because of the disturbances in ground conditions.

Unfortunately the infrared imagery is dependent on the landmine type, moisture, shadow and time of day and on the soil type. When mines have been buried over a period of time, the ones detected would be those buried within 10cm of the surface (MacDonald and Lockwood, 2003).

#### 2.3.4 Dogs and Rodent detection

Because dogs have an acute sense of smell, after a period of training they can be used in the detection of mines. They also can undergo training to locate trip wires. The dogs along with their trainers firstly detect landmines and then the positions where these mines are located are marked for further investigation and removal of the landmines.

The performance of the dog is dependent on the individual dog, how it was trained and how good the handler is in utilising the dog. Furthermore dogs require further retraining periodically and also become tired or bored often. As with other methods that rely on the detection of vapours, the performance of dogs is dependent on the environmental or weather conditions that cause explosive vapours to leave the mine or when the concentrations of vapours are too low for the dog.

Amongst other demining technologies used to clear landmines, trained rodents are also being used. APOPO<sup>2</sup> is a Belgian NGO that is based in Mozambique that has developed such a technique for landmine detection using African rodents. The rats have a natural tendency of smelling and sniffing and this feature gives them an advantage of locating landmines by smell. Figures 2.6 and 2.7 show the landmine clearance method using dogs and rodents respectively.



Figure 2.6: Photograph of Landmine clearance using dogs.  
(MgM People Against Landmines)

---

<sup>2</sup><http://www.apopo.org>



Figure 2.7: Landmine clearance using rodents.  
(MgM People Against Landmines)

### 2.3.5 Ground Penetrating Radar

As mentioned in Chapter 1 GPR is a non-invasive sensing technique that uses electromagnetic waves in order to locate targets. The transmitter generates an electrical signal and reflections of the radiated wave above and below the ground are measured by the receiving antenna. The electromagnetic wave is reflected from various buried objects or when the wave comes into contact between different earth materials that have contrasting dielectric properties. The different kinds of GPR systems were discussed in Chapter 1.

GPR, unlike the above mentioned techniques, is a time-dependent geophysical technique that can provide an accurate three dimensional subsurface image from which the accurate depth estimates for many targets can be determined. The signal processing is considered to be the most critical part in the design of GPRs. These signal processing algorithms need to remove the clutter signals and select the object to be declared as the mine. The various clutter removal techniques are discussed in Section 2.8.1 of this chapter.

GPRs have several advantages over conventional systems which include the fact that they can detect both metallic and non metallic targets. Conventional systems are the metal detector technology and GPRs are not conventional because they have recently evolved and are successful at detecting not metallic landmines. The major disadvantage is when used in inhomogeneous soils, where the false alarm rate is increased. But innovative algorithms such as the *SIMCA* algorithm need to be developed to remove the clutter and allow landmine clearance. Other advantages of GPRs were already discussed in Chapter 1 of this thesis.

Having devoted time in this section to talk about the various technology available to clear landmines, the next section details the protocols used in the clearance of landmines. This is required because an understanding of the protocols used is necessary to understand the requirements of an algorithm to help with landmine clearance.

## 2.4 Typical protocol used in the clearance of landmines

The clearance process used to clear landmines is divided into the following (International Campaign, 2011):

- The location and identification of a mine field so that it can be mapped.
- Cutting vegetation, collecting metal fragments from the surface, etc. so that the mine field can be prepared for the clearance operation.
- The locating and marking of the individual mines within the area under consideration.
- Removal or detonation of the detected mines so as to remove the threat.
- Enforce quality control measures.
- During landmine clearance activities in the field, areas where anti-personnel mine's are suspected of being buried are divided into 1m gridded squares. Then each square meter is manually probed with a plastic rod; the probing is done at an oblique angle to the ground so the fuse is not tripped because the rod will hit the side of a landmine. But this is very dangerous and is a time consuming activity.

The cleared area should be verified to make sure that it is clear from mines with a high level of confidence. A clearance priority rating is usually given to each mapped field which considers the social and economic factors along with factors such as weather and ground conditions.

According to a report by Kerner et al. (1999) produced for the Defence threat reduction agency of Dulles, VA; the United Nations (UN) demining experts (Extracted from Enclosure 5 to NVESD Memorandum, 1995) stipulated that one of the requirements for humanitarian demining is that the deminers have to clear landmines down to 30cm depth and that most antipersonnel mines are buried within 16cm of the surface. The report further states that UN requires deminers to work in at least 90% of soil conditions and that they have to detect lone buried landmines and plastic landmines.

The UN deminer's standards are given in the UN Statement of Requirement (United Nations, 1997) and is reproduced:

*'The area should be cleared of mines and UXOs to a standard and depth, which is agreed to be appropriate to the residual/planned use of the land and which is achievable in terms of the resources and time available. The contractor must achieve at least 99.6% of the agreed standard of clearance. The target for all UN sponsored clearance programmes is the removal of all mines and UXO to a depth of 200mm'.*

From the above stipulation it can be understood that mines/IEDs below the 200mm depth are not cleared.

The Geneva International Centre for Humanitarian Demining (GICHD) is a non-profit organization based in Switzerland and deals in the business of eliminating mines, the explosive remnants



of war and other explosive hazards.<sup>3</sup> The role of the GICHD is also in the formulation and dissemination of International Mine Action Standards (IMAS). The above is required in case the reader likes to read further on the protocols of landmine clearance.

The IMAS are now the worldwide recognised standards that are necessary for all UN mine action operations.<sup>4</sup>

Once having discussed the various technology available to clear landmines and having established in Chapter 1, in this chapter, in Chapters 3 and 4 that GPR technology is a well accepted innovative technology that is able to clear both metallic and plastic landmines; the next step would be to discuss the various GPR design options that can be used in the field to detect the landmines. Such design options include either a single array hand held system or a multi-array vehicle based system. The next section details these options, so that for future study beyond this PhD a viable design option can be designed which when integrated with the *SIMCA* algorithm enables the detection of the landmines or targets of interest.

However, since in using manual demining systems such as a hand held GPR the deminer is not able to scan the ground in a uniform manner taking note of the separation between the B scans; therefore there is some degree of erratic scan pattern. This is more in the case of detecting landmines because the operator would always be scared that a landmine will be triggered so he would be concentrating to ensure that the GPR head is not in contact with the ground. Therefore in this case and also in the vehicle based system, an added complexity is required in a field based system that integrates a spatial positioning system.

## 2.5 Single array and Multi-array Systems available in the market

GPR measurements can be acquired by towing the antennas continuously over the surface or at discrete points along the ground. These two modes are shown in Figure 2.8. The fixed mode is generally used by the hand-held system where the antennas are moved independently to different points and discrete measurements are made. Whilst the moving mode which is used in vehicle-based systems is when the transmitter and receiver are at a fixed distance and the pair of antennas are traversed along the ground by pushing or pulling them with the help of a vehicle (MacDonald et al., 2003b). The vehicle based system can be either with the radar looking down into the ground or it can look ahead in a forward looking mode. The forward looking mode has advantages because it removes the need for the vehicle to have overpass capability (Daniels, 1996). Furthermore Daniels (2004) states that for a given height, the radar performance is dependent on the relative permittivity of the soil and the radar forward velocity. It is also pointed out by Daniels (2004) that the effective range of the vehicle is dependent on the speed and the dielectric permittivity of the soil.

One can argue that the advantage of the hand-held system is its flexibility, whilst the advantage of the vehicle based system is its ability of acquiring data rapidly in comparison to the hand held system. A disadvantage of a hand-held system is that the sensor position is random and cannot

<sup>3</sup><http://www.gichd.org/>

<sup>4</sup><http://www.mineactionstandards.org/>

be attained by a hand-held system (Feng and Sato, 2005). Since landmine clearance personnel are concerned about not triggering the landmine the scan pattern is often erratic and the receiver position is random. Because of this an interpolation processing is required to provide a uniformly gridded data system. Furthermore, with the antennas looking forward and by the separation of the antennas from the ground, a vehicle based system offers advantages over the conventional hand held GPRs because the measured return from the subsurface is minimal (Fortuny-Guasch, 2002). By using arrays of antennas, vehicle based systems produce 3D data which can be processed and they provide a rolling map of detections. Vehicle based technology is used mainly to detect anti-tank mines because it is not easy to get enough cross range resolution at realistic budgets. The various image and signal processing methods used on data attained from vehicle based systems include image inversion and synthetic aperture techniques, principal components analysis and hidden Markov models (Daniels, 2004).

A discussion of some of the key vehicle based and hand held technologies available in the market are detailed in the following section. With all array systems it is vital that the surface clutter has to be removed. One method is to orientate the array head so that it is close to the ground and another method is coherent subtraction but in this case the ground should be smooth (Daniels, 2004). Array systems usually produce an image of the landmines and therefore there needs to be accurate positioning of the array elements. According to Daniels (2004) this is done by using a differential Global Positioning System and a inertial navigation systems in parallel. Various array systems include US systems such as - Planning Systems, GeoCenters, Jaycor and Mirage; UK systems such as ERA Technology, Thales and PipeHawk (Daniels, 2004).

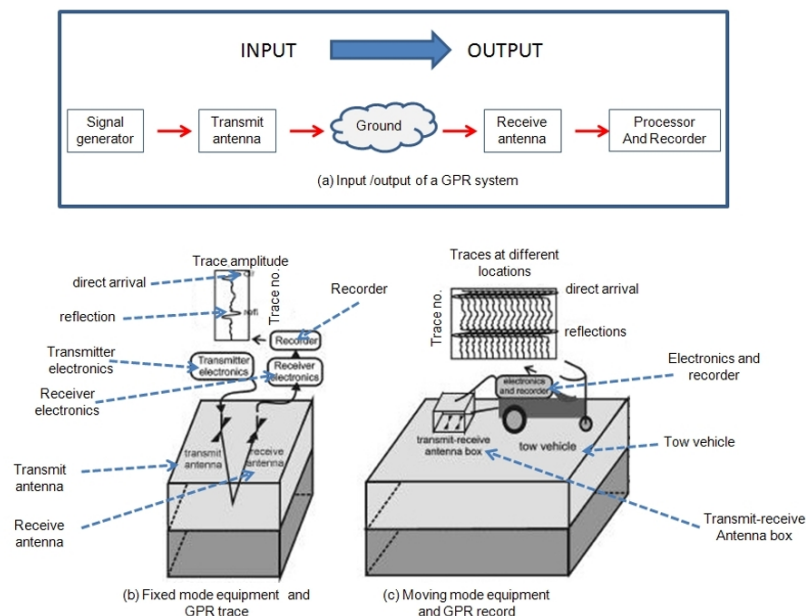


Figure 2.8: A pictorial representation of a hand-held and vehicle based system.  
(Daniels et al., 1997)

### 2.5.1 Hand-held single-array system

The versatile and advanced hand-held systems available in the market include such systems as the US Army *HSTAMIDS* hand-held detector developed by *Cyterra*, US<sup>5</sup> and the *Vallon MINEHOUND VMR3*; which is a dual sensor consisting of a Ground Penetrating Radar developed by Cobham, UK<sup>6</sup> and is a *Vallon GmbH*<sup>7</sup> commercial off the shelf product. Some hand-held systems are now outlined.

#### 2.5.1.1 HSTAMIDS

The US army's handheld standoff mine detection system is a dual sensor landmine detector and consists of ground penetrating radar and a metal detector. The system has an in-built software suite that can perform advanced data fusion algorithms that allow the deminer to detect landmines. When the deminer scans the ground, the algorithm updates the terrain model and so the system can adjust to varying soil profiles. The terrain model is generated using Principal components analysis and the threshold is set by the operator. If a mine is detected, an audio cue alerts the deminer. The advanced microprocessor and software enables detection of large and small metallic/non-metallic landmines. The sensor integration is done using a high-speed digital parallel processor and the deminer has both an audio and visual display. Some systems also have a passive IR sensor to allow for standoff mine detection.

The GPR is based on a wide-band stepped frequency radar trans receiver. The search head is made up of one transmitter and two receiver antennas. The metal detector (MD) coil forms a circle around the diameter of the sensor head. Any changing current passing through the MD coil will create an electromagnetic field like a magnet and that will induce an electrical current in any metallic target. The head of the sensor senses this electromagnetic field and alters the operator via an alarm. Figure 2.9 shows a photograph of the *HSTAMIDS* system.



Figure 2.9: *HSTAMIDS* hand-held detector.  
([http://www.itep.ws/pdf/HSTAMIDS\\_FS.pdf](http://www.itep.ws/pdf/HSTAMIDS_FS.pdf))

<sup>5</sup><http://www.cyterra.com/index.htm>

<sup>6</sup><http://www.cobham.com/>

<sup>7</sup><http://www.vallon.de/>

### 2.5.1.2 Vallon MINEHOUND VMR3

The *Vallon MINEHOUND VMR3* system like the *HSTAMIDS* system consists of a metal detector and GPR. The system alerts the user via an alarm which can be sensed as a vibration and/or an audio signal is activated when a metallic object such as a mine is detected by the sensors. The metal detector audio provides position information and the mine can be further pinpointed with accuracy using the GPRs audio which gives position and depth information. The radar cross section of the object is also provided by the GPR. One of the features of this system is that the detectors can be used in isolation or as a combination. The designers of the system claim that the system responds to mine targets whilst leaving out metallic clutter. The GPR has a frequency of 1 GHz and the control and signal processing functions are accomplished by a DSP processor. The selection of the GPR or metal detector is done by pressing a button on the handle. The sensitivity of the MD is set by using an LED displayed bar graph.



Figure 2.10: The *MINEHOUND* hand-held dual sensor technology.  
(Cobham)

### 2.5.1.3 Advanced landmine imaging system (ALIS) - Hand-held GPR Metal detector system

Feng and Sato (2005) designed a landmine detector which uses a metal detector and GPR. The metal detector and GPR signals can be acquired together along with the positions of the sensors which are

obtained using a CCD camera. As shown in Figure 2.11, the CCD camera is used in the tracking of two reference points and the sensors when scanning the ground. A wireless display shows the image which can be used by a non-operator to interpret the image and to control the system; whereas the operator can see the CCD image and the metal detector image via a head-up display. A computer is integrated into the system and is kept in a backpack carried by the operator that processes the data and displays the images. As explained above, interpolation is used to prepare a uniform gridded data. Then the system uses Kirchhoff migration to improve the SNR ratio to reconstruct the image. Results from a field test in Afghanistan as shown by Figure 2.11[C], illustrated the system was feasible.

The ALIS system has in-built software that produces images of the subsurface and this production of images is similar to the *SIMCA* algorithm. Feng and Sato (2005) conclude that giving the operator of the equipment an image of the subsurface has advantages over a system which alerts the user via an alarm. This is because a tired deminer has a chance of misinterpreting an audible signal but not an image.

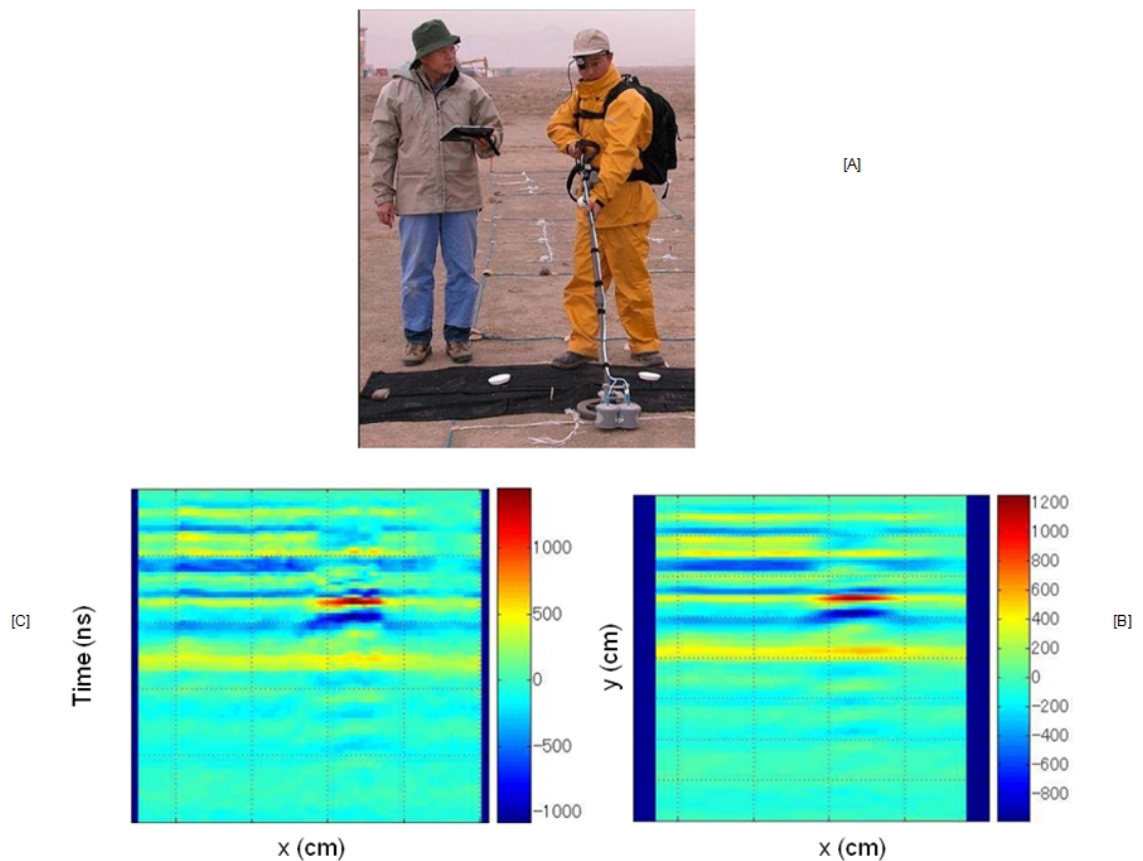


Figure 2.11: The ALIS hand-held detector. [A]: Actual system; [B]: Interpolated GPR vertical slice; [C]: Migrated GPR vertical slice.

(Feng and Sato, 2005)



### 2.5.2 Vehicle based multi-array system

Chen et al. (2000) have developed an UXO classification technology based on fully polarimetric gpr signatures. This surface-based radar system operates in the frequency range from 20 MHz to 800 MHz. Based upon knowledge gained during the study in 2000 at the Tyndall AFB UXO test site, they proposed improvements in system configuration, measurement approach and processing technique. 'When the radiated fields are received by the radar, the time domain response appears as damped sinusoids with its fundamental frequency related to the target dimensions and the soil property' (Baum, 1993). Using this resonance signature the length estimation of the target can be obtained. They used a downward-looking vehicle mounted approach, as shown in Figure 2.12 and a possible problem of this system is that the antenna head is in contact with the ground and may detonate up the UXO. The antenna head oriented in a stand-off position is a better orientation.



Figure 2.12: Downward-looking vehicle mounted antenna oriented at  $45^0$  with respect to the motion direction.

(Chen et al., 2000)

(Gu et al. (2004); Bradley et al. (2002)) present the downward looking and forward looking GPR vehicle based system to detect landmines. The systems are designed by Planning Systems, Inc. and they use UWB stepped frequency. Figure 2.13 shows a downward and forward looking system. The GPR synthetic aperture radar used by this system produces a spatial map of changes in the dielectric reflective properties of the ground as a function of its burial depth.

The downward system has a frequency range from 0.766 - 2.726GHz. Two separate antenna arrays, each having 15 transmitters and 15 receivers are used for the data acquisition at 58 channels and the separation distance is 0.0746m. Two dimensional images of objects are presented by the in-built software.

The forward looking system on the other hand, has antennas that are mounted in the front of the

vehicle. The EM fields generated are sampled at equal spaced distances of 0.1m when the vehicle advances forward. The large beam width ensures that an area of  $\geq 4\text{m}$  by 4m is traversed. Unlike its downward looking counterpart, the frequency range is 0.766 - 2.166GHz. The transmit antennas are 2.5m above the ground in a standoff configuration. The system has 2 receiver antennas each having 15 antennas at 1.9m and 2.05 above the ground respectively.



[A]



[B]

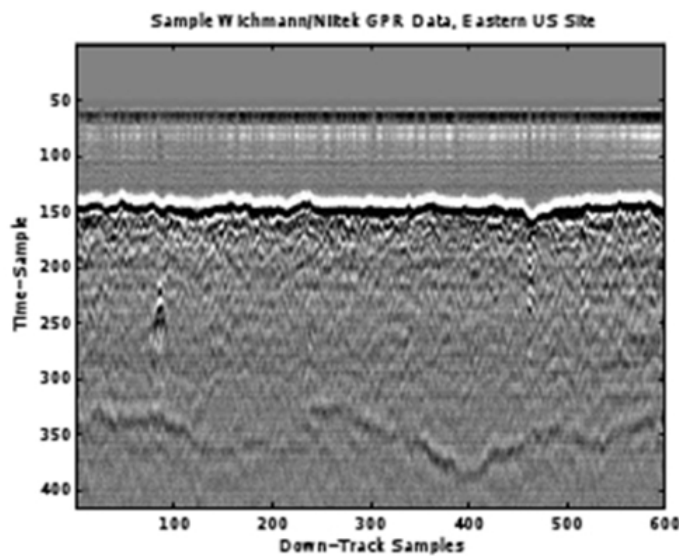
Figure 2.13: PSI developed system - [A]: Downward looking system; [B]: Forward looking system.  
(Bradley et al., 2002)

Torrione et al. (2006) present the Wichmann/Niitek wideband (200 MHz - 7 GHz) GPR which is mounted on a vehicle. This vehicular system is also integrated with a global positioning system (GPS) sensor so that the systems location can be tracked and to also allow the tying of the survey to ordnance survey maps. Furthermore a marking system is mounted on the vehicle to allow the

marking of targets. The actual radar is 1.2m in width and has 24 channels spaced 5cm. During the forward movement of the vehicle all the 24 channels are sampled once every 5cms. Figure 2.14[A] shows such a system and Figure 2.14[B] shows typical output from the system.



[A]



[B]

Figure 2.14: The Wichmann/Niitek GPR system - [A]: actual system; [B] GPR B scan produced by the system.

(Torrione et al., 2006)

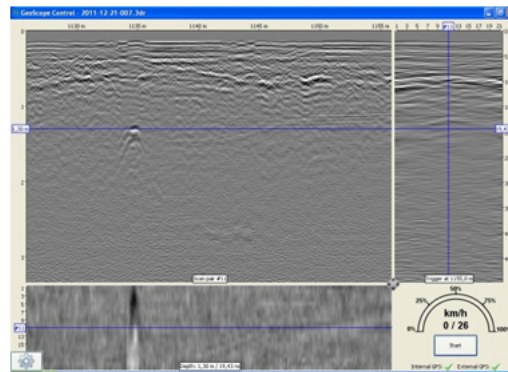
3d-Radar have developed a next generation 3d GPR by using step frequency range radar technology and innovative multi channel antenna design. Their selection of arrays range from 9 transmitting and receiving antennas up to 41 pairs. The width of the antenna array is between 90 cm to 3.3 m and has frequency ranges from 200 MHz to 3 GHz. Using a Geoscope Mk IV step frequency



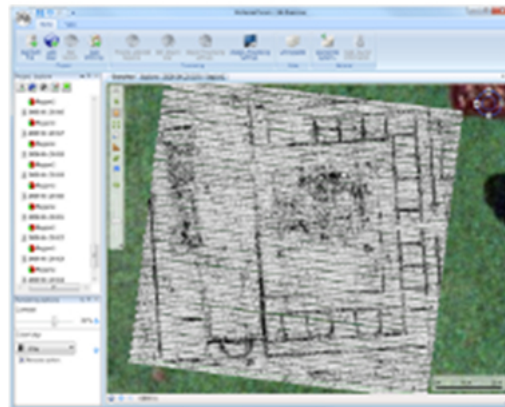
radar, 3D data can be collected with dense line spacing. The Geoscope MK IV is a fourth generation 3d - radar and it uses step frequency technology. The antenna also has a built-in GPS receiver to get positional information. Figure 2.15 shows the 3d-Radar multi-channel system, whilst Figure 2.16 shows images produced from the integrated software.



Figure 2.15: 3d-Radar multi-channel system.  
(3d-Radar)



[A]



[B]

Figure 2.16: Images produced from software integrated in 3d-Radar. [A]: control software used during collection of data; [B]: processed archaeological data with a satellite imagery overlay.

(3d-Radar)

### 2.5.2.1 Vehicle based multi-array robotic system

Fukushima et al. (2005) present a mobile robotic system to help with the sensing and clearance of Anti-personnel mines. The system is made up of a manipulator which has been balanced in terms of the weight and is mounted on a mobile platform. The authors make use of a commercially available all terrain vehicle (ATV) for the mobile platform. Their system as shown in Figure 2.17 has been tested in a prepared test field. A metal detector and a GPR for detection of the landmines is included in their system, and the equipment has facilities for the marking of the located landmines in the surface. The systems integrated on-board computer registers this location for future use.

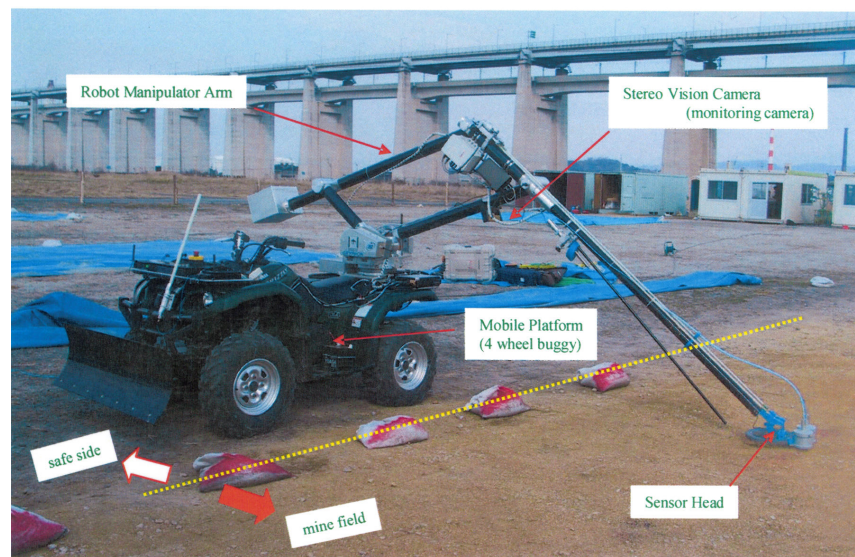


Figure 2.17: The teleoperated buggy vehicle used as a robotic landmine detection and clearance system

(Fukushima et al., 2005)

Apart from manually controlling the manipulator arm, further success has been attained by the use of a stereo vision camera that automatically maps and scans the ground. The system can be operated by the deminer by using a remote controller from a safe distance. Automatic topographic mapping production and the scanning of the ground is achieved by the use of passive stereo-vision cameras that are mounted on the manipulator link. The system uses a stereo vision camera with a resolution of 1024x768 pixels and is the camera designed by Point Grey Research.

Experimental results indicated that the proposed system was feasible. Results also demonstrated that the integration of the GPR was very important and better results were achieved this way than when using only a metal detector.

The depth and subsurface information attained using GPR equipment would need to be integrated into an ordnance survey map, so that locational and position information can be attained. This can be accomplished by using a Global Positioning System (GPS) and the next section discusses this topic.

## 2.6 GPR and Global Positioning Systems

All walls, floors, street, channels, pits, graves, archaeological areas of significance, etc have to be defined by a clear drawing and description in addition to the depth and sub-surface information attained using a GPR. Therefore the integration of the GPR data with a geographical information system (GIS) or computer aided design (CAD) system is essential, where the image can be combined with other sources.

The SPRScan GPR system which has been used by researchers in Europe and at the Indian Institute of Technology in their sandbox experiments is detailed in this thesis. Such a SPRScan can be used together with a modern total station theodolite system for acquiring positioning of surveyed areas and to tie the GPR survey to an Ordnance Survey map.

*SS3DI*<sup>8</sup> uses GPR and GPS system measurements to allow for the location, mapping and modelling services.

Figure 2.18 shows a GPR survey which has been overlaid on top of a map using a GPS system. The location of the objects is performed using the GPR, whilst the GPS is used to reference the data generated by the scan to points on a map. The GPR B scan can give depth and positional information. By using grid formats, the lines of GPR data collection can be referenced to known points on the map. In this system they also use *AutoCAD* to produce high quality 2D diagrams of the survey using GPR and GPS.

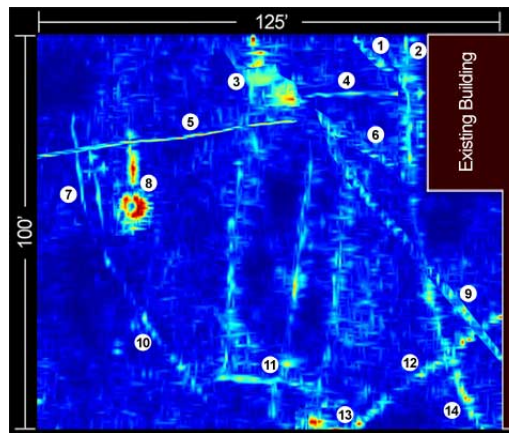


Figure 2.18: Underground locating is accomplished using a GPR scan overlaid on top of a map using a GPS system.

(SS3DI)

Sun et al. (2011) propose a method to carry out a topographic survey under the water using a GPR and a GPS. The elevation information is attained from GPR, whereas the plane co-ordinates are attained from the GPS. The GPS system gives the plane positions of the features of interest. The GPS approach uses Real Time Kinematic Technology, which consists of the base station for GPS, the data link and the mobile station. During data collection the mobile station carries out real time differential processing and therefore positional results can be attained. Whilst carrying

<sup>8</sup><http://ss3di.com/Imaging/GPR.aspx>

out the survey, the antenna of the mobile station for the GPS is attached above the GPR antenna. Acquisition software synchronises the GPR and GPS data.

There are only a very few commercial packages covering all the necessary aspects of data processing, the price is also very high and normally a good geophysical background is necessary. The next section explores the soil properties and their effect on GPR performance as it is well known that GPR is influenced by the soil dielectric permittivity as GPR mainly governs Electromagnetic ('EM') wave propagation (Jol, 1994). And also in order to predict the electrical properties of soil, various theoretical and empirical models are considered in the next section.

## 2.7 Soil properties and their effect on GPR performance

The detection performance of GPR is influenced by the electromagnetic (EM) properties of the soil ((Das et al., 2001); (Rhebergen et al., 2004)). The detection performance of GPR is also influenced by the features of the target ((Rhebergen et al., 2005); (der Kruk et al., 2003)).

When using GPR for landmine detection, the contrast in the relative permittivity that occurs between the landmine and the soil it is buried in, is the most important parameter to be taken into consideration. For the majority of materials the dielectric constant ranges from 3 to 30, with dry sand at the lower end of this range and has values from 3 to 5. Antitank mines that are non-metallic have dielectric constants in the range of 3 to 10. Both materials present  $\epsilon$  values which overlie, therefore a deminer faces great difficulties. Table 2.1 lists the common values of the relative permittivity,  $\epsilon$ , because water saturation is a key component of attenuation and thus it would be beneficial to know what the typical range of values of  $\epsilon$  are for water.

Material	Relative permittivity ( $\epsilon$ )
Air	1
Sea water	80
Dry sand	3-5
Saturated sand	20-30
Limestone	4-8
Silts	5-30
Granite	4-6
Ice	3-4

Table 2.1: List of relative permittivity for some typical earth materials.  
(Annan and Cosway, 1992)

A deminer faces great difficulties in finding out whether soil conditions are suited to GPR mine detection. This difficulty also arises because of the many variables involved, including soil type, climate, topography and vegetation. Military personnel have also designed minefields to be very complex so as to deter their clearance and often minefields are integrated with natural obstacles such as steep slopes, ditches and dense vegetation.

Fritze (1995) showed by modelling GPR signals at 900 MHz, that the signals would be strongly attenuated in moist soils and in clay soils especially. Trang (1996) found in simulations and in actual laboratory conditions using a GPR in the 600-800 MHz range that the detection of non-metallic mines was easier when the soil was moist. Johnson and Howard (1999) state that increasing the soil moisture improves the contrast that occurs between arid soils and plastic mines.

An ultra-wideband GPR in the 1-5 GHz range for metallic mine detection was used by Scheers et al. (2000) and they found that the maximum depth at which a mine is detected decreases as the soils moisture increased. The dielectric properties of a soil are determined by its bulk density, the texture of the soil particles and the density of the soil particles (Jury and Garener, 1991). If a plastic landmine is buried in sand, then the soil water content causes the bulk dielectric constant of the soil to increase, whilst for the landmine the dielectric constant is the same. This increase in dielectric constant of the soil will lead to an improved image of the landmine because a larger reflection results in the soil. The dielectric constant of a soil also changes with respect to the frequency of radar waves (Hoekstra and Delaney, 1974).

In terms of GPR usage, losses in soils introduce frequency dependence in velocity, attenuation and cause transmission and reflections; furthermore there are concerns in terms of signal strength. From this it can be concluded that the shape of the radar pulse changes as it goes through the soil (Roth, 2004). The overall strength of these losses is related to water content and dry soils generally have very low losses.

GPR signal loss attenuation is a result of four loss mechanisms:

1. Conductive losses - A large source of loss which occur at frequencies above 300 MHz and below. The greater the soil/medium conductivity the more the attenuation and as a result loss of resolution happens.
2. Molecular relaxation losses - Occur when polar molecules rotate and oscillate in response to the EM field. The energy applied is converted into kinetic energy. Kinetic energy results in thermal energy as a result of the frictional drag. The kinetic or thermal energy is not captured by GPR so is lost. This causes loss of signal strength.
3. Scattering losses - Caused by irregularly-shaped targets causing redirection of GPR signal from the receiver. This results again in loss of signals.
4. "Clay" losses - Loss is attributed to clay or colloidal particles. GPR signals cannot reach clay layers and loss of signal strength causes attenuation.

Attenuation of the propagating EM pulse is as a result of the transfer of energy to ionic charges as they accelerate on the rising edge of the pulse, this causes an increased number of collisions between the ions and therefore heat which results in loss of energy, (Jol, 1994). In addition soils with high Magnetic Permeability will attenuate the signal, as the EM field interacts with the spin of the permanent magnetic dipole moment. However this only occurs when soils comprise a large quantity of magnetic minerals, i.e. magnetite, maghemite or free iron in a disseminated form (Jol, 1994).

Experimentally it has been demonstrated that for most materials which reside in the sub-surface of the earth, the attenuation of electromagnetic radiation rises with frequency and that at a given frequency wet materials show a higher loss than dry ones. The velocity of propagation is dependent on the relative permittivity of soil. The relative permittivity depends on its water content and the absolute permittivity varies with frequency of soil. Soils that have high electrical conductivity cause rapid attenuation of the radar energy and restrict depth of penetration and thus limit the effectiveness of the GPR (Kovalenko, 2006). The clay content and the amount and type of salts in solution influence the electrical conductivity of soils.

In order to predict the electrical properties of field soils, theoretical and empirical models of the electrical components of the soil have been included into semi-empirical models. Topp et al. (1980) introduce a semi-empirical model which relates the soil volumetric water content with the relative permittivity. They use it on sandy soils and therefore when other soils are used it needs to be adjusted. In Peplinski et al. (1995), a semi-empirical dielectric model is reported. This model covers the 0.3-1.3 GHz frequency range and the textural composition of the soils related to electrical parameters. The model is based on a model by Dobson et al. (1985), which gives electrical permittivity, in the 1.4-18 GHz frequency range. The real part of the complex relative permittivity for the bulk soil is approximated as equations below adapted from (Peplinski et al. (1995) and Lopera and Milisavljevic (2007)):

$$\varepsilon' = \left[ 1 + \frac{\rho_S}{\rho_P} (\varepsilon_P^\varphi - 1) + \Theta^{\beta'} \varepsilon_{fw}'^\varphi - \Theta \right]^{\frac{1}{\varphi}} \quad (2.7.1)$$

And in Dobson et al. (1985) - The imaginary part is derived as (equations below adapted from (Dobson et al. (1985)):

$$\varepsilon' = 1.15 \left[ 1 + \frac{\rho_S}{\rho_P} (\varepsilon_P^\varphi - 1) + \Theta^{\beta'} \varepsilon_{fw}'^\varphi - \Theta \right]^{\frac{1}{\varphi}} - 0.68 \quad (2.7.2)$$

The imaginary part in Peplinski et al. (1995) is derived as:

$$\varepsilon'' = \left[ \Theta^{\beta''} \varepsilon_{fw}''^\varphi \right]^\varphi, \quad (2.7.3)$$

where:

- $\rho_P = 2.66g/cm^3$  is a typical value; attained from laboratory experiments
- $S$  is the fraction of sand particles
- $C$  is the fraction of clay particles
- $\Theta$  is the volumetric water content
- $\rho_S$  is the bulk density of the soil
- $\varepsilon_P = (1.01 + 0.44\rho_P)^2 - 0.062$  is the empirical model of the relative permittivity of the soil particles,

- $\beta' = 127.48 - 0.519S - 0.152C$  and  $\beta'' = 1.33797 - 0.603S - 0.166C$  are two frequency independent constants which join the soil type into the model,
- $\varphi = 0.65$  is empirically derived in Peplinski et al. (1995).
- $\varepsilon'_{fw}$  and  $\varepsilon''_{fw}$  are the real and imaginary parts of the dielectric constant for free water
- $\varepsilon''_{fw}$  depends on the effectivity conductivity  $\sigma_{eff}$ , and according to Dobson et al. (1985) the following relationship can be derived:

$$\sigma_{eff} = 1.645 + 1.939\rho_S - 2.25622S + 1.594C \quad (2.7.4)$$

Peplinski et al. (1995) derive the same formulae as:

$$\sigma_{eff} = 0.0467 + 0.2204\rho_S - 0.4111S + 0.6614C \quad (2.7.5)$$

From here once the value of  $\epsilon$  is found out the other factors influencing the performance of the GPR can be derived; such as the attenuation factor  $\alpha$  and the relative permeability contrast  $\varepsilon_{contrast}$ . The attenuation factor  $\alpha$  can be derived from:

$$\alpha = \omega \sqrt{\frac{\mu\varepsilon_{eff}}{2} \left[ \sqrt{1 + \left(\frac{\varepsilon''}{\varepsilon'}\right)} - 1 \right]} \quad (2.7.6)$$

- where  $\mu = \mu_0 + \mu_0\chi FD$  and  $\mu_0 = 4\pi \times 10^{-7} H/m$ ,  $\mu$  is the permittivity of soil.
- $\omega$  is the angular frequency of the radar wave
- $\varepsilon_{eff} = \varepsilon' \varepsilon_0$  is the effective electrical permittivity of soil and  $\varepsilon_0 = 8.85 \times 10^{-12} F/m$
- $\frac{\varepsilon''}{\varepsilon'}$  is the loss factor
- Equation (2.7.6) is only valid when  $\mu \leq 1$

The relative permeability contrast  $\varepsilon_{contrast}$  between the target and the background is calculated using:

$$\varepsilon_{contrast} = \frac{\sqrt{\varepsilon} - \sqrt{\varepsilon_{tg}}}{\sqrt{\varepsilon} + \sqrt{\varepsilon_{tg}}} \quad (2.7.7)$$

where  $\varepsilon_{tg}$  is the relative permittivity of the target

Lopera and Milisavljevic (2007) state that since the buried target strength is dependent on the wave penetration and the dissimilarity between the soil and targets electrical permittivity,  $\alpha$  and  $\varepsilon_{contrast}$  have an influence on the Signal-to-noise ratio.

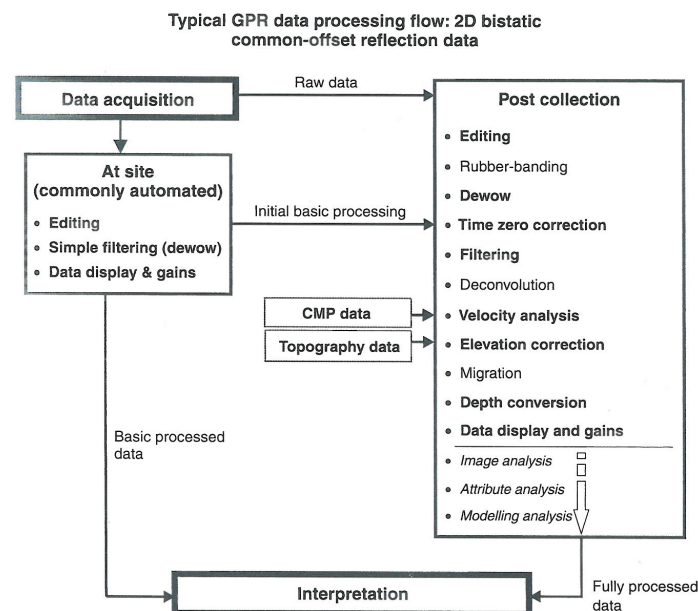
The soil dielectric permittivity depends on a number of factors of which the most significant is the volumetric water content, which can vary considerably over time and space and the soil dielectric permittivity affects the GPR performance. The GPR signal contains not only responses from a



target, but also undesirable effects from system ringing, antenna coupling and soil reflections that distort the target response. This clutter has to be removed from the signal to enhance landmine detection. Therefore the next section details the various data processing and clutter removal technique available to the GPR practitioner.

## 2.8 GPR data processing

Figure 2.19 illustrates the typical processing flow sequence for a set of 2D common-offset, bistatic, reflection mode GPR data and it is to be noted that the processing steps are in their relevant order. It is important to note that the processing order depicted in the diagram is not the order followed by all users, but according to Jol (1994) this order is representative of good GPR practice. The processing steps that are bold are considered as essential for decent interpretations. A brief description of each processing step is also included in Figure 2.19.



### GPR data processing and analysis steps: Basic descriptions

- Editing** - Removal and correction of bad/poor data and sorting of data files.
- Rubber-banding** - Correction of data to ensure spatially uniform increments.
- Dewow** - Correction of low-frequency and DC bias in data.
- Time-zero correction** - Correction of start time to match with surface position.
- Filtering** - 1D & 2D filtering to improve signal to noise ratio and visual quality.
- Deconvolution** - Contraction of signal wavelets to "spikes" to enhance reflection events.
- Velocity analysis** - Determining GPR wave velocities.
- Elevation correction** - Correcting for the effects of topography.
- Migration** - Correction for the effects of survey geometry and spatial distribution of energy.
- Depth conversion** - Conversion of two-way travel times into depths.
- Display gains** - Selection of appropriate gains for data display and interpretation.
- Image analysis** - Using pattern or feature recognition tools.
- Attribute analysis** - Attributing signal parameters or functions to identifiable features.
- Modelling analysis** - Simulation of GPR responses.

Figure 2.19: Typical GPR data processing flow for 2D bistatic common-offset reflection data.  
(Jol, 1994)



### 2.8.1 Clutter Removal

A GPR signal contains not only the response from a potential target, but also undesirable effects from antenna coupling, system ringing and soil reflections, which obscure the target response (Daniels et al., 2004). These effects have to be filtered out from the signal to enhance landmine detection. Different techniques are used to reduce this clutter and thus to identify the buried object signal. Some pre-processing techniques as filtering and deconvolution are necessary to enhance the quality of the data, so that the extraction of signal features is easier and more accurate in future steps. Different signal processing techniques in the area of landmine detection are provided by (Robinson and Treitel (1980b); Daniels (2004)) and an excellent overview of the Mathematics of digital images is provided by Hoggar (2006).

Daniels (2004) presents a method of removing the clutter and he states that the clutter reduction can be accomplished by calculating averaged values over an ensemble of A scans and subtracting this from each of the A scans. This can be expressed as (equations taken from Brooks (2000)):

$$A'_{n,a}(t) = A_{n,a}(t) - \frac{1}{Na} \sum_{a=1}^{Na} A_{n,a}(t) \quad (2.8.1)$$

where  $n = 1$  to  $N$  and  $N$  is the number of samples;  $a = 1$  to  $Na$  and  $Na$  is the number of A scan waveforms;  $A_{n,a}(t)$  is the unprocessed A scan and  $A'_{n,a}(t)$  is the processed A scan.

Peak subtraction has also been used for reducing the ground surface return. Using a sinc-approximation, the early time peak can be synthesized in the time domain and subsequently subtracted (Jol, 1994). It can be argued that a bias in the amplitude and location of the early time estimate will be created due to the presence of shallow targets. Therefore, the clutter reduction may not be accurate.

Gupta et al. (1998) propose an improved peak subtraction approach in which the early time contributions are approximated using a superposition of damped exponentials in the frequency domain.

Savelyev et al. presented in Daniels (2004) deconvolution techniques aiming to extract the target reflection ideally. But for success in using this technique the exact knowledge of each transfer function along the complete ray path from the transmitting antenna to the receiving antenna is vital.

van Kempen and Sahli (2001) state that deconvolution is a useful technique for data processing but because of the band limited nature of the emitted wave and the effect of noise, deconvolution is an ill posed operation.

Convolution of a target impulse response with that of a GPR can be expressed as a system of linear equations (equations below adapted from Brooks (2000)):

$$y = Hx \quad (2.8.2)$$

where  $x$  is the target response,  $H$  is the convolution matrix and  $y$  is the received signal. The deconvolution problem is to find  $x$ . The  $y$  and  $x$  contain noise. As stated above deconvolution is an ill posed problem and to solve such a problem, various regularization methods were developed. A classical method called *Tikhonov regularization* solves such ill posed problems. Therefore a

solution to Equation (2.8.2) can be found.

Brooks (2000) also uses the Wiener filter<sup>9</sup> (Andrews and Hunt, 1977) to solve Equation 2.8.2. From here the noise level can be properly estimated and Brooks (2000) states that the noise can be determined and removed from the data.

The system identification method is another approach for ground clutter reduction (Hsia, 1976). Brooks (2000) presents a technique where the system model is also based on a convolution process. Because of the ill-posed deconvolution problem he used an additive GPR signal model process. van Kempen and Sahli (2001) present a method for characterizing the clutter using parametric system identification, whose aim is to determine the parameters of a time-invariant (LTI) signal. The authors use Farhang-Boroujeny (1998) discrete LTI system model to characterize the clutter. The target signal can then be determined by removing the clutter from the original data.

A number of studies have dealt with the elimination of leakage and ground-bounce effects that occur in GPR data ((Abrahamsson et al., 2001); (Clement et al., 2001)). A signal processing technique was developed to reduce clutter due to the bounce from the ground on GPR measurements by der Merwe et al. (1999). The goal of their study was to detect small dielectric landmines buried close to the ground surface in a lossy soil. To account for the variability in a typical subsurface scene, they use a parametric model to represent the clutter contributions. They assume that the total frequency domain scattered field received by the GPR can be represented by the following (the following equation has been taken from der Merwe et al. (1999)):

$$S(\omega) = H_C(\omega) + T(\omega) + n(\omega) \quad (2.8.3)$$

where  $H_C(\omega)$  is the clutter contribution and represents all unwanted contributions such as scattering from the rough surface and contributions from the subsurface soil in homogeneities,  $T(\omega)$  is the contribution from the desired target,  $n(\omega)$  is the additive Gaussian noise and  $\omega = 2\pi f$  in equation (2.8.3). The authors propose an iterative method to remove clutter due to surface scattering and interaction terms and state that subsurface in homogeneities are false alarms and can be separated from the target contribution using the match filter detector.

They then say that the characteristics of the desired target, represented by  $T(\omega)$  and its counterpart in Equation 2.8.2 differs from this in two ways. The first is that the depth of the subsurface target is unknown and results in a complex phase change in the scattered field. Secondly, the incident transmitted field through the rough surface is not a plane wave anymore and gets dispersed as it goes through the soil due to the frequency dependence of the index of refraction. They compensate for the above two differences by adding a frequency dependent damping factor. Hence by including this factor, they say, the estimated target signature can be derived as:

$$\hat{T}^n(\omega) = A_r^n e^{-\omega \gamma_r^n} e^{-j\omega t_r^n} T_r(\omega) \quad (2.8.4)$$

where  $A_r^n$  is a complex amplitude,  $\gamma_r^n$  is a damping factor and  $t_r^n$  is a time delay at the  $n^{th}$  iteration.

---

<sup>9</sup>The Wiener filter is an adaptive digital filter that calculates its parameters, according to the data present locally in the image.

der Merwe et al. (1999) go further to define the following data set :

$$\tilde{S}^{n+1}(\omega) - \hat{T}^n(\omega) \quad (2.8.5)$$

which contains the unwanted contribution of the GPR data. They assume that the target return is zero for  $n = 0$ . They state that a damped exponential model is suitable for most of the contributions. Therefore, they represent the data set  $\tilde{S}^n(\omega)$  using damped exponential as follows;

$$\tilde{S}^n(\omega) = \sum_{k=1}^{I_t} A_k e^{-\omega \alpha_k} e^{-j\omega t_k} \quad (2.8.6)$$

where  $I_t$  is the total number of damped exponentials terms needed to model the data set,  $\alpha_k$  is the damping factor and  $t_k$  is the time delay of the  $k^{th}$  term for  $k = 1, \dots, I_t$ .

They say that it is desirable at this point to estimate the dominant early time clutter contributions such as the surface return and because dominant clutter resides in the earlier time contribution. It can be used in choosing an appropriate time window. The window size is varied between the iterations. A very narrow window is chosen in the beginning to ensure that the contribution from the shallow target is not also removed. The window size is then increased at later iterations. The selected complex exponential parameters are used to reconstruct the clutter contributions and are defined as:

$$\hat{C}^n(\omega) = \sum_{k=1}^{I_C} A_k^c e^{-\omega \alpha_k^c} e^{-j\omega t_k^c} \quad (2.8.7)$$

where  $I_C \leq I_t$  and  $A_k^c$ ,  $\alpha_k^c$ , and  $t_k^c$  is the complex exponential parameters of the  $k^{th}$  early time pole.

The iterative signal processing technique is then used in the decomposition of a frequency domain measurements into the corresponding signature and clutter contributions using the above models.

der Merwe et al. (1999) state that the estimated clutter from the GPR data yields the residual data set given by:

$$R^n(\omega) = S(\omega) - \hat{C}^n(\omega) \quad (2.8.8)$$

which contains the left-over clutter contribution and/or the target contribution. This residual data in accordance with der Merwe et al. (1999) is used to obtain an estimate of the target. The parameters needed to estimate the target at iteration  $n$ , can be obtained by the optimization of the following least squares error:

$$Cost^n(\theta) = \arg \min_{\theta} \left[ \sum_{\omega_1}^{\omega_N} |R^n(\omega) - A_r^n e^{-\omega \gamma_r^n} e^{-j\omega t_r^n} T_r(\omega)|^2 \right] \quad (2.8.9)$$

where  $\omega_1$  and  $\omega_N$  are the end band frequencies and  $\bar{\theta}$  is the parameter vector defined as  $\bar{\theta} = [\gamma_r^n, t_r^n]$ . They say that since the target model is linear in amplitude,  $A_r^n$  can be removed

from the cost function by linear least-squares and therefore no optimization is needed for this parameter.

The iterations are then terminated when the change in the estimated target is less than an agreed threshold. The output of the iteration is the estimated clutter contribution and the residual data set. The residual data set contains the buried target signature and can be processed to yield target identification or detection. The algorithm also gives an estimate of the buried target depth. The authors tested their algorithm using simulated data using the time domain (Finite-difference-time-domain) FDTD algorithm and demonstrate that the proposed algorithm is effective for clutter reduction. However, the technique by der Merwe et al. (1999) requires precise knowledge about the object signal, which in reality is not always available.

The TLS-Prony technique can be used to estimate the necessary exponential components outlined above. The estimated early time clutter is then subtracted from the data to reduce its participation (Rahman and Yu, 1987). This method is also sometimes referred to as early time subtraction (ETS) and is equivalent to a single iteration of the algorithm proposed by der Merwe et al. (1999).

Fritze (1995) uses five different algorithms on synthetic data which consisted of a diffraction hyperbola and a number of background clutter signals:

- *Subtraction of the average A scan.* Here an average A scan over the whole B scan is calculated and subtracted from the individual A scan. A major disadvantage of this method is that one only succeeds in eliminating the perfectly horizontal background clutter signals. However, this is the most popular background subtraction method used by GPR users.
- *FK-filtering.* This method is the most time consuming method and the results are not satisfactory in comparison to the other five methods.
- *A horizontal high pass Butterworth filter.* The author shows that this method will reduce the different background signals effectively. One disadvantage however of this method is that the diffraction hyperbolas are modified substantially which is not an ideal thing to do.
- *Windowed average subtraction.* This is a modified version of the general average subtraction method. The A scan is not calculated over the whole B scan, but only over the A scans within a window around the signal that is treated. The advantage of this is that the subtraction can adapt to slowly varying signals so the slightly oblique surface reflections are eliminated.
- *Discrete Wavelet Transform.* The transform was applied in the horizontal direction and the coefficients of the lowest octaves which correspond to horizontal energy were set to 0, after which the inverse transform was applied. The wavelet the author uses is Daubechies wavelet with 20 coefficients. The results are satisfactory but some additional fine tuning on the choice and the length of the wavelet should be done.

It can be concluded from this paper that wavelet and sliding average gave the best results in removing the various background signals, whilst also keeping the diffraction hyperbolas. The sliding window averaging will only result in better background subtraction if the number of A scans that is

present over the width of one diffraction hyperbola is large. Furthermore, the quality of the background subtraction depends on the width of the averaging window. Also the estimated average will be affected by the presence of a buried object and hence the subtraction may not be accurate.

The input-output relationship between the radiated electric field and the received one can be written as (Daniels, 1996):

$$\vec{E}_{rec'd}(k) = \vec{E}_{rad}(k) \otimes (h_c(k) + h_t(k)) + n \quad (2.8.10)$$

where  $h_c(k)$  and  $h_t(k)$  are the impulse responses of the clutter and target, respectively, and  $n$  is the measurement noise. In order that the target parameters are found, the other factors have to be eliminated out of the measured signal. The effects of the antenna can be measured under laboratory conditions. Clutter includes scatterers from the soil and surface interface and is estimated from the data.

Kaiser. (2009) developed a clutter reduction algorithm based on *wavelet decomposition and reconstruction*. If  $x(t)$  is the real signal in the time-domain, and  $\psi(t)$  is an analytical wavelet, then the wavelet transform of  $x(t)$  with respect to  $\psi(t)$  is:

$$W_x(u, s) = \frac{1}{\sqrt{s}} \int_{-\infty}^{+\infty} x(t) \psi^* \left( \frac{t-u}{s} \right) dt \quad (2.8.11)$$

In the above,  $u$  is the time delay,  $s$  is the scaling factor,  $x(t)$  is the real signal in time domain,  $\psi(t)$  is an analytical wavelet and  $\psi^*$  is the complex conjugate<sup>10</sup> of  $\psi$ .

Here each of the A scans can be decomposed into a number of triplets  $(u, s, W_x(u, s))$ . Each of the triplets gives an indication of how well that particular wavelet can be found in the signal and therefore the base wavelet is chosen as the emitted signal itself. When the reconstruction of the signal is performed using only a limited number of the triplets, the clutter can be reduced. However, choosing the reconstruction triplets can be difficult.

Carevic (1999a) attains an estimate of the background signal (return of the air-soil interface) and this estimate is found locally. Any sudden changes in this estimate are assumed to correspond to the returns from the buried object. Sudden or abrupt changes from the estimated values are detected using a translation invariant wavelet packet decomposition. Then the detection statistic is the summation of several of the peak energy values of the translation invariant wavelet signal.

(Saito. (1994); van Kempen et al. (1998)) propose an algorithm based on *Shannon entropy*. In this method, a clutter reference signal and the A scan are decomposed and each of the triplets are linked to a discriminant measure. In order to carry reconstruction, only the triplets with the highest discriminant value are chosen.

Some of the above developed clutter removal techniques will be explored further during the development of the 2D algorithm in Chapter 3 of this thesis and also during the development of the 3D algorithm in Chapter 4 of this thesis.

Once the above techniques remove the clutter, the next logical step is to try and carry out further

---

<sup>10</sup>a pair of complex numbers, both having the same real part, but with imaginary parts of equal magnitude and opposite signs.

steps to help in the detection/identification of the target signal. Processing methods used for further processing include, advanced algorithms for hyperbola detection ((Milisavljevic, 2001); (van Kempen et al., 1998)), convolution models (Roth, 2004) and migration which is described in detail later on in this chapter. An overview of other different signal processing techniques using GPR can be found in (Daniels (2004); MacDonald et al. (2003a)).

Fourier analysis, which has been extensively used in signal processing, is useful but is limited by its inability to localize events within a signal in the frequency and time domain (Daniels et al., 2004). The basic approach to inverse filtering using Fourier transforms is (adapted from Brooks (2000)) :

$$g(t) = f(t) * h(t) \quad (2.8.12)$$

where  $g$  is the observed distortion of a kernel  $h$  over the original image  $f$

In the frequency domain this would be represented as, by using discrete time Fourier Transforms:

$$G(k) = F(k) \times H(k) \quad (2.8.13)$$

Deconvolution of the original image  $f$  in the frequency domain is given by:

$$F(k) = \frac{G(k)}{H(k)} \quad (2.8.14)$$

$F$  can be converted back into the time domain using the inverse discrete time Fourier transform. The inverse discrete Fourier Transform representation of a time domain signal can be expressed as:

$$f(t) = \frac{1}{2\pi} \int_{-\pi}^{+\pi} F(k) e^{i\omega k} d\omega \quad (2.8.15)$$

For the removal of clutter from the original GPR signal the following methods were used:

- The mean vector of a number of A scans is computed and then subtract this value from each A scan.
- Another technique investigated was the windowed average subtraction method. This is an adapted version of the general average subtraction method. Here the average A scan is not calculated over the whole B scan, but only over the A scans within a window around the signal that is treated. This subtraction should adapt to slowly varying signals so that slightly oblique surface reflections can be eliminated.
- The use of the clutter removal technique that was given earlier on in the section on clutter removal. This technique is presented by Daniels (2004) and is represented by Equation 2.8.1.

Paik et al. (2002) present an extensive literature review of various image processing techniques that could be used in the field of landmine detection. The survey commences by outlining the consequences of landmines and provides an overview of landmines and their characteristics. The

authors consider GPR systems and a number of other technologies. Various signal and image processing techniques such as segmentation, contrast enhancement, feature extraction, and filtering are presented. The experimental results provided by the authors are promising.

### 2.8.1.1 Signal identification and analysis

It is to be noted that noise characterisation and reduction is a separate operation to signal identification and analysis. Once the undesirable clutter has been reduced by the above techniques the next objective would be to actually detect the target. Some processing methods for detecting the target signal and hence the target include migration techniques ((Loewenthal et al., 1976); (Lopera et al., 2005b); (Ruthenberg, 1998)), algorithms for the detection of hyperbolas (Milisavljevic, 2001) and convolution models (Roth, 2004). Some techniques that look for hyperbolas in B scans are (Gader et al. (2001a); Zhu and Collins (2005); Potin et al. (2006b)).

It is quite clear that an A scan detection is not sufficient to find the areas when an object might be present. A method that has been developed for B scan detection is based on Gabor filters that enhance the edges of the hyperbola-like structures that exist in the B scans. Finally, now having determined the hyperbola-edges, the actual hyperbola estimation can be done using a generalized Hough transform (Hough, 1962). The estimation of the hyperbolas will enable the parameter estimation to give an estimate of the object's depth, position and the velocity of propagation in the subsurface. It can be demonstrated that these are only coarse estimates since many assumptions are made by the methods, such as point scatterer model and a perfect hyperbolic shape.

A technique based on the Hough Transform that allows the calculation of the hyperbolas in a B scan is now presented.

Capineri et al. (1998) present a method for calculating the hyperbolas that exist in a B scan. Their method is a modified version of the Hough Transform (HT).

First the authors consider a point  $(x, y)$  that lies on a line with an equation  $\rho = x \cos \theta + y \sin \theta$  in which  $\rho$  and  $\theta$  are the polar contributions of the co-ordinates of the line. To proceed with HT, the polar co-ordinates are discretized. Therefore when a bright pixel for  $(x, y)$  occurs in the image all values of  $\theta$  are used and the corresponding  $\rho$  is calculated. The net result will be a sinusoidal curve when considering the Hough space. The intersecting points of the sinusoidal curve and the line will result in the detected line. A threshold has to be specified for finding the bright pixels for the detected line selection.

Then the authors consider the case for hyperbolas. For hyperbolas, if  $d$  is the depth of the scattering object,  $x_1$  is the horizontal position and  $x$  is the corresponding horizontal position of the antenna. Then the time of flight ( $T$ ) is:

$$T = \frac{2\sqrt{(d^2 + (x - x_1)^2)}}{v} \quad (2.8.16)$$

where  $v$  is the propagation velocity.

Since both axes are displayed with discrete values and the discretization will result in the following equation of the hyperbola:

$$j^2 = \alpha + \beta (i - \gamma)^2 \quad (2.8.17)$$

with:

$$\alpha = \frac{4d^2}{\Delta T^2 v^2},$$

$$\beta = \frac{4\Delta x^2}{\Delta T^2 v^2} \text{ and}$$

$$\gamma = i_c.$$

where  $\Delta T$  is the horizontal scanning step and  $\Delta x$  is the vertical scanning step.

Then the combining of votes of the  $\alpha, \beta, \gamma$  that corresponds to the possible hyperbolic arcs are performed. The high spots in the combined space will identify the parameters of the most likely hyperbolas. The authors then state that this technique is computationally intensive and propose a randomized Hough Transform (RHT). The RHT accumulates votes only on curves passing through triplets of randomly selected points. Results show a promise for the method. The RHT method is thus based on probabilistic method and slice sampling is used, only a small subset of the points are considered and this reduces computation time and storage. A disadvantage of the RHT method is that current versions of RHT only function on binary images, therefore for greyscale images, thresholding or filtering has to be applied beforehand. The RHT method also only detects analytical geometrical shapes rather than arbitrary ones and this can be a problem in detecting landmines (Fung et al., 1996).

Once having removed the clutter and having explored a Hough transform technique, the next section explores a modelling technique which can be used to predict the reflected signals and fields from buried targets.

Forward modelling has been shown to be a useful tool for studying the effect of soil type, target properties and the burial depth on the GPR signal response of buried objects. During an initialization phase, *SIMCA* carries out radar simulation using the system parameters of the radar and the soil properties. This is done using a forward modelling approach using *GPRMAX 2D/3D v1.5* developed by Giannopoulos (1997) which uses the finite-difference time-domain method (FDTD) to solve Maxwell's equation. It can be concluded that the forward modelling approach allows the practitioner to understand the influence of target, soil properties and also the burial depth on the GPR signal. This also allows the designer to develop novel algorithms and to simulate various conditions and use the knowledge gained in the development of the algorithm. Therefore bearing this in mind, the next section details the forward modelling of GPR data using a GPR simulator as this simulation is fundamental to the development of the *SIMCA* algorithm.

### 2.8.2 GPRMAX 2D/3D v1.5 used for forward modelling

*GPRMAX 2D* is an electromagnetic wave simulator for GPR modelling. In order to perform the modelling the program solves Maxwell's equations using the FDTD method. Maxwell's equations are first order partial differential equations which state the relationship between the electromagnetic field quantities and their dependence on their sources. The general expression can be written as (the following equation has been taken from Giannopoulos (1997)):



$$\nabla \times E = -\frac{\partial B}{\partial t} \quad (2.8.18)$$

$$\nabla \times H = \frac{\partial D}{\partial t} + J_c + J_s \quad (2.8.19)$$

$$\nabla \cdot B = 0 \quad (2.8.20)$$

$$\nabla \cdot D = q_v \quad (2.8.21)$$

where  $t$  is time in seconds and  $q_v$  is the volume electric charge density in coulombs/cubic meter.

The field vectors are assumed to be single-valued, bounded and continuous functions of position and time. But for a GPR response where simulation is required from target or targets, the above equations have to be solved with respect to the geometry of the problem and the initial conditions.

In order to obtain a solution, the excitation of the GPR transmitting antenna has to be defined and then to allow for the resulting fields to propagate through space and reach a zero value at infinity. This is because there is no specific boundary which limits the problem geometry and where the electromagnetic fields can take a value.

The approach taken by FDTD to the solution of Maxwell's equations is to discretize both the space and time continua. The discretization spatial  $\Delta x$ ,  $\Delta y$  and  $\Delta z$  and temporal  $\Delta t$  steps play an important role, this is because the smaller they are the closer the model is to representing the real situation. The only problem that arises is because computers have a limited amount of storage and finite processing speed, the values of the discretization steps have to be finite. This discretized FDTD grid is the Yee Cell named after Kane Yee who is the inventor of the FDTD method (Yee, 1966). This is illustrated for the 3D case in Figure 2.20.

The numerical solution can be obtained directly in the time domain by using a discretized version of Maxwell's curl<sup>11</sup> equations which are applied to each FDTD cell. The solution is obtained in an iterative way because the equations are discretized in both space and time. The electromagnetic fields propagate in the FDTD grid in each iteration and each of the iterations relate to an elapsed simulated time. An approximation condition known as absorbing boundary condition (ABC) is applied at a sufficient distance from the source to limit the computational space. The ABC simulates an unbounded space, as is required (Powers, 1995). The remaining boundary conditions which apply at interfaces between different media are automatically assigned in the program.

Since the beam pattern of the GPR antenna is widely spread and hence the spatial resolution of the image is reduced, this resulting problem needs to be corrected. This can be explained by the fact that an Anti-personnel mine can have a volume of approximately 99 cubic centimetres, a diameter of 56mm and a height of 40mm (M14 mine). The dimensions of such a mine is relatively small compared to the footprint of a GPR beam at 200mm. The migration technique is a tool available

<sup>11</sup>The curl of a vector field can be taken as a vector operator which calculates the infinitesimal rotation of a 3D vector field. The curl is given by a vector at every point of the field. Combining the attributes of the vector give the rotation at that point.

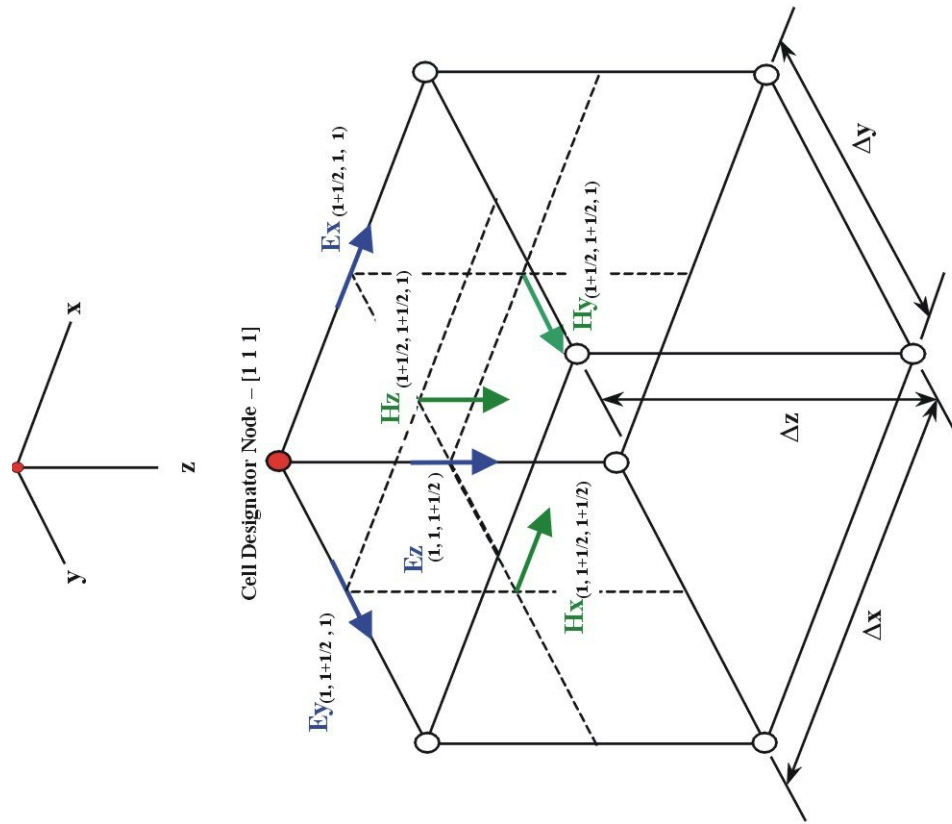


Figure 2.20: The 3D FDTD Yee Cell  
(Yee, 1966)

to correct this problem and needs to be explored. The next section details the classical techniques available in the field of migration and the section outlines contemporary work subsequent to the start of this PhD project.

## 2.9 Migration technique to process GPR data

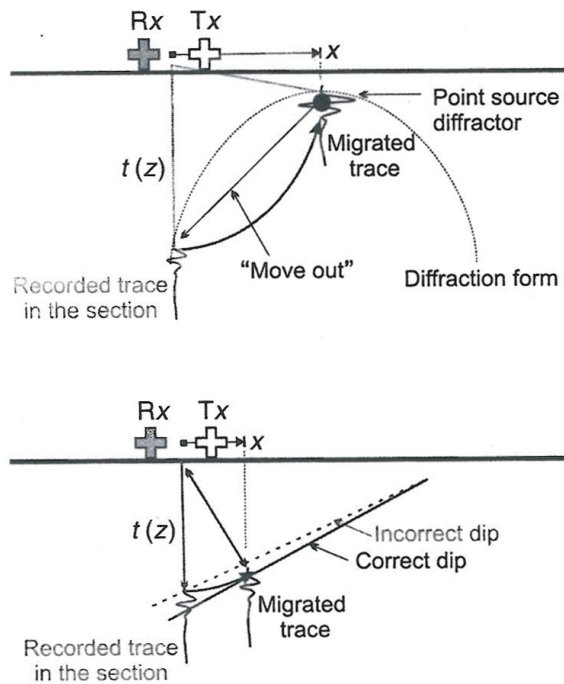
Some algorithms that process GPR data can be used to convert the raw GPR images to ones that are much closer to true subsurface objects. They can be viewed as a class of inverse problems ((Holzrichter and Sleefe, 2000); (Carin et al., 2002)). Because of the beam-width of the transmitting and receiving antenna, the reflections on a structure will not be focused. This is because the radar antenna transmits energy with a beam width pattern and even before the radar is directly below the target and is several centimetres away from the beam axis it may be detected. This is because radar antennas are constrained to transmit/receive a hemispheric beam which expands with time, therefore even before the antenna is directly above a target the target can be detected. Thus, objects of finite dimensions appear as hyperbolic reflectors on the B scans. The reason as to why a hyperbolic shape is formed is explained in detail in Chapter 4, Section 4.1.

Migration is used for improving the section resolution and producing more spatially realistic images of the subsurface. The section resolution refers to the re-constructed physical shape of the object. One of the processing algorithms that reconstruct the reflecting structure from the B scans at the surface, is called Migration. The technique can also be viewed as the focusing of reflections in the recorded data back into the true position and physical shape of the target. Migration can thus be considered as a form of spatial deconvolution that aims at improving the spatial resolution.

Migration techniques were initially developed for the acoustic, seismic and geophysical applications but GPR practitioners have used the technique for image reconstructions and in producing realistic images. Hagedoorn (1954) originally developed the migration technique in two-dimensions. (Gazdag (1978); Gazdag and Sguazzero (1984)) present the original migration techniques that were used in the seismic industry. Current developments include the employment of wave equation methods such as Kirchhoff migration, finite difference migration and frequency wave number migration. The main advantage of migration is that it makes no assumptions of the object's shape and size. However, the disadvantage is that it requires the propagation velocity of the GPR signal in the soil. (Berkhout (1981); Schneider (1978); Özdoğan Yilmaz (1987) and Robinson and Treitel (1980a)) present excellent material on migration.

As shown by Figure 2.21, the geometric migration problem can be thought of as a technique which migrates a segment of an A scan time sample to the apex of a curve of maximum convexity. The ideal migration would be one which performs an accurate transformation from the position time domain to the position depth domain. This results in the reconstruction of the point scatterers with a certain dip in some cases and the point scatterers cause the presence of a hyperbolic structure in the image. But this causes the receiving antenna to get reflections of point scatterers that are not directly below it. But since this reflection is not perpendicular to the antenna surface, the two way travel time is going to be larger than when the antenna is directly above the object. It can be said that

because the migration process sums the amplitudes along the hyperbolic curve, the signal-clutter ratio is going to be improved.



### Methodological principles of migration

**Diffractors** – Migration tries to corrects the position and amplitude of the recorded signal on the “legs” of the diffraction hyperbola by reconstructing the wavelet at the target point source.

The algorithm attempts to either match an ideal hyperbolic function to the diffractor’s form, or calculate/model the degree of recorded signal “move out” of the trace from its true position. The calculation needs to know the horizontal distance ( $x$ ) and depth ( $z$ ) from time ( $t$ ) using an accurate velocity-depth relationship. The Migration results in the diffraction hyperbola’s legs being collapsed into a single point.

**Reflections** – Migration tries to corrects the position and, therefore, dip of the recorded reflection by moving the reflected signal back to its original position.

This, as with the diffractor, is due to the fact that the recorded signal is plotted beneath the mid-point of the antenna pair but, in fact, the reflection signal emanates from a position which is “ahead” of the antenna. Again, the horizontal distance ( $x$ ) and depth ( $z$ ) needs to be known. The Migration results in the dip of sloping reflectors being corrected to a steeper angle.

Figure 2.21: Principle of migration: The diffracted energy is collapsed back to its point-source and the incorrect dip is corrected.

(Jol, 1994)

### 2.9.1 Exploding source model

The exploding source model is a model often used in the area of seismics to illustrate the mathematics behind some of the methods. The model would be good because it fits in well to explain the migration problem. In terms of using the same exploding source model for GPR data where there is two way travel time from the transmitter to the object and from the object to the receiver; the angle of the cone is changed so that it will now take twice as long in terms of time. Or to make the data comparable one can also say assume that the propagation velocity is half the value of the actual velocity in the model.

The 2D situation of the exploding reflector model is shown in Figure 2.22[B] and it can be seen that the radiated wave propagates only from the source towards the antenna. The configuration of the same model is shown in Figure 2.22[A]. It can be seen that the exploding source commences from the  $xz$ -plane and is also known as the object plane. The sources in the object plane explode as the name suggests and waves are sent out at time( $t$ )=0. The waves then move with respect to time and are shown on a horizontal axis and then reach the surface. The receiver is located on the  $x$ -axis at  $z=0$  and the receiver records the data. This plane is also referred to as the data plane. This

recorded data can be expressed as  $b(x, z = 0, t)$ . The migration method which is the best one will transform the data from the data plane back into the object plane at  $b(x, z, t = 0)$ . The resulting migrated image is called the migration re-constructed image  $\hat{O}(x, z)$  and is an estimation of the object plane (Zhang et al., 2000).

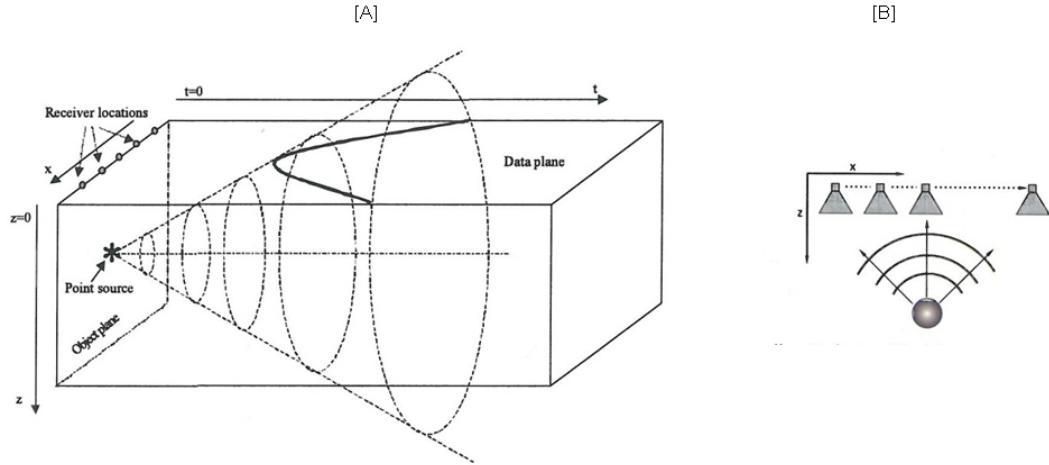


Figure 2.22: [A]: Configuration of exploding source model; [B]: Exploding Reflector model.

[A]: (Scheers et al., 2000); [B]:(Zhang et al., 2000)

### 2.9.2 Different types of migration

Migration is really successful in applications where there is a relatively uniform environment such as deep geological conditions and is less successful with GPR because of the complex and heterogeneous environment (Jol, 1994). However, some practitioners have extracted the potential of the migration application and have used it to a range of areas. These include reverse time migration ((Fisher et al., 1992); (Meats, 1996)), Kirchhoff migration (Moran et al., 1998) and Frequency-Wavenumber migration ((Fisher et al., 1994); (Yu et al., 1996)). (Berkhout (1981); Berkhout (1982)) showed that wave field extrapolation techniques are done on the basis of three methods: plane wave method or F-K, finite-difference method and Kirchhoff summation method. Migration applied to conventional down-looking GPR systems are presented in (Lertniphonphun and McClellan (2000); Binningsbo et al. (2000); Fischer et al. (2000)).

Because some of the seismic migration methods have some limitations when used with GPR systems, practitioners have made modifications to the seismic migration techniques. These include the matched filter migration technique (Leuschen and Plumb, 2000); variations to the Frequency-wavenumber migration when applied to landmine data (Song et al., 2006) and modification of the Kirchhoff migration technique to take care of different radiation patterns (Moran et al., 1998).

Leuschen and Plumb (2000) present a pair of finite-difference-time domain reverse time migration algorithms for use in GPR data processing. By using linear inverse scattering theory they are able to develop a matched-filter response to the problem domain. Thus by the use of EM wave propagation and the scattering theory accompanied by the matched filter, they developed a reverse-

time migration algorithm. By using point scatterers a separate filter is developed for each pixel and then each filter is made independent by assuming linear scattering. The image that is generated by the reverse time migration algorithm can be thought of as a wave front image reconstruction. This image is expressed as a convolution of the received and the estimated signals.

Song et al. (2006) develop two dimensional migration methods that can process GPR data and obtain images close to the actual geometry of the target, using a non uniform fast Fourier transform algorithm. They state that Phase-shift migration is a widely used method but that there is a non uniform relationship between the uniform frequency samples and the wave numbers. According to the author's conventional methods obtain uniform wave number samples using linear interpolation.

The algorithm carries out approximation of the non uniform discrete Fourier transform. They then compare their technique to existing migration techniques on synthetic and real data. Results show that the technique is feasible and allows estimation of the target dimensions. Figure 2.23 shows the results obtained from their algorithm.

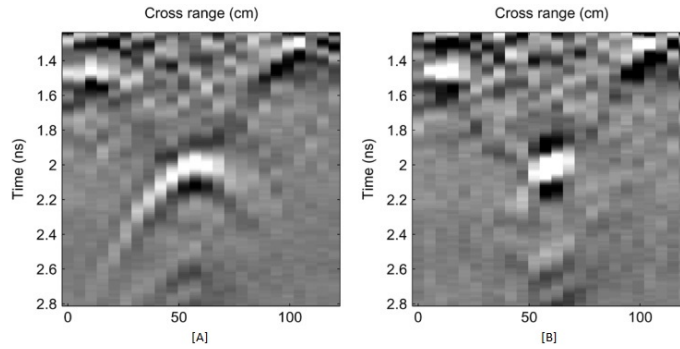


Figure 2.23: GPR data from a plastic landmine. [A]: Raw image; [B]: Migrated image.

(Song et al., 2006).

Van Gestel and Stoffa (2000) state that ‘due to the radiation pattern of the GPR antennas, the amplitude of the reflection is not only dependent on the distance between the target and the antennas, but also on the angle of orientation between the antennas and this target’. They use a method of rotation and apply this to the radiation pattern of the antenna and then extract the location of the origin of the reflected wavefield. Using this information the authors are able to improve the migration scheme. They state ‘that in conventional migration schemes, recorded data are migrated to all angles’. But in their method the recorded data are migrated to certain grid points only and they say that it makes the migration scheme much faster than conventional methods.

### 2.9.2.1 Diffraction-summation Migration

Assuming a constant velocity medium, the unfocussed data of the point-reflector is indicated by a diffraction hyperbola. Therefore for each point on the object plane, say of a 3D data set  $b(x, y, t)$ , one has to construct a diffraction hyperbola in the image plane and find out where the hyperbola intersects with each trace. The object plane is the plane where the point source is located and can be seen on Figure 2.22. Once having found out this intersection, the method takes the value of each

trace at the point of intersection and finds the sum of all these values. The result is the value of the pixel and is placed in the object plane at that point. In Figure 2.24 for example the principle of the diffraction summation principle is outlined. When an object exists in the apex of the diffraction hyperbola, the amplitudes add. Although the algorithm is easy to implement, it is computationally intensive because the diffraction template on which one has to sum has to be calculated again and again for each depth. Also this method introduces artefacts in the migrated image because of the fact that the summation of data along a diffraction hyperbolae do not always tend to zero when a target does not exist (Scheers et al., 2001).

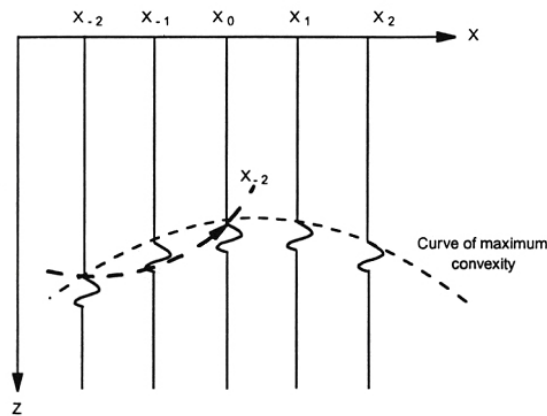


Figure 2.24: Diffraction summation migration.  
(Daniels, 1996)

Herman (1997) uses a 3D migration technique based on diffraction-summation to focus the widely spread energy and remove the artefacts due to the wide beam width of the antenna. Thus using a digital beam forming technique by post processing the digital representation of the GPR output they were able to focus the energy of the antenna. He calculates the migrated value of a voxel by summing the raw value of the voxels along the reflection profile. He then thresholds the migrated data on the basis of the intensity at a voxel. This threshold can be used to decide whether a target is present or not. The migration technique is used by an autonomous robot for subsurface mapping and in the retrieval of targets such as landmines.

Herman (1997) further proposes another method which he calls surface based processing. This technique uses a template matcher which allows the 3D data to be reduced into 2.5D. The advantage is the low overhead due to only containing the target information. The author concludes that most of the required target information is obtained at the points where the wave changes phase. The peak detector therefore detects the peaks and neglects the rest of the data. The reduced data is called a range image. After template matching the thresholding described above enables target detection.

### 2.9.2.2 Kirchhoff Migration

Kirchhoff migration can be thought of as the wave-equation based successor to the diffraction stack procedure outlined above. The wave-equation formulation for Kirchhoff migration is outlined by

Schneider (1978). The principle behind Kirchhoff migration is the back propagation of the data plane measured wavefront to the object plane at time=0 by use of an integral solution method to the scalar wave equation. The feasibility of applying Kirchhoff migration to EM waves is because of the fact that the vector wave equation is reduced to a scalar wave in a homogeneous and isotropic medium.

Kirchhoff migration produces a significantly higher quality image and lower sidelobe levels than the diffraction stack migration. Furthermore according to Scheers et al. (2001) the following differences are observed when looking at diffraction summation method and Kirchhoff migration method:

1. A oblique factor  $\cos(\theta)$  that is included because the normal to the wavefront is not parallel to the normal of the measuring surface.
2. Because there are spreading losses of spherical waves in Kirchhoff's migration, a spreading factor has to be included.
3. The summation over the hyperbola has to be taken on the time derivative of the recorded wave. Hence before performing the summation, the time derivative of each A scan needs to be established.

Although Kirchhoff migration is quite flexible, a problem arises if we assume a single spike on the unmigrated signal. In such a situation Kirchhoff migration will spread out the spike over the locus of all possible reflection points, which will unfortunately bring up the sidelobes and thus reduce the dynamic range of the system (Feng and Sato, 2004).

### 2.9.2.3 Finite-Difference Migration

This kind of migration is similar to the Kirchhoff's migration and is a method of back-propagation of the wavefront and is measured in the data-plane towards the object plane at time=0. The only difference with the Kirchhoff migration lies in the difference in solving the scalar wave equation and the finite-difference migration is based on the differential solution. Therefore at time  $t$  the wavefront, calculation of the wavefront at time  $t - \Delta t$  is performed using finite difference and the back propagation takes place until time=0.

### 2.9.2.4 Frequency-Wavenumber Migration

Stolt devised Fourier transform in migration and was derived from the scalar wave equation for isotropic medium that is without any sources (Stolt, 1978a). Variations of the original Stolt method were formulated and are grouped under the names Frequency-Wavenumber or f-k migration. The f-k migration that Stolt developed is a means of focusing the scattered response field which is produced by a monostatic radar back to its original location using 2D Fourier transform. The Stolt method is based on the exploding reflector model. Some artefacts are introduced by this migration because of the Fourier transformations (Scheers et al., 2001).



Kabourek and Cerny (2010) present two migration techniques, namely Synthetic Aperture Radar (SAR) and Stolt Migration. They state that the SAR technique results in the reflected wave transformation into a spatial wavenumber domain. According to the authors the difference between the two algorithms is that the Stolt migration data are multiplied by a correction term before transformation. Results indicated that similar results are obtained from both the methods.

### 2.9.2.5 Phase-shift Migration

Phase-shift migration was developed by Gazdag (1978) and it falls under the wavenumber migration family and is used in the re-focusing of radar images. The wavenumber migration is a general representation of the frequency-wavenumber migration. It is based on the back propagation of the scalar wave equation. The steps used by the algorithm are:

1. Fourier transform of the data over position,  $x$  and time,  $t$ .
2. Calculation of the fields at a new depth as a result of the phase-shift operation.
3. Inverse Fourier transformation of the wavenumber data over the  $x$  direction co-ordinate of the wavenumber vector and  $\omega$ .

Lopera et al. (2005b) use a denoising and migration technique to refocus scattered GPR signals to their original location. They remove ground clutter from the image with a high pass filter. According to them, using a small window for the filter length causes further noise to be added; whereas a large window reduces the contrast of the image. The hyperbolic curves are then detected using a Randomized Hough Transform (RHT) (Lopera et al., 2004). From this RHT they say they are able to determine the position of the target. Finally they integrate the information from the RHT with phase shift migration to determine the size of the object and its accurate position.

Gu et al. (2004) state that spatial aliasing that occurs in migrated GPR data has not been considered by other authors. A migration algorithm is applied to a forward looking GPR system by the authors. They state that such forward looking systems have an advantage over conventional hand held GPR systems because of their higher standoff distance. In terms of migration they use Phase-shift migration. They state such a phase shift migration causes spatial aliasing and minimize this by zero padding in space. Results showed that the phase shift migration improves Signal-Noise ratio and the detection of the target is also improved.

### 2.9.2.6 Migration by deconvolution

Scheers (2001) developed a migration method that took into account the characteristics of the acquisition system and the ground characteristics. Hence the time domain model of the GPR is included in the migration scheme. Using forward modeling a synthetic 3D point spread of the GPR is calculated using a point scatterer at a certain depth. The 3D point spread function which contains the system characteristics such as the waveform of the excitation source, the antenna footprints and impulse response of the antennas is then utilized in the deconvolution of the recorded data. Hence

the migration scheme is a back propagation technique based on the deconvolution of the C scans with the point spread function (Scheers, 2001).

Using the co-ordinate system depicted in Figure 2.25 and considering a bistatic antenna configuration and that variation in propagation velocity occur only in the downward direction, the 3D data  $b(x, y, z = 0, \text{time} = t)$  are recorded on a regular grid when the antennas are in motion in the  $(xy)$  plane at  $z = 0$ . At any position  $\vec{r}_a = (x_a, y_a, z = 0)$  for the antennas, the received voltage given by an A scan is (the following equations have been taken from Scheers (2001)):

$$b(\vec{r}_a, t) = \frac{T_{a-g}T_{g-a}}{8\pi^2 R_t R_r c} g_d(t) \otimes h_{N,Tx}(\vec{a}_i, t) \otimes \Lambda_{1,1}(\vec{a}_i, \vec{a}_s, t) \otimes h_{N,Rx}(-\vec{a}_s, t) \otimes \frac{dV_S(t)}{dt} b(\vec{r}_a) \quad (2.9.1)$$

where  $V_S(t)$  is the excitation voltage applied at the transmitting antenna

$h_{N,Tx}(\vec{a}_i, t)$  is the normalized IR of the transmitting antenna in the direction  $\vec{a}_i$

$h_{N,Rx}(-\vec{a}_s, t)$  is the normalized IR of the transmitting antenna in the direction  $-\vec{a}_s$

$g_d(t)$  is the response of the impulse representing the 2-way path length loss and the ground dispersion

$\Lambda_{1,1}(\vec{a}_i, \vec{a}_s, t)$  is the IR of the target  $= \sqrt{r}$  where  $r$  is the target radar cross section

$R_t$  is the total length of the path traversing the transmitting antenna to the target

$R_r$  is the total length of the path traversing the receiving antenna to the target

$T_{a-g}$  is the transmission coefficient at the air to ground interface

$T_{g-a}$  is the transmission coefficient at the ground to air interface

$\vec{a}_i$  is the direction of radiation of the transmitting antenna toward the target

$\vec{a}_s$  is the direction of the scattered field from target towards the receiving antenna.

Scheers (2001) then groups all the factors, but not the IR of the point target, into one factor  $w(\vec{r}_a, \vec{r}_o, t)$  and equation becomes:

$$b(\vec{r}_a, t) = w(\vec{r}_a, \vec{r}_o, t) \otimes_t \Lambda_0(t) \quad (2.9.2)$$

Equation (2.9.2) can be re-written as for the antennas at  $z = 0$  with the point scatterer at a fixed depth  $z = z_0$ , the response  $w(\vec{r}_a, \vec{r}_o, t)$  is related to  $\vec{r}_0$  and  $\vec{r}_a$  by their difference only:

$$b(\vec{r}_a, t) = w(\vec{r}_a - \vec{r}_o, t) \otimes_t \Lambda(r_0, t) \quad (2.9.3)$$

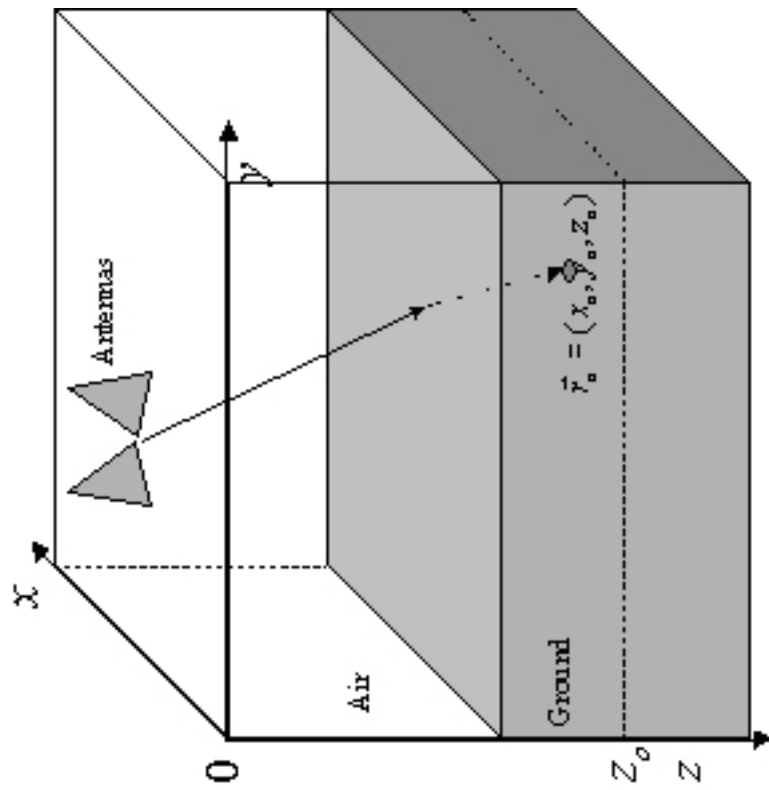


Figure 2.25: Representation of the co-ordinate system for migration by deconvolution.  
(Scheers, 2001)

'If an object can be modelled by a set of independent small isotropic point scatterers, all at approximately the same depth  $z = z_0$ , the output voltage  $b(\vec{r}_a, t)$  will be a combination of the contribution of each individual point scatterer that is clearly a convolution in space if we assume that the operation is linear' (Scheers, 2001).

The point spread function of the GPR is represented by the 3-dimensional matrix  $w(x, y, z_0, t)$  for a depth  $z_0$ . Figure 2.26 illustrates the 3D point spread function of the system at a depth of 6cm below the ground and is obtained by forward modelling.

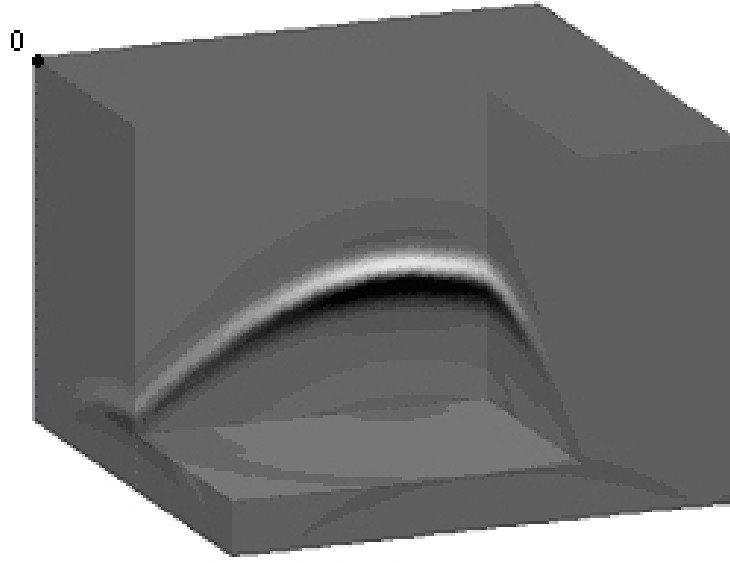


Figure 2.26: A C scan of the point scatterer at a depth of 6cm below the ground calculated by forward modelling.

(Scheers, 2001)

Scheers (2001) states that the point spread function at a given depth can be used for different depth ranges.

Scheers (2001) calculates the 3D Fourier transform of the recorded data using the below formulae when related to the  $x, y$  and  $t$  co-ordinates:

$$B(k_x, k_y, \omega) = \iiint b(x, y, t) e^{ik_x x + ik_y y - i\omega t} dx dy d\omega \quad (2.9.4)$$

where  $B(k_x, k_y, \omega)$  is the 3D Fourier transform and  $b(x, y, t)$  is the recorded data.

Scheers (2001) states that a much faster and computationally less intensive solution of the deconvolution is to carry it out in the frequency wavenumber domain using the Wiener filter (Andrews and Hunt, 1977). This thus gives the migrated image, found by the inverse 3D Fourier transform of the Wiener filter.

Scheers et al. (2001) technique is compared to the *SIMCA* algorithm in Chapter 3 for the 2D technique and in Chapter 4 for the 3D technique. Having given the various methods available in processing a raw GPR radargram and producing images of the subsurface to help deminers locate and clear landmines, it would be good to explore the commercial software available in the market and to assess how they present images. *REFLEXW* software has been used and comparison of its cleaned image has been made with the cleaned image of the subsurface produced by the *SIMCA* algorithm in Chapters 3 and 4 of this thesis.

## 2.10 Commercial software available for GPR data processing.

Numerous commercial software packages are available which allow almost any imaginable data manipulation. In this section, two pieces of software that are used by GPR users to process and display their data are discussed. They are namely, *GPR-SLICE*<sup>12</sup> software produced by 'Geophysical Archaeometry Laboratory Inc.' and *REFLEXW*<sup>13</sup> software developed by 'Sandmeier Scientific software'.

### 2.10.1 GPR-SLICE software

GPR-SLICE is interactive software and is used for the processing and image creation of GPR reflection data. The software basically integrates radargram profiles that have been taken over a gridded area and produces horizontal time slice maps of anomalies. Time slices involve the mapping of reflection anomalies horizontally across a site and at various depths. The software takes the radargrams and causes them to be "binned" or spatially averaged in both the horizontal and vertical windows to look at the pulse energy and then the software interpolates between the slices to create 3D volumes. The software can apply a series of filtering operations to remove background noise before carrying out the time slice analysis. The user can specify which filtering operations to perform.

The software also can integrate with GPS navigation. By using OpenGL 3D modules, real time isosurface rendering can be achieved. The OpenGL consists of about 250 functions which are used to draw 3D scenes. The software can also apply a number of the conventional migration algorithms such as Kirchhoff Migration and Variable velocity migration to name a few. The process can involve the fitting of a hyperbola so they match the hyperbolas on the B scan. This hyperbola is applied throughout the B scan and all the waves that fall along the hyperbola are added and this calculated result is put at the top of the vertex of the hyperbola. This process is repeated for every point on the B scan.

In terms of isosurfaces, the software uses shading to illuminate the surfaces so they match those on the site. The isosurfaces are displayed by an isosurface threshold setting. The user specifies the level of threshold to use and the software does not calculate the optimum threshold. Users can also overlay the relative target reflections onto a single time slice.

<sup>12</sup><http://www.gpr-survey.com/>

<sup>13</sup><http://www.sandmeier-geo.de/>

Table 2.2 also highlights the cost to licence the GPR-SLICE software along with the outright purchase price for the software.

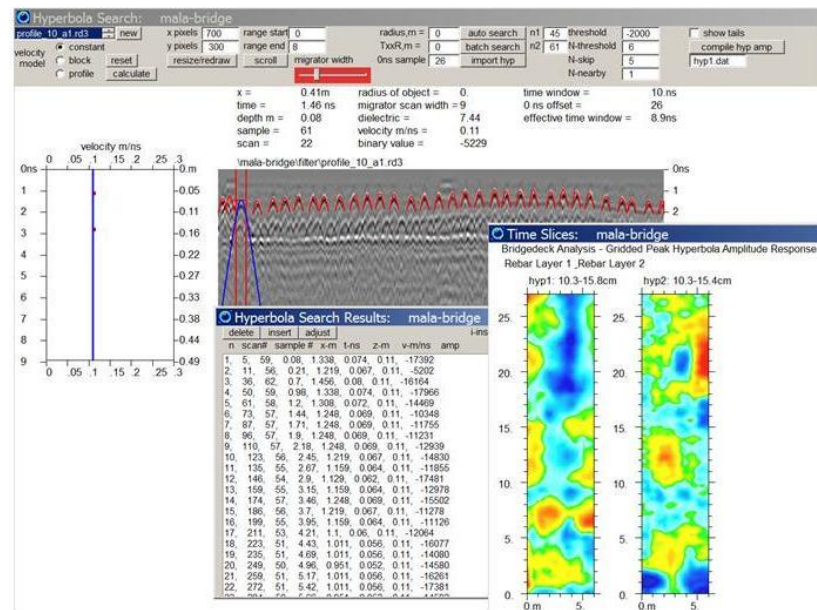


Figure 2.27: Time slices and recorded hyperbolas on a B scan produced by GPR-SLICE software.  
(GPR-SLICE - <http://www.gpr-survey.com/>)

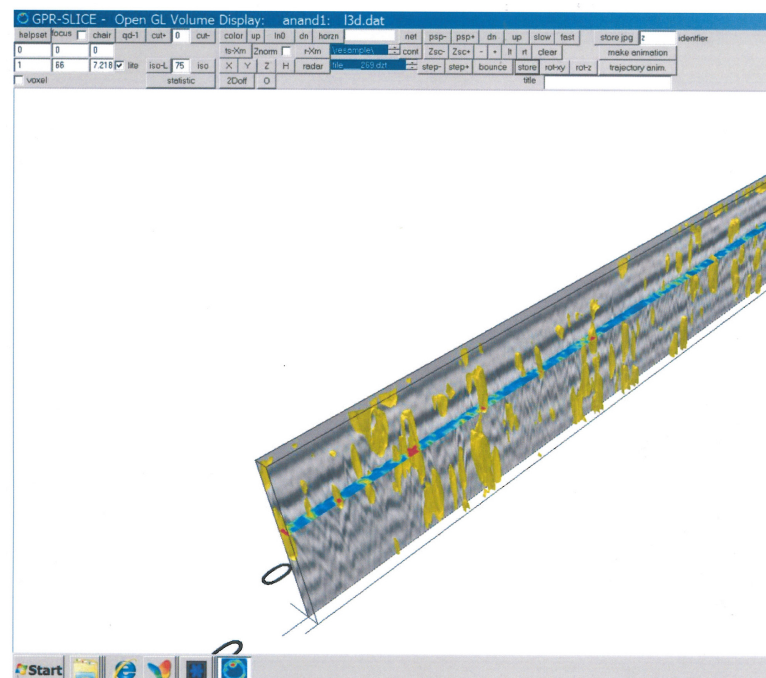


Figure 2.28: A 3D isosurface of some tree root data produced by GPR-SLICE  
(GPR-SLICE)

Mode of use	Price (USD)	Price (GBP)
Subscription for Government agencies or companies with >5 employees	2100	1325
Subscription for universities, NPO and companies <4 employees	1890	1193
Purchase	10900	6878

Table 2.2: Price of annual subscriptions and outright purchase of GPR-SLICE software.

(GPR-SLICE - <http://www.gpr-survey.com/>)

### 2.10.2 REFLEXW software

REFLEXW is a windows based program that carried out the processing and helps users interpret GPR data. The program imports data from a number of formats used by most of the commercial GPR systems. The software can provide the user with a number of filter algorithms to remove clutter from the GPR data. Initially editing operations such as the removing, extraction of single trace/trace range, stacking, subtracting or adding or profiles can be performed by the user. The 2D processing included in the system are the basic filter operations and the various migration algorithms. Two dimensional data interpretation tools such as diffraction hyperbola mapping and filter operation such as time dependent, bandpass, arithmetic function, averaging, median filter, deconvolution, background removal.

Various gain functions in the horizontal and vertical directions can be utilized. Furthermore an adaptive adaptation of the hyperbola to determine the average velocity from a zero offset GPR profile can be carried out. Migration algorithms such as 2D Kirchhoff, 2D fk-migration, prestack migration and diffraction stack can be carried out by the software. The processing can be done using single profiles or a set of profiles as a batch processor.

A 3D dataset can then be formed from equidistant 2D lines or from freely distributed data by the use of a spatial interpolation scheme. This resulting 3D data can be displayed as  $x$ -,  $y$ - or  $z$ -slices. These slices can be displayed in a scrolling window or through the 3D cube using a track bar. The 3D module allows loading a maximum of 25 different 2D files so as to display them. The 3D profiles can be interactively rotated and can be zoomed. The software allows for interactive videos to be developed that display the 2D processed profiles as a 3D cube. Figure 2.29 shows REFLEXW processed 2D GPR data and Figure 2.30 shows the 3D processed data using the REFLEXW software.

Table 2.3 gives an indication of the price of the REFLEXW software. What can be concluded from Tables 2.2 and 2.3 is that commercial software is beyond the limited budgets of many individuals and small companies who acquire GPR data. Furthermore GPR processing and visualization can require the use of multiple commercial software applications. Using such separate programs is often inconvenient and may require data format conversions between the programs. Therefore a less expensive and convenient method is to write processing and visualization software. Such writing of software also has advantages such as reduced expenses, ease of code modifications to address new requirements and practitioners can better understand their algorithms. This has been accomplished by writing the *SIMCA 2D* (Chapter 3) and *SIMCA 3D* (Chapter 4) algorithms to produce 2D and

3D images respectively.

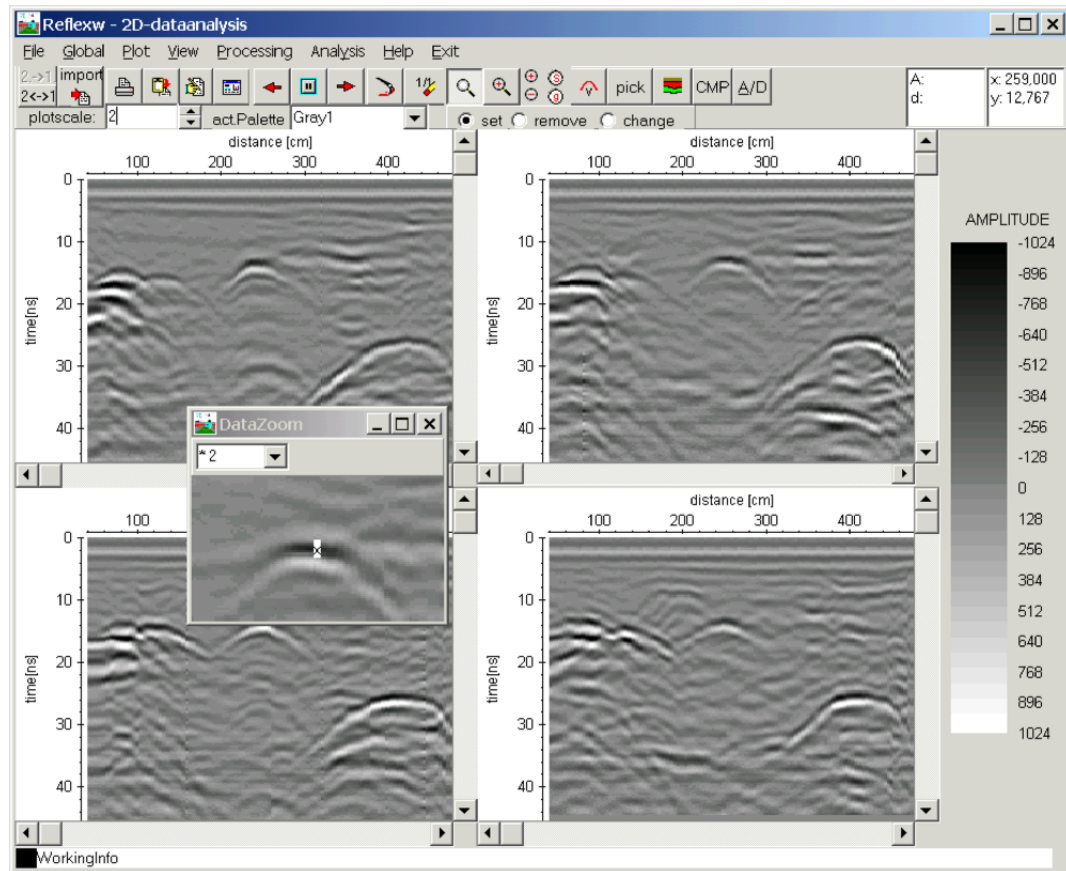


Figure 2.29: Processed GPR 2D profiles by the REFLEXW software.  
(REFELXW)

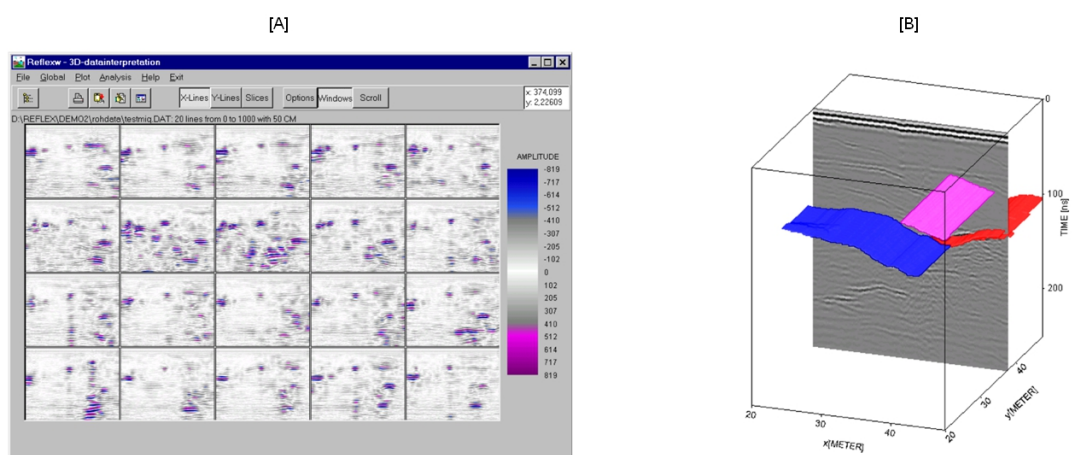


Figure 2.30: Processed 3D data by the REFLEXW software - [A]: Time slices; [B]: Subsurfaces included within a 3D data cube.

(REFELXW)



<i>Type</i>	<i>standard licence price (GBP)</i>	<i>academic licence price (GBP)</i>
<i>REFLEXW GPR/reflection seismic with 2D data analysis</i>	<i>1569</i>	<i>1176</i>
<i>REFLEXW GPR/reflection seismic with 3D data analysis</i>	<i>1486</i>	<i>1094</i>

Table 2.3: Price of REFLEXW software.

## 2.11 Summary and Discussions

In this chapter the history of landmines was presented and the reason for this was to understand the evolution of landmines as it is a known fact that the material used on the casing of the landmine along with the characteristics of the landmine affect the ability of GPR to detect landmines. It was noted that there was some similarity to the currently available metallic landmines. Also it was learnt that the German Army produced the first antitank mines and that the Germans were very meticulous in laying of landmines. Also since one of the themes of this thesis is the detection of landmines, the chapter considered the approach of laying these landmines as adapted by the German army.

The chapter next detailed the various demining techniques available in the market ranging from prodding to GPRs. It was established in Chapter 1 and in this chapter that the GPR was one of the most promising and successful technologies available in the detection of plastic and minimum metal mines. Also the various protocols used in landmine clearance were given in the chapter.

Having come to the conclusion that GPR is a feasible landmine detection tool, this chapter next outlined the different single and multi array systems available in the market, because potential future work would involve the development of a suitable single array or multi array system based on the application area. Also since the depth information obtained by the GPR would need to be tied to an Ordnance survey map, a section of this chapter outlined the literature and methods in this area. It was also noted in the chapter that a spatial positioning system would need to be integrated into a field system to make it fully usable in the field and to give acceptable results. Finally the chapter considered the other commercial software available to process GPR data.

The chapter also explored the various factors that affect the performance of a GPR on the basis of the soil properties and the materials' electrical and magnetic properties. As a summary Jol (1994) concluded that the relative permittivity of a material increases when the amount of water content is increased, whereas the attenuation is proportional to the frequency and conductivity combined. The chapter considered the various mixing models that can be used to simulate the bulk effective permittivity of a material from knowledge of its component parts. This can then be used to understand the performance of the GPR.

In this chapter the various literature available in the field of clutter reduction of GPR data has been discussed. Landmines are usually buried close to the surface of the ground, where the clutter scattering from the ground surface is strong and the actual target signal is very small. Such clutter prevents the detection of the lethal targets and the clutter that affects the GPR can be defined as those signals that are unrelated to the target scattering but occupy the same frequency band. The chapter considered the various clutter reduction solutions like parametric system identification, wavelet packet decomposition, subspace techniques and simple mean subtraction. The section also

presented a technique using HT to calculate the hyperbolae present in a B scan.

The ability of forward modelling using FDTD to determine the ideal trace of a GPR and to allow the formation of the correlation kernel was discussed. This forward modelling using a GPR simulator is fundamental to predicting and modelling a GPR by giving the program with the properties of the radar and the soil properties.

A GPR profile portrays an unfocussed, distorted image of the subsurface structure due to the wide beam pattern of the antennas. Migration algorithms can be used to produce a much focused image. This chapter considered the various migration methods available in the literature.

A 3D approach using C scans has a number of advantages over 2D approaches which use B scans because determining the dimensions of the target from B scans is not possible. Furthermore, 3D approaches allow the visualization of the complete volume of data using a single image. There are not many approaches in the literature that present clear 3D isosurface reconstructions to users. To the author's knowledge 3D landmine detection is new in GPR images using their 3D nature. Two techniques that are comparable to the *SIMCA* algorithm include (Ligthart et al. (2004); Scheers et al. (2001)). Ligthart et al's technique uses two procedures, firstly object detection based on self-developed adaptive thresholding technique and object classification (Groenenboom and Yarovsky, 2002). The obtained data are preprocessed to remove the clutter and to get a better object position accuracy. For the object detection, an adaptive threshold level is used to find out the different threshold levels for each of the depth slices of the 3D image. Then the threshold level which gives the maximum number of targets is chosen. Object classification is based on the extraction of features with selective properties that favor the wanted targets.

In particular the study by Scheers et al. (2000) is very fundamental to this thesis and therefore a detailed description of this method was outlined. The author also states that none of the current techniques considered the characteristics of the acquisition system and the ground characteristics.

The proposed *SIMCA* algorithm like Scheers et al's method includes the system aspects of the GPR such as the waveform of the excitation source, the impulse response of the antennas, the antenna patterns and the characteristics of the ground by using different soil properties. Using the corresponding radar properties along with the soil conditions is an important factor in obtaining a good re-construction of the mine target. Furthermore, Scheers presents 3D isosurfaces of single objects such as a barbed wire, PMN mine and a brick. He has not shown results of multiple targets buried in the same condition.

To this end, at the beginning of this research project, the following gaps in the current literature of target detection using GPR were identified: firstly, that a technique is necessary that is able to remove the clutter and present an image that is easily interpretable to the deminer. These images should be easy to analyze and expert knowledge of the system and the physics behind the operating principle of the system should not be required for correct interpretation of the results. Secondly the development of an algorithm which is capable of producing 3D reconstructions of volumes of real targets is required.

In order to advance the current state-of-the-art research and address the shortfall of the current techniques, it is proposed to develop an algorithm like the Scheers' method that takes into con-

sideration the system aspects of the GPR along with the characteristics of the ground. Then it is proposed to develop the 2D version of the *SIMCA* algorithm that takes the B scans and produces the 2D image after processing. Chapter 3 of this thesis will be dedicated to the development of the 2D algorithm. Furthermore, as stated above a 3D technique has advantages over a 2D approach and Chapter 4 of this thesis explores the 3D version of the *SIMCA* algorithm.

The data required to test the 2D *SIMCA* algorithm was obtained from European researchers who modified the setup used by GPR researchers at the Ecole Polytechnique Fédérale de Lausanne (EPFL); whilst data required to test the 3D *SIMCA* algorithm was obtained from researchers at the Indian Institute of Technology. Also the testing of the *SIMCA* algorithm in the location of foundations in a demolished building was acquired by the author and his colleague from the Archaeology Department at the University of Glasgow.

The next chapter details the development of the *SIMCA 2D* algorithm and uses the developed algorithm to test the data from a laboratory sandbox containing landmines and obtained by the author from European researchers. The experimental data source used to obtain the landmine data is also detailed in the next chapter. The *SIMCA 2D* algorithm is also tested on car park data and is conducted in Appendix B.2. Furthermore the data acquisition procedure to obtain the car park data is detailed in the same Appendix. The validation procedures to validate the *SIMCA 2D* results are also detailed in the next chapter.

## Chapter 3

# ***SIMCA 2D* and its validation**

*The literature review section stated that a technique that is able to remove the clutter and present an image that is easily interpretable by the deminer is a necessity. The produced images have to be easy to analyze and no expert knowledge of the system or the physics behind the system should be required to interpret the results. This chapter details the SIMCA 2D algorithm which works on the raw 2D GPR data and produces a clutter removed GPR image. In order to test the algorithm data obtained from researchers conducting GPR experiments in a laboratory setting and data acquired by the author and a researcher in archaeology (location of foundations in a car park standing on the site of a former terraced building) is used. The results of the laboratory experiment using landmines are detailed in this chapter whereas the results of the car park data are given in Appendix B. It is to be noted that real GPR data is going to be used rather than synthetic data. The chapter outlines the experimental data source for the landmine data. Then this chapter describes the development of the SIMCA 2D algorithm. The chapter also compares the SIMCA technique to another comparable technique called migration by deconvolution or the Scheers's algorithm. Validation of the algorithm has been done using qualitative evidence and quantitative evidence. Qualitative evidence has been performed by comparing the B scans produced by the SIMCA algorithm with the B scans produced by the best alternative systems reported in the open literature. Quantitative evidence has been accomplished by comparing absolute error values obtained from the SIMCA algorithm against the ground truth values and the Scheers's algorithm against the ground truth values. Furthermore, the quantitative evidence was done by presenting human users with the B scans produced by the SIMCA algorithm and asking them to locate the targets.*

### **3.1 Introduction**

It was stated in Chapters 1 and 2 that GPR technology has been widely cited in the literature by the scientific community since it has shown great promise in the detection of landmines. Furthermore, GPR is considered as the most promising technologies suitable for close range detection of metallic and non-metallic landmines. Chapter 2 considered the different technologies available to detect landmines.

The GPR sends EM waves into the ground and samples any backscattered echoes that are re-

flected from a target. Figure 3.1 indicates the principle of the GPR. When the GPR antenna is at a particular location, the recorded pulse is an A scan; which can be considered as a plot of the magnitude of the reflected wave versus the time. Therefore the A scan can be considered as a time amplitude plot. The image that results from the concatenation of A scans that are recorded on a survey line are B scans. Therefore the B scan can be referred to as a series of A scans as the GPR is swept in a straight line along the scanning direction above the ground and at a constant height. Furthermore, the horizontal axis of the B scan relates to the GPR spatial location whilst the vertical axis is the time or depth. The B scan is also referred to as an image of a vertical slice of the ground. Figure 3.1 shows diagrammatically what an A scan and a B scan are.

Figure 3.2[A] shows raw GPR data and Figure 3.2[B] shows the same raw GPR data whose clutter have been removed.

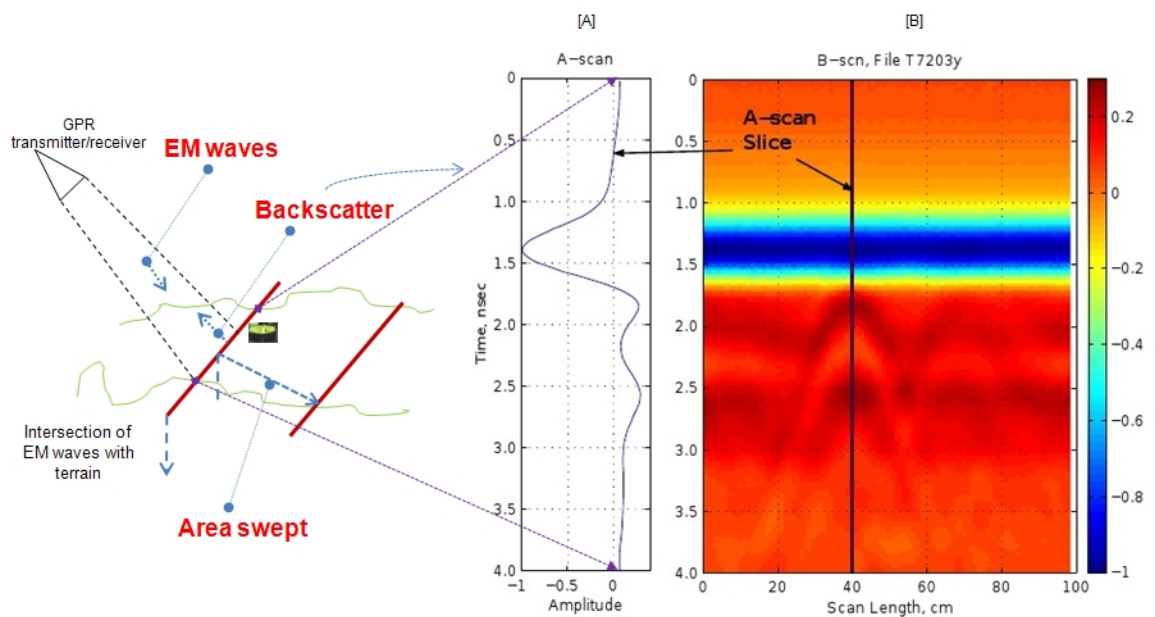


Figure 3.1: [A]: A scan and [B]: B scan.

(Brooks, 2000)

Considering a raw B scan as shown in Figure 3.1 the effect of the M14 plastic landmine is not visible because a GPR image contains artefacts also known as clutter. Therefore the GPR signal contains not only the response of the target, but also unwanted effects which obscure the target. According to (Groenenboom and Yarovoy (2002); Annan (1993)), the raw data from a GPR system consists of:

1. Reflections by the ground surface. This is because of the high levels of dielectric permittivity contrasts at the air ground interface, there are strong responses received by the GPR at an early time. This is the main component of clutter noise and causes targets such as landmines buried at shallow depths not to be detected.
2. Coupling induced by the transmitter and receiver antenna.

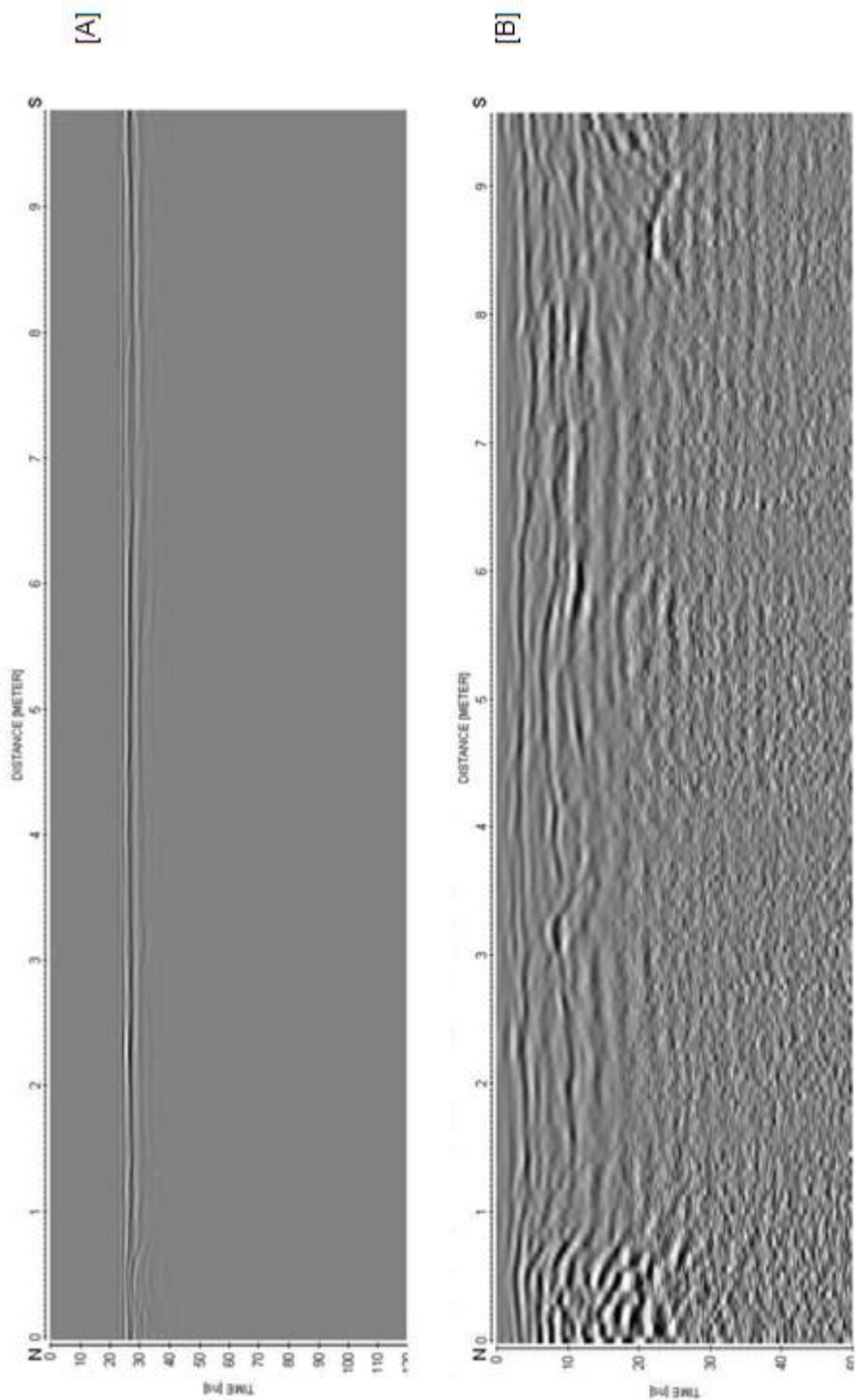


Figure 3.2: [A]: Raw GPR radargram; [B]: Same GPR radargram having clutter removed.

3. Interference from either the GPR system itself or from the environment.
4. Reflections from subsurface targets.
5. Reflection by the underground inhomogeneities.

As noted in Chapter 2 these unwanted components of the received signal must be removed for the improvement of the quality of the image of the target. In order to extract useful information about the target, proper signal processing of the raw GPR data is required.

As outlined in the literature review, various clutter removal techniques are available and some can be classified into those based on classical filtering in the time or frequency domains ((Daniels, 2004); (van der Merwe and Gupta, 2000)). Other statistically based techniques obtain a model of the clutter ((Gupta et al., 1998); (Caevic et al., 2008); (Farina and Protopa, 1998); (Ho and Gader, 2002)).

Chapter 2 stated that due to the beam-width of the transmitter and receiver antenna, a target in the ground is seen by the GPR even if the target is not exactly under the antennas. This causes the reflections on the target to be smeared out over a large region in the data. The migration corrects the defocusing and can focus the energy into its true location (Lopera et al., 2005a). The next section is going to outline the procedure of calculating the depth and velocity of propagation because such information is required in processing algorithms such as migration.

### 3.2 Calculating depth and velocity of propagation

In many processing algorithms based on GPR data such as migration, the physical properties of the soil are required. Amongst the properties, the velocity with which the signal will propagate in the material is important. Since velocity is dependent on permittivity and conductivity, getting an estimate of these parameters is useful. This is because knowing these properties will improve the use of the GPR for mine detection at the acquisition and processing stages.

If the propagation velocity can be determined, then the depth can be calculated. For a homogeneous isotropic material the relative velocity of propagation can be calculated from:

$$v = \frac{c}{\sqrt{\epsilon}} \quad (3.2.1)$$

where  $c$  is the speed of light  $= 3 \times 10^8 \text{ m/s}$ ,  $\epsilon$  is the relative permittivity. From this the depth can be derived:

$$d = \frac{vt}{2} \quad (3.2.2)$$

where  $t$  is the transit time to the target and back.

Practically the relative permittivity is unknown and the propagation velocity has to be measured in the original or natural place and found by measurement of the depth to a physical interface or target using trial holing or by calculating based on multiple measurements. That is the relative permittivity is an unknown physical material property prior to and during data collection. Therefore

the velocity has to be measured in the original or absolute location and found by measuring to the depth of a physical interface or target.

Referring to Figure 3.3, if a hyperbolic function can be measured it causes the propagation velocity to be calculated using (Equation adopted from Daniels (1996)):

$$v = 2\sqrt{\frac{x_{n-1}^2 - x_0^2}{t_{n-1}^2 - t_0^2}} \quad (3.2.3)$$

Therefore the depth to the target is:

$$d_0 = \frac{vt_0}{2} \quad (3.2.4)$$

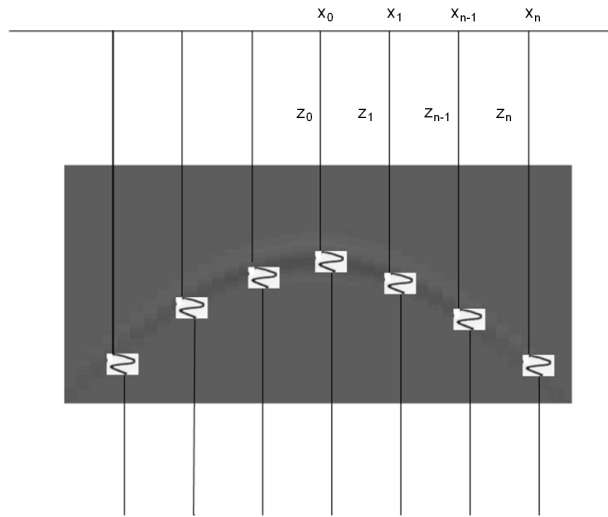


Figure 3.3: Hyperbolic formation.  
(Daniels, 1996)

Fruwirth and Schmoller (1996) present another approach by placement of a known object at a depth to measure the two way travel time. But since the ground would have been disturbed above the emplaced target the measurements may not be correct. Conyers and Lucius (1996) say that often a two way travel time can be measured near a cut in the ground and then an object can be inserted from the side so that the upper material is not affected.

The next section outlines the Scheers method which is the best alternative system reported.

### 3.3 Scheers et al's migration by deconvolution method

It was mentioned in Chapter 2 that the migration by deconvolution method by Scheers et al. (2001) is the best alternative system reported in the open literature. In the Scheers method a synthetic C scan of a small point scatterer is determined by forward modelling. This 3D point spread function has the system characteristics such as the waveform of the source, the antenna footprint and the IR



of the antenna. This 3D point spread function is used to deconvolve the recorded B scan. The author uses the Wiener filter to deconvolve the point spread function out of the recorded data. The role of the Wiener filter is the minimisation of the variance of the error between a restored image and the original image before degradation. The Wiener filter can thus be thought of as a deconvolution algorithm. More detailed information about the Scheers' algorithm can be found in Chapter 2.

Having outlined the Scheers method, the next section develops the *SIMCA 2D* technique.

### 3.4 Development of the *SIMCA 2D* technique

Data focusing or migration can be easily seen when considering a point reflector and the resulting measured wavefront as shown in Figure 3.4, which is simulated data. As stated in the literature review section of this thesis, migration can be considered as an image processing technique whose purpose is the reconstruction, based on the reflection data (obtained at the surface) of the entire reflecting structure that is present in the sub-surface. Migration therefore gives an idea of the physical position and shape of the subsurface reflectors.

When considering data coming from GPRs, the type of reflectors that are of significance are the point scatterers. A point spread function, which is derived by using the GPR simulator can be thought of as the output of an imaging system for a point source. A raw GPR image as shown in Figure 3.1 can be thought of as being derived from the superimposition of a scaled point spread function.

The *SIMCA* algorithm addresses the detection problem by carrying out system level analysis of the issues involved in order to synthesise an image which people can readily understand. *SIMCA* takes the raw data as the radar is scanned over the ground and removes various clutter such as cross talk, initial ground reflection and antenna ringing. In order to remove the clutter a two step process is used:

1. the mean vector of a number of scans is computed and subtracted from each of the scans
2. windowed average subtraction.

This is one of the clutter removal techniques investigated by Sengodan and Javadi (2005) to remove such clutter. Section 3.4.2 outlines the clutter removal technique investigated by Sengodan and Javadi (2005).

*SIMCA* compares the trace that would be returned by an ideal point reflector in the soil conditions at the site with the actual traces obtained and from this it works back to the collection of objects that might have generated the observed traces. The trace that would be generated by the ideal point reflector was obtained using *GprMAX2D v1.5* developed by Giannopoulos (2005); an electromagnetic simulator for ground probing radar. The simulation solves Maxwell's equations using the finite-difference-time-domain method.

The properties of the soil can be determined by Time domain reflectometry (TDR) where a signal generator transmits a pulse type signal to a probe which is filled with or inserted into the soil surface. The reflected signal is received by a receiver and from here the dielectric permittivity

is estimated. The simulation takes as input a data file describing soil conditions, domain size, discretization step, time window, details of the buried object, details of radar and the location of the transmitter and receiver. This allowed the derivation of a mathematical model of the response of a point reflector and then to build a deconvolution system.

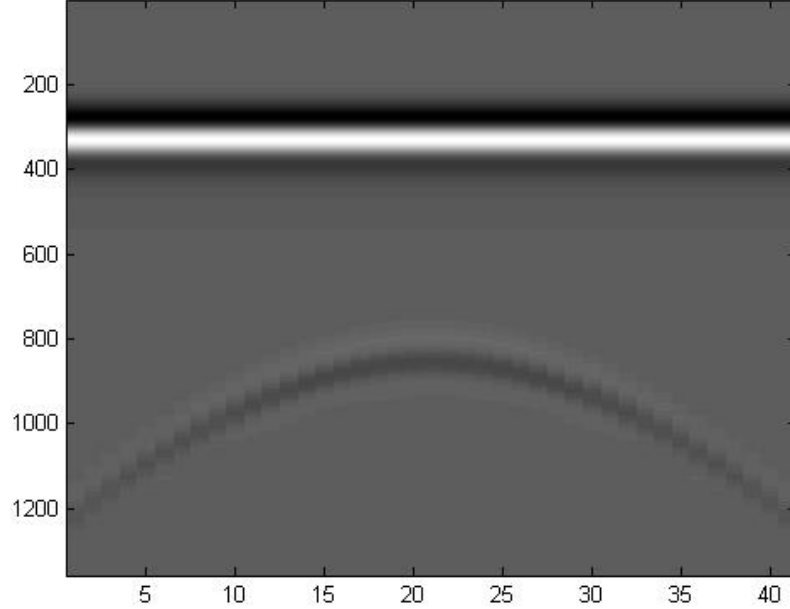


Figure 3.4: Simulated results showing the migration of a waveform from a point source. Please note that this simulation is based on data collected in a laboratory setting where a flat surface exists, the soil is homogeneous and a spherical reflector response can be used.

Once the trace that would be returned by an actual point reflector was worked out from the simulation, an area correlation was performed between the point reflector trace and the actual trace in *MATLAB*. This resulted in a correlated image which is brightest at points most similar to the canonical target. Raising the image to an odd power  $>2$  enhances the target/background separation.

The order of magnitude of the *SIMCA 2D* algorithm is:

$$[x \times y] \times [m \times n] \quad (3.4.1)$$

where  $x$  and  $y$  are the dimensions of the B scan and  $m$  and  $n$  are the dimensions of the kernel.

Various visualization techniques such as false color and mesh generation were used to display the final image by *SIMCA*. Figure 3.5 shows the flowchart of the *SIMCA 2D* algorithm and Figure 3.6 shows the process diagram of the *SIMCA 2D* algorithm. The *SIMCA 2D* algorithm uses GPR simulations to generate kernels and the next section outlines the procedure.

### 3.4.1 GPR Simulations carried out to develop the kernels

The use of the *GprMAX2D v1.5* developed by Giannopoulos (2005) which uses the finite-difference-time-domain method (FDTD) to solve Maxwell's equations, enabled the replication of the original test setup to better understand the test situation and to quickly derive the convolution kernel. The advantage of using such a GPR simulation for calculating the point spread function in comparison to the mathematical calculation of a point spread function using the equation for a hyperbola is that the use of the GPR simulator ensures that the antenna pattern information is included. Some methods like Radzevicius and Daniels (2000) make use of a mathematically calculated point spread function to convolve against the data like the Scheers et al. (2001) method. Further advantages of using such a GPR simulator include:

1. The method when integrated with the *SIMCA 2D* algorithm substantially reduces the computational resources needed.
2. Such a simulation can lead to a database of the response of the soil plus a target and a library of kernels can be developed to be used for the correlation process.

The theory of waveguides was developed using (Leonard (1951); Dietrich (1991); Daniels (2004)). From these results a convolution kernel was developed. The actual process involved in deriving the kernel from the ideal trace of the reflection generated by the simulator is by the selection of a rectangular area covering the hyperbolic shape (this is because the presence of landmines is depicted by distinctive hyperbolic shapes) and then normalisation of this signal in *MATLAB*.

This aimed at developing a correlation kernel to aid in the correlation process and this required running simulations of a point source reflector such as a spherical object placed in the same soil conditions used in the laboratory setup.

The landmines were in a number of soil conditions, so accurate replication of the test conditions needed to be done in the simulations.

The program takes a data file as input containing soil conditions, the domain size, the discretization step, the time window and the details of the object buried (in this case a spherical object), the details of the GPR and the location of the transmitter and receiver in the co-ordinate system. Then the program runs the simulation and produces a geographical file describing the original test conditions input into the simulation and the output file containing the simulated data. This simulated data is then imported into *MATLAB* for further processing and carrying out the convolution and correlation.

For running the simulations, a 0.025m radius of sphere buried at a depth corresponding to the burial depth of the target was used because this closely resembled the test condition used in the laboratory during the acquiring of the landmine data and produced a centralised kernel which was large and included a large proportion of the hyperbola sidelobes. The hyperbola sidelobes cause better localisation in the B scan and hence the target can be easily distinguished. The removal of clutter that is a problem in raw GPR data is considered in the next section.

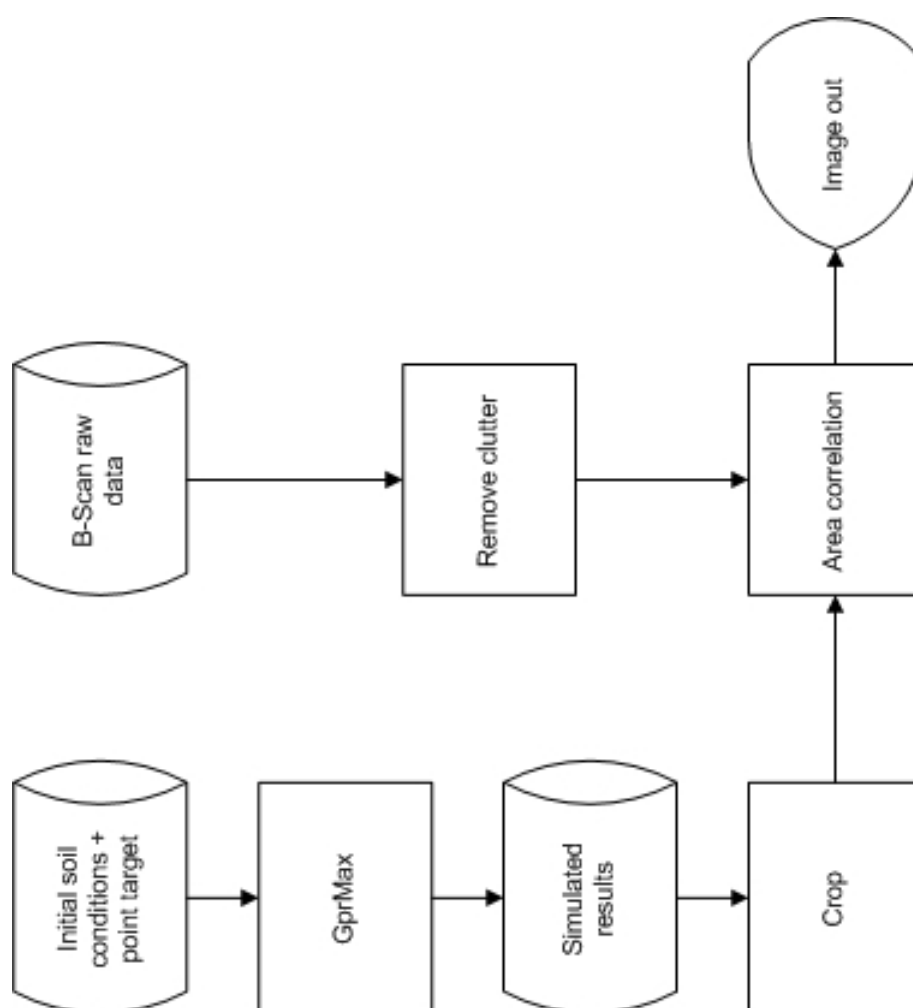


Figure 3.5: The flowchart of the SIMCA 2D algorithm.

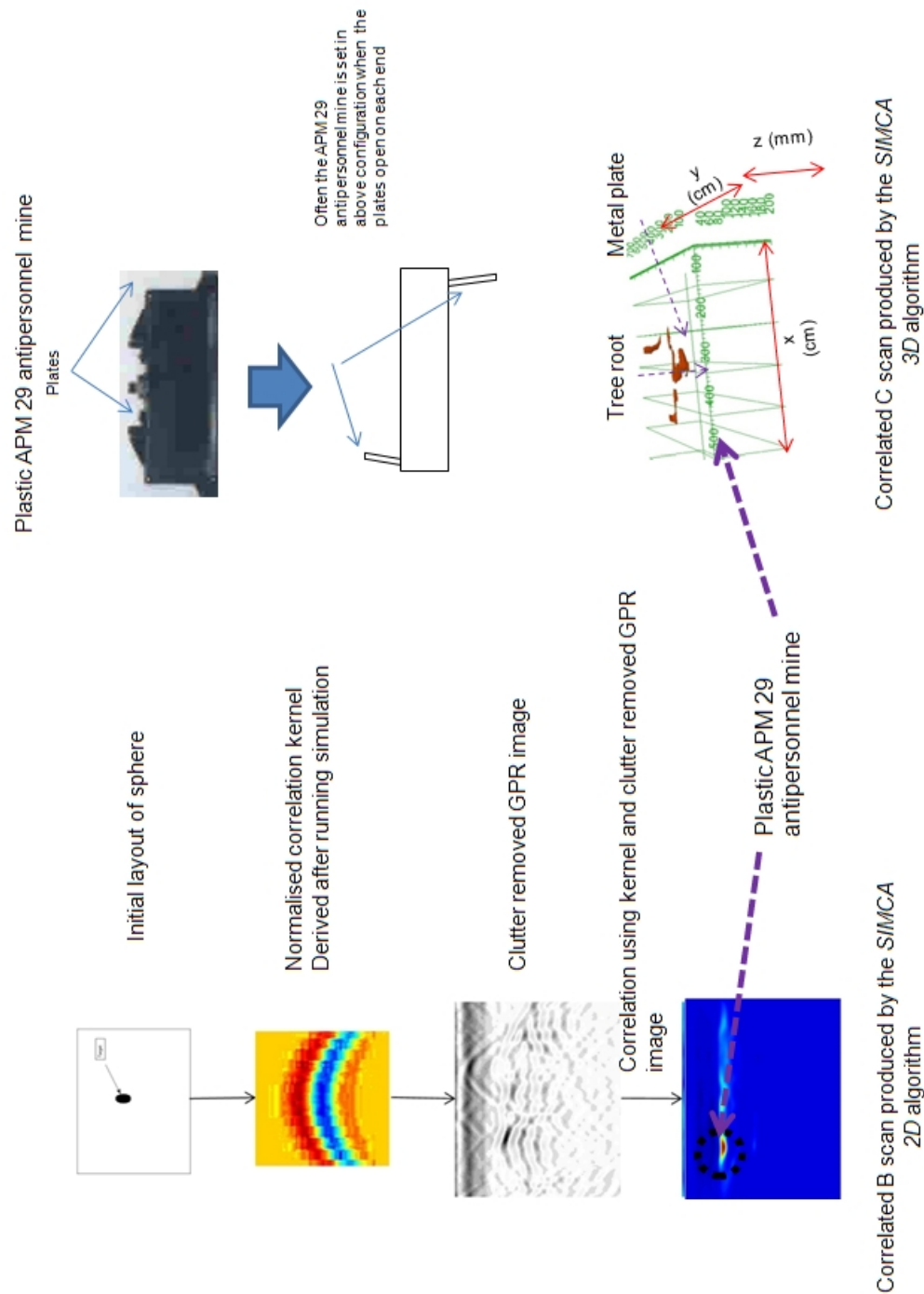


Figure 3.6: Process diagram of the SIMCA 2D algorithm. The diagram also shows the B scan along with the 3D isosurface. Note the 3D isosurface indicates that the plates of the plastic mine are open.

### 3.4.2 Removal of clutter from the raw GPR data

Clutter detected by the GPR includes many components: cross talk from transmitter to receiver antenna, initial ground reflection and background resulting from scatterers within the soil. A clutter removal technique developed by Sengodan and Javadi (2005) is used to remove such clutter. As stated in Chapter 2, the most applied clutter removal technique is the average and moving average background subtraction. Chapter 2, Section 2.8.1 and also Chapter 4, Section 4.2 outline the other key relevant information with regard to clutter removal. Also Equation 2.8.1 (Chapter 2) and Equation 4.2.1 (Chapter 4) give the equation for the clutter removal technique used. Assuming soil properties produce only random variables around a location independent mean and also that target echoes occur only in a small amount of data, then one can take the mean of a large number of traces as a measure of the fixed background and then subtract this from the raw data.

Random noise or a signal not directly related to the radar source can be strongly reduced by the averaging hardware which is integrated in the radar head and this combined with the stacking of several A scans improves the result. Low pass filter then reduces the clutter response caused by the irregularities in the ground. As stated in the introduction section of this chapter and in Chapters 1 and 2, the background component of the image has to be removed because landmines are placed just underneath the surface.

A time dependent gain is usually applied to GPR data when processing so as to correct for intrinsic attenuation from the soil and the spreading losses from propagation of the wave. Furthermore a *dewow* (Jol, 1994) filter is applied when the data is collected to remove low frequency system noise. The *dewow* filter can be thought of as a high pass temporal filter which removes ground and antenna induced low frequency transients from the raw data. The next section gives an overview of correlation (as used by the *SIMCA* algorithm) and convolution (as used by the Scheers' algorithm).

### 3.4.3 Convolution and Correlation

Correlation can be used in image-processing to search for specific features or characteristics within an image. Kernels are used to filter geophysical data and for image processing ((Russ, 1992); (Rees, 2003); (Lu, 1998)). The kernel is a two dimensional array but it can be flattened to a vector by row concatenation making it suitable for application of vector correlation. For each of the pixel positions a window centered on the position is selected. The matrix representing the window is flattened to a vector and the correlation vector is computed and then correlated with the kernel.

The *Pearson's correlation coefficient* between two variables which is defined as the covariance of the two variables divided by the product of their standard deviations is used:

$$\rho_{X,Y} = \frac{\text{cov}(X,Y)}{\sigma_X \sigma_Y} \quad (3.4.2)$$

Chapter 4 gives a detailed discussion of correlation and convolution. The chapter also outlines the key differences of the *SIMCA* algorithm and the Scheers' algorithm. The key differences are:

1. Correlation is independent of the gains used in obtaining the two images (kernel and raw

image)

2. Correlation is independent of the black levels used in obtaining the two images (kernel and raw image).

To go further, Chapter 4 points out that area correlation as done by the *SIMCA* algorithm gives sub-pixel accuracy in locating the sources of targets [(Siebert and Boguslaw, 2008) Chapter 6, section 6.6, pp. 238]. Furthermore in Chapter 4 it is stated that the advantage of correlation over convolution is that it compensates for differences in gain and black level between the kernel and the area of the image being matched.

The next section uses simulated data to test the proof of concept of the *SIMCA* algorithm before using real GPR data.

### 3.5 Results using simulated data

The *SIMCA 2D* algorithm was firstly tested on the simulated data to verify that it produced acceptable results. Therefore this involved putting a spherical object in the soil and then running the simulator. From this it is possible to see if the *SIMCA* algorithm was able to pick up the object at the known location. This is shown in Figure 3.7, where it can be seen that the *SIMCA* algorithm (correlation) produces better results in comparison to the Scheers' method (convolution). It was also possible to test the proof of concept of the *SIMCA* algorithm, to ensure that the final burial depth obtained using the *SIMCA* algorithm was close to the actual burial depth of the spherical object.

Furthermore from Figure 3.7 it can be noted that for the B scan produced by the *SIMCA* algorithm, the diffraction hyperbolae is clearly visible. Also the spherical target is more focused in the image produced by the *SIMCA* algorithm in comparison to Scheers algorithm. The simulation was only run for a single test data and the standard deviation had yet to be determined.

Table 3.1 shows the actual burial depth of the spherical object, along with the burial depths obtained by the two methods. It can be seen that the *SIMCA* method is more accurate in predicting the location of the target in comparison to the other method. Having obtained accurate results using simulated data the next section details the GPR data source for acquiring landmine data in an experimental setup to test the *SIMCA* algorithm.

	<i>Burial depth (cm)</i>
<i>Ground truth</i>	5.6
<i>SIMCA</i>	5.5
<i>Scheers</i>	5.9
<i>Error in SIMCA</i>	1.8%
<i>Error in Scheers</i>	5.4%

Table 3.1: Actual burial depth, depth obtained from the *SIMCA* method, depth obtained from the Scheers's method for the Spherical object in centimetres. Calculation of the absolute errors of the two methods when compared with the ground truth is also presented.

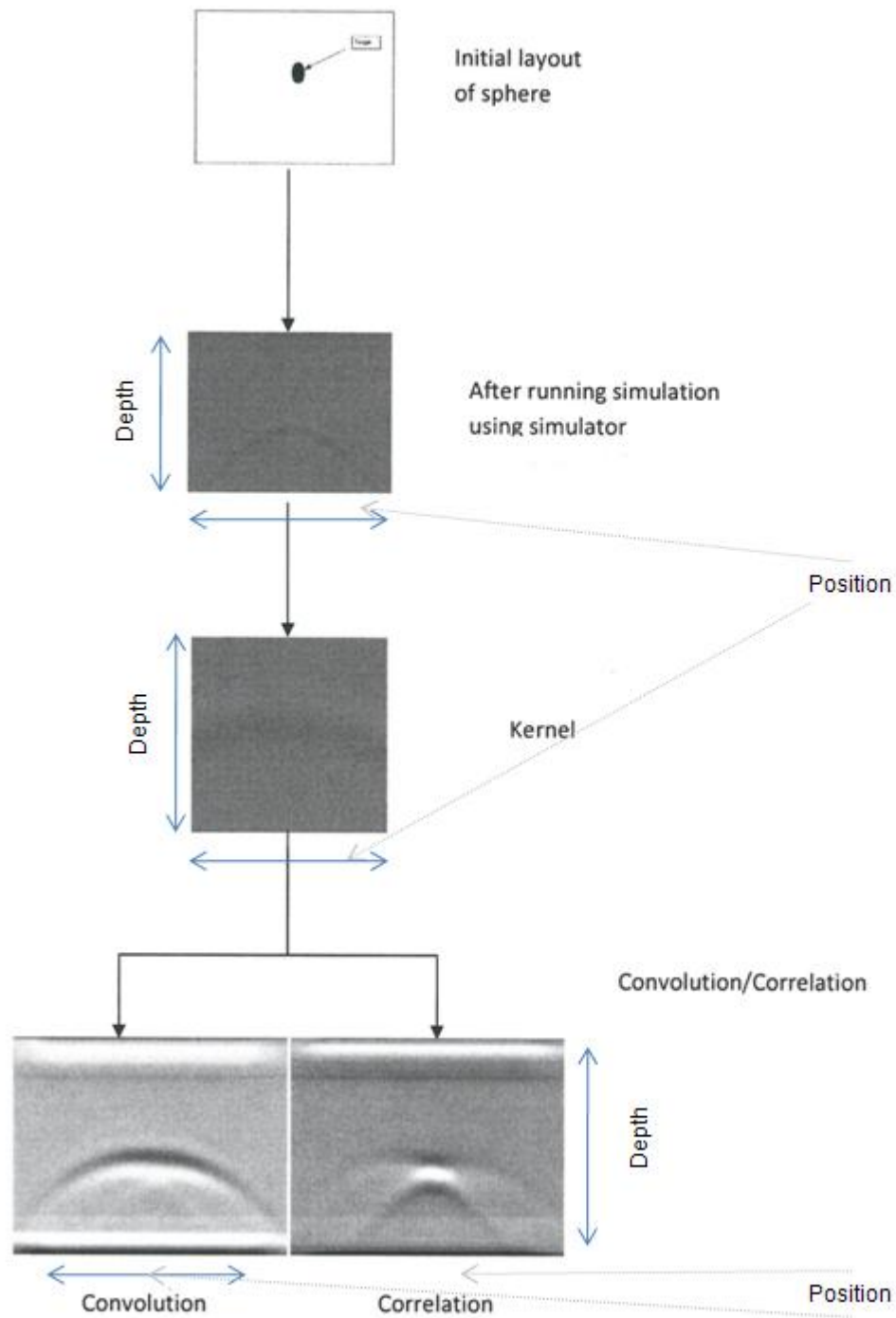


Figure 3.7: Results using the *SIMCA* algorithm and the Scheer's algorithm. Also note that the *SIMCA* method produces a focused image of the spherical object in comparison to the Scheers' method.



### 3.6 Experimental data source used in the laboratory to obtain the landmine data used to test the *SIMCA 2D* algorithm

In this section, the experimental setup used by GPR researchers in a laboratory setup using a robotic positioning table system is detailed. The data used to test the *SIMCA 2D* algorithm was kindly given by researchers who modified the setup used by GPR researchers at the Ecole Polytechnique Fédérale de Lausanne (EPFL). For testing the *SIMCA 3D* algorithm data kindly provided by researchers at the Indian Institute of Technology is used. The reason for not using the actual data from EPFL was because details about the actual landmines, mine like and false targets that were buried could not be obtained. Some of the details of the experimental setup have been attained via email communication from the researchers. The author and the university did not have funding to buy or hire GPR equipment and also there was no laboratory space to set up a data acquisition facility. The object of this PhD research was to develop algorithms to improve the detection of landmines and therefore it was not really necessary to deal with the data collection. The thesis aimed at developing a technique for clearing the GPR images of undesired noise so that they were easily interpretable by human operators. This was described in detail in Chapter 1.

The radar used for the experiment was the SPRScan commercial system. The sampling head allows for the acquisition of 195 A scans of 512 points each per second. The resolution is 16 bits and a maximum equivalent sampling rate is 40 GHz. By analogically averaging the signal allows for the improvement of the signal-to-noise-ratio. Further details of the SPRScan system are outlined in Section 4.5 of chapter 4.

Figure 3.8 shows the actual SPRScan system when used as a hand held device. Figure 3.8 was taken by the author at a test lane containing landmines during work experience at Cobham plc (formerly ERA Technology). Due to a confidentiality agreement the author was unable to use the data in his PhD. Figure 3.9 shows the same SPRScan system mounted on a robotic positioning table system. The laboratory setup consisted of a sandbox which is approximately 4.4m x 4.0m, into which either wet or dry sand is placed. The robotic positioning table system used is shown in Figure 3.9. On top of this a  $x, y$  translation table is placed on which the GPR sensor can be mounted. Therefore the test setup consisted of a sandbox filled with different soil types. The experimental setup was replicated to be similar to a real deactivated landmine field. The GPR measurements were acquired immediately after the soil was wet and also after a number of weeks to investigate the effect of the drying of soil on the detection of landmines.

The B scans were taken at 1.0cm intervals and each of the A scans were also taken every 1.0cm. Various interfering objects such as roots, rocks and additional material which can all cause serious false alarms with the GPR were included. The fact that the sensors are mounted on a platform, which is moved over the minefield either manually or by a small motorised arm allows the acquisition of uniformly gridded data. The experiments were performed with the bottom of the antenna fixed at one centimetres above the surface. The start and end positions of the scan were recorded in absolute co-ordinates. This allowed an exact map of the presence of the objects to be created and the scanning direction was also recorded (erl email, 2012). The next section details the results

obtained using landmine data.



The SPRscan GPR head that is similar to the radar head used in the lab as a robotic system to acquire landmine data



The display unit which shows the B scans.

Figure 3.8: Photograph showing the SPRScan GPR head used which is mounted in the laboratory setup on a robotic positioning table system. This photograph shows the author carrying out scanning of a field laid with landmines at the Cobham plc (ERA Technologies) training facility. This was done during a work placement at Cobham.



Figure 3.9: The SPRScan radar shown in Figure 3.8 is mounted on a robotic positioning table system.

## **Part I**

**Results obtained by using the *SIMCA 2D* algorithm on landmine data obtained from GPR experiments conducted by European researchers.**

### 3.7 Introduction

As stated in Chapter 1 of this thesis, the landmines scattered over the globe hinder the social and economic development of the concerned country. These landmines are also lethal to human beings. Therefore effective algorithms to aid in the removal of these lethal targets is a necessity not a luxury<sup>1</sup>. But as stated in Chapters 1 and 2, the fact that some landmines are small, others have less metal content and are sophisticated tax any algorithm. Furthermore the cluttered environment within the first few centimetres of the soil where landmines are buried, exhibits strong reflections with highly non-stationary statistics ((Chen et al., 1994); (Chen and Peters, 1997)). The main challenge of ground penetrating radar (GPR) based land mine detection is to have an accurate image analysis method that is capable of reducing false alarms. However an accurate image relies on having sufficient spatial resolution in the received signal. An APM can have a diameter as low as 2cm whereas many soils have very high attenuation at frequencies above 450 MHz. In order to solve the detection problem a system level analysis of the issues involved with recognition of landmines using image reconstruction is required.

A large number of these landmines contain little to no metal and as a result, GPR is one of the current technologies receiving attention as an alternative or adjunct to the metal detector. Detection and removal of these landmines is necessary. The presence of landmines is usually depicted by the presence of a hyperbolic shape. GPR images obtained from GPR experiments and available from European researchers are used in the testing of the algorithm.

In this section the developed *SIMCA 2D* algorithm is used in the location of APM using real data acquired in the laboratory sandbox. Then having obtained the B scan using the *SIMCA* algorithm, the results are validated using *qualitative evidence* and *quantitative evidence*. *Qualitative* evidence is accomplished by comparing the B scans from the *SIMCA* algorithm with the B scans produced by the best alternative systems reported in the open literature. For the quantitative evidence two methods are used:

1. Validation of the results from the *SIMCA* algorithm was done by an expert GPR user and 4 other general users who predict the location of landmines. These predicted results are compared with the ground truth data. The details of the experimental setup used to validate the results using the human subjects is detailed in Section 3.11.2.1 of this chapter.
2. Validation of the results from the *SIMCA* algorithm using *AMIRA* software. This is presented in Section 3.9 of this chapter.

The next section outlines the procedure of generating the kernels and illustrates the kernels used for a wet sandy soil and a dry sandy soil. It is to be noted that in actual field conditions, a library of kernels will be used by the *SIMCA* algorithm. This is detailed in Section 3.8.2 of this chapter.

---

<sup>1</sup><http://www.bactec.com/>

### 3.8 Generation of Kernels

In order to generate the kernels required for the correlation process, the GPR simulator as described in Section 3.4.1 was used. These kernels were developed for a wet sandy soil and for dry sandy soil. Figure 3.10 shows a picture of the kernel obtained using the GPR simulator, the normalised kernel and the 3D representation of the kernel. In order to conduct a more systematic mapping of the problem space, a number of different sized kernels were used and the kernel which produced the better results based on the absolute error between the ground truth burial depth and the burial depth calculated using the *SIMCA* algorithm was adapted. Also the absolute error was calculated for the position of burial of the target in the  $x$  direction. Section 3.9 details the method used to derive the burial depth and the position of burial of the target in the  $x$  direction.

Figure 3.11 shows the different kernels derived for a dry sandy soil, whereas Figure 3.12 shows the different kernels for a wet sandy soil. From the diagrams it can be seen that the kernels for the wet sandy soil are less shallow than the kernels for the dry sandy soils. This can be explained by the fact that in a wet sandy soil, the signal is strongly attenuated and hence the GPR signature is not strong ((Roth, 2004); (Pizurica et al., 1999)). Further reasons and a discussion on the soil properties and their effect on GPR performance were given in Chapter 2, Section 2.7.

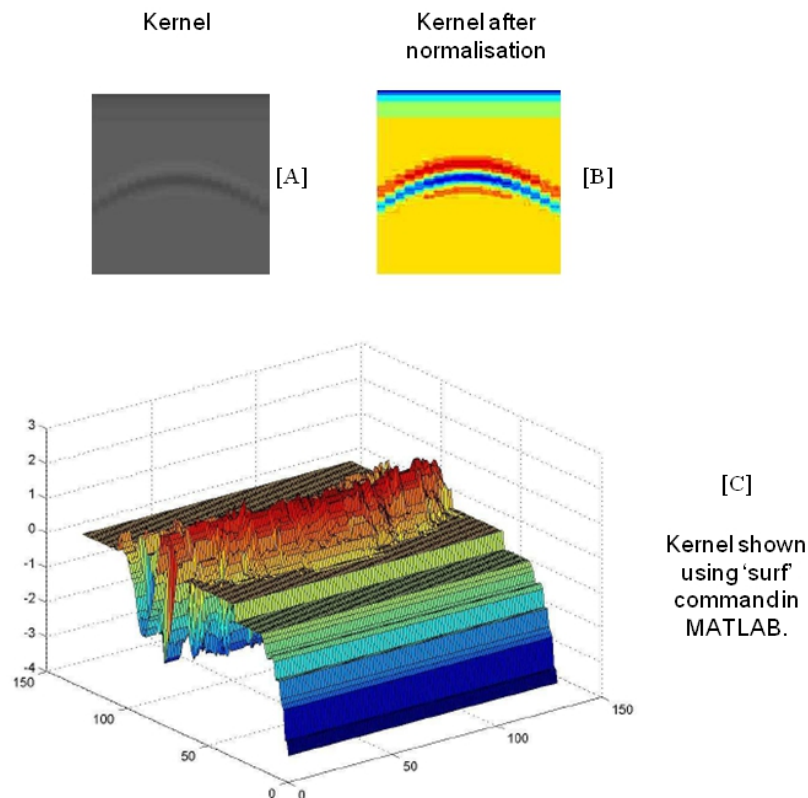


Figure 3.10: Pictorial representation of the kernel. [A]: The kernel derived from the GPR simulator; [B]: The normalised kernel and [C]: 3D representation of the kernel produced using the 'surf' command in *MATLAB*.

The use of a complete hyperbolic signature may produce better localisations in the targets and therefore the next section finds out if this is true.

### 3.8.1 Use of the complete hyperbolic signature as a kernel during correlation.

It was pointed out in Section 3.4.1 of this chapter that the use of the GPR simulator to derive the point spread function is advantageous because it ensures that the antenna pattern is included. Scheers et al. (2001) also conclude that including the system aspects of the GPR such as the waveform of the excitation source, the impulse response of the antenna patterns and the characteristics of the ground is really important for the accurate detection and identification of landmines.

Therefore, bearing this in mind the correlation using a complete hyperbolic signature for the kernel is carried out, such as the one shown in Figure 3.11[E], and compared it to the correlation attained using an in-complete hyperbolic signature such as in Figure 3.11[C]. It was found from the results that the use of a complete hyperbolic signature for the kernel produces more accurate results in terms of calculating the absolute errors for the burial depth and the position of burial of the target in the  $x$  direction. Furthermore, the use of a complete hyperbolic signature for the kernel produces better localisation of the landmines as is evident from Figure 3.13. Furthermore, as can be noticed in Figure 3.13 a complete hyperbola uncovers the 4 landmines that are now visible in comparison to not using a complete hyperbola. The hyperbola sidelobes cause better localisation of the data and hence the target can be easily distinguished. Bearing this in mind, a complete hyperbolic signature for the kernel was used when correlating the results using the *SIMCA* algorithm. Also to ensure a 'like for like comparison', a complete hyperbolic kernel was used to produce the results from the Scheers' method.

The next section is going to explore the influence of the depth on the kernel and its effects on the final correlated image.

### 3.8.2 Influence of the depth on the kernel and its effects on the final correlated image

As a priori, we do not know the depth of the buried object, and the raw B scan would be correlated with a point spread function calculated from the most probable depth of an object. In order to test the effect of depth on the shape of the kernel, use of the GPR simulator is made and calculation of the point spread function for the following depths: [A]: 12.3cm; [B]: 12.0cm; [C]: 11.5cm; [D]: 10.0cm; [E]: 9.5cm; [F]: 8.0cm; [G]: 7.5cm; [H]: 6.9cm is undertaken. From Figure 3.14 it can be seen that the point spread functions have a small variation in shape and in practice the shape of the diffraction hyperbola does not change very much with depth demonstrating that the same hyperbola can be used for a broad depth range. From the figure (Figure 3.14) it can be seen that at trace number 21 (as indicated by the value of  $X$ ) the value of time (as indicated by the value of  $Y \times 0.01\text{ns}$ ) increases slightly as the target is placed at greater depths. However, when using the *SIMCA* algorithm in the field, the use of a library of kernels is recommended and then reconstructions of the 3D volumes using each of the library of kernels are performed. Kernels are generated at different depths (e.g. 10cm, 20cm, 30cm etc) depending on the actual depth of burial of targets and then using the *SIMCA* algorithm reconstructions of the 3D volumes using each of the

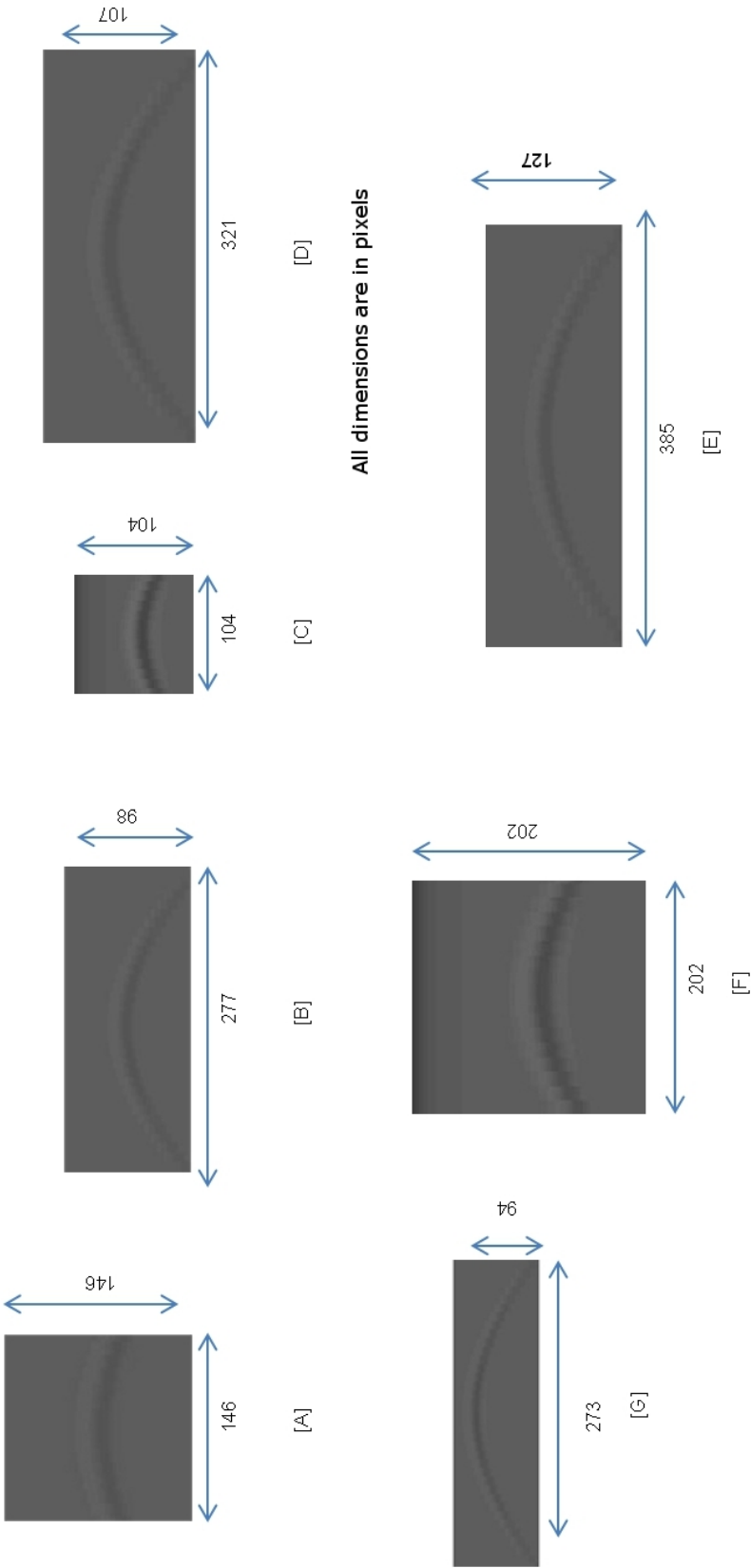


Figure 3.11: Kernels of various sizes for a dry sandy soil, generated using the GPRMAX simulator.

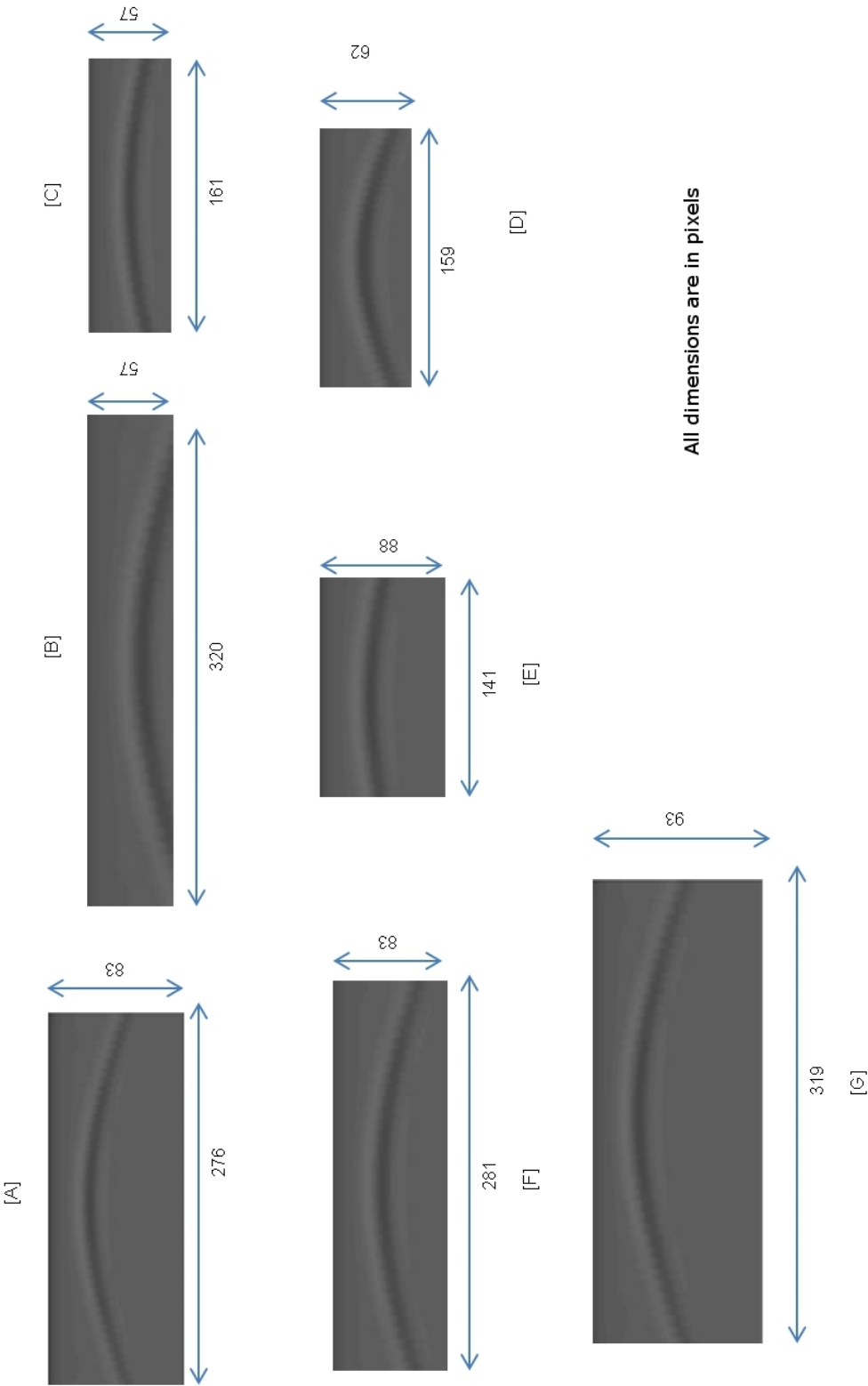


Figure 3.12: Kernels of various sizes for a wet sandy soil, generated using the GPRMAX simulator.



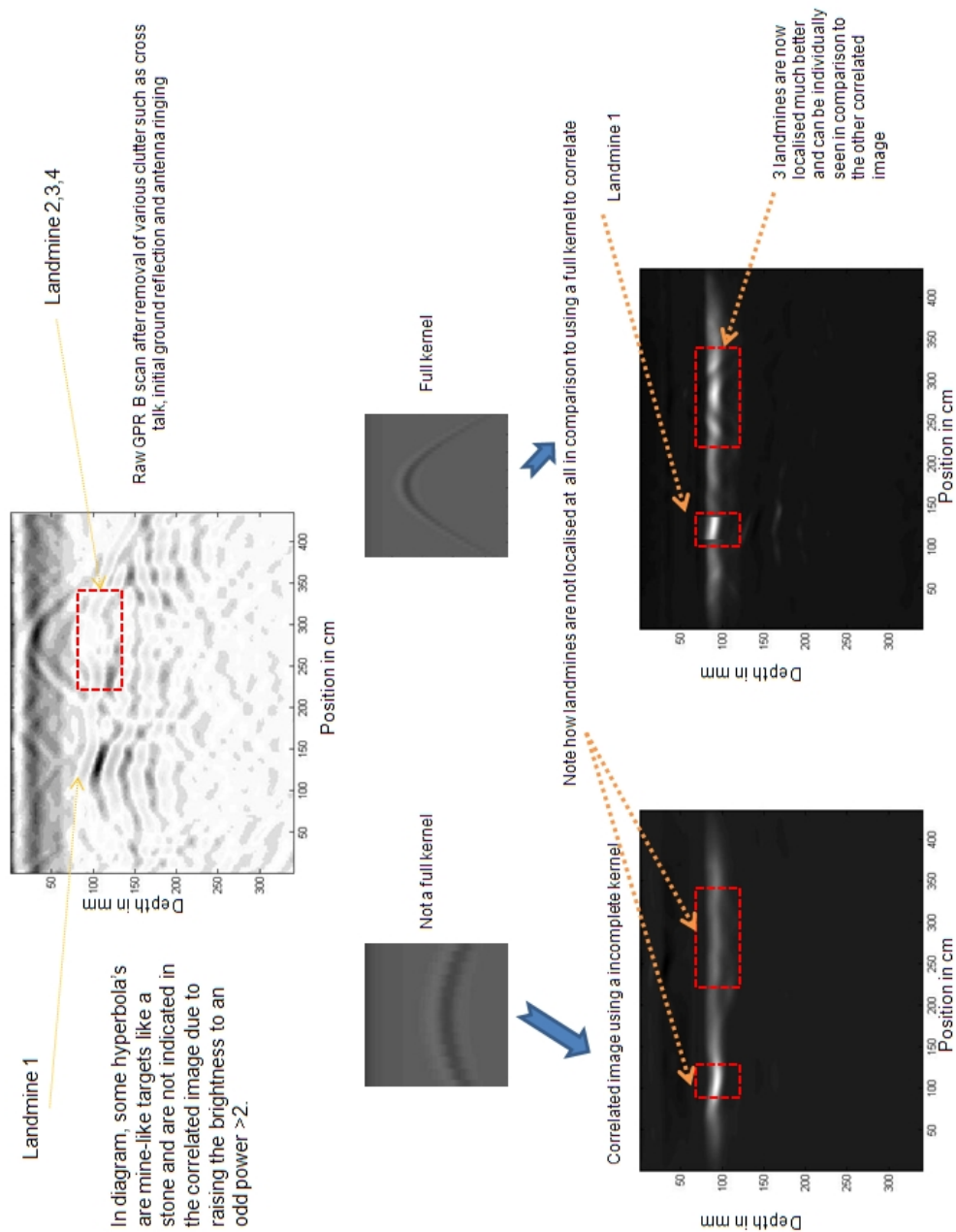


Figure 3.13: Correlated result using the *SIMCA* algorithm. The correlation using a full hyperbolic signature produces better localisation of the landmine in comparison to using a portion of the hyperbolic signature.

above generated kernels are performed. From these reconstructions the first slice (or B scan) from the first reconstruction is taken and then the second slice from the second reconstruction and so on for the remainder of the reconstructions. Then the slices are merged into one complete reconstructed volume and this will be the final reconstructed image.

The next section presents how the *SIMCA* method obtains the burial depth and the position of burial in the  $x$  direction by using the *AMIRA* software.

### 3.9 Obtaining the burial depth and the position of burial in the $x$ direction using *AMIRA* software

The use of the *AMIRA* software enabled the burial depth and position of the target along the  $x$  direction to be derived. *AMIRA* is a visualization system which allows visualization of GPR data sets. Loading the 2D B scans and drawing a bounding box around the location of the target allows the *AMIRA* system to give the values to the above parameters. The *AMIRA* software gives the co-ordinates for the centroid of the object. From this centroid the burial depth of the target can be determined. Also the position of burial of the target along the  $x$  direction can be obtained from these centroid co-ordinates. It is to be noted that the correlated image with brightness raised to the power of 3 as shown in Figure 3.17[D] is loaded into the *AMIRA* software in order to obtain the above mentioned values.

The physical dimension of the object is unknown to *AMIRA*, therefore this can be achieved by the *Image Read Parameters* dialog that via a prompt gets the physical extent of the bounding box. After the correlated images are loaded into the *AMIRA* software and a bounding box drawn around the suspect target location area, the *MaterialStatistics* module available in the *AMIRA* system computes some statistical quantities for the regions. Amongst these statistical values are values of the centroid of the object. Figure 3.15 indicates *AMIRA*'s ability to calculate centroid of object.

The procedure for calculating the centroid of a curved area which is similar to calculating the centroid of the target in a B scan can be outlined if we attempt to find the centroid of an area covering the function  $f(x)$  and the vertical lines  $x = a$  and  $x = b$ .

The centroid can be calculated using total moments in the  $x$  direction as (equation adapted from inmath.com):

$$x_1 = \frac{Sum_{moments}}{Sum_{area}} = \frac{1}{Area} \int_a^b x f(x) dx \quad (3.9.1)$$

or

$$x_1 = \frac{\sum x_i A_i}{\sum A_i} \quad (3.9.2)$$

where  $Sum_{moments}$  is the total of the moments,  $Sum_{area}$  is the sum of the area of the shape,  $x_i$  is the distance from shapes centroid to the reference axis ( $x$ ) and  $A_i$  is the Area.

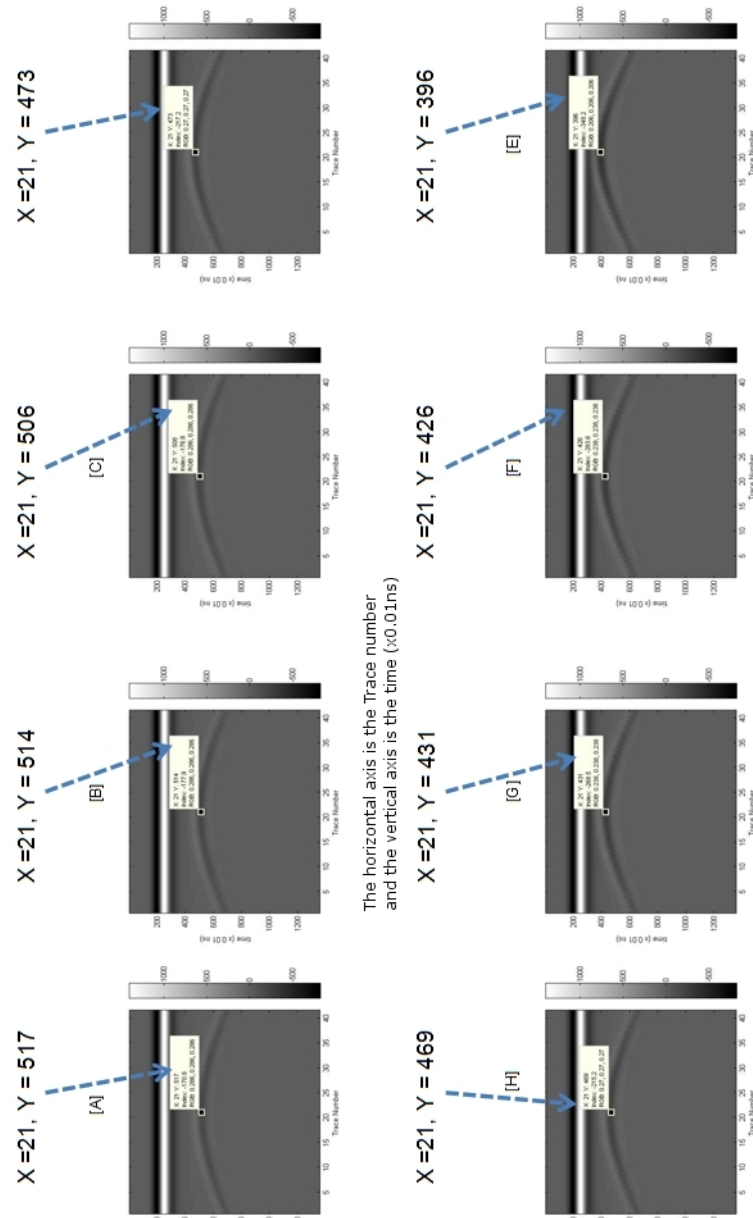


Figure 3.14: The effect of depth on the shape of the kernel when targets are at the following depths: - [A]: 12.3cm; [B]: 12.0cm; [C]: 11.5cm; [D]: 10.0cm; [E]: 9.5cm; [F]: 8.0cm; [G]: 7.5cm; [H]: 6.9cm. Note in the diagrams the Trace Number is on the horizontal axis and the Time (x0.01 ns) is on the vertical axis. Also the value of X is the trace number and the value of Y is the time (x0.01) ns.

drawing a bounding box around the target causes AMIRA to obtain values of the parameters. AMIRA calculates co-ordinates of centroid of object. The 'Image Read Parameter' calculates the centroid.

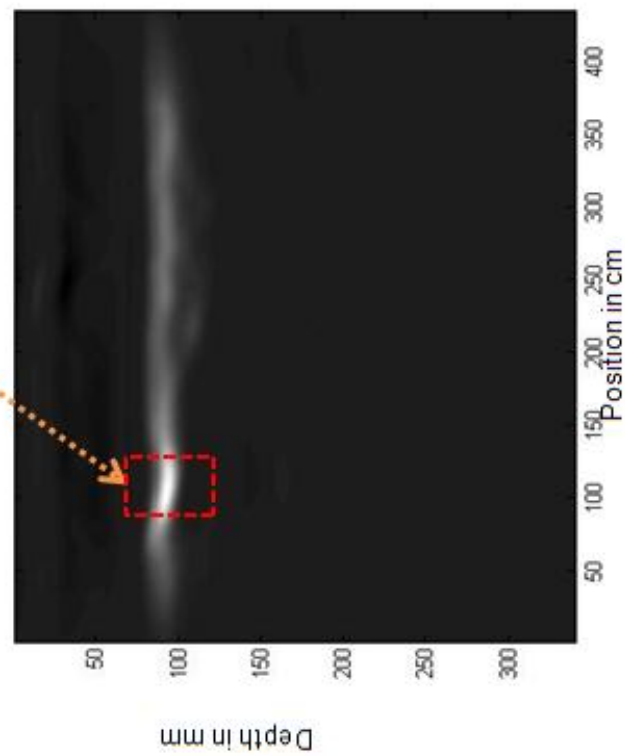


Figure 3.15: Calculating centroid of object using AMIRA software.

Likewise in the  $y$  direction:

$$y_1 = \frac{Sum_{moments}}{Sum_{area}} = \frac{1}{Area} \int_c^d y f(y) dy \quad (3.9.3)$$

or

$$y_1 = \frac{\sum y_i A_i}{\sum A_i} \quad (3.9.4)$$

where  $y_i$  is the distance from shapes centroid to the reference axis ( $y$ ).

The results from the *SIMCA* algorithm are illustrated in the next section.

### 3.10 Results

The algorithm was firstly tested on the simulated data and it produced promising results and the algorithm was able to show the spherical object at the correct depths very accurately. Also it was found that the results from the *SIMCA* algorithm (correlation) outperformed the results from the Scheers' algorithm (convolution) for the simulated data. Results are also surprisingly good considering the profile of the relevant detail in the hyperbolic kernel is more horizontal than vertical. Having established that results from the simulated data produced accurate results, the *SIMCA* algorithm is now used on real data obtained from the laboratory. Comparison of the results from the *SIMCA* algorithm with the results from the Scheers' algorithm is also made. Various visualization techniques ((Ware, 2004); (Russ, 1992); (Pavlidis, 1982); (Daniels, 2006)) were used to present the data for mine clearing personnel and the following visualization techniques were useful:

- Correlation to a false colour.
- Brightness raised to power of 3. This raising to a power of 3 is similar to using an adaptive threshold. Furthermore the non-linear operation of raising to the power identifies the correct peak area.
- Mesh generation. E.G. Figure 3.17[C].

As a consequence of applying the visualization techniques described above the generated mesh (Figure 3.17[C]) shows the peak clearly but it is less easy to localise the peak in this representation than in Figure 3.17[D]. From Figure 3.17[D] the peak value is clearly seen and this peak value shows the location of the landmine. The B scans produced by the *SIMCA* algorithm are cleaner and it will be easier for the landmine clearance personnel to locate the target(s) than from the B scan produced by the Scheers algorithm. This is evident in Figure 3.17 where the B scan produced by the *SIMCA* algorithm (Figure 3.17[D]) is much cleaner than the B scan produced by the Scheers' algorithm (Figure 3.17[E]). The same clearer B scan is produced by the *SIMCA* algorithm in comparison to the Scheers' algorithm for the remainder of the test cases (Figures 3.18-3.27). Furthermore as shown in Section 3.11.2.2 the *SIMCA* method is more accurate in locating the targets than the Scheers

method, when computing the absolute errors when comparing the corresponding burial depths and position in the  $x$  direction from the two methods with the ground truth. Figures 3.17 to 3.27 show the results from the *SIMCA* and Scheers algorithms.

The vertical spatial resolution of the technique is better than the horizontal resolution because most of the energy of the kernel section used is in the vertical direction.

There are hundreds of different types of APM that are produced in over 50 countries (Ordata, 1998). The most difficult to detect are the “minimum-metal” mines which are found in the recent conflict areas and this was stated in Chapters 1 and 2. The construction details along with the pictures of the landmines which are going to be presented in the results are now given. Some of the mines that are used are detailed in Chapter 4 and rather than repeat them here, the reader is directed to the relevant details in that chapter (Chapter 4). Figure 3.16, gives the construction details of the mines used in this chapter which have not been included in the next chapter (Chapter 4).

The Type 72 mine shown in Figures 3.17 and 3.18, contains only 74g of high explosive and is known as a “*toe topper*” in military terms. Once the safety ring is removed, the only metallic parts is a ring pin about the size of a small thumbtack. The spring mechanism is made up of plastic/composite materials. The Type 72 is a very sensitive mine and can be triggered in the presence of magnetic mine detectors. These mines are very difficult to detect and it is promising that the *SIMCA* algorithm is able to localise the mine in a more accurate manner and the resulting B scan is much clearer to interpret than the B scan produced by the Scheers’ method. This is evident in Figures 3.17 and 3.18 where the B scan produced by the *SIMCA* algorithm as shown by part D of the image is clearer than the B scan produced by the Scheers’ algorithm as shown by part E of the image. In a wet soil, the signal is strongly attenuated and the target is not clearly visible. However, after a number of days when the soil becomes dry the same target is clearly visible. The soil used in Figure 3.18 was in wet sandy soil; the wet sandy soil was allowed to dry and the GPR survey was repeated after 23 days to allow the sand to dry. The resulting B scan is shown in Figure 3.17. Lopera and Milisavljevic (2007) concluded that increasing the soil’s moisture content, regardless of soil texture, eases the detection of plastic landmines and exacerbates the detection of the metallic mines. This is evident in the B scan after 23 days drying, the plastic Type 72 mine is not clearly localised by the *SIMCA* algorithm. This is because a wet soil has a higher electrical permittivity than a dry soil. This phenomena increases the impedance contrast between the soil and the landmine causing a larger GPR response.

The sole metallic content in the PMA-3 shown in Figure 3.26 is an aluminium covering on the detonator cap. The assembly, small size and small metallic content makes the mine difficult to detect, but in Figure 3.26, the *SIMCA* algorithm is able to show the landmine clearly when compared to Scheers method. The M14 mine is a very small non metallic mine and the mine body, fuze body and pressure plate are plastic. The only metal in the mine is the steel striker tip. Despite the smallness of the mine, its minimum metal content and the fact that the mine is buried only 2.2cm from the surface of the ground (where there are strong reflections), the *SIMCA* algorithm is successful in showing the landmine (Figure 3.24). Furthermore the PFM-1 mine is in essence a plastic bag containing explosive liquid and is a principal target of the International Campaign to

Ban Landmines. But in Figure 3.24 despite the fact that the PFM-1 mine is buried at a depth of only 2.0cm, the *SIMCA* algorithm can show the landmine. Another pleasing fact to note in Figure 3.22 is that the *SIMCA* algorithm is able to show that the plastic M14 mine is buried in a tilted position. This is important because sometimes in field conditions environmental conditions result in soil erosion and movement caused by rain over several seasons, then the landmines may be lifted, tilted or moved. Also in Figure 3.25, the *SIMCA* algorithm illustrates that the plastic M14 mine has been buried in a horizontal position by the researchers.

GPR data from the sand and silt soils provides convincing evidence that the increase of soil water content above a non metallic landmine improves detection (Lopera et al., 2005b). It also suggests that the detection of metallic landmines also reduces with increasing soil water content. This is because the cross section of plastic mines is reduced by a factor, caused by the reduced dielectric contrast between the mine and the surrounding soil. This is evident in Figure 3.24 where for the Metallic M26 mine, the *SIMCA* algorithm is able to produce a better localisation in dry soil (Figure 3.24) than in Figure 3.20 (wet soil). Furthermore despite the careful burial of the targets, some disturbance of the sand cannot be prevented in a laboratory sandbox and this results in clutter and in some of the resulting B scans it is noticeable that a horizontal line runs continuously across the B scans as shown in Figure 3.23. But in other cases, for example in Figure 3.17, the continuous horizontal line is because more than one target is buried in the laboratory test setup at the same depth (Plastic Type 72 mine and a glass bottle), and the reflections are continuous in nature and extend along the objects. Another explanation is because the variation in compaction of the soil caused the constant horizontal line.

Although numerous interfering objects such as stones, metal clutter (metal ring in Figure 3.22), and other clutter such as the glass bottle (Figure 3.17) are buried in the setup, the *SIMCA* algorithm still shows the landmines much better than the Scheers algorithm. A stone is chosen and buried in the sandbox because it was necessary to depict the actual field conditions and often it is difficult to differentiate a stone from a mine in a GPR. For example a large stone was buried amongst the targets in Figure 3.19. But it is pleasing to note that the *SIMCA* algorithm is able to show the large stone and also the other targets like the Plastic No. 4 and Plastic T/79 mines when compared to the Scheers algorithm. Although a small stone was buried in the setup in Figure 3.27, the *SIMCA* algorithm can clearly show the stone in comparison to the Scheers' method. Burial of a copper wire does not affect the setup and the performance of the *SIMCA* algorithm, and it is possible to differentiate the copper wire amongst the plastic MAUS mine, metallic M26 mine and the wooden cased PMD-6 mine in Figure 3.20.

In summary, it is clear that the *SIMCA* algorithm can clearly show the location of plastic mines better than the Scheers algorithm. An important factor because the majority of mines are now plastic in nature. Figures 3.17-3.27 part D of the B scan show that the *SIMCA* algorithm produces clearer B scans than the B scan produced in part E (Scheer's algorithm).

Having presented the results it is necessary to validate the *SIMCA* algorithm, therefore the next section validates the results.

[1]		<b>T/79 Antipersonnel Mine</b>	<p>This is a small circular mine which was used for delivery from the air or placed by hand. The blast resistance of the mine will prevent removal of the mine using explosives.</p>	<p><u>Constructional information</u></p> <ul style="list-style-type: none"><li>-Cylindrical</li><li>-Height = 45mm</li><li>-- Weight = 0.190 kg</li><li>-- Plastic case</li></ul>
[2]		<b>No. 4 Antipersonnel Mine</b>	<p>A pressure initiated mine. It is similar to the wooden No. 3 mine, A downward pressure on a raised lid causes the lid to go down and triggers the fuse.</p>	<p><u>Constructional information</u></p> <ul style="list-style-type: none"><li>- Rectangular</li><li>- Length = 135mm</li><li>- Width = 65mm</li><li>- Height = 50mm</li><li>-- Weight = 0.348 kg</li><li>- Plastic case</li></ul>
[3]		<b>Type 72 Antipersonnel Mine</b>	<p>A small plastic mine. The mine is very sensitive and can be detected when a magnetic mine detector is used.</p>	<p><u>Constructional information</u></p> <ul style="list-style-type: none"><li>-Cylindrical</li><li>-Height = 38.5mm</li><li>- Diameter = 78.5mm</li><li>-- Weight = 0.14 kg</li><li>-- Plastic, rubber case</li></ul>

Figure 3.16: Information about the buried targets.  
(Cameo Landmine clearance)



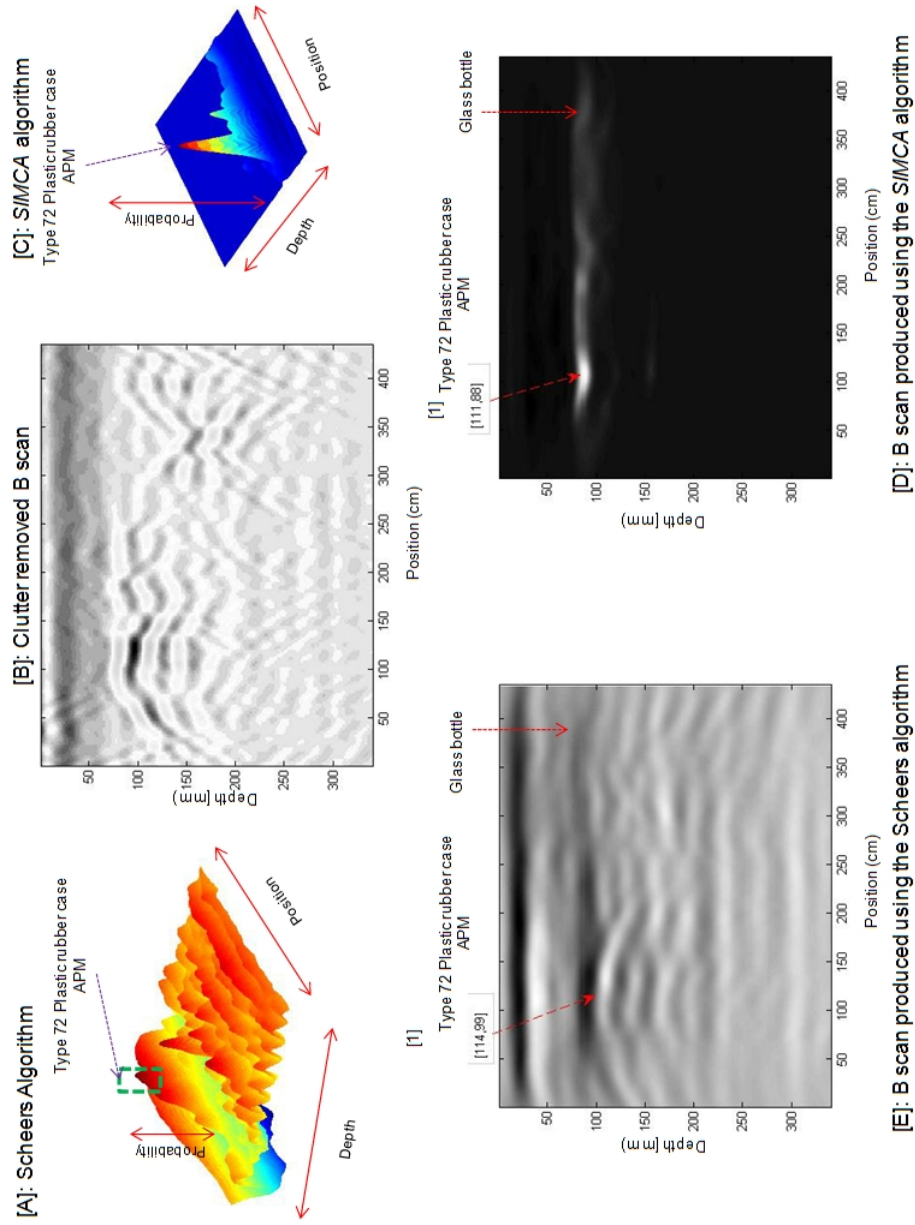


Figure 3.17: Results of real targets in a dry sandy soil. The GPR survey was conducted 23 days after the survey in Figure 3.18 - [A]: 3D plot showing probability of occurrence of objects with respect to depth and position on the scan line produced by the Scheers algorithm; [B]: Clutter removed raw B scan; [C]: 3D plot showing probability of occurrence of objects with respect to depth and position on the scan line produced by the SIMCA algorithm; [D]: B scan produced from the SIMCA algorithm with brightness raised to power of 3; [E]: B scan produced by the Scheers algorithm.

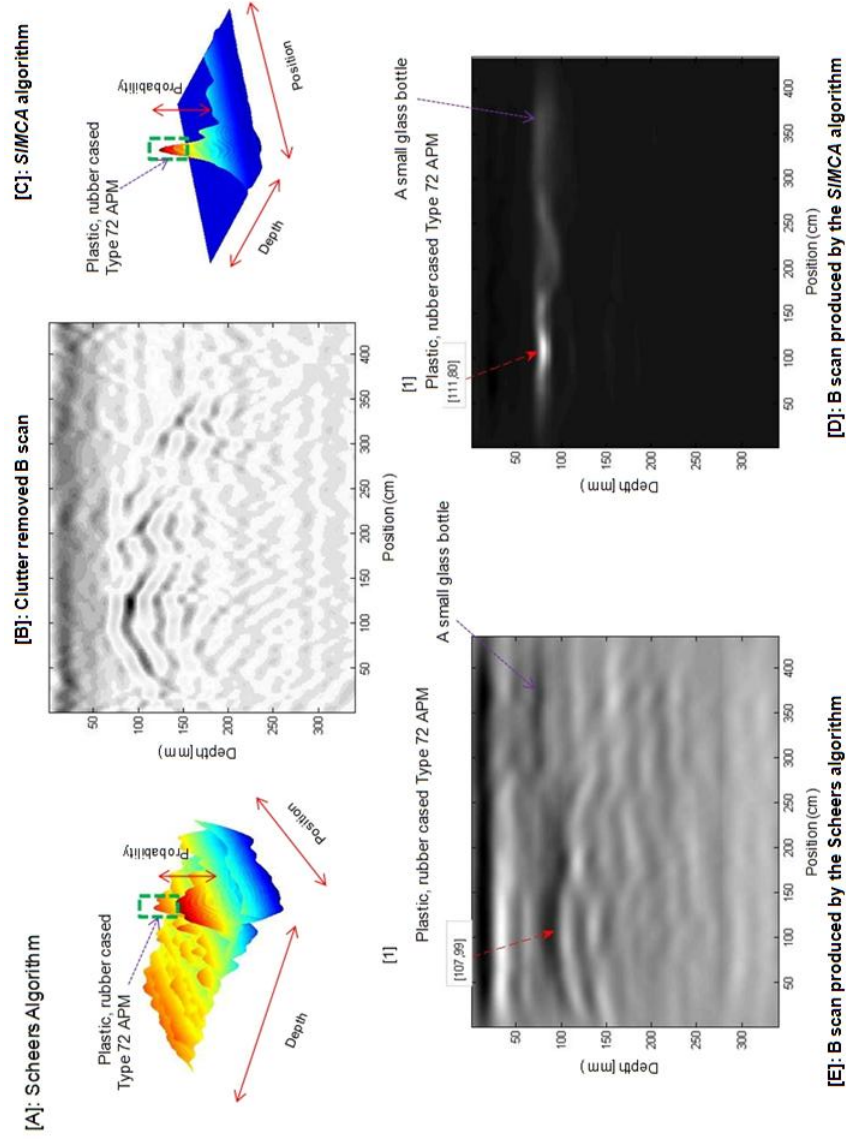


Figure 3.18: Results of real targets in a wet sandy soil - [A]: 3D plot showing probability of occurrence of objects with respect to depth and position on the scan line produced by the Scheers algorithm; [B]: Clutter removed raw B scan; [C]: 3D plot showing probability of occurrence of objects with respect to depth and position on the scan line produced by the SIMCA algorithm; [D]: B scan produced from the SIMCA algorithm with brightness raised to power of 3; [E]: B scan produced by the Scheers algorithm.

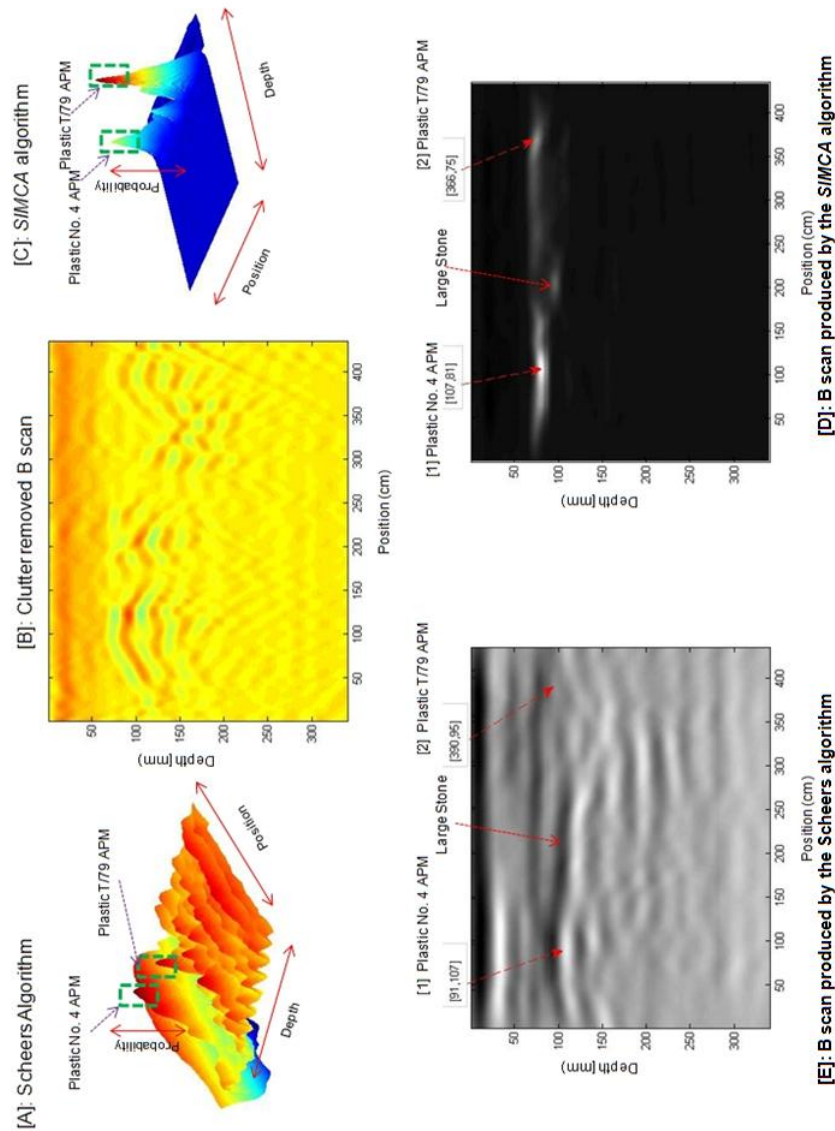


Figure 3.19: Results of real targets in a wet clay soil - [A]: 3D plot showing probability of occurrence of objects with respect to depth and position on the scan line produced by the Scheers algorithm; [B]: Clutter removed raw B scan; [C]: 3D plot showing probability of occurrence of objects with respect to depth and position on the scan line produced by the SIMCA algorithm; [D]: B scan produced from the SIMCA algorithm with brightness raised to power of 3; [E]: B scan produced by the Scheers algorithm.

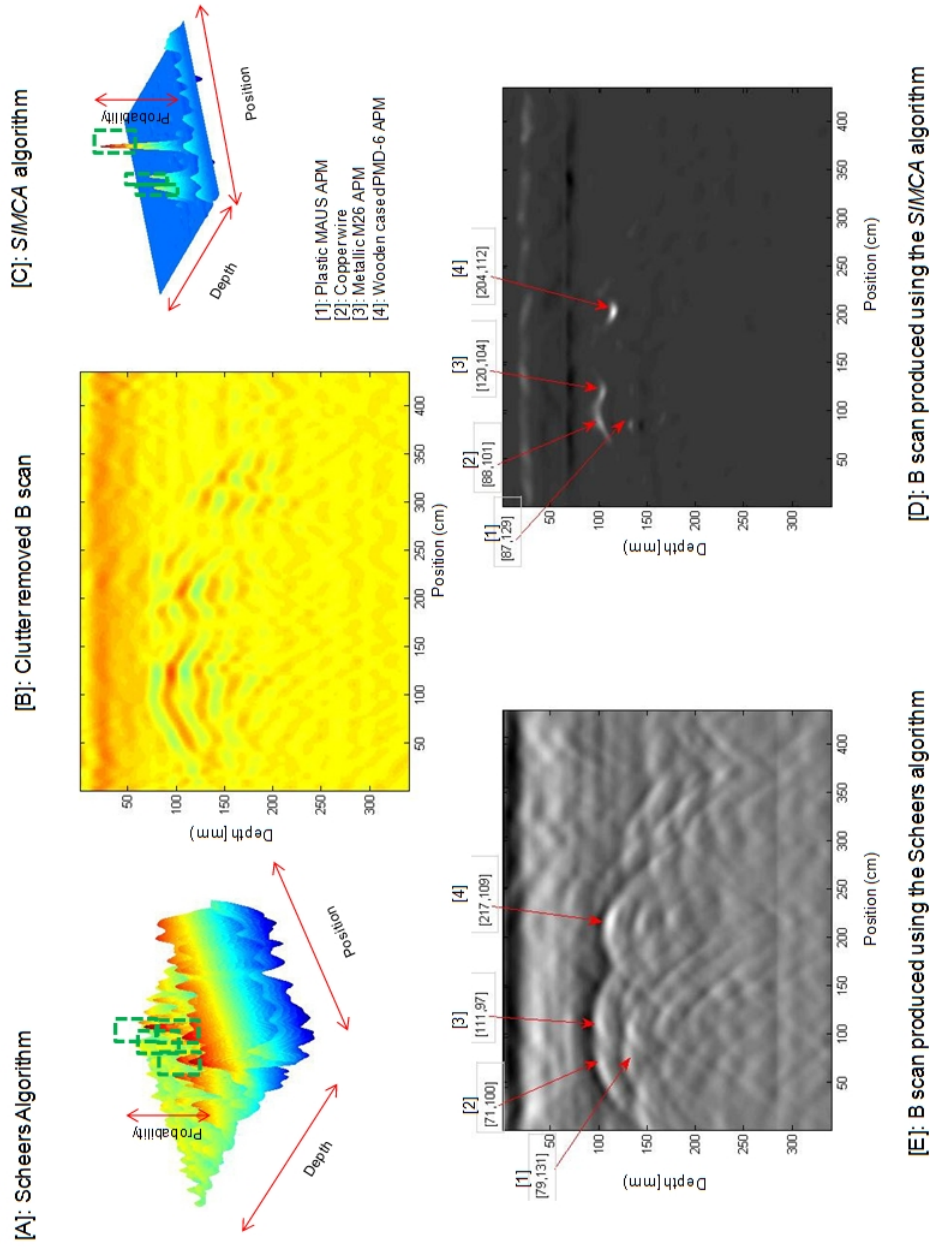


Figure 3.20: Results of real targets in a wet sandy soil - [A]: 3D plot showing probability of occurrence of objects with respect to depth and position on the scan line produced by the Scheers algorithm; [B]: Clutter removed raw B scan; [C]: 3D plot showing probability of occurrence of objects with respect to depth and position on the scan line produced by the SIMCA algorithm; [D]: B scan produced from the SIMCA algorithm with brightness raised to power of 3; [E]: B scan produced by the Scheers algorithm.

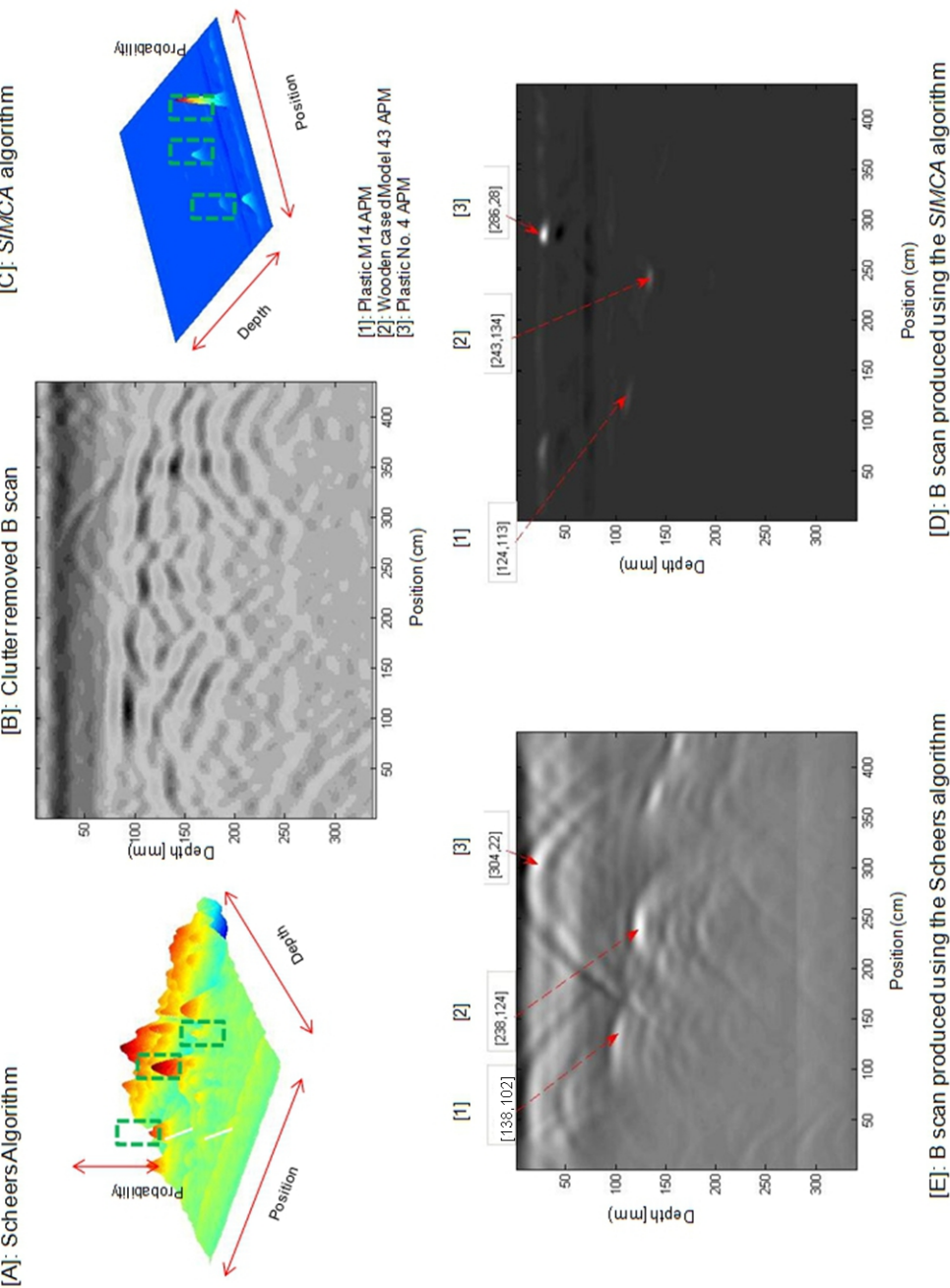


Figure 3.21: Results of real targets in a dry sandy soil - [A]: 3D plot showing probability of occurrence of objects with respect to depth and position on the scan line produced by the Scheers algorithm; [B]: Clutter removed raw B scan; [C]: 3D plot showing probability of occurrence of objects with respect to depth and position on the scan line produced by the SIMCA algorithm; [D]: B scan produced from the SIMCA algorithm with brightness raised to power of 3; [E]: B scan produced by the Scheers algorithm.



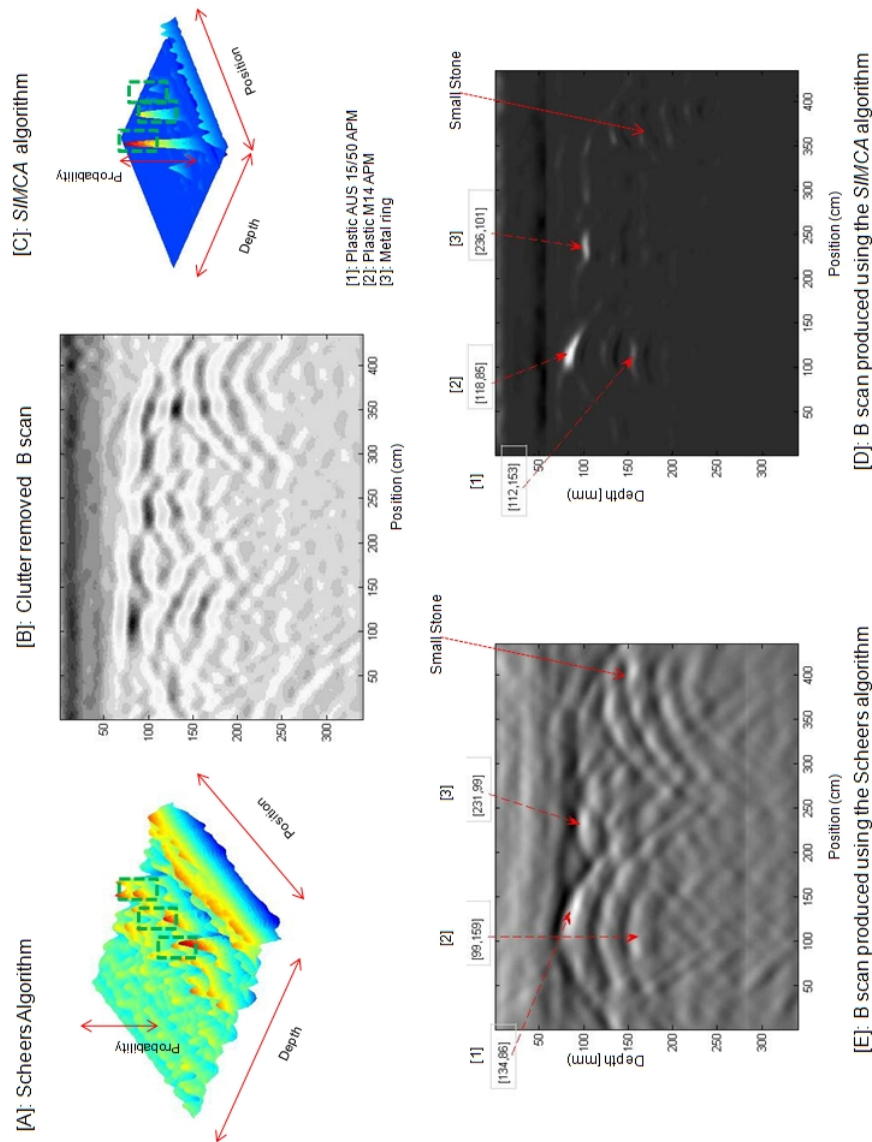


Figure 3.22: Results of real targets in a wet clay soil - [A]: 3D plot showing probability of occurrence of objects with respect to depth and position on the scan line produced by the Scheers algorithm; [B]: Clutter removed raw B scan; [C]: 3D plot showing probability of occurrence of objects with respect to depth and position on the scan line produced by the SIMCA algorithm; [D]: B scan produced from the SIMCA algorithm with brightness raised to power of 3; [E]: B scan produced by the Scheers algorithm.

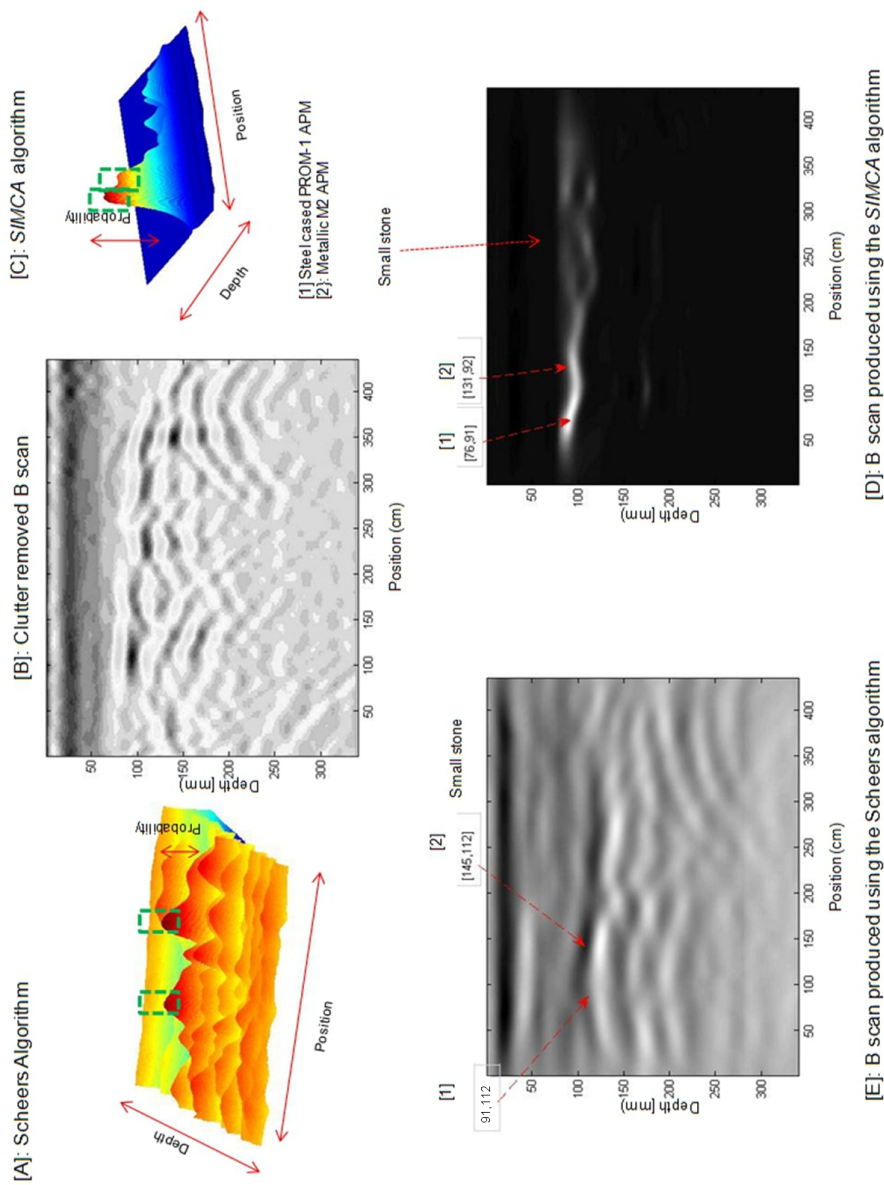


Figure 3.23: Results of real targets in a wet clay soil - [A]: 3D plot showing probability of occurrence of objects with respect to depth and position on the scan line produced by the Scheers algorithm; [B]: Clutter removed raw B scan; [C]: 3D plot showing probability of occurrence of objects with respect to depth and position on the scan line produced by the *SIMCA* algorithm; [D]: B scan produced from the *SIMCA* algorithm with brightness raised to power of 3; [E]: B scan produced by the Scheers algorithm.

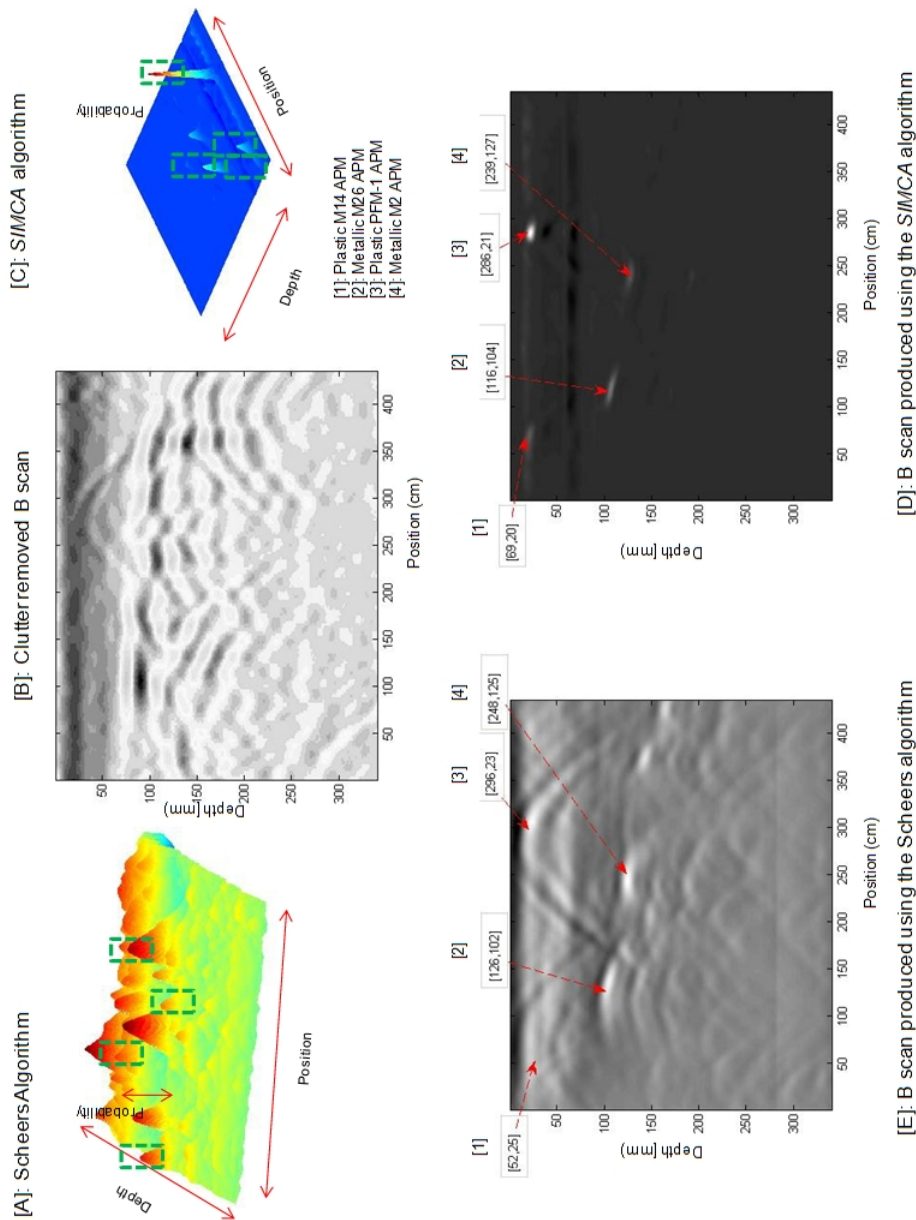


Figure 3.24: Results of real targets in a dry sandy soil - [A]: 3D plot showing probability of occurrence of objects with respect to depth and position on the scan line produced by the Scheers algorithm; [B]: Clutter removed raw B scan; [C]: 3D plot showing probability of occurrence of objects with respect to depth and position on the scan line produced by the SIMCA algorithm; [D]: B scan produced from the SIMCA algorithm with brightness raised to power of 3; [E]: B scan produced by the Scheers algorithm.



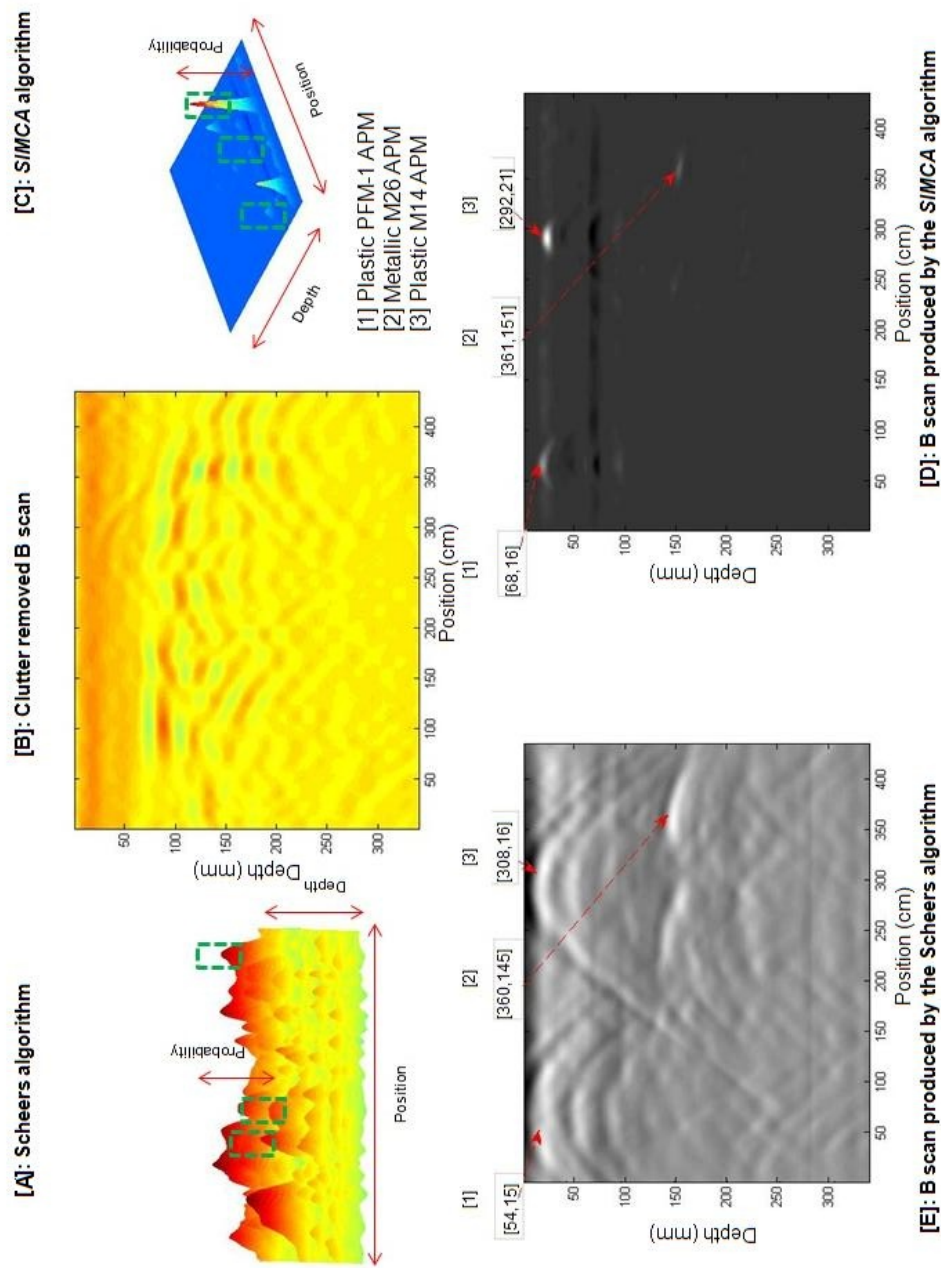


Figure 3.25: Results of real targets in a dry clay soil - [A]: 3D plot showing probability of occurrence of objects with respect to depth and position on the scan line produced by the Scheers algorithm; [B]: Clutter removed raw B scan; [C]: 3D plot showing probability of occurrence of objects with respect to depth and position on the scan line produced by the SIMCA algorithm; [D]: B scan produced from the SIMCA algorithm with brightness raised to power of 3; [E]: B scan produced by the Scheers algorithm.

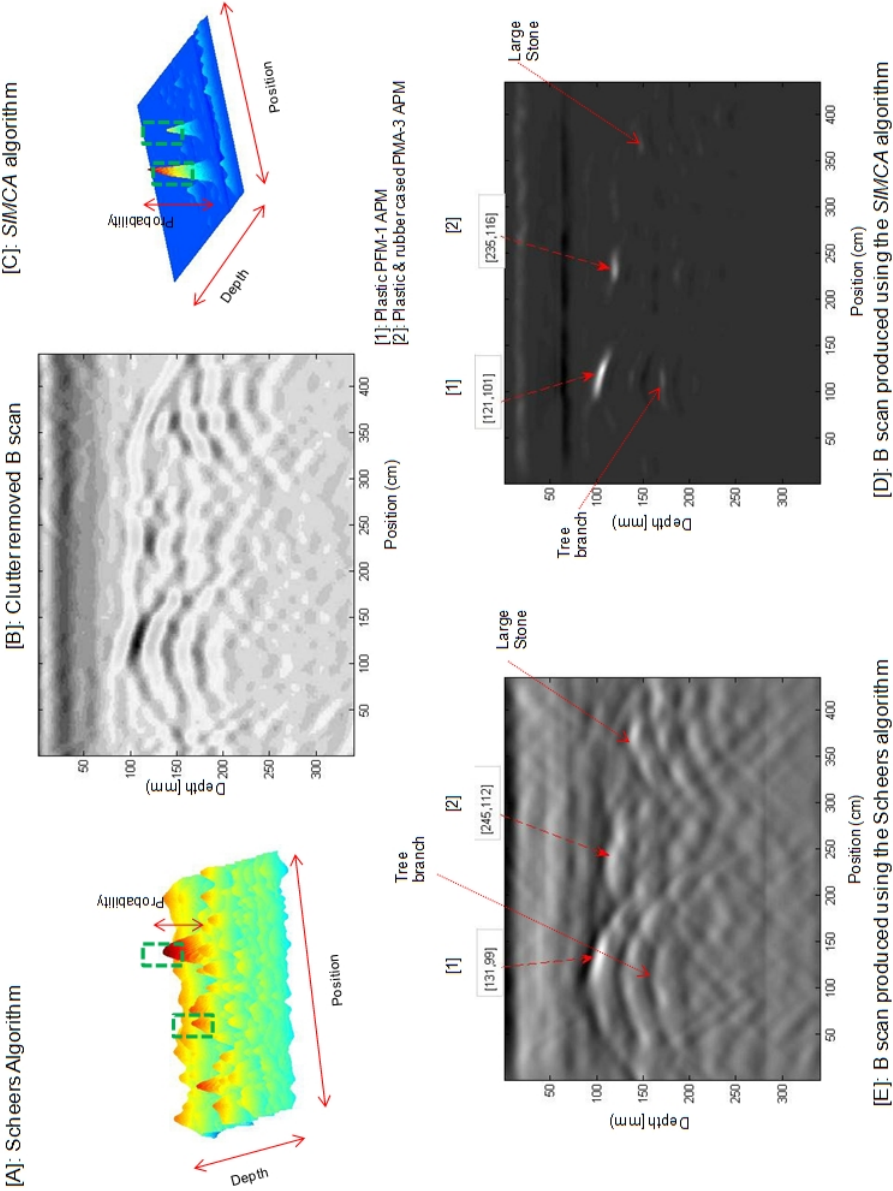


Figure 3.26: Results of real targets in a wet clay soil - [A]: 3D plot showing probability of occurrence of objects with respect to depth and position on the scan line produced by the Scheers algorithm; [B]: Clutter removed raw B scan; [C]: 3D plot showing probability of occurrence of objects with respect to depth and position on the scan line produced by the SIMCA algorithm; [D]: B scan produced from the SIMCA algorithm with brightness raised to power of 3; [E]: B scan produced by the Scheers algorithm.

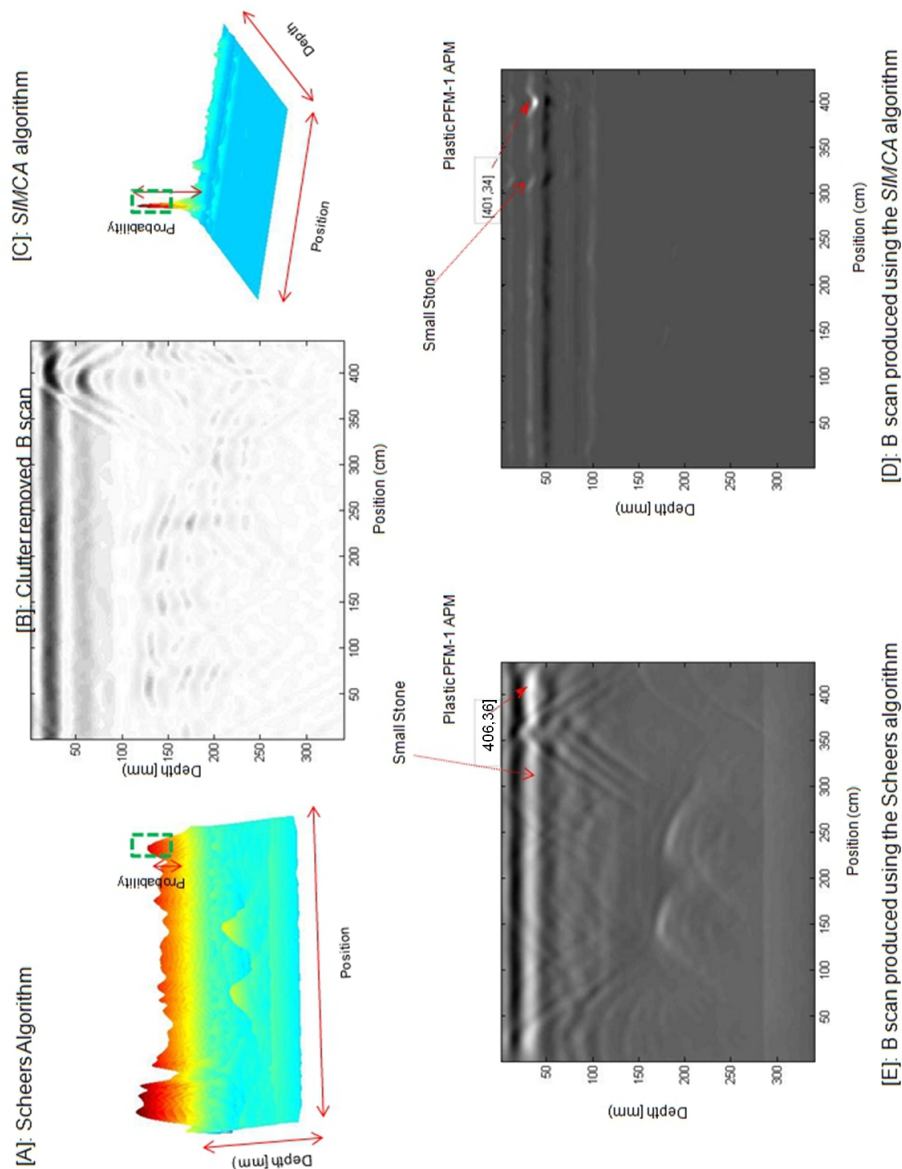


Figure 3.27: Results of real targets in a dry sandy soil - [A]: 3D plot showing probability of occurrence of objects with respect to depth and position on the scan line produced by the Scheers algorithm; [B]: Clutter removed raw B scan; [C]: 3D plot showing probability of occurrence of objects with respect to depth and position on the scan line produced by the *SIMCA* algorithm; [D]: B scan produced from the *SIMCA* algorithm with brightness raised to power of 3; [E]: B scan produced by the Scheers algorithm.

### 3.11 Validation of Results from the SIMCA 2D algorithm

As was stated earlier the results from the *SIMCA* algorithm was validated using three approaches. The details of the approaches were already briefly given in Section 3.7 of this chapter. Now detailed explanations of the validation methods are given.

#### 3.11.1 Validation of results from the SIMCA 2D algorithm using *qualitative evidence*

The B scans produced by the *SIMCA* algorithm are compared with some techniques which are the best alternative systems reported in the open literature. From Figures 3.28 and 3.29 it is clearly evident that the *SIMCA* algorithm produces clearer B scans in comparison to the other techniques. In Figures 3.28 and 3.29 the raw B scans are different due to the fact that different data was used by the authors. It was not possible to obtain the raw data nor the code, as a result a comparison is made of the final cleared image against the *SIMCA* technique. This clearer image will help the landmine clearing personnel locate and clear the landmines much easier. This is important because in the case of landmine clearance, the GPR data will ultimately have to be interpreted by non experts. Figure 3.30 compares the *SIMCA* algorithm with the below techniques from other studies and identifies the advantages and disadvantages of the different approaches. It is evident from this figure (3.30) that the *SIMCA* algorithm produces much better results.

##### 3.11.1.1 Al-Nuaimy et al.

Al-Nuaimy et al. (2000) propose a system comprising a neural network classifier, pattern recognition, further pre-processing, feature extraction and image processing stages. They begin by removing background clutter, compensate for path loss, rectify antenna separation and perform low pass filtering. The neural network using the spectral features of the data identifies areas in the B scan that have useful reflection. The HT is used as a pattern recognition tool to locate and detect the buried targets by making use of the hyperbolic anomalies. This identifies the depth and position of the buried targets. Figure 3.28[B] shows the raw B scan on the left and the processed B scan on the right.

##### 3.11.1.2 Potin et. al.

Potin et al. (2006a) present a clutter removal method based on the design of a 2D digital filter, which is adapted to B scan data. They carry out frequency analysis of a clutter geometrical model of a signal coming from a landmine. This results in building a high-pass digital filter and determines the cut-off frequencies. In their approach, they aim at reducing the clutter in B scan data whilst protecting the landmine response. They use detection techniques such as HT to search for the targets (hyperbola) in B scan. But a disadvantage of their technique is that to get perfect clutter reduction on B scan data, the clutter has to be made of horizontal bands. This implies a flat-air

ground interface which in reality is not possible. If the interface is not flat some of the clutter residues exist after the digital filtering. Figure 3.29 [B] shows the raw B scan on the left and the processed B scan on the right.

#### 3.11.1.3 Daniels and Allan

Daniels and Allan (2009) use multi-channel radar data and use various spatial deconvolution techniques such as blind deconvolution, Wiener, Lucy and regular deconvolution. They state that blind deconvolution provided the best image reconstruction, but was computationally intensive compared to the other methods. They also say that Lucy deconvolution has reduced sidelobes over Wiener and also has spotted the single point target. Furthermore they state that regular deconvolution appeared to fall between Wiener and Lucy. Blind deconvolution is performed iteratively, either each iteration improves the estimate of the 'Point spread function' or non-iteratively where one application of the algorithm obtains the Point spread function. Figure 3.28[C] shows the raw B scan on the left and the processed B scan on the right.

#### 3.11.1.4 Groenenboom and Yarovoy

Groenenboom and Yarovoy (2002) use adapted imaging algorithms and also several pre-processing and clutter removal techniques. They propose removing the DC offset and DC offset drift, removal of traces with duplicates in position, alignment of time zero for traces, subtraction of the direct wave and filtering and removal of the strong surface reflections. They also use hyperbolic shape masking to improve the detection process. In terms of the imaging algorithm they use migration algorithms such as diffraction stack, which estimates the image value at a certain position by stacking up scans associated with the same arrival times for that location. Figure 3.29[C] illustrates the raw B scan on the left and the processed B scan on the right. The next section uses a quantitative evidence method to validate the *SIMCA* algorithm.

### 3.11.2 Validation of the *SIMCA* 2D algorithm using *quantitative evidence*

In this section, validation of the *SIMCA* algorithm is going to be done using quantitative evidence. As was already described in Section 3.7 of this chapter, for quantitative evidence validation two methods are going to be used and now an outline of the validation protocol is going to be given in the next section.

#### 3.11.2.1 Use of an expert GPR user and 4 other general users who predict the location of landmines and validate the *SIMCA* 2D algorithm

As was outlined in Section 3.11.1 of this chapter, using general users who are not experts in using or interpreting GPR data and locating landmines is important because often in a field scenario the mine

clearing personnel are not experts. It is important to note that the validation was done as a blind test and the human users did not know the type, depths, positions and numbers of buried objects prior to validation. Validation was done by an expert GPR user and 4 other general users who predict the location of landmines. Also the size of the validation data is acceptable because using such a test size is in accordance with current research (Guyon et al., 1995). A human validation approach was used as opposed to an automated procedure, because it clearly replicates the actual situation in a field where a human user interprets the images. Chapter 4, Section 4.13 further discusses the reasons for using a human validation approach. The experimental protocol used is now described:

- The correlated images with the brightness raised to the power of 3, produced by the *SIMCA 2D* algorithm as shown in Figure 3.17[D] is used and presented to the human users. So the first step was to collect and print out the correlated images with brightness raised to the power of 3. This formed the set of data used for the validation procedure. The procedure is used to validate the results and not performed in the field.
- The next procedure involves briefly explaining the test setup to the users and explaining to them without letting them know the type, depths, positions and numbers of buried objects prior to validation. Sample B scans as detailed in Step 1 above was given to the users and the users were told that they should look for bright spots in the image and that the bright spots indicated the location of the targets. The human subjects were asked to mark the location of the targets on a printed correlated image by placing a cross using a pen on the target locations. Then on the basis of the method detailed in Section 3.2 of this chapter, the burial depths of the targets were calculated. Also the position of the target in the  $x$  direction was calculated for the target identified by the human user. This is because it is important to know where to dig to find the mine. These results were also timed and then fed into a Microsoft Access database.
- The final step involved analysing the results. The presentation of the analysed data is going to be done using tabular format showing the actual depths along with the estimated depths of the targets and is presented in Tables 3.2 to 3.6. An expert user of GPR was first used to estimate the location of the object and this gave an indication of how easy it was for the expert user to locate the targets. The absolute error values for the depth based on the ground truth values and the depth values estimated by the expert user were then calculated (Table 3.2). The horizontal error is obviously also important since it is important to know where to dig to find the mine. The correlated images with brightness raised to power of 3 were given to 4 other people who have never seen GPR data. It is to be noted that when the user (general user) was not able to identify the presence of a landmine a dash is used and the mean and standard deviation are worked out on the basis that the concerned dataset was not used to get meaningful results (Table 3.3). Table 3.3 also shows the mean and standard deviation values for the general users predictions of the mines in terms of the depth and the position in

the  $x$  direction. In any experiment systematic bias does exist (Table 3.4), but it is important that the final data is corrected to take care of the systematic bias (Table 3.5). The systematic bias is the error between the average position estimated by the subjects and the true position. 'Systematic errors are biases in measurement which lead to the situation where the mean of many separate measurements differs significantly from the actual value of the measured attribute' (Guyon et al., 1995). The splitting (correction) in is done in Table 3.5 using the calculated values of the systematic bias, mean and standard deviation from Tables 3.3 and 3.4.

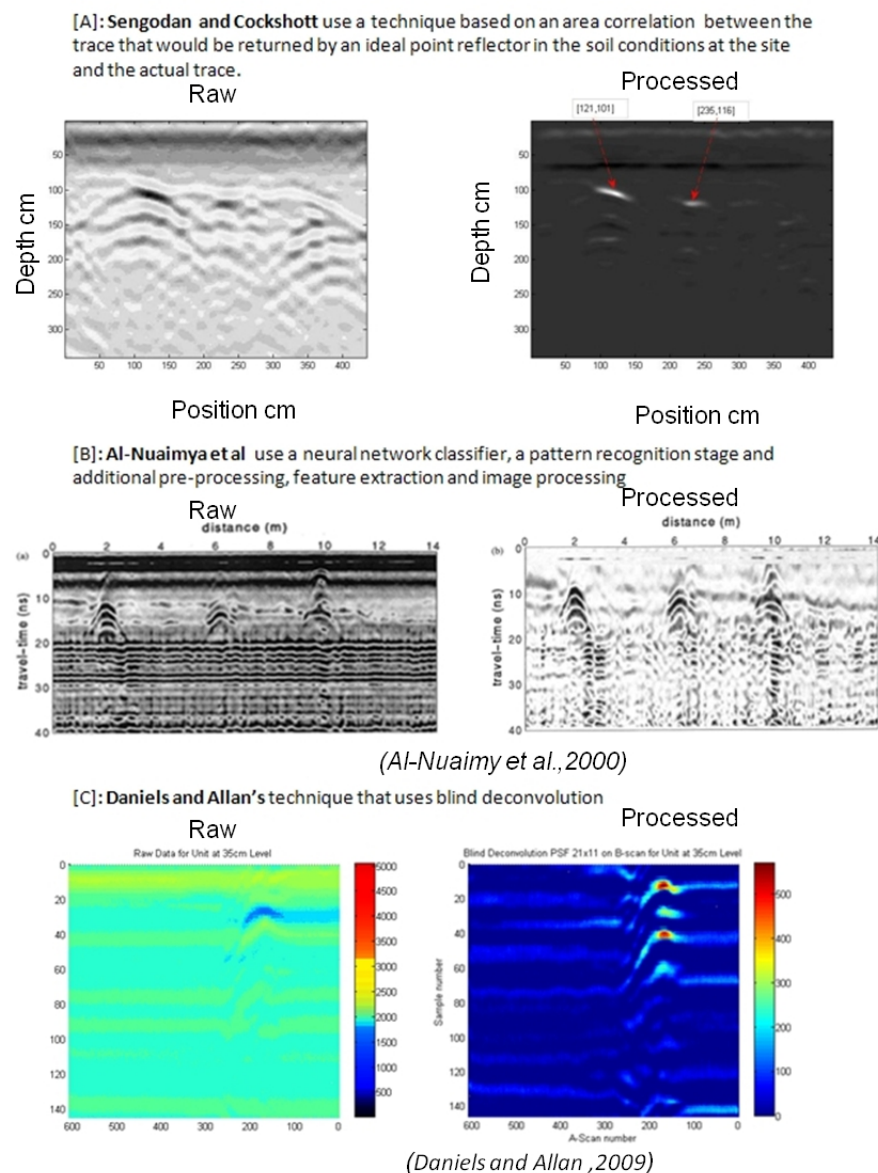


Figure 3.28: A comparison of the resulting B scans from - [A]: SIMCA algorithm; [B]: Al-Nuaimya et al.; [C]: Daniels and Alan.



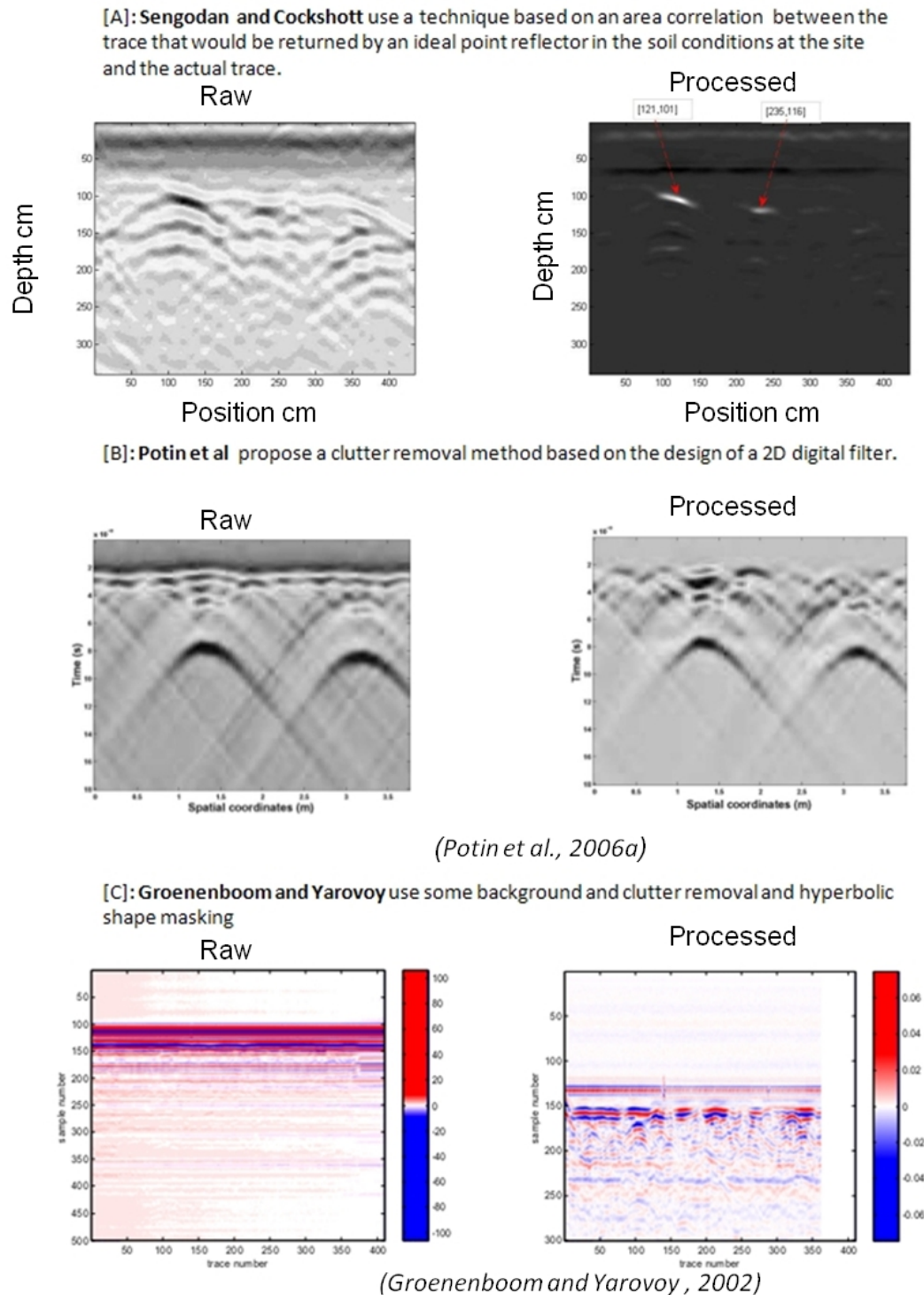


Figure 3.29: A comparison of the resulting B scans from - [A]: SIMCA algorithm; [B]: Potin et al.; [C]: Groenenboom and Yarovoy.



Sengodan and Cockshott	<ul style="list-style-type: none"> <li>• <b>Location of target easy to interpret</b></li> <li>• <b>No unwanted artifacts</b></li> <li>• <b>No excessive depth echoing</b></li> </ul>
Daniels and Allan's	<ul style="list-style-type: none"> <li>• Published data in poor format</li> <li>• Histogram uses few colours and is poorly separated</li> <li>• Lot of artifacts in cleaned image</li> <li>• Excessive depth echoing</li> </ul>
Al-Nuaimya et al	<ul style="list-style-type: none"> <li>• No major difference between raw and cleaned image</li> <li>• The cleaned image has introduced more artifacts</li> </ul>
Potin et al	<ul style="list-style-type: none"> <li>• Although image slightly cleaned some artifacts not removed</li> <li>• Not easy to isolate location of target</li> </ul>
Groenenboom and Yarovoy	<ul style="list-style-type: none"> <li>• The cleaned image still has a lot of artifacts and it is difficult to identify the targets from the clutter</li> </ul>

Figure 3.30: Figure comparing the *SIMCA* algorithm with other techniques illustrated in Figures 3.28 and 3.29.

- Whenever data is collected in an experiment, there is always some error or uncertainty. It is however important to quantify that uncertainty so that the precision of the results can be found and we can provide proof that the conclusions are valid. The method of random error treatment was adapted from Hughes and Hase (2010) where the authors present the use of errors when dealing with data.
- Also during the experiment, just to compare some false positive and false negative rates a

validation setup from the whole experimental dataset which had 21 targets was used and the expert and non expert users were asked to identify the location of the mines. Out of the 21 mines it was noted how many of the mines, mine like targets and false targets were wrongly classified. Then the false positive and false negative rates for the mines were analysed. Table 3.6 presents the results of this validation procedure.

It can be concluded from Table 3.2 that the expert user is able to locate a majority of the landmines and the highest percentage error for the burial depth is only 16%, whilst for the position in the  $x$  direction it is 25% and these results are good for initial results in comparison with contemporary research conducted by Kovalenko (2006). From the table it can be seen that the correlated results from the *SIMCA* algorithm are accurate when compared with the corresponding ground truth values and results published by research conducted by Groenenboom and Yarovoy (2002).

The results obtained were also better at middle depths than at lower depths because the clutter environment within the first few centimetres of a soil surface has strong reflections and highly non stationary statistics (Brooks, 2000). Also at depths close to the surface, there is strong interference of mine clutter in the mine backscatter. Similarly with the increase in depth, there is damping of the electric field and therefore a corresponding decrease in backscatter from the mine and increase in the soil clutter.

Therefore it can be concluded that the *SIMCA* algorithm is capable of predicting the depth correctly subject to the accuracy of the observed backscatter and the content of soil clutter in it. The presentation of the analysed data is going to be done using tabular format showing the actual depths along with the estimated depths of the targets and is presented in Tables 3.2, 3.4. Table 3.4 and Table 3.3 illustrates that the general users were able to locate the landmines within an acceptable degree of confidence.

From Table 3.3 it can be seen that the standard deviation for the estimated values for the depth and position in the  $x$  direction for the predictions from the general users are close to each other showing promise in the results. Furthermore, the standard deviations are small indicating the variations from the mean are small (Guyon et al., 1995). Also the systematic bias is small indicating the acceptability of the results when compared to the extreme conditions depicted. Furthermore Scheers (2001) says that accurate results cannot be achieved from B scans.

Scheers et al. (2001) also concludes from his study that accurate results are not attainable from B scans. Much more accurate results can be attained using C scans and therefore this is going to be demonstrated in Chapter 4. In Table 3.5, the systematic bias has been corrected in the  $x$  direction and in the depth. The horizontal error is also important since it is important to know where to dig to find the landmine.

From Table 3.6, it is positive to note that the 'False negative' rates are low and this is really important for landmines as it is not mission critical to overestimate that a mine is present but missing out the presence of a landmine is dangerous. Also the table shows that the results for the expert and general users are promising and have a low false alarm rate. These error rates are low and therefore acceptable when compared to the results produced by other studies such as (Abujarad (2007); Ekstein (1997)). From the chart in Figure 3.6, the estimated depth versus actual depth is

<i>APM Type</i>	<i>Actual depth (cm)</i>	<i>Estimated depth (cm)</i>	<i>% error</i>	<i>Actual position in x (cm)</i>	<i>Estimated position in x (cm)</i>	<i>% error</i>
<i>Type 72</i>	9.3	9	-3.2	109.0	125.0	14.7
<i>Type 72</i>	8.3	8.6	3.6	109.0	90.0	-17.4
<i>Plastic No. 4</i>	8.6	9.0	4.7	100.0	125.0	25.0
<i>T79</i>	7.8	8.1	3.8	368.0	380.0	3.3
<i>MAUS</i>	13	12.0	-7.7	88.0	89.0	1.1
<i>Copper wire</i>	10.3	9.0	-12.6	99.0	105.0	6.1
<i>M26</i>	10.5	9.1	-13.3	123.0	140.0	13.8
<i>PMD-6</i>	11.1	10.0	-9.9	206.0	205.0	-0.5
<i>M14</i>	12.3	13.0	5.7	130.0	129.0	-0.8
<i>Model 43</i>	13.8	14.0	1.4	246.0	247.0	0.4
<i>No. 4</i>	3.0	2.8	-6.7	280.0	279.0	-0.4
<i>AUS 15/50</i>	15.5	17.0	9.7	116.0	126.0	8.6
<i>M14</i>	8.3	9.0	8.4	120.0	140.0	16.7
<i>Metal ring</i>	10.3	11.0	6.8	241.0	248.0	2.9
<i>PROM-I</i>	9.9	11.0	11.1	83.0	75.0	-9.6
<i>M2</i>	9.0	8.0	-11.1	121.0	131.0	8.3
<i>M14</i>	2.2	2.1	-4.5	73.0	74.0	1.4
<i>M26</i>	10.5	9.0	-14.3	105.0	120.0	14.3
<i>PFM-I</i>	2.0	1.8	-10.0	290.0	288.0	-0.7
<i>M2</i>	13.3	12.0	-9.8	242.0	230.0	-5.0
<i>PFM-I</i>	1.9	2.0	5.3	79.0	70.0	-11.4
<i>M26</i>	15.3	16.0	4.6	366.0	367.0	0.3
<i>M14</i>	2.6	2.3	-11.5	296.0	297.0	0.3
<i>PFM-I</i>	10.5	11.0	4.8	124.0	140.0	12.9
<i>PMA-3</i>	12.3	11.0	-10.6	239.0	243.0	1.7
<i>PFM-I</i>	3.1	2.6	-16.1	403.0	401.0	-0.5

Table 3.2: Actual depth from the ground truth, estimated depth for the expert user, Actual position of the buried target in the  $x$  direction, Estimated position of the buried target in the  $x$  direction, The table also gives the percentage errors. The values of the depth and the position in the  $x$  direction are in centimetres.

APM Type	1 depth (cm)	2 depth (cm)	3 depth (cm)	4 depth (cm)	Mean	Standard deviation	1 position (cm)	2 position (cm)	3 position (cm)	4 position (cm)	Mean	Standard deviation
Type 72	8	10.0	9.0	9.1	9.0	0.8	129	130	90	125	118.5	19.1
Type 72	8	9.0	8.7	8.5	8.6	0.4	80	87	90	121	94.5	18.2
Plastic No. 4	10	7.9	8.3	9.8	9.0	1.1	130	120	80	88	104.5	24.2
T779	7	6.3	8.1	8.4	7.5	1.0	390	380	383	381	383.5	4.5
MAUS	11	10.0	12.0	12.1	11.3	1.0	89	87	85	80	85.3	3.9
Copper wire	8	11.0	12.0	9.0	10.0	1.8	110	109	89	80	97.0	14.9
M26	11	9.0	8.0	11.0	9.8	1.5	145	110	141	143	134.8	16.6
PMD-6	9	10.0	10.3	11.0	10.1	0.8	200	197	195	201	198.3	2.8
M14	14	11.0	12.0	12.8	12.5	1.3	135	120	121	134	127.5	8.1
Model 43	15	12.0	12.9	13.0	13.2	1.3	249	243	244	243	244.8	2.9
No. 4	2	3.1	2.9	2.4	2.6	0.5	270	273	274	283	275.0	5.6
AUS 15/50	18	16.0	15.1	14.0	15.8	1.7	130	100	129	131	122.5	15.0
M14	9	7.0	7.8	9.0	8.2	1.0	145	146	141	100	133.0	22.1
Metal ring	12	11.0	10.5	11.0	11.1	0.6	240	250	251	249	247.5	5.1
PROM-1	12	11.0	7.0	6.0	9.0	2.9	70	71	89	72	75.5	9.0
M2	7	8.0	8.4	7.6	7.8	0.6	133	135	99	132	124.8	17.2
M14	1	2.0	3.0	2.8	2.2	0.9	76	76	73	71	74.0	2.4
M26	8	9.5	11.0	9.9	9.6	1.2	121	119	116	90	111.5	14.5
PFM-1	2	1.1	1.9	2.2	1.8	0.5	286	280	299	281	286.5	8.7
M2	13	11.0	12.0	14.0	12.5	1.3	229	228	250	227	233.5	11.0
PFM-1	3	2.0	1.6	3.0	2.4	0.7	69	89	70	68	74.0	10.0
M26	17	15.0	16.1	15.0	15.8	1.0	369	356	260	361	336.5	51.3
M14	2	2.1	1.9	2.0	2.0	0.1	299	300	290	291	295.0	5.2
PFM-1	9	11.6	10.0	9.0	9.9	1.2	148	141	110	121	130.0	17.6
PMA-3	10	11.0	12.9	13.0	11.7	1.5	245	248	229	230	238.0	9.9
PFM-1	2	4.0	1.9	3.0	2.7	1.0	400	390	421	413	406.0	13.7

Table 3.3: Estimated depth and estimated position in the  $x$  direction for the 4 general users, mean and standard deviation on the depth and the position in the  $x$  direction. The values for the position in the  $x$  direction and the depth are in centimetres.

APM Type	Actual depth (cm)	1 depth (cm)	2 depth (cm)	3 depth (cm)	4 depth (cm)	Systematic bias	Actual position (cm)	1 position (cm)	2 position (cm)	3 position (cm)	4 position (cm)	Systematic bias
Type 72	9.3	8	10.0	9.0	9.1	-0.3	109.0	129	130	90	125	9.5
Type 72	8.3	8	9.0	8.7	8.5	0.3	109.0	80	87	90	121	-14.5
Plastic No. 4	8.6	10	7.9	8.3	9.8	0.4	100.0	130	120	80	88	4.5
T779	7.8	7	6.3	8.1	8.4	-0.4	368.0	390	380	383	381	15.5
MAUS	13	11	10.0	12.0	12.1	-1.7	88.0	89	87	85	80	-2.8
Copper wire	10.3	8	11.0	12.0	9.0	-0.3	99.0	110	109	89	80	-2.0
M26	10.5	11	9.0	8.0	11.0	-0.8	123.0	145	110	141	143	11.8
PMD-6	11.1	9	10.0	10.3	11.0	-1.0	206.0	200	197	195	201	-7.8
M14	12.3	14	11.0	12.0	12.8	0.1	130.0	135	120	121	134	-2.5
Model 43	13.8	15	12.0	12.9	13.0	-0.6	246.0	249	243	244	243	-1.3
No. 4	3.0	2	3.1	2.9	2.4	-0.4	280.0	270	273	274	283	-5.0
AUS 15/50	15.5	18	16.0	15.1	14.0	0.3	116.0	130	100	129	131	6.5
M14	8.3	9	7.0	7.8	9.0	-0.1	120.0	145	146	141	100	13.0
Metal ring	10.3	12	11.0	10.5	11.0	0.8	241.0	240	250	251	249	6.5
PROM-1	9.9	12	11.0	7.0	6.0	-0.9	83.0	70	71	89	72	-7.5
M2	9.0	7	8.0	8.4	7.6	-1.3	121.0	133	135	99	132	3.8
M14	2.2	1	2.0	3.0	2.8	0.0	73.0	76	76	73	71	1.0
M26	10.5	8	9.5	11.0	9.9	-0.9	105.0	121	119	116	90	6.5
PFM-1	2.0	2	1.1	1.9	2.2	-0.2	290.0	286	280	299	281	-3.5
M2	13.3	13	11.0	12.0	14.0	-0.8	242.0	229	228	250	227	-8.5
PFM-1	1.9	3	2.0	1.6	3.0	0.5	79.0	69	89	70	68	-5.0
M26	15.3	17	15.0	16.1	15.0	0.5	366.0	369	356	260	361	-29.5
M14	2.6	2	2.1	1.9	2.0	-0.6	296.0	299	300	290	291	-1.0
PFM-1	10.5	9	11.6	10.0	9.0	-0.6	124.0	148	141	110	121	6.0
PMA-3	12.3	10	11.0	12.9	13.0	-0.6	239.0	245	248	229	230	-1.0
PFM-1	3.1	2	4.0	1.9	3.0	-0.4	403.0	400	390	421	413	3.0

Table 3.4: Estimated depth and estimated position in the  $x$  direction for the 4 general users, systematic bias on the depth and the position in the  $x$  direction. The values for the position in the  $x$  direction and the depth are in centimetres.

plotted and series 1, 2, 3, and 4 are the estimated depths on the basis of the general user's predictions of where the mines were located. The chart shows that the users were able to predict the location of landmines to acceptable degrees of accuracy as indicated by the closeness of the predicted and the actual depths.

The next section validates the results from the *SIMCA* algorithm using a quantitative approach.

### 3.11.2.2 Use of *AMIRA* software to obtain values of the burial depth and position of the target in the $x$ direction and hence validate the *SIMCA* 2D algorithm

The *AMIRA* software is then used to obtain the values of the burial depth and the position of the target in the  $x$  direction as per the method stated in Section 3.9. Then the absolute error values for the burial depth along with the absolute error values for the position in the  $x$  direction obtained from the *SIMCA* algorithm and the Scheer's algorithm when compared to the corresponding ground truth values were calculated. The tables in the next few pages of this chapter (Tables 3.7 to 3.16) show the actual burial depth of the targets from the ground truth, along with the burial depth of the targets obtained using the *SIMCA* and Scheers methods. To go further the tables also show the actual position in the  $x$  direction for the ground truth, and the corresponding values from the two methods and the processing time for the two methods. Furthermore, the tables also show the absolute error values for the burial depth and the position in the  $x$  direction for the *SIMCA* method and the Scheers method. From the tables, the maximum absolute error in terms of the burial depth are 19.2% (plastic M14 APM) and 91.6% (plastic M14 APM) for the *SIMCA* method and the Scheers method respectively. Whilst the minimum absolute error for the burial depth are 0.8% each for the plastic MAUS APM. The maximum absolute errors for the position in the  $x$  direction are 13.9% (plastic PFM-1 APM) and 31.6% (plastic PFM-1 APM) for the *SIMCA* and Scheers methods respectively. Whilst the minimum error for the position in the  $x$  direction for the *SIMCA* and Scheers methods are 0.5% (plastic T/79 APM) and 0.7% (plastic PFM-1 APM) respectively. This clearly illustrates two facts:

1. The *SIMCA* algorithm is considerably more accurate in its ability to present clearer images from which the burial depth and the position in the  $x$  direction can be calculated when compared to the Scheers method.
2. The plastic mines are the most critical mines and this can be concluded from the fact that the plastic mines are the ones that give the maximum and minimum values for the absolute errors for both the *SIMCA* and Scheers methods. The plastic mines are the most critical mines because conventional methods such as metal detectors cannot find plastic mines.

Finally considering the processing time, the tables show that the maximum time the *SIMCA* algorithm takes to run is only 0.4s when compared to the 1.4s for the Scheers method. This quicker processing time for the *SIMCA* algorithm is critical because both the battery power and the processing speed are limiting factors in the GPR system. Also the harsh environments make the actual landmine clearance task considerably more difficult and a quicker processing time can give more time for the operator to interpret the images before the battery runs out.

APM Type	1 depth (cm)	2 depth (cm)	3 depth (cm)	4 depth (cm)	1 position (cm)	2 position (cm)	3 position (cm)	4 position (cm)
Type 72	7.7	9.7	8.7	8.8	128.8	129.8	89.8	124.8
Type 72	7.7	8.7	8.4	8.2	79.8	86.8	89.8	120.8
Plastic No. 4	9.7	7.6	8.0	9.5	129.8	119.8	79.8	87.8
T/79	6.7	6.0	7.8	8.1	389.8	379.8	382.8	380.8
MAUS	10.7	9.7	11.7	11.8	88.8	86.8	84.8	79.8
Copper wire	7.7	10.7	11.7	8.7	109.8	108.8	88.8	79.8
M26	10.7	8.7	7.7	10.7	144.8	109.8	140.8	142.8
PMD-6	8.7	9.7	10.0	10.7	199.8	196.8	194.8	200.8
M14	13.7	10.7	11.7	12.5	134.8	119.8	120.8	133.8
Model 43	14.7	11.7	12.6	12.7	248.8	242.8	243.8	242.8
No. 4	1.7	2.8	2.6	2.1	269.8	272.8	273.8	282.8
AUS 15/50	17.7	15.7	14.8	13.7	129.8	99.8	128.8	130.8
M14	8.7	6.7	7.5	8.7	144.8	145.8	140.8	99.8
Metal ring	11.7	10.7	10.2	10.7	239.8	249.8	250.8	248.8
PROM-1	11.7	10.7	6.7	5.7	69.8	70.8	88.8	71.8
M2	6.7	7.7	8.1	7.3	132.8	134.8	98.8	131.8
M14	0.7	1.7	2.7	2.5	75.8	75.8	72.8	70.8
M26	7.7	9.2	10.7	9.6	120.8	118.8	115.8	89.8
PFM-1	1.7	0.8	1.6	1.9	285.8	279.8	298.8	280.8
M2	12.7	10.7	11.7	13.7	228.8	227.8	249.8	226.8
PFM-1	2.7	1.7	1.3	2.7	68.8	88.8	69.8	67.8
M26	16.7	14.7	15.8	14.7	368.8	355.8	259.8	360.8
M14	1.7	1.8	1.6	1.7	298.8	299.8	289.8	290.8
PFM-1	8.7	11.3	9.7	8.7	147.8	140.8	109.8	120.8
PMA-3	9.7	10.7	12.6	12.7	244.8	247.8	228.8	229.8
PFM-1	1.7	3.7	1.6	2.7	399.8	389.8	420.8	412.8

Table 3.5: The corrected depth and position in the  $x$  direction for the general users. The values for the position in the  $x$  direction and the depth are in centimetres.

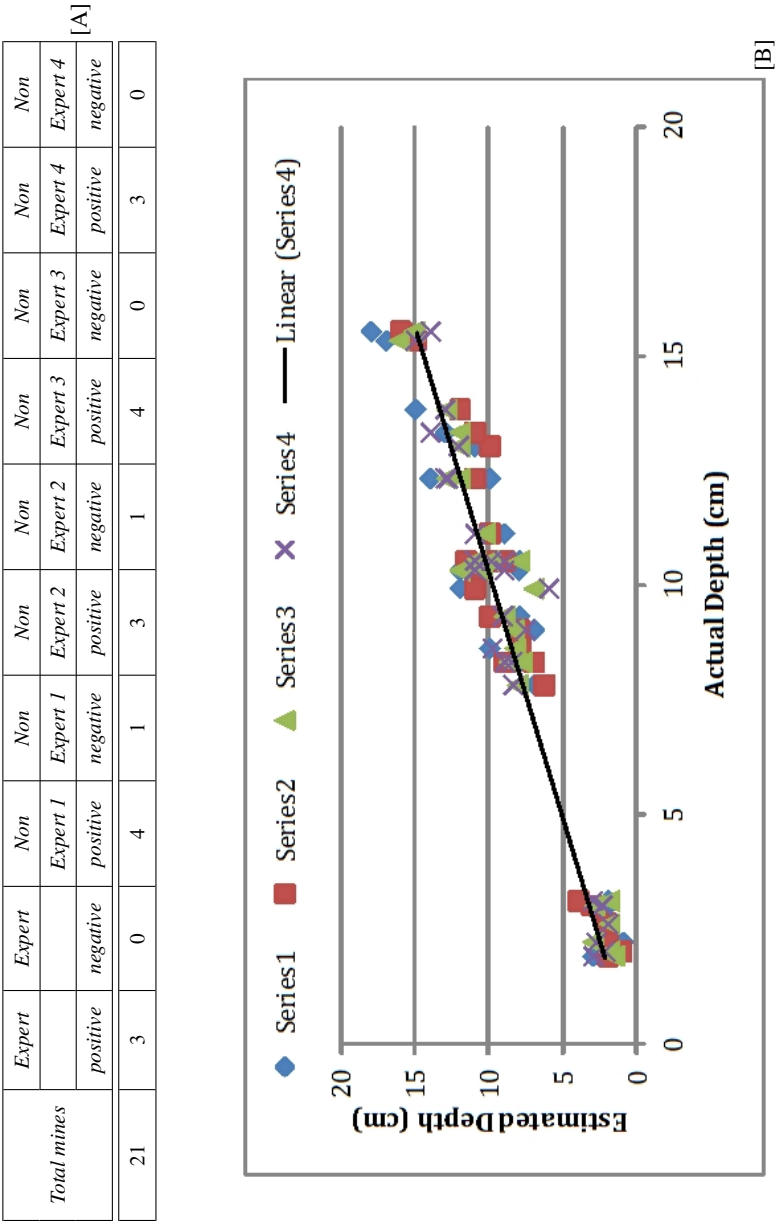


Table 3.6: [A]: False positive and False negative rates. This validation step had a total of 21 mines and the expert and non expert users were asked to identify the locations of the mines and the results were collated from the validation process.; [B]: Error plot of estimated depth versus actual depth. Series 1 to Series 4 indicates the 4 general users. Also the linear trend line analysis has been included.



	Burial depth of [1] (cm)	Position in $x$ direction for [1] (cm)	Processing time (s)
Ground truth	9.3	109	-
SIMCA	8.8	111	0.1
Scheers	9.9	114	0.2
Error in SIMCA	5.4%	1.8%	-
Error in Scheers	6.5%	4.6%	-



Plastic, rubber cased Type 72 APM

Table 3.7: Actual burial depth, depth obtained from the *SIMCA* method, depth obtained from the Scheers's method for each of the targets, Actual position in the  $x$  direction, position in the  $x$  direction obtained from the *SIMCA* method, position in the  $x$  direction obtained from the Scheers method. All values of depth and the position in the  $x$  direction are in centimetres for Figure 3.17. The table also gives the percentage errors for both the *SIMCA* and Scheers algorithms and also the processing time for the algorithms in seconds.

	Burial depth of [1] (cm)	Position in $x$ direction for [1] (cm)	Processing time (s)
Ground truth	8.3	109	-
SIMCA	8.0	111	0.2
Scheers	9.9	107	0.4
Error in SIMCA	3.6%	1.8%	-
Error in Scheers	19.3%	1.8%	-



Plastic, rubber cased Type 72 APM

Table 3.8: Actual burial depth, depth obtained from the *SIMCA* method, depth obtained from the Scheers's method for each of the targets, Actual position in the  $x$  direction, position in the  $x$  direction obtained from the *SIMCA* method, position in the  $x$  direction obtained from the Scheers method. All values of depth and the position in the  $x$  direction are in centimetres for Figure 3.18. The table also gives the percentage errors for both the *SIMCA* and Scheers algorithms and also the processing time for the algorithms in seconds.

	Burial depth of [1] (cm)	Position in <i>x</i> direction for [1] (cm)	Burial depth of [2] (cm)	Position in <i>x</i> direction for [2] (cm)	Processing time (s)
Ground truth	7.8	368	8.6	100	-
SIMCA	7.5	366	8.1	107	0.3
Scheers	9.5	390	10.7	91	0.6
Error in SIMCA	3.8%	0.5%	5.8%	7.0%	-
Error in Scheers	21.8%	6.0%	24.4%	9.0%	-

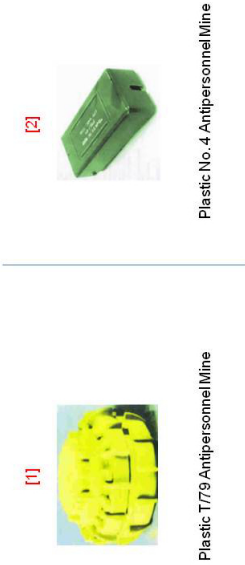


Table 3.9: Actual burial depth, depth obtained from the SIMCA method, depth obtained from the Scheers’s method for each of the targets, Actual position in the *x* direction, position in the *x* direction obtained from the SIMCA method, position in the *x* direction obtained from the Scheers method. All values of depth and the position in the *x* direction are in centimetres for Figure 3.19. The table also gives the percentage errors for both the SIMCA and Scheers algorithms and also the processing time for the algorithms in seconds.

	depth [1] (cm)	Position in $x$ [1] (cm)	depth [2]	Position in $x$ [2]	depth [3]	Position in $x$ [3]	depth [4]	Position in $x$ [4]	Processing time (s)
Ground truth	13	88	10.3	99	10.5	123	11.1	206	-
SIMCA	12.9	87	10.1	88	10.4	120	11.2	204	0.4
Scheers	13.1	79	10.0	71	9.7	111	10.9	217	1.0
Error in SIMCA	0.8%	1.1%	1.9%	11.1%	1.0%	2.4%	0.9%	1.0%	-
Error in Scheers	0.8%	10.2%	2.9%	28.3%	7.6%	9.8%	1.8%	5.3%	-



Table 3.10: Actual burial depth, depth obtained from the SIMCA method, depth obtained from the Scheers’s method for each of the targets, Actual position in the  $x$  direction, position in the  $x$  direction obtained from the SIMCA method, position in the  $x$  direction obtained from the Scheers method. All values of depth and the position in the  $x$  direction are in centimetres for Figure 3.20. The table also gives the percentage errors for both the SIMCA and Scheers algorithms and also the processing time for the algorithms in seconds.

	depth [1] (cm)	Position in <i>x</i> [1] (cm)	depth [2] (cm)	Position in <i>x</i> [2] (cm)	depth [3] (cm)	Position in <i>x</i> [3] (cm)	Processing time (s)
Ground truth	12.3	130	13.8	246	3.0	280	-
SIMCA	11.3	124	13.4	243	2.8	286	0.1
Scheers	10.2	138	12.4	238	2.2	304	0.4
Error in SIMCA	8.1%	4.6%	2.9%	1.2%	6.7%	2.1%	-
Error in Scheers	17.1%	6.2%	10.1%	3.3%	26.7%	8.6%	-



Table 3.11: Actual burial depth, depth obtained from the SIMCA method, depth obtained from the Scheers’s method for each of the targets, Actual position in the *x* direction, position in the *x* direction obtained from the SIMCA method, position in the *x* direction obtained from the Scheers method. All values of depth and the position in the *x* direction are in centimetres for Figure 3.21. The table also gives the percentage errors for both the SIMCA and Scheers algorithms and also the processing time for the algorithms in seconds.

	depth [1] (cm)	Position in $x$ [1] (cm)	depth [2] (cm)	Position in $x$ [2] (cm)	depth [3] (cm)	Position in $x$ [3] (cm)	Processing time (s)
Ground truth	15.5	116	8.3	120	10.3	241	-
SIMCA	15.3	112	8.5	118	10.1	236	0.2
Scheers	8.6	134	15.9	99	9.9	231	1.4
Error in SIMCA	1.3%	3.4%	2.4%	1.7%	1.9%	2.1%	-
Error in Scheers	44.5%	15.5%	91.6%	17.5%	3.9%	4.1%	-



Table 3.12: Actual burial depth, depth obtained from the SIMCA method, depth obtained from the Scheers’s method for each of the targets, Actual position in the  $x$  direction, position in the  $x$  direction obtained from the SIMCA method, position in the  $x$  direction obtained from the Scheers method. All values of depth and the position in the  $x$  direction are in centimetres for Figure 3.22. The table also gives the percentage errors for both the SIMCA and Scheers algorithms and also the processing time for the algorithms in seconds.

	depth [1] (cm)	Position in x [1] (cm)	depth [2]	Position in x [2]	Processing time (s)
Ground truth	9.9	83	9.0	121	-
SIMCA	9.1	76	9.2	131	0.2
Scheers	11.2	91	11.2	145	0.4
Error in SIMCA	8.1%	8.4%	2.2%	8.3%	-
Error in Scheers	13.1%	9.6%	24.4%	19.8%	-



Table 3.13: Actual burial depth, depth obtained from the *SIMCA* method, depth obtained from the Scheers's method for each of the targets, Actual position in the  $x$  direction, position in the  $x$  direction obtained from the *SIMCA* method, position in the  $x$  direction obtained from the Scheers method. All values of depth and the position in the  $x$  direction are in centimetres for Figure 3.23. The table also gives the percentage errors for both the *SIMCA* and Scheers algorithms and also the processing time for the algorithms in seconds.



	depth [1] (cm)	Position in x [1] (cm)	Processing time (s)
Ground truth	3.1	403	-
SIMCA	3.4	401	0.1
Scheers	3.6	406	0.5
Error in SIMCA	9.7%	0.5%	-
Error in Scheers	16.1%	0.7%	-







Table 3.16: Actual burial depth, depth obtained from the *SIMCA* method, depth obtained from the Scheers's method for each of the targets, Actual position in the  $x$  direction, position in the  $x$  direction obtained from the *SIMCA* method, position in the  $x$  direction obtained from the Scheers method. All values of depth and the position in the  $x$  direction are in centimetres for Figure 3.27. The table also gives the percentage errors for both the *SIMCA* and Scheers algorithms and also the processing time for the algorithms in seconds.

	depth [1] (cm)	Position in $x$ [1] (cm)	depth [2] (cm)	Position in $x$ [2] (cm)	Processing time (s)
Ground truth	10.5	124	12.3	239	-
SIMCA	10.1	121	11.6	235	0.2
Scheers	9.9	131	11.2	245	0.8
Error in SIMCA	3.8%	2.4%	5.7%	1.7%	-
Error in Scheers	5.7%	5.6%	8.9%	2.5%	-

[A]

	depth [1] (cm)	Position in $x$ [1] (cm)	depth [2] (cm)	Position in $x$ [2] (cm)	depth [3]	Position in $x$ [3]	depth [4]	Position in $x$ [4]	Processing time(s)
Ground truth	2.2	73	10.5	105	2.0	290	13.3	242	-
SIMCA	2.0	69	10.4	116	2.1	286	12.7	239	0.2
Scheers	2.5	52	10.2	126	2.3	296	12.5	248	0.8
Error in SIMCA	9.1%	5.5%	1.0%	10.5%	5.0%	1.4%	4.5%	1.2%	-
Error in Scheers	13.6%	28.8%	2.9%	20.0%	15.0%	2.1%	6.0%	2.5%	-

[B]

Table 3.14: Actual burial depth, depth obtained from the *SIMCA* method, depth obtained from the Scheers's method for each of the targets, Actual position in the  $x$  direction, position in the  $x$  direction obtained from the *SIMCA* method, position in the  $x$  direction obtained from the Scheers method. All values of depth and the position in the  $x$  direction are in centimetres. The table also gives the percentage errors for both the *SIMCA* and Scheers algorithms and also the processing time for the algorithms in seconds; [A]: for Figure 3.26; [B]: for Figure 3.24. The table also gives the percentage errors for both the *SIMCA* and Scheers algorithms and also the processing time for the algorithms in seconds.

	depth [1] (cm)	Position in x [1] (cm)	depth [2]	Position in x [2]	depth [3]	Position in x [3]	Processing time (s)
Ground truth	1.9	79	15.3	366	2.6	296	-
SIMCA	1.6	68	15.1	361	2.1	292	0.2
Scheers	1.5	54	14.5	360	1.6	308	0.8
Error in SIMCA	15.8%	13.9%	1.3%	1.4%	19.2%	1.4%	-
Error in Scheers	21.1%	31.6%	5.2%	1.6%	38.5%	4.1%	-



Table 3.15: Actual burial depth, depth obtained from the *SIMCA* method, depth obtained from the Scheers’s method for each of the targets, Actual position in the *x* direction, position in the *x* direction obtained from the *SIMCA* method, position in the *x* direction obtained from the Scheers method. All values of depth and the position in the *x* direction are in centimetres for Figure 3.25. The table also gives the percentage errors for both the *SIMCA* and Scheers algorithms and also the processing time for the algorithms in seconds.



### 3.12 Summary graphs and statistics

Tables 3.17 and 3.18 summarises the results for the burial depth and computes some statistics for data. Tables 3.19 and 3.20 summarises the results for the position in  $x$  and again computes some statistics. The tables indicate that the *SIMCA* algorithm is more accurate than the Scheers algorithm because of the lower values of the Root mean square of the differences between the estimated values from the algorithms and the ground truth. Figure 3.31 is summary graph of ground truth depth versus estimated depth and Figure 3.32 is summary graph for ground truth position in  $x$  versus estimated position in  $x$ . It can be concluded from the graphs that the *SIMCA* algorithm is more accurate than the Scheers algorithm because it is closer to the actual values of the parameters. The chi-square test for independence, for the above data sets, is chitest function. Furthermore for chitest values of probability of 0.04 or less is considered significant (Hughes and Hase, 2010). Therefore for Scheers, there is a significant difference between the observed frequencies and the expected frequencies, which is unlikely to be simply due to sampling error. In conclusion *SIMCA* results are more accurate than Scheers.

Having validated the *SIMCA 2D* algorithm using buried landmines, Appendix B demonstrates the testing of the *SIMCA 2D* algorithm on the location of foundations in demolished buildings. The next section summarises this chapter.

### 3.13 Summary and Discussions

Due to the high dielectric permittivity contrast at the air ground interface, a strong response is apparent in an GPR image. This response is the main component of clutter and it causes the responses of landmines buried at shallow depths to be blurred. Therefore the landmine detection task requires a pre-processing step which reduces this clutter. The chapter therefore discussed the techniques used in order to reduce this clutter. The objective of GPR image presentation is to give a display of the processed data that is an image of the subsurface and in which the anomalies that represent the target are in their true spatial position. When a real size of the buried target is required by the recognition process, migration is necessary for the transformation of the target response into a more compact one.

The chapter next introduced the formulation of the *SIMCA 2D* algorithm using B scans. The resulting B scans from the *SIMCA* algorithm were compared to results obtained from the Scheers method. The results are also good because one can never really get great horizontal localisation in a B scan approach due to the fact that the profile of the relevant detail in the hyperbolic kernel is more horizontal than vertical. Also in the chapter it was found that an increase in soil moisture causes a higher impedance contrast with the non metallic mine body and thus the greater the anomaly response. The plastic landmine can be visible in a high attenuating soil.

It was shown in this chapter for the location of landmines detection that the *SIMCA* algorithm was an improvement over the Scheers algorithm. To go further the chapter used *qualitative evidence* and demonstrated that for the landmine data the *SIMCA* algorithm produced clearer images of B scans and was an improvement over the techniques used by other studies. Also using an expert user

	Ground truth (cm)	SIMCA (cm)	Scheers (cm)	Difference_SIMCA	Difference_Scheers
1	9.3	9.8	9.9	0.5	0.6
1	8.3	8.0	9.9	-0.3	1.6
1	7.8	7.5	9.5	-0.3	1.7
1	13.0	12.9	13.1	-0.1	0.1
1	12.3	11.3	10.2	-1.0	-2.1
1	15.5	15.3	8.6	-0.2	-6.9
1	9.9	9.1	11.2	-0.8	1.3
1	3.1	3.4	3.6	0.3	0.5
1	10.5	10.1	9.9	-0.4	-0.6
1	2.2	2.0	2.5	-0.2	0.3
1	1.9	1.6	1.5	-0.3	-0.4
2	8.6	8.1	10.7	-0.5	2.1
2	10.3	10.1	10.0	-0.2	-0.3
2	13.8	13.4	12.4	-0.4	-1.4
2	8.3	8.5	15.9	0.2	7.6
2	9.0	9.2	11.2	0.2	2.2
2	12.3	11.6	11.2	-0.7	-1.1
2	10.5	10.4	10.2	-0.1	-0.3
2	15.3	15.1	14.5	-0.2	-0.8
3	10.3	10.4	9.7	0.1	-0.6
3	3.0	2.8	2.2	-0.2	-0.8
3	10.3	10.1	9.9	-0.2	-0.4
3	2.0	2.1	2.3	0.1	0.3
3	2.6	2.1	1.6	-0.5	-1.0

Table 3.17: Summary statistics for burial depth (1). All values in cm. *Difference\_SIMCA* and *Difference\_Scheers* is the difference between the ground truth value and the estimated value from the *SIMCA* algorithm and Scheers respectively. *Root\_mean\_square\_difference* is found using  $\sqrt{(d * d / N)}$  where  $d$  is the values of the differences between the estimated values and the ground truth and  $N$  is the total number of differences.

	Ground truth (cm)	SIMCA (cm)	Scheers (cm)	Difference_SIMCA	Difference_Scheers
4	11.1	11.2	10.9	0.1	-0.2
4	13.3	12.7	12.5	-0.6	-0.8
Sum of differences <sup>2</sup>					
Root_mean_square_difference_SIMCA			0.406		
Root_mean_square_difference_Scheers			2.273		
Correlation coefficient for SIMCA			0.997		
Correlation coefficient for Scheers			0.843		
Chi test for SIMCA			1.000		
Chi test for Scheers			0.978		

Table 3.18: Summary statistics for burial depth (2). All values in cm.

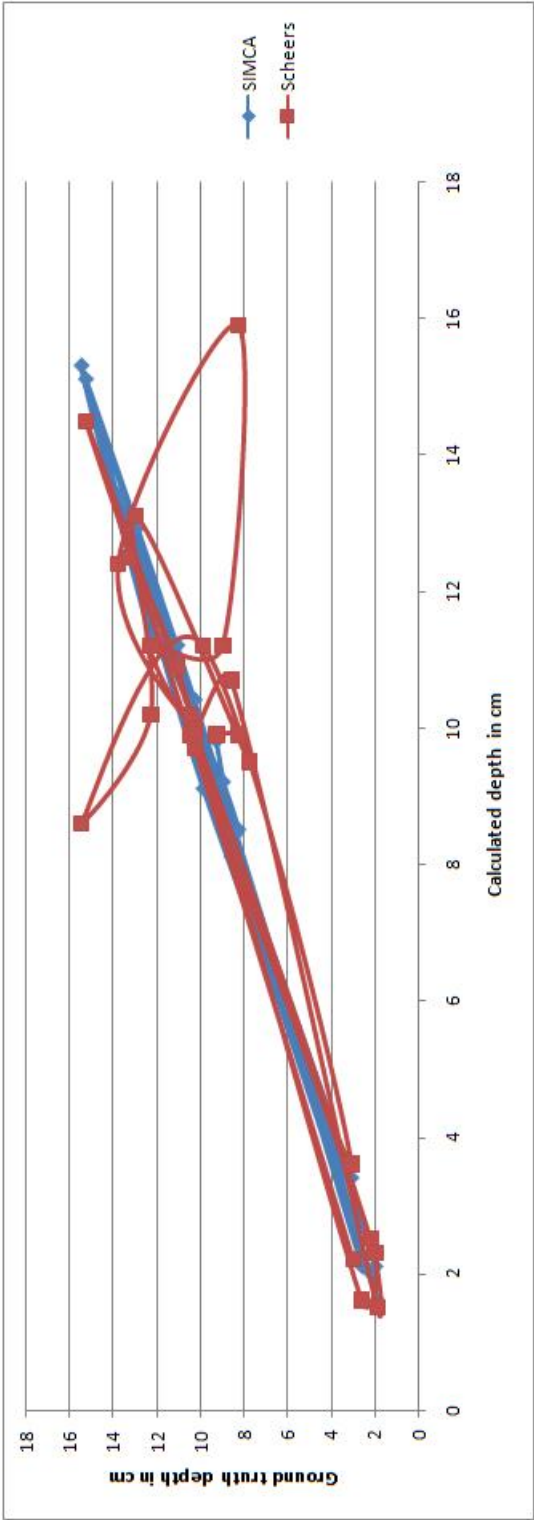


Figure 3.31: Summary graph of ground truth depth vs estimated depth for Tables 3.17 and 3.18.

	<i>Ground truth (cm)</i>	<i>SIMCA (cm)</i>	<i>Scheers (cm)</i>	<i>Difference_SIMCA</i>	<i>Difference_Scheers</i>
<i>I</i>	109.0	111.0	114.0	2.0	5.0
<i>I</i>	109.0	111.0	107.0	2.0	-2.0
<i>I</i>	368.0	366.0	390.0	-2.0	22.0
<i>I</i>	88.0	87.0	79.0	-1.0	-9.0
<i>I</i>	130.0	124.0	138.0	-6.0	8.0
<i>I</i>	116.0	112.0	134.0	-4.0	18.0
<i>I</i>	83.0	76.0	91.0	-7.0	8.0
<i>I</i>	403.0	401.0	406.0	-2.0	3.0
<i>I</i>	124.0	121.0	131.0	-3.0	7.0
<i>I</i>	73.0	69.0	52.0	-4.0	-21.0
<i>I</i>	79.0	68.0	54.0	-11.0	-25.0
2	100.0	107.0	91.0	7.0	-9.0
2	99.0	88.0	71.0	-11.0	-28.0
2	246.0	243.0	238.0	-3.0	-8.0
2	120.0	118.0	99.0	-2.0	-21.0
2	121.0	131.0	145.0	10.0	24.0
2	239.0	235.0	245.0	-4.0	6.0
2	105.0	116.0	126.0	11.0	21.0
2	366.0	361.0	360.0	-5.0	-6.0
3	123.0	120.0	111.0	-3.0	-12.0
3	280.0	286.0	304.0	6.0	24.0
3	241.0	236.0	231.0	-5.0	-10.0
3	290.0	286.0	296.0	-4.0	6.0
3	296.0	292.0	308.0	-4.0	12.0

Table 3.19: Summary statistics for position in the  $x$  direction (1). All values in cm.

	Ground truth (cm)	SIMCA (cm)	Scheers (cm)	Difference_SIMCA	Difference_Scheers
4	206.0	204.0	217.0	-2.0	11.0
4	242.0	239.0	248.0	-3.0	6.0
Sum of differences <sup>2</sup>					
	Root_mean_square_difference_SIMCA	5.630			
	Root_mean_square_difference_Scheers	14.918			
	Correlation coefficient for SIMCA	0.999			
	Correlation coefficient for Scheers	0.991			
	Chitest for SIMCA	1.000			
	Chitest for Scheers	0.001			

Table 3.20: Summary statistics for position in the *x* direction (2). All values in cm.

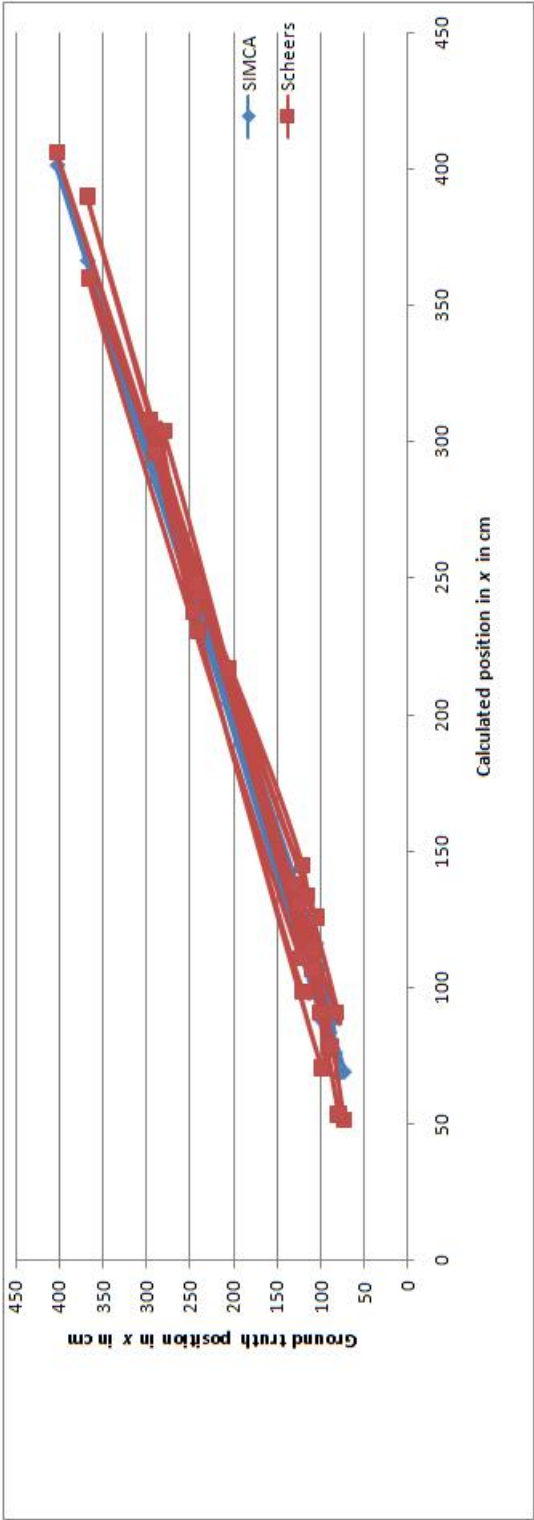


Figure 3.32: Summary graph of ground truth position in x vs estimated position in x for Tables 3.19 and 3.20.

and 4 other general users who were asked to locate the targets using a pen and marking the location of the target on the B scan produced by the *SIMCA* algorithm, the chapter concluded that general users were able to locate the targets from B scans produced by the *SIMCA* algorithm.

What was mentioned in Chapter 1 that the *SIMCA* algorithm produces an improvement over other current studies has now been demonstrated in this chapter. This improvement can be judged by the following criteria:

- The landmines can be located more accurately than other techniques. This was demonstrated by the *quantitative* and *qualitative* studies where results were compared with the Scheers algorithm and the B scans from state-of-the art techniques.
- Because the images produced by the *SIMCA* algorithm are much clearer and easier to interpret with less artifacts, the landmine clearance personnel will spend less time interpreting the image.
- The *SIMCA* algorithm allows plastic mines to be detected and this is important because of the wide presence of plastic landmines.

The *SIMCA* algorithm could be an advantage in other application areas such as in the utility detection market. Especially when considering utility detection is also undertaken by non-experts and targets like PVC and ceramic pipes are difficult to distinguish in a noisy urban environment. There are some studies already using GPR techniques in the utility detection market ((Daniels, 1985); (Daniels, 1988); (Ciochetto et al., 1999); (Gamba and Lossani, 2000); (Daniels and Schmidt, 1995); (Gunton and Scott, 1987); (Lester and Bernold, 2007)).

Although acceptable results are obtained using B scans processed by the *SIMCA 2D* algorithm, volumetric displays using C scans allow the personnel to visualize the entire data volume using one image. Also objects that are buried at a single depth can be identified using horizontal slices. But the difficulty arises if the target spans multiple depths. These horizontal or depth slices which are used by the majority of algorithms in the literature have a limiting factor in the above situation. The reliable and accurate interpretation of GPR data can only be accomplished by high quality three-dimensional images. These will illustrate accurate target geometries. Acquiring dense data and the use of 3D reconstruction algorithms such as the *SIMCA 3D* algorithm described in the next chapter (Chapter 4) are necessary to get the target geometry of targets such as landmines. Also in a hand held system it is difficult to maintain a constant sweeping pattern and therefore a non uniform displacement occurs. Therefore, reliable position information system has to be used to give positional data to the system to allow for the correction due to the non uniform displacements. Chapter 5 demonstrates such an issue.



## Chapter 4

# ***SIMCA 3D and its validation***

*This chapter extends the 2D SIMCA algorithm already discussed in Chapter 3 and develops the 3D SIMCA technique. It was concluded in the previous chapter that there is difficulty in interpreting 2D reflections from B scans and that from such 2D results, the determination of the dimensions of the target directly from the B scans is not possible. Also it was stated that a deminer would have an easier job of locating targets from 3D volumes in its entirety using a single image. The key relevant prior work in this area is detailed because it is important to report on this and contrast those techniques with the 3D SIMCA technique. The development of the 3D SIMCA algorithm is conducted and then the experimental data source for landmine data is detailed. Then the chapter uses the landmine data obtained from the Indian researchers at the Indian Institute of Technology and using the SIMCA 3D technique produces the 3D reconstructions of the targets based on optimised threshold levels. The chapter goes on further to report the results and to compare the results obtained by the SIMCA 3D technique with the Scheers Migration by deconvolution technique. Appendix B then uses the car park data to process the GPR data using the SIMCA 3D technique and to locate the foundations in demolished buildings. The chapter also considers the advantages of using an image as opposed to an audible signal and the reasons why validation of the SIMCA algorithm was carried out using human users rather than an automated testing mechanism. Furthermore recommendations for a system to be used in a landmine scenario and non landmine case are made.*

### **4.1 Introduction**

As stated previously the algorithm called the *SIMCA* is a technique based on an volume correlation between the trace that would be returned by an ideal point reflector in the soil conditions at the site and the actual trace.

The trace which would be returned by a target under these conditions are then used to form a correlation kernel using a GPR simulator. The equivalent 3D kernel is formed by rotating the 2D kernel along the polar co-ordinates, whilst the 3D data is formed by the stacking 2D slices. The *SIMCA* algorithm carries out correlation between the intersecting parts of the kernel and the data using the Pearson's correlation coefficient, resulting in a correlated image which is brightest at points most similar to the canonical target. The algorithm then uses the *ParaView* software to create

isosurfaces of the slices raised to an odd power  $>2$  to enhance the target/background separation.

This chapter also compares the *SIMCA* algorithm to another technique that uses migration by deconvolution. The volumetric errors of the targets for the two methods at their respective optimised threshold levels indicate that the *SIMCA* method is able to produce more accurate reconstructions of the targets in terms of volume. Also the *SIMCA* method produces lower error rates for estimating the burial depth of targets and is computationally less intensive when compared to the method that uses migration by deconvolution. To validate the algorithm an objective validation process which compares the actual target volume to the corresponding volume at that threshold using the *ParaView* software is used.

The literature contains a lot of papers in this area and also on the development of robust landmine detection solutions ((MacDonald and Lockwood, 2003); (Gader et al., 2001b); (Collins et al., 1999); (Carin et al., 1999)) and different signal processing techniques in the area of landmine detection are provided by (Gunatilaka and Baertlein (2000); Brooks (2000); van der Merwe and Gupta (2000); Fritze (1995); Robinson and Treitel (1980a)). GPR is a non-destructive geophysical technique in which short pulses of electromagnetic energy are sent into the ground and the reflections from buried targets are recorded. Accordingly, an image of the sub-surface can be formed as the radar is moved across the ground. A large number of these landmines contain little to no metal and as a result, GPR's are one of the current technologies receiving attention as an alternative or adjunct to the metal detector. The chosen image analysis method should be capable of reducing false alarms, but an accurate image relies on having sufficient spatial resolution in the received signal. The wavelengths that propagate in the soil are such that the target dimension is often sub-wavelength. An anti personnel mine can have a diameter as small as 2cm whereas many types of soils have very high attenuation at frequencies above 450 MHz. Daniels (2004) has written a definitive text on GPR theory, methods and applications.

GPR terminology describes data in terms of A scans, B scans and C scans. An A scan is a one dimensional array of returned energy readings indexed by time. A B scan is a two dimensional array indexed by spatial distance in the  $x$  direction and time in the  $y$  direction, formed by abutting successive A scans taken from different spatial positions as column vectors. A C scan is formed by abutting successive B scans to form a 3 dimensional array of readings. Figure 4.1 shows the terminology used above along with the naming conventions of the axes.

A single GPR B scan is typically hard to interpret being heavily cluttered by artifacts produced by the imaging modality. A GPR B scan contains artifacts because of interference caused by interactions between the ground and the antenna, soil reflections, major antenna effects from the GPR signal and clutter (cross talk, initial ground reflection and antenna ringing). Figure 4.2 shows such a B scan after removal of clutter, which partially or totally hide or distort the response of the landmine. GPR signal processing methods are given in Zoubir et al. (2002) and Carevic (1999b).

There is difficulty in interpreting 2D reflections from B scans and also in determining the dimensions of the target directly from them such as in Figure 4.2. However a deminer would find it much easier to interpret 3D isosurfaces such as those in Figures 4.10 and 4.17 and to find the dimensions of the target/s.

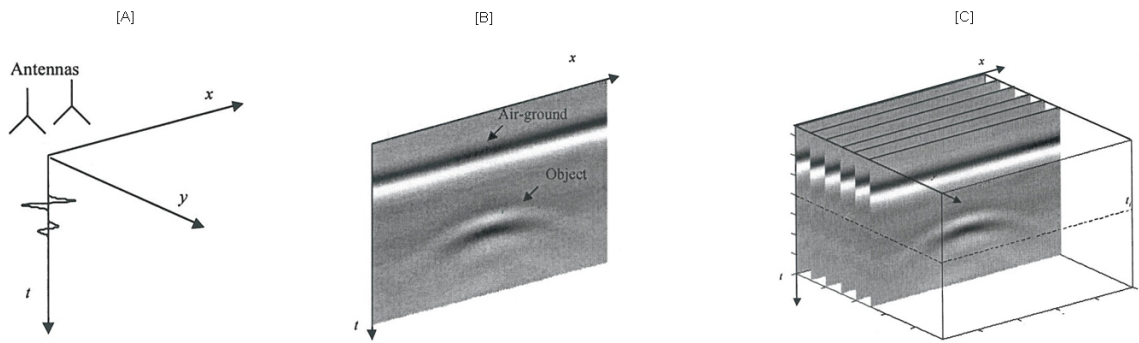


Figure 4.1: Examples of [A]: A scan; [B]: B scan; [C]: C scan. Please note in the figure that the  $t$ -axis in the C scan is also referred to as the  $z$ -axis.

Images adapted from Scheers (2001)

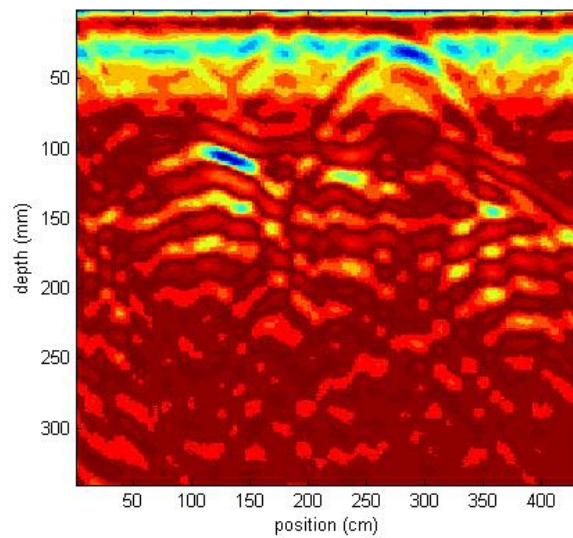


Figure 4.2: Actual B scan slice from the GPR after removal of various clutter such as cross talk, initial ground reflection and antenna ringing.

Further reasons for using a 3D approach are that such volumetric displays enable the deminer to visualize the data volume in its entirety using a single image. Also whilst objects buried at a single depth are easily seen using horizontal slices, objects that span multiple depths are difficult to interpret using such depth slices. Many depth slices are required for full reconstruction of the geometry of targets whose principal axes are set at an inclined angle to the direction of the scan. These tilted objects are best displayed using volumetric displays so that the object in its entirety is visualised using a single display.

The presence of an object in a GPR image is depicted by a hyperbolic shape as depicted by Figure 4.3 and the reason for this is given in the next statement. If the buried object size and the wavelength of the radar are comparable then we can consider the buried object as a scattering point (Arbel and Felsen, 1963). Let us consider an object buried in a non-heterogeneous medium on a

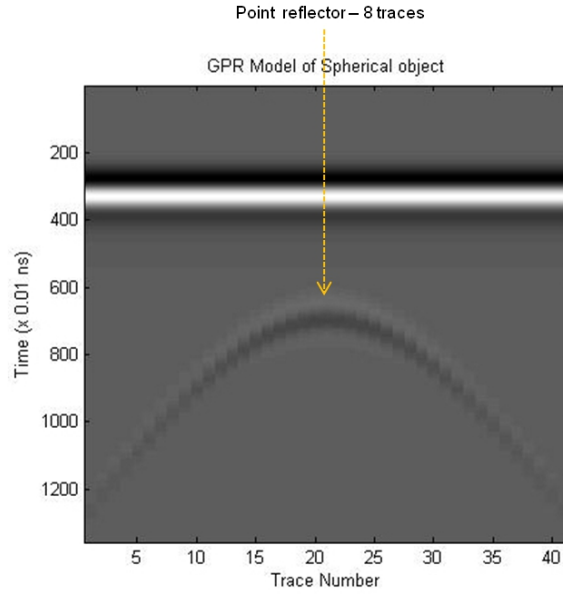


Figure 4.3: Simulation of point reflector using a 0.025m radius sphere buried at a depth corresponding to the burial depth of the target in the sandbox. It is to be noted that this simulation is based on data collected in a laboratory condition where a flat surface exists, the soil is homogeneous and a spherical reflector response can be used. Once the algorithm worked in test conditions it can be tuned to work in actual soil conditions using a realistic simulation.

plane perpendicular to the direction of the motion of the transmitter/receiver (Figure 4.4). Then it can be seen from the figure, the depth to the top of the object  $D_1$  is given by (adapted from Idi and Kamarudin (2012)):

$$D_2 = \frac{vt_2}{2} \quad (4.1.1)$$

where  $v$  is the velocity of propagation and  $t$  is its two-way travel time at that position. Likewise the apparent depth  $D_1$  when the antenna is at  $R_1$  is:

$$D_1 = \frac{vt}{2} \quad (4.1.2)$$

Now using *Pythagoras' Theorem* where  $R_1$ , and  $R_2$  are the horizontal positions in Figure 4.4:

$$(D_1 + r)^2 = (R_2 - R_1)^2 + (D_2 + r)^2 \quad (4.1.3)$$

Substituting Equation 4.1.1 and Equation 4.1.2 in Equation 4.1.3 yields:

$$\left( \frac{t + \frac{2r}{v}}{t_2 + \frac{2r}{v}} \right)^2 - \left( \frac{R - R_2}{\frac{vt_2}{2} + r} \right)^2 = 1 \quad (4.1.4)$$

Now Equation 4.1.4 defines a hyperbola. The next section outlines the key relevant prior work in the area and compares this with the 3D SIMCA technique as this is key to the development of the SIMCA 3D technique.

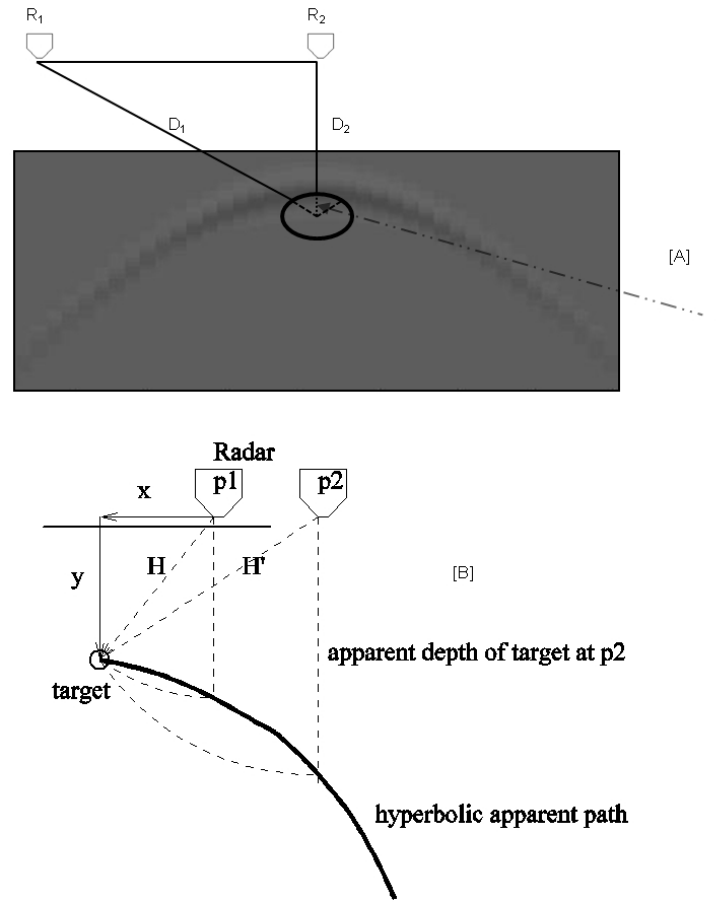


Figure 4.4: Clockwise from left: [A]: Hyperbolic signature spread due to a buried object; [B]: Hyperbolic formation as the radar moves from position  $p1$  to position  $p2$ .

## 4.2 Key relevant prior work

Since most GPRs have broad beamwidth antennas, it would be necessary to focus the energy of the reflections in order to obtain a sharper image. This is necessary because the beamwidth of the antenna is quite wide relative to the target (Scheers et al., 2001). Migration is a technique that reconstructs from the data recorded at the surface, the reflecting structures in the sub-surface; hence a reconstruction of an accurate surface map is obtained to reconstruct subsurface structures. A comprehensive review of the various migration techniques is presented in (Gazdag and Sguazzero (1978); Berkhout (1982); Berkhout (1981); Lee et al. (1987); Yilmaz (2001); Song and Liu (2005); Gazdag (2005); Stolt (1978b); Schneider (1978); Leuschen and Plumb (2000); Scheers et al. (2001)).

Wave equation migration can be used when migrating complex velocity structures and they migrate data by propagating waves backward in time (Radzevicius et al., 2005). If we assume that the source and receiver are co-localised in space then a wave propagated halfway in time will be located at the reflector, from which the reconstruction of the target geometry is correct (Berkhout, 1981). However, for GPR applications the approximation of the constituents of the wave equation is computationally intensive. Alternative techniques such as the *SIMCA* method proposed in Section

4.4 are available.

Gazdag (2005) uses phase shift migration which is based on a transformation from the radar frequency domain  $\omega$  to the wavenumber domain  $\kappa$  by Fourier transforming the original wave equation. The transmitter and receiver positions are lowered by means of a phase shift, or a rotation of the phase angle of the Fourier coefficient. Using a 3D Fourier transform the entire 3D data is transformed into the frequency and wavenumber domains. Thereafter each of the depth slices are imaged by the application of the appropriate phase-shift to each of the time slices, summing over the frequencies and 2D inverse Fourier transforming along the two wavenumber directions. The phase shifting, summation and 2D inverse transforms obtained from the previous steps are performed again for each of the depth slices in the 3D array (Radzevicius et al., 2005). Compared to the *SIMCA* method presented in Section 4.4, the wave-equation method and the above method are computationally intensive because the imaging of each of the depth slices requires phase shifting and summations over all frequencies.

Stolt migration performs a 3D forward and inverse Fourier transform of the 3D data matrix to its entirety (Stolt, 1978a). The diffraction summation method involves the summing of energy values along all possible diffraction curves and the positioning of the summed energy at the peak of the curves and this will migrate target geometries (Radzevicius et al., 2005).

Kirchhoff migration is similar to diffraction summation but with phase corrections and added amplitude which is applied to ensure the summation is similar to the wave equation method (Schneider, 1978).

Scheers et al. (2001) state that 'almost none of these methods however include system aspects of the GPR such as the waveform of the excitation source, the impulse response of the antennas, the antenna patterns and do not take into account the characteristics of the ground'. Furthermore, the above migration methods assume that the ground is loss-less and that it does not have dispersion. This cannot be strictly true and furthermore it can be concluded that an imaging method that does take into consideration the characteristics of the system and the characteristics of the ground would produce better results.

Scheers et al present a migration method called migration by deconvolution. They use the time domain model of the GPR and calculate by forward modelling a synthetic point spread function of a UWB GPR. They then use this calculated point spread function and deconvolve it from the recorded data. Therefore the method firstly calculates the point spread function for a given soil type and burial depth. The burial depth is chosen to be the most likely depth for an object and they calculate the point spread function only once. Then a 3D Fourier transform of the recorded data is calculated and the data is filtered by the Wiener filter. Finally, performing the inverse Fourier transform of the filtered data produces the final migrated image.

The proposed *SIMCA* algorithm like Scheers et al's method includes the system aspects of the GPR such as the waveform of the excitation source, the impulse response of the antennas, the antenna patterns and the characteristics of the ground by using different soil properties. Using the corresponding radar properties along with the soil conditions is an important factor in obtaining a good re-construction of the mine target.

Comparison of the accuracy of the *SIMCA* system with Scheers' algorithm the best alternative system reported in the open literature has been performed and is shown in Section 4.9 of this chapter. Scheers et al in their work only produce 3D reconstructions of single objects such as a PMN mine, a brick and a barbed wire. But experiments conducted by the author show that it is necessary to test the algorithm on multiple buried objects.

The *SIMCA* algorithm commences by carrying out GPR simulation using a GPR simulator. It then takes the raw B scans as the radar is scanned over the ground and removes various clutter such as cross talk, initial ground reflection and antenna ringing. The removal of the clutter is carried out by firstly calculating the mean vector of a number of scans and then subtracts this from each of the scans. Also a windowed average subtraction technique was used. The mentioned techniques are often referred to as complex average subtraction and moving average subtraction methods respectively. *SIMCA* uses the clutter removal technique developed by Sengodan and Javadi (2005) to remove such clutter. The study used a shifting mechanism so that the resulting reflection from the air ground interface can be eliminated from all A scans in one single processing pass. The clutter detected by the GPR includes many components: cross talk from transmitter to receiver antenna, initial ground reflection and background resulting from scatterers within the soil. The antenna cross talk and noise can be reduced by proper system design. The C scan is formed by stacking up of the individual clutter removed B scans.

The clutter removal technique reduces clutter by calculating averaged values over an ensemble of A scans and subtracting this from each of the A scans (Daniels, 2004) (Equation adapted from Daniels (2004)):

$$a'_{n,a}(t) = a_{n,a}(t) - \frac{1}{Na} \sum_{a=1}^{Na} a_{n,a}(t) \quad (4.2.1)$$

where  $n = 1$  to  $N$  and  $N$  is the number of samples;  $a = 1$  to  $Na$  and  $Na$  is the number of A scan waveforms.  $a_{n,a}(t)$  is the unprocessed A scan and  $a'_{n,a}(t)$  is the processed A scan.

The *SIMCA* technique then carries out area correlation between the trace obtained by the GPR simulation and the clutter removed trace.

Some of the key novelty factors of the *SIMCA* technique in comparison to Scheers et al. (2001) technique and other existing techniques are:

- None of the techniques available report on using correlation based on template matching the kernel developed using actual GPR simulations against the clutter removed GPR data but use convolution. A study by Sengodan et al. (2012) revealed correlation is better because it compensates for differences in gain and black level between the kernel and the area of the image being matched. Furthermore by using a kernel developed by using a point target buried in the same soil conditions using a GPR simulator, the complete GPR signature (antenna pattern) is obtained rather than part of the signature and this is really important to obtain accurate reconstructions of the targets.
- *SIMCA* considers the fact that often the spatial separation between A scans that make up a B scan is typically smaller than, and not always an integer multiple of, the spatial separation

between the B scans that make up a C scan.

- The *SIMCA* algorithm is computationally less intensive than the method proposed by Scheers et al because *SIMCA* algorithm only correlates between the intersecting parts of the kernel and the data; thus reducing the data by considering only the relevant sections. Therefore the *SIMCA* algorithm runs much faster than Scheers et al's method.
- Since the *SIMCA* system uses the rendering mechanisms available in the open-source *ParaView* software a flexible 3D isosurface of the targets, along with a flexible approach of rotating the isosurfaces and obtaining slices along a number of planes is produced. *ParaView* is open-source software that runs on multiple platforms and performs the analysis and visualization of scientific data which can be either 2D or 3D (Squillacote, 2008)<sup>1</sup>.
- This *SIMCA* 3D technique is able to obtain an accurate volume of the rendered mine as shown in the results and validation section of this chapter; existing techniques do not calculate the volume. Furthermore the estimation of the depth by the *SIMCA* algorithm is more accurate than that produced by the Scheers' method.
- Finally, although raising the brightness to an odd power  $>2$  to enhance the target/background separation is not new in image processing, none of the GPR techniques make use of this concept.

Having detailed the key relevant work in the area relevant to the 3D *SIMCA* technique, the next section details the simulation method used in order to develop the 3D kernels.

### 4.3 Simulation carried out to develop kernels

The trace that would be generated by the ideal point reflector is obtained using *GprMAX2D v1.5* developed by Giannopoulos (2005) and the simulation solves Maxwell's equations using the finite-difference-time-domain method. The simulation takes as input a data file describing soil conditions, domain size, discretization step, time window, details of the buried object, details of radar and the location of the transmitter and receiver.

The *GPRMAX 2D* program was run in order to generate a kernel. The equivalent 3D kernel is formed by rotating the 2D kernel along the polar co-ordinates. The reason why the 3D kernel is created in such a way rather than use the *GPRMAX 3D* program to generate a 3D kernel is because for another study using a 2D case a 2D kernel was generated using *GPRMAX 2D* (Chapter 3) and rather than re-run *GPRMAX 3D* and generate a 3D kernel the 2D kernel was used.

A kernel is an array of coefficients used in filtering. The kernel is set prior to correlation so as to enhance a particular feature in an image.

When running simulations, a sphere of radius 0.025m buried in the same soil conditions used in the sandbox in the laboratory was used. Care was taken to ensure the use of a centralised kernel which was large and included a large portion of the hyperbola.

<sup>1</sup><http://www.paraview.org/>



Figure 4.3 shows such a simulation of a point reflector and it can be argued that what is seen in Figure 4.2 is a sum of multiple point reflectors superimposed. This concept is also commonly used in the field of optics (Lipson et al., 1998). The GPR trace in Figure 4.2 could be obtained by the superposition of shifted and scaled point spread functions.

Such modelling has proven extremely beneficial to this study because apart from allowing the derivation of the kernel, it allowed the running of parametric studies on specific aspects of a problem which could not be adequately simulated over the full range of parameters using an experimental setup. The combination of experimental and numerical results is useful as was shown and stated in Chapter 3 of this thesis where the 2D *SIMCA* algorithm was presented. The next section then goes on to develop the *SIMCA 3D* technique.

#### 4.4 Description of *SIMCA 3D* Algorithm

The flowchart of the *SIMCA 3D* algorithm is as shown in Figure 4.5. The basic concept used by the *SIMCA* algorithm is outlined by Algorithm 1. A full listing of the *SIMCA* algorithm can also be obtained by going to <https://sites.google.com/site/3dsimcaalgorithm/> or referring to Appendix A of this thesis.

Here are details of the algorithm:

*SIMCA* compares the trace that would be returned by an ideal point reflector in the soil conditions at the site with the actual traces obtained and from this it works back to the collection of objects that might have generated the observed traces. In image processing, area correlation can give sub-pixel accuracy in locating the source of targets [(Siebert and Boguslaw, 2008) Chapter 6, section 6.6 pp. 238].

The second phase of the algorithm involves performing a volume correlation between the 3 D kernel and the C scan data to yield a volumetric correlation potential. This volumetric potential can then be visualised using isosurfaces.

*SIMCA* algorithm uses Pearson's correlation coefficient between the kernel and the returned data as the goodness of fit metric. Pearson's correlation coefficient between two variables is defined as the covariance of the two variables divided by the product of their standard deviations:

$$\rho_{X,Y} = \frac{cov(X,Y)}{\sigma_X \sigma_Y} \quad (4.4.1)$$

The benefit of using correlation when compared to a mean absolute error metric (or convolution) is that correlation compensates for differences in gain and black level between the kernel and the area of the image being matched. The simplest image metric is convolution as used by the Scheers' algorithm (Scheers et al., 2001). The convolution operation can be thought of as simply a point by point inner product operation. For this application domain, convolution has disadvantages and these are going to be now outlined. In the case of the detection of landmines in the subsurface, the highly cluttered environment causes a low contrast hyperbola, but if the shape fits the hyperbola shape of the kernel, one would want this to be shown up as a likely target.

Using a 3D hyperbolic kernel a volumetric convolution may return a low score. The likely

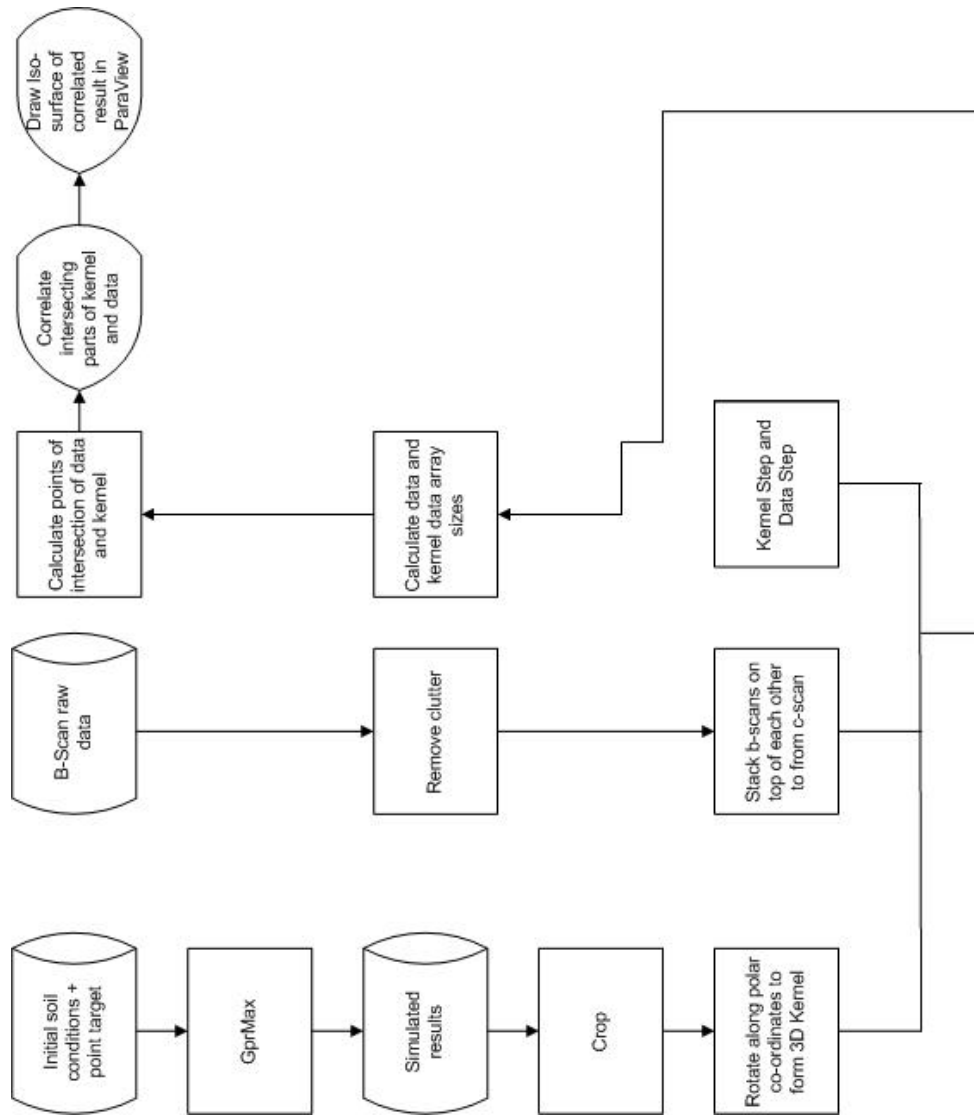


Figure 4.5: The flowchart of the 3D *SIMCA* algorithm. Note in the figure that to improve the performance of the processing in *MATLAB* the B-scans are stacked on top of each other but after processing they are stacked adjacent each other.

reasons for this could be that the hyperbolic shape did not exist in the C scan volumetric data. Another reason may be that as previously stated the echo returning from the target was relatively weak (because of it having poor reflectivity) or the signal was being attenuated by the cluttered environment due to the target burial depth being large. In the B scan the weak reflector will appear as a low contrast hyperbola. *MATLAB* provides the facility to calculate the normalized correlation coefficient by means of the function *corrcoef* (The Mathworks Inc, 2009a, 2009).

A method to compensate for such changes in contrast is to use a normalised inner product or cosine operator. Figure 4.6 gives a 2D vector representation of what in reality is a much higher dimensional problem. The kernel vector is indicated in the figure as being normalised (length=1). Convolution as mentioned previously does an inner product operation. In terms of the figure it is equivalent to projecting down onto the basis vector provided by the kernel. This basically tests to see how much of the length of the kernel is contained within the target vector. There are chances that the reflected signal may be weak or in terms of the figure has a shorter overall length as a vector when compared to the length of the kernel one uses. The cosine metric shown on the right of Figure 4.6 compensated for this and basically projects the target vector as well out onto the unit circle (or hypersphere in the multidimensional case). The operation of an inner product computes the cosine of the angle between the two vectors. Two vectors that point in roughly the same direction but are of different lengths will now be shown as much more similar than they would using the simple inner product.

Correlation used by the *SIMCA* algorithm includes a further normalisation level by modifying the signal zero level in the target and kernel vectors so that both arrays of data have the same mean as that prior to carrying out the normalised inner product. Looking at a raw B scan as in Figure 4.2, the conclusion can be reached that the mean brightness varies with depth and therefore this extra normalisation as in the *SIMCA* algorithm compensated for attenuations with depth.

A further problem the *SIMCA* algorithm encounters is that often the spatial separation between the A scans that make up a B scan is typically smaller than, and not always an integer multiple of, the spatial separation between the B scans that make up a C scan. The 2D kernel produced by the GPR simulator uses the B scan spatial settings and is therefore suitable for carrying out correlation between the kernel and the B scan. When one creates the 3D kernel by rotating the 2D kernel, the spatial separation will not correspond to the spatial separations of the C scans. The reason to why a 2D kernel is rotated along the polar co-ordinates to form a 3D kernel was given in Section 4.3.

As an example, if the spatial separation between A scans was 1 cm, but the successive B scans are 7.5 cm apart. A kernel of size 50x50 which is derived from the simulator would have a spatial width of half a meter along the B scan, and upon rotation, this kernel would have generated a 3D array that corresponds to a cube with a 50cm side. Correlation is accomplished by sweeping the kernel through the C scan space. But since there is a 1 cm spatial scale in the kernel, a 3D array of correlations could be generated which is also on a 1cm grid. This is finer than the separation between the B scans.

Clearly, if this is to be done one must only compute the correlation for those elements of the 3D kernel that actually coincide with slices from the B scans. That is carry out correlation between

the sections of the B scans that intersect the kernel. When, because of non integral spatial steps, a B scan slice does not exactly coincide with a slice through the kernel, linear interpolation is used between the two nearest actual kernel slices before performing the correlation. Figure 4.7 shows this case where the filled circles representing the data points do not coincide with the kernel points indicated by the un-filled circles.

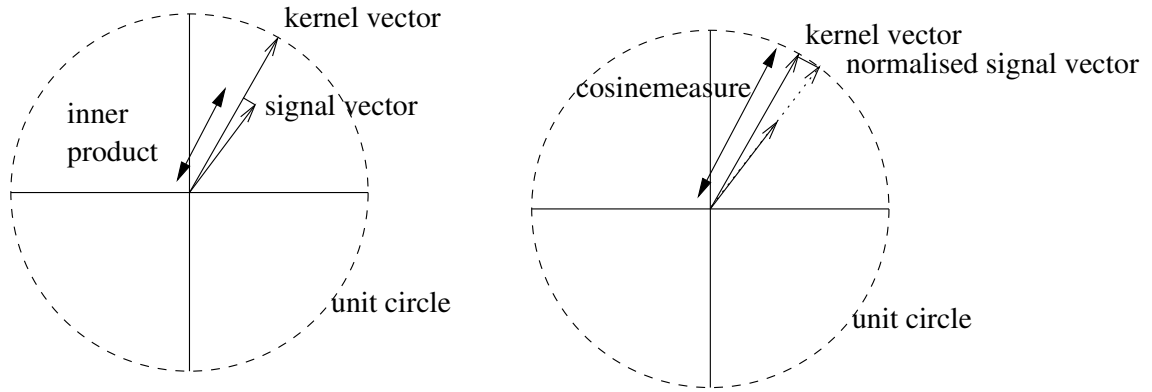


Figure 4.6: Contrast between the inner product and normalised inner product or cosine measures.

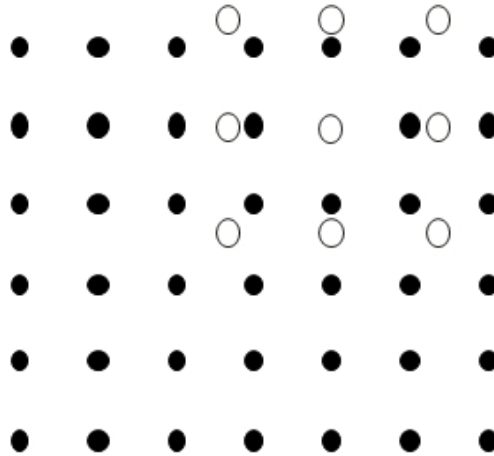


Figure 4.7: A pictorial representation of data and kernel points. The black filled circles are the data points and the unfilled black circles are the kernel points.

In order to carry out this linear interpolation use is made of *MATLABs trilinear interpolation* that is an extension of linear interpolation. It works on a 3D regular grid and is a method of multivariate interpolation. It calculates an approximate value of an intermediate point  $(x,y,z)$  in a local axial rectangular prism in a linear way. The full algorithm of this interpolation is given in Appendix A, Algorithm 6.

As a contrast enhancing phase the correlation array is raised to the power of 3. Raising the 3D correlated data to an odd power greater than 2 enhances the target/background separation. Using *ParaView* software the correlated slices are loaded up and using threshold levels computed in Sec-

tion 4.9, the 3D isosurfaces are created. The isosurfaces created using the *ParaView* software are shown in the results and discussion section of this chapter. The *ParaView* software also allows for the volume of the target at that level of threshold to be calculated.

Having developed the *SIMCA 3D* technique and given details of the technique the next section gives the experimental data source for acquiring the data and the results obtained for the landmine data are detailed.

---

**Algorithm 1** *SIMCA 3D* Algorithm to consider spacing in  $x, y$  and  $z$  directions. The full version of the *SIMCA* algorithm can be found in Appendix A and also by going to the following url: <https://sites.google.com/site/3dsimcaalgorithm/>.

---

```

for all  $x$  do
  for all  $y$  do
    for all  $z$  do
      take the center to be position  $(x, y, z)$ .
      take slices out of B scans centered on position, out to distance of kernel in cm.
      i.e. find the sections of the B scans that intersect the kernel.
      Correlate the intersecting parts with parts of the kernel they intersect with.
      Store result at  $x, y, z$  in output.
    end for
  end for
end for

```

---

## 4.5 Experimental data source used in the laboratory to obtain the landmine data used to test the *SIMCA 3D* algorithm

The GPR data used for this experiment was obtained from data provided by Indian researchers at the Indian Institute of Technology. The GPR they used for data acquisition was developed by ERA Technology, UK and is called the SPRScan commercial system<sup>2</sup>.

The researchers claim the reason for using the SPRScan GPR was because after an extensive literature survey, they found the SPRScan system to be more versatile when used as a robotic scanner. SPRScan is modular, has a lightweight design and it can be easily set up and transported by one person. This modular construction increases flexibility and allows the optimization of the system configuration for different measurement scenarios. This combined with the fact that the SPRScan can be powered by batteries worn on a belt around the operator's waist means that surveying can be done in remote or confined areas and this makes the SPRScan more versatile than existing systems. Having chosen the system, the researchers sought advice from the supplier of the SPRScan in India and the technical representative for the SPRScan system who recommended the following experimental setup as this has been used successfully by researchers in Europe and America.

The SPRScan GPR has been used by researchers at the Demining Technology Centre of EPFL, Swiss Federal Institute of Technology. The SPRScan radar system consists of 3 main parts, the

---

<sup>2</sup><http://www.usradar.com/index.html>

controller (which in effect is a ruggedized PC personal computer), an antenna, and the transmitter (TX)/receiver (RX) head electronics unit which transmits the information from the antenna to the controller. This system can acquire up to 195 A scans, of 512 points each, with 16 bit resolution and a maximum equivalent sampling rate of 40 GHz.

As per manufacturer's recommendation, an operational time varying gain of 0.4 db/ns is applied to partially compensate for the soil attenuation. The acquired data has to be buffered in two 'First in First out' caches so as to be able to store one A scan each. The data is displayed in real time as a scrolling B scan on the screen of a PC; again as recommended by the manufacturer. A prototype resistively loaded parallel dipole antenna has been used for the data acquisition.

The pulse generator has a pulse width of 200ps and a repetition rate of 1MHz and the pulse generator is integrated into the antenna case to minimize losses and transmission reflections. The antenna's nominal bandwidth is 800 MHz to 2.5 GHz, hence leading to an expected resolution of less than 5cm. The Ultra wideband pulse generator is the most critical part in a GPR system and usually to obtain higher resolution bandwidth, more phase shifter sections can be used and the transmission line lengths can be made shorter. For GPR systems, the pulse generator design plays a vital role in the performance of the system. It substantially determines the quality of the raw data obtained from the GPR.

The experimental setup consisted of a large sandbox which is approximately 9.9m x 7.8m, and the acquisition of the B scans was repeated for varying soil conditions. The stored mine file consisted of B scans taken at 2.0cm intervals and each B scan consisted of 102 A scans. The A scans are taken every 1.0cm and the effective sampling rate is 40 GHz. Various mines developed by the Colombian guerrillas, various landmines and interfering objects such as tree roots and metal plates which can all cause serious false alarms were included to see how the algorithm performed. The GPR head was mounted on a platform and used a robotic head to acquire data (IIT email, 2012). The details about the landmines used are detailed in Chapter 4, Section 4.6. The mines were buried in a wet sandy soil, dry sandy soil and clayey soil so as to represent the extremes of soil that are encountered in the field. The next section details the results produced using the *SIMCA 3D* algorithm.

## **Part II**

**Results produced by the *SIMCA 3D* algorithm using landmine data obtained from GPR experiments at the Indian Institute of Technology.**

This section used the GPR data acquired by Indian researchers from laboratory controlled experiments conducted at the Indian Institute of Technology. The details of the experimental data source were already outlined.

The main challenge of GPR based landmine detection is to have an accurate image analysis method. The detection problem can be solved by the system level analysis of the issues involved with the recognition of landmines using image reconstruction.

## 4.6 Results and Discussion

It is very important to note that for all the results presented below the reconstruction of volumes of real targets using the *SIMCA 3D* algorithm are presented after scanning by a GPR.

Most APMs are small, and are about 60 to 120 mm in diameter and 40 to 70 mm thick and are usually made up of plastic. The triggering mechanism in most APMs has little or no metal. These mines are similar in size to a hockey puck. Examples of typical APMs used in this study are given before the 3D reconstructions of targets. The small size and the fact that many have little or no metal make them really hard to detect using less sophisticated algorithms.

Unlike the standard GPR applications, the depth of burial of these landmines is less than a metre and the data must be reduced to a direct indication in real time. Furthermore, the radar head cannot be used in contact with the ground for safety reasons. All these above requirements cause a lot of clutter problems that are inherent in the near surface zone and need to be tackled in order for success in mine detection.

In order to discuss the results obtained using the *SIMCA 3D* algorithm 3D reconstructions of volumes of real targets using the *SIMCA* algorithm and Scheers et al's algorithm after scanning by a GPR using their respective optimised threshold values for different soil conditions are shown. The results section is divided into the different test set-ups used in the laboratory to acquire the data using different soils. As noted various metallic mines, plastic mines and interfering objects such as tree roots, metal plates and stones were included in the sandbox. A stone was chosen because it could be difficult to differentiate it from a mine with a GPR.

The method used to obtain the optimised threshold values are outlined in the validation section. The diagrams also show the 3D isosurface along with the name of the landmine or objects they represent along with their position in the  $x$ -direction in centimetres ( $x$  is the direction along B scan), position in the  $y$ -direction in centimetres ( $y$  is direction between B scans) and their depth in mm. It is to be noted that the values mentioned above are the ground truth values based on the positions the original landmines were laid out in the sand box.

Also included in the results section are constructional and material characteristics of the different targets used in each of the test setups. Figure 4.9 for example gives the details about the plastic MAUS mine, metallic M26 mine and the pistol. Then the volumetric errors are calculated for the *SIMCA 3D* and Scheers' algorithms when compared to the ground truth. Tables that give the volumetric errors also give the time taken by each of the two methods to run. It can be noted from the tables that the slowest time taken by the *SIMCA* algorithm is 1.0 seconds whereas the slowest



time by the Scheers' method is 2.4 seconds. Therefore the *SIMCA* algorithm runs 2.4 times faster than the Scheers method. This is particularly pleasing because of the limited processing resources available in GPR equipment. Because in landmine clearance the burial depth of the target is also important, calculated results of the percentage errors in terms of the burial depth for both methods are a requirement. It is to be noted that the ground truth is based on the actual burial depth of the target in the sandbox during the laboratory experiments and the burial depth for each of the two methods is calculated using the *ParaView* software. In terms of the volumes the ground truth is calculated from the dimensions of the actual target. Section 4.9 also discusses the error rates for the volumes and does a comparison for each of the methods.

Also included in the results are vertical slices taken through the isosurfaces Figure 4.8 shows the position and direction through which these vertical slices are taken.

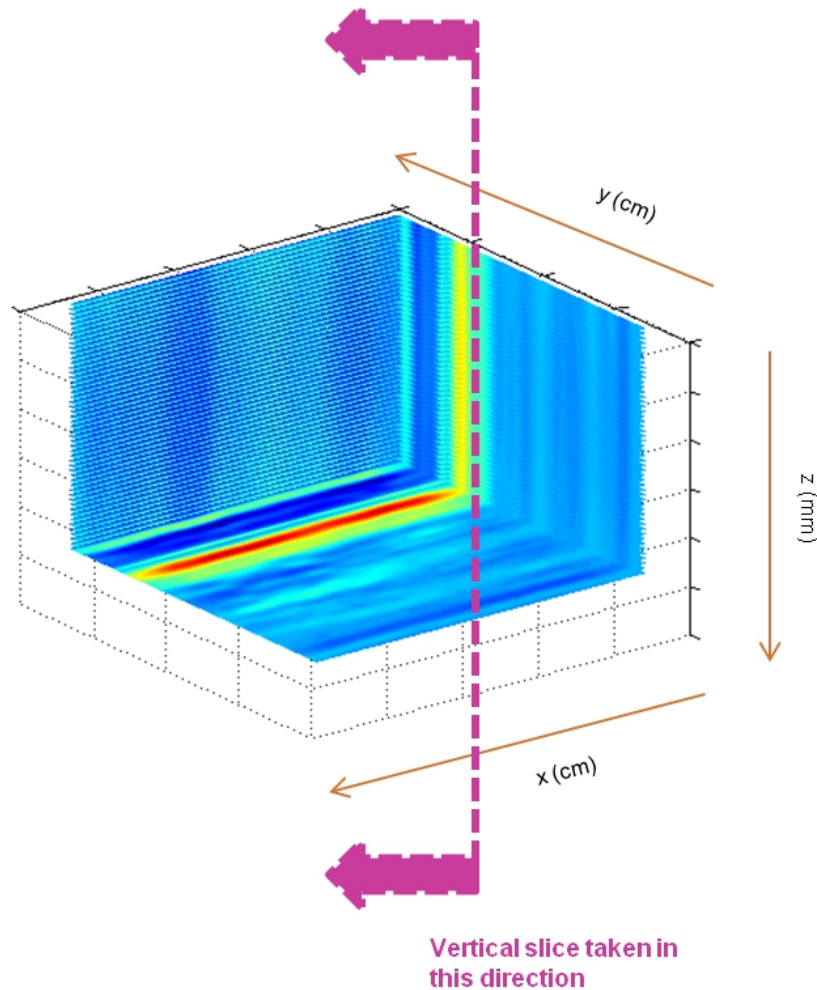


Figure 4.8: Diagram showing position and direction of the vertical cross sectional slices shown in this chapter.

### 4.6.1 Setup 1 - Wet Sandy Soil

#### 4.6.1.1 A plastic mine, a metallic mine and a wooden handled Browning pistol

In this case, a plastic MAUS antipersonnel mine, a metallic M26 antipersonnel mine and a wooden handled pistol are buried in a wet sandy soil. The layers of material inside the plastic mine produce interfering echoes as can be seen in 4.10[C] which shows the vertical slice taken through the isosurface. An important factor to note is that the researchers for safety reasons have included explosive stimulants such as beesWax, paraffin or nylon and these match the dielectric properties of explosives commonly used in APMs such as TNT and Component B.

The detailed spatial structure of the MAUS mine is much smaller than the GPR resolution and hence this factor causes difficulty in detecting the plastic landmine. Ideally the GPR bandwidth would be increased to the point that the geometrical shape of the target could be clearly imaged and therefore provide a means of target discrimination. But this criteria is difficult to achieve and one has to accept that GPR resolution is limited by attenuation in the operating environments.

The construction of the Browning pistol is shown in Figure 4.9. The researchers had removed the bullets from the handle again for safety reasons but still the *SIMCA* algorithm is able to successfully render the wooden handled pistol and produces an accurate reconstruction of the wooden handle in comparison to the Scheers' algorithm as can be seen from the isosurface in Figure 4.10. Therefore the Scheers' algorithm is only able to reconstruct the metallic spring of the magazine. For the plastic MAUS mine, the reconstruction produced by the Scheers algorithm is really alarming and the same figure shows how accurately *SIMCA* deals with the rendering.

The electromagnetic response of any object can be found by natural responses at frequencies and their values are determined by the shape of the target and its internal structure and is invariant with the target orientation relative to the probing wave (Baum, 1993). The resonances of APMs with a metal case such as the M26 mine are highly reduced and difficult to detect. Although the internal structure of the M26 mine is complex the *SIMCA* algorithm is able to produce an accurate rendering of the mine.

Table 4.1 gives the error rates for the volumes of the targets for each of the *SIMCA* and Scheers' et al method. Section 4.9 of this chapter also discusses the error rates for the volumes and does a comparison for each of the methods. Furthermore, since in landmine detection the estimation of the depth is of concern; the same table gives the actual burial depths, along with the depths found using the *ParaView* software for each of the two methods and the Table also outlines the error rates for the burial depths.

It is noticed from Table 4.1 that the *SIMCA* algorithm runs in half the time compared to the Scheers' method for the wet sandy soil condition.

Measurements and modelling carried out by other researchers and reported by Daniels (2006) indicate that under conditions of negligible attenuation losses, such as in the case of the M26 mine at a depth of only 4.9cm, metal landmine to clutter ratios drop on burial by 10 dB. Whilst in the case of plastic landmines such as the MAUS mine the cross section of the mine drops by a larger factor. This is because of reduced dielectric contrast between the mine material and the surrounding soil.

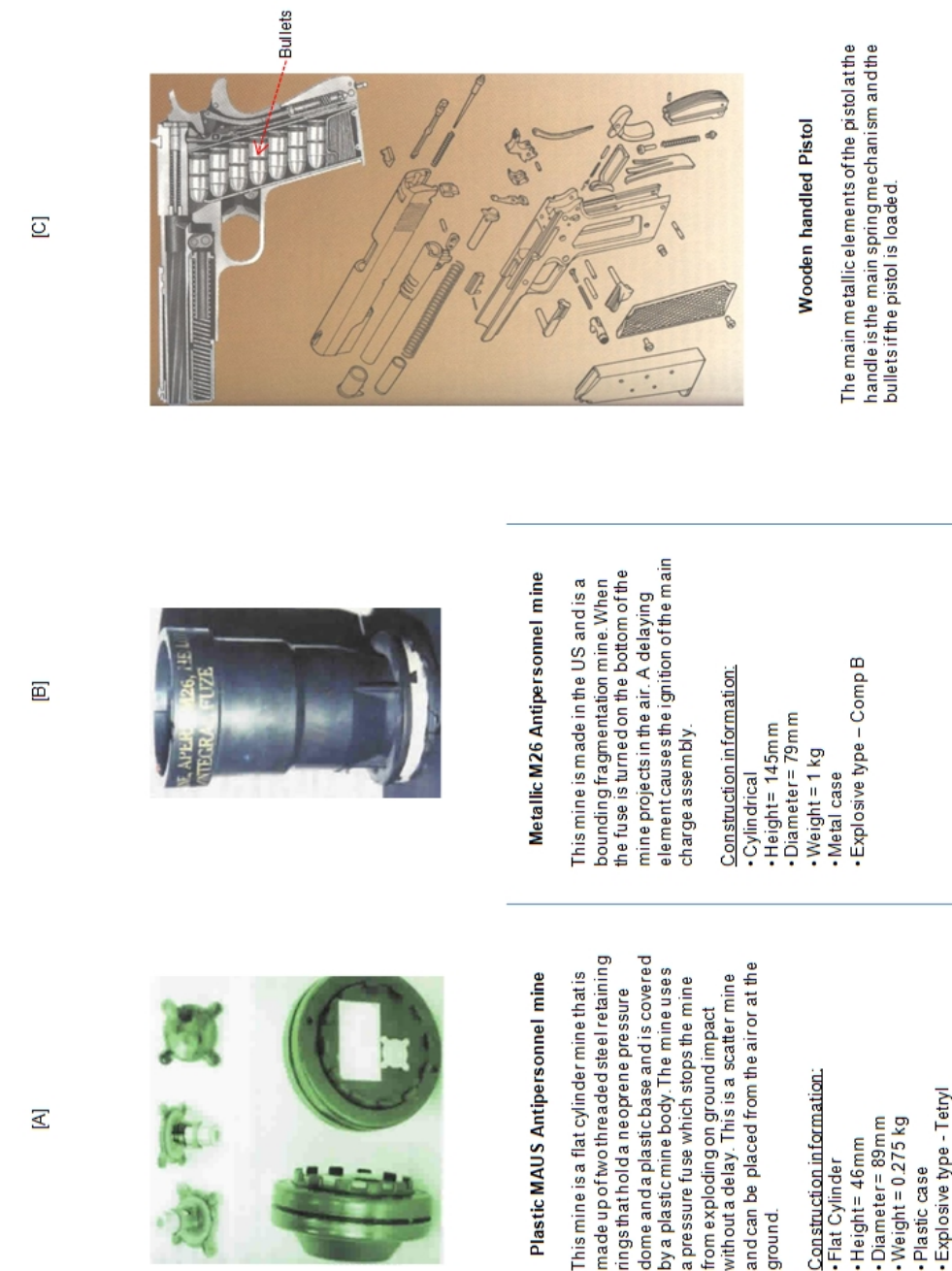


Figure 4.9: Details of the targets buried in Figure 4.10.  
(Cameo Landmine clearance)

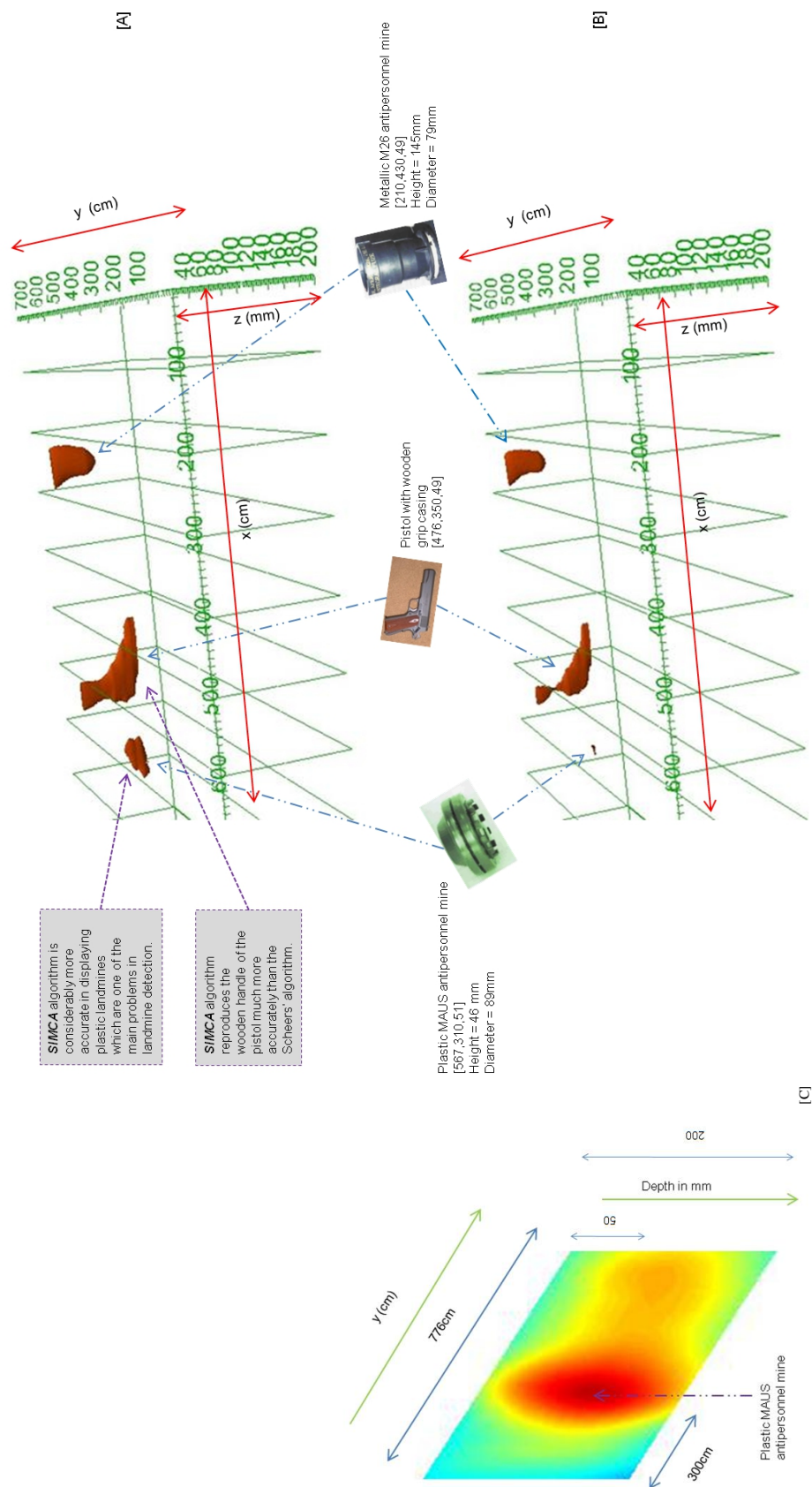


Figure 4.10: Reconstruction of volumes of real targets in a wet sandy soil using: [A]: *SIMCA* system after scanning by a GPR at optimised threshold = 230; [B]: Scheers et al algorithm after scanning by a GPR at optimised threshold=252. Note the clearer rendering of non metal objects and parts using *SIMCA* algorithm; [C]: Vertical cross-sectional slice showing the plastic MAUS mine.

	Burial depth of plastic MAUS mine (cm)	Burial depth of Pistol (cm)	Burial depth of metallic M26 mine (cm)
Ground truth	5.1	4.9	4.9
SIMCA	5.0	4.7	4.8
Scheers	4.8	4.5	4.6
Error in SIMCA	2.0%	4.1%	2.0%
Error in Scheers	5.9%	8.2%	6.1%

[A]

	Volume of plastic MAUS mine (cm) <sup>3</sup>	Volume of Pistol (cm) <sup>3</sup>	Volume of metallic M26 mine (cm) <sup>3</sup>	Processing time (s)
Ground truth	286	500	711	-
SIMCA	280	491	698	0.9
Scheers	57	380	590	1.8
Error in SIMCA	2.1%	1.8%	1.8%	-
Error in Scheers	80.1%	24.0%	17.0%	-

[B]



Table 4.1: [A]: Actual burial depth, depth obtained from the *SIMCA* method, depth obtained from the Scheers’s method for each of the targets in centimetres for Figure 4.10. The table also gives the percentage errors for both the *SIMCA* and Scheers algorithms; [B]: Actual Volume, Volume of reconstructed target for *SIMCA* system, Volume of reconstructed target for Scheers algorithm, and processing time (CPU time) for Figure 4.10. The volumes are in cubic centimetres and the processing time is in seconds.

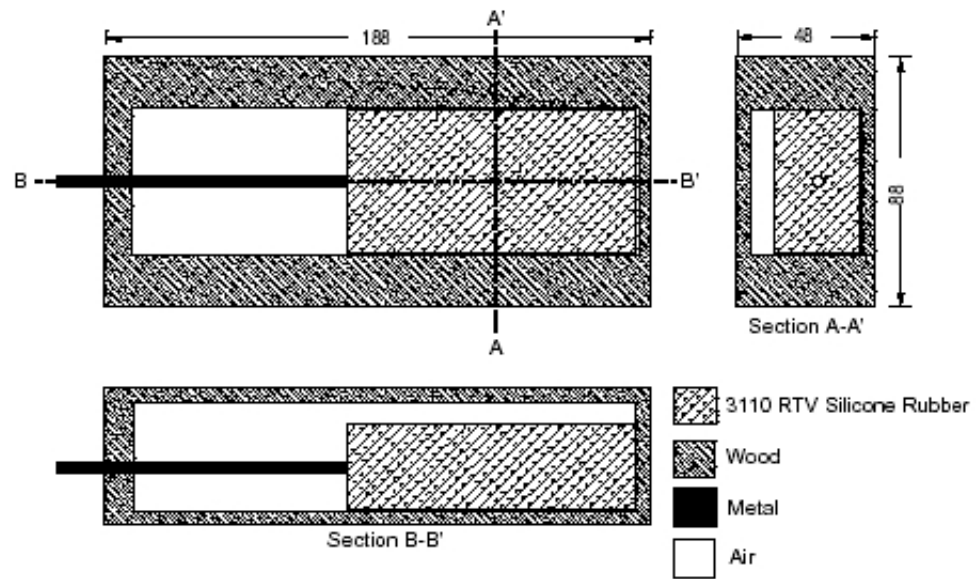


Figure 4.11: The internal structure of the PMD-6 wooden cased mine.  
(MacDonald and Lockwood, 2003)

#### 4.6.1.2 A wooden cased mine, a metallic mine, steel cased mine and metal plate buried in wet sandy soil

In this subsurface, a metallic M26 mine, a wooden cased PMD-6 mine, a steel-cased PROM-1 mine and a metallic plate is buried in a wet sandy soil. Like the pistol in the previous section, the PMD-6 is a wooden cased mine and again the *SIMCA* algorithm is extremely successful in rendering the mine and this is evident in Figure 4.13. The only metallic part of the PMD-6 mine is the metal fuse that may contribute to the GPR response. Although for the metallic mines the Scheers' algorithm is able to render the mines better than the wooden mine, it still falls below the rendering capability of the *SIMCA* algorithm. Figure 4.11 shows the metallic parts of the PMD-6 wooden cased mine.

Soil character is controlled by the water content. Whilst changes in soil composition have a small impact, the major factor is the variation in water content. The water content controls the velocity, the attenuation as well as the impedance contrast with the target. Even small amounts of water such as in this setup cause substantial attenuation.

The metal plate is included to compare their response to an APM target and see if they degrade the response of the APMs but as can be seen in the 3D reconstructions this is not the case.

Another important thing to note here is that most APMs are laid within 10cm of the surface to allow for the triggering upon a pressure being applied on them. In such near surface regions the soil surface exhibits strong radar reflections with non-stationary statistics (Brooks, 2000). However, since the pre-processing step involved the removal of clutter as discussed in Section 4.4 of this chapter; the *SIMCA* algorithm successfully reconstructs the isosurface of near surface targets.

Furthermore, as shown in Figure 4.14 the *SIMCA* algorithm is able to reconstruct the trip wires of the wooden cased PMD-6 mine. Researchers who emplaced the landmines stated also that the

metallic M26 mine was buried at an oblique angle. This obliqueness is also clearly shown in the isosurface.

The GPR vector signal character is also a factor that needs to be taken into consideration. The polarization of the excitation and detected signals fluctuates significantly with the geometry and construction of APMs (Redman et al., 2003). The presence of metal leads to very polarization dependent responses. Also the metal fuse often forms long linear rod shapes and couples maximally with the electric fields aligned parallel to a long axis (Song et al., 2006).

#### **4.6.1.3 A metallic mine, 2 plastic mines and a metallic plate.**

Here the researchers had buried a metallic M26 mine, 2 plastic mines and a metallic plate. According to the researchers the burial of two plastic mines in close proximity to a metal plate causes a lot of interference patterns and this is clearly evident in the vertical cross section diagram shown in Figure 4.16[C]. Although there are such interferences which could potentially distort the isosurface reconstructions, the *SIMCA* algorithm is still able to accurately produce reconstructions for the plastic landmines.

The plastic PFM-1 mine is in essence a plastic bag containing explosive liquid. This mine is lethal and is on the target list of most mine clearing teams because a single press of 5kg or more will make it go off. It is particularly pleasing to note the clear rendering of the mine by the *SIMCA* algorithm.

For the plastic MAUS mine the *SIMCA* algorithm is able to produce an accurate reconstruction and the top threaded steel retaining ring that holds the neoprene pressure dome has been properly rendered. Also the circular nature of the plastic base of the mine has a good reconstruction when compared to the Scheers' algorithm.

### **4.6.2 Setup 2 - Dry Sandy Soil**

#### **4.6.2.1 A Colombian guerrilla developed glass bottle mine, a metallic mine and a metal plate.**

Here a metallic M26 mine, a glass bottle mine and a metal plate have been emplaced by the researchers. The glass bottle mine is a glass bottle containing explosive charge. The glass bottle mine contains only a small portion of metal parts such as the spring, striker tip and shear wire. Such minimum metal mines are very difficult to detect unless sophisticated algorithms such as the *SIMCA* methods are employed. For the metallic M26 mine the *SIMCA* algorithm produces a more accurate reconstruction as can be seen in Table 4.4.

The signal levels from such minimum metal mines that can generate an electromagnetic contrast to its surrounding medium are extremely small and after the removal of clutter the *SIMCA* algorithm successfully reconstructs the shape of the glass mine. Figure 4.17 shows that the *SIMCA* method produces a much more accurate image than the Scheers algorithm. Again the error rates for the volumes and the burial depth when compared to the ground truth are given in Table 4.4.



[A]



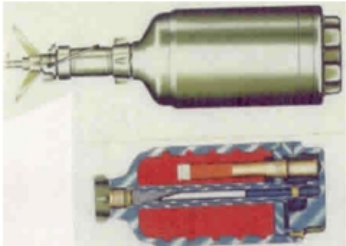
**Wooden cased PMD-6 Antipersonnel mine**

This mine is a wooden mine with a 2 piece case. The bottom section is rectangular in shape and has the main TNT charge, the fuse and the detonator. The top section closes the box, but can be opened. When a weight is applied on the mine, the lid removes a pin and the mine begins to detonate.

Construction information:

- Rectangular
- Length = 180mm
- Height = 61mm
- Width = 13mm
- Weight = 0.4 kg
- Wooden case
- Explosive type - TNT

[B]



**Steel cased PROM-1 antipersonnel mine**

A bounding fragmentation mine. The trip wire fuse is in the front of the mine and is dual pressure. A delay in the upward ejection ensures that anything that functions the fuse would be clear and a omnidirectional fragmentation pattern is accomplished.

Construction information:

- Cylindrical
- Height = 260mm
- Diameter = 75mm
- Weight = 3.0 kg
- Steel case
- Explosive type - TNT

Figure 4.12: Details of the targets buried in Figure 4.13.  
(Cameo Landmine clearance)



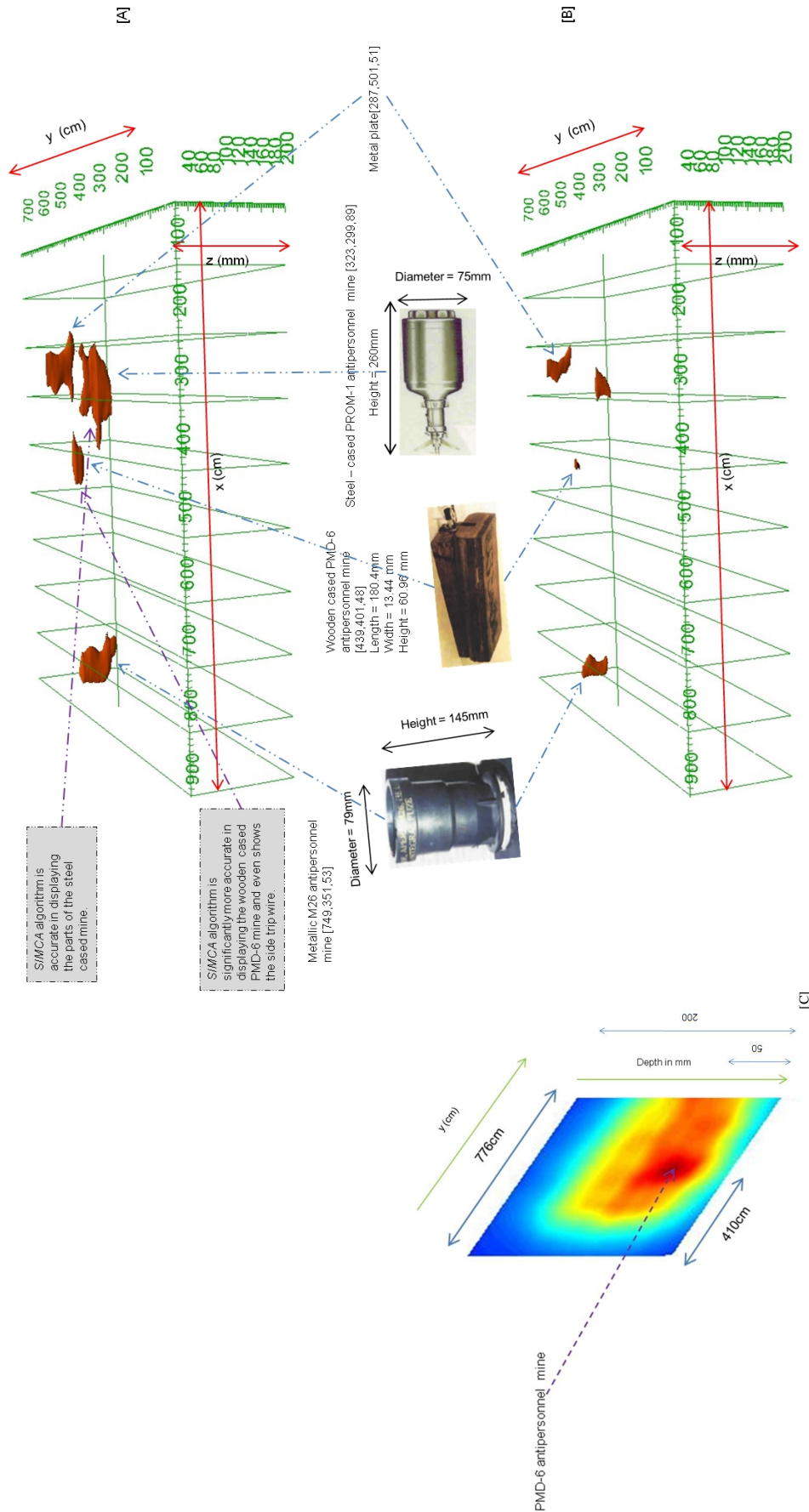


Figure 4.13: Reconstruction of volumes of real targets in a wet sandy soil using: [A]: *SIMCA* system after scanning by a GPR at optimised threshold = 230; [B]: Scheers et al.'s algorithm after scanning by a GPR at optimised threshold=252. Note *SIMCA* algorithm can render the steel-cased PROM-1 mine and even show the trip wire. Same ability for the *SIMCA* algorithm in case of the wooden cased mine; [C]: Vertical cross-sectional slice showing wooden cased PMD-6 mine.

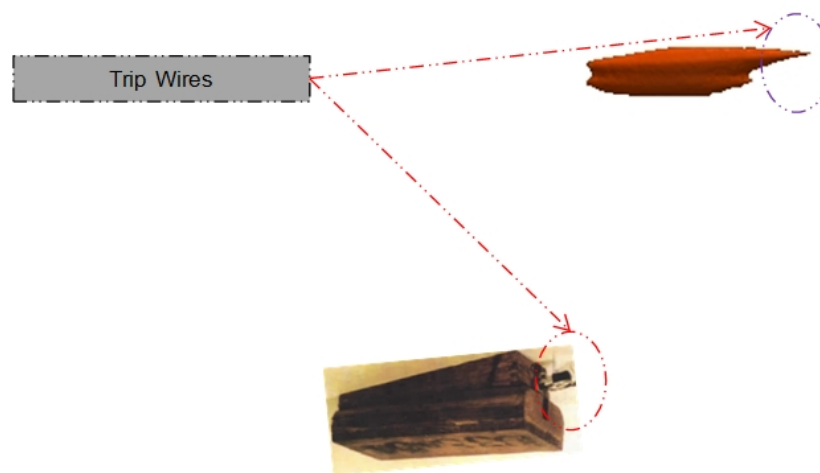


Figure 4.14: Trip Wires of Mines.

**Plastic PFM-1 Antipersonnel mine**

A small plastic mine which has a pressure-fused liquid explosive in a plastic case. It is a very severe mine that results in a lot of deaths.

Construction information:

- Length = 120.4 mm
- Width = 19.81 mm
- Height = 60.96 mm
- Plastic case
- Explosive type – Liquid plastic explosive

Figure 4.15: Details of the targets buried in Figure 4.16.  
(Cameo Landmine clearance)

	Burial depth of steel-cased PROM-1 mine (cm)	Burial depth of wooden-cased PMD-6 mine	Burial depth of metallic M26 mine	Burial depth of metal plate
Ground truth	8.9	4.8	5.3	5.1
SIMCA	9.2	5.0	5.4	4.9
Scheers	9.5	5.2	5.7	4.7
Error in SIMCA	3.4%	4.2%	1.9%	3.9%
Error in Scheers	6.7%	8.3%	7.5%	7.8%

[A]

	Volume of PROM-1 mine (cm) <sup>3</sup>	Volume of wooden cased PMD-6 mine	Volume of Metallic M26 mine	Volume of metal plate	Processing time (s)
Ground truth	1149	143	711	830	-
SIMCA	1169	146	708	840	1.0
Scheers	669	25	465	459	2.4
Error in SIMCA	1.7%	2.1%	0.4%	1.2%	-
Error in Scheers	41.8%	82.5%	34.6%	44.7%	-

[B]



Table 4-2: [A]: Actual burial depth, depth obtained from the SIMCA method, depth obtained from the Scheers’s method for each of the targets in centimetres for Figure 4.13. The table also gives the percentage errors for both the SIMCA and Scheers algorithms. ; [B]: Actual Volume, Volume of reconstructed target for SIMCA system, Volume of reconstructed target for Scheers algorithm, and processing time (CPU time) for Figure 4.13. The volumes are in cubic centimetres and the processing time is in seconds.

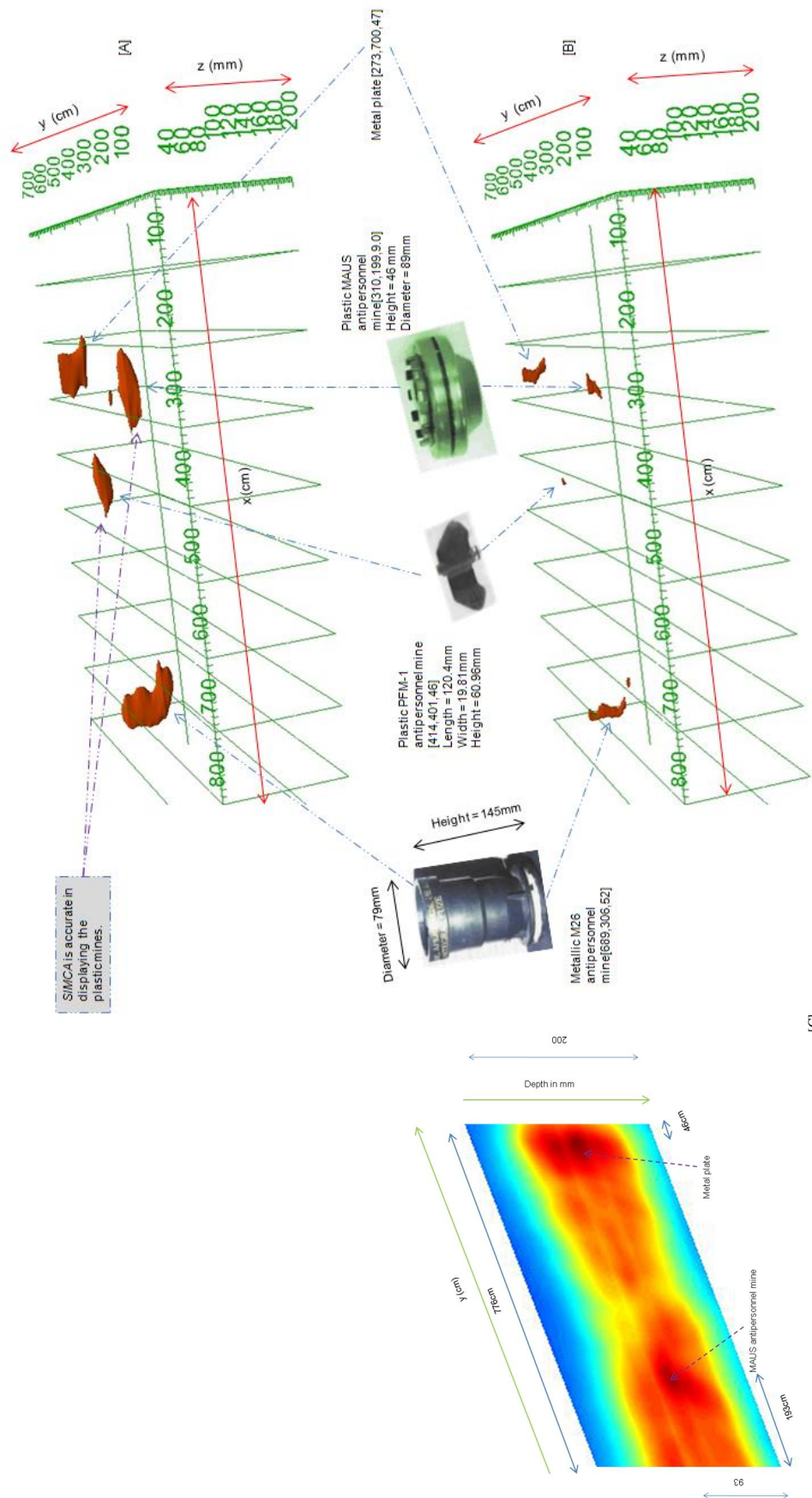


Figure 4.16: Reconstruction of volumes of real targets in a wet sandy soil using: [A]: SIMCA system after scanning by a GPR at optimised threshold = 230; [B]: Scheers et al's algorithm after scanning by a GPR at optimised threshold=252. Note plastic mines are rendered more accurately by the SIMCA algorithm; [C]: Vertical cross-sectional slice showing the plastic MAUS mine.

	Burial depth of metallic M26 mine (cm)	Burial depth of plastic PFM-1 mine	Burial depth of plastic MAUS mine	Burial depth of metal plate
Ground truth	5.2	4.6	9.0	4.7
SIMCA	5.4	4.4	9.3	4.6
Scheers	4.7	5.0	8.4	5.1
Error in SIMCA	3.8%	4.3%	3.3%	2.1%
Error in Scheers	9.6%	8.7%	6.7%	8.5%

	Volume of metallic M26 mine (cm) <sup>3</sup>	Volume of plastic PFM-1 mine	Volume of plastic MAUS mine	Volume of metal plate	Processing time (s)
Ground truth	711	146	286	680	-
SIMCA	708	144	288	671	0.9
Scheers	271	12	91	200	1.9
Error in SIMCA	0.4%	1.4%	0.7%	1.3%	-
Error in Scheers	61.9%	91.8%	68.2%	70.6%	-



Metallic M26 antipersonnel mine [1]



Plastic PFM-1 antipersonnel mine [2]



Plastic MAUS antipersonnel mine [3]



Metal plate [4]

Table 4.3: [A]: Actual burial depth, depth obtained from the SIMCA method, depth obtained from the Scheers’s method for each of the targets in centimetres for Figure 4.16. The table also gives the percentage errors for both the SIMCA and Scheers algorithms; [B]: Actual Volume, Volume of reconstructed target for SIMCA system, Volume of reconstructed target for Scheers algorithm, and processing time (CPU time) for Figure 4.16. The volumes are in cubic centimetres and the processing time is in seconds.



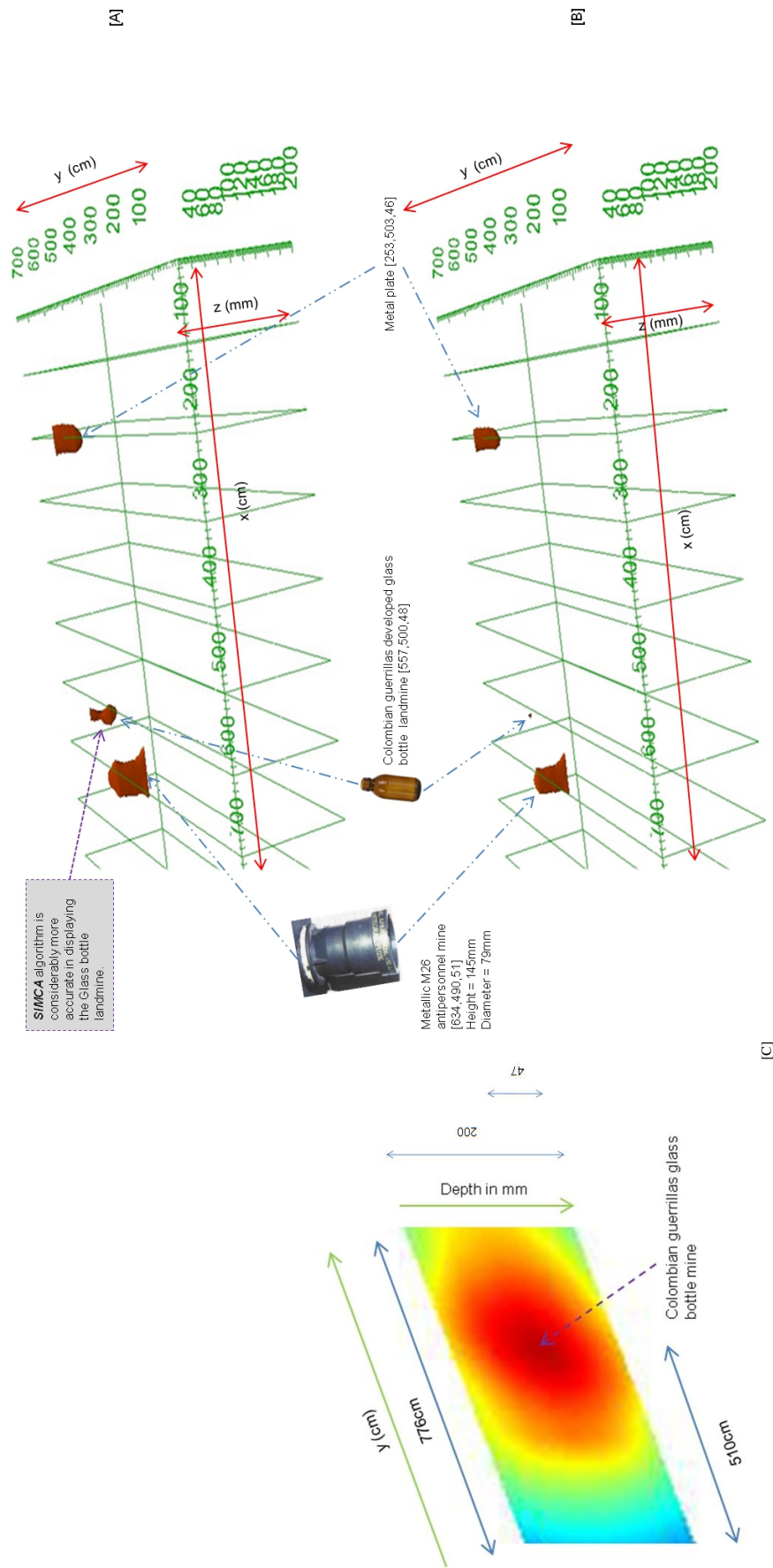


Figure 4.17: Reconstruction of volumes of real targets in a dry sandy soil using: [A]: *SIMCA* system after scanning by a GPR at optimised threshold = 230; [B]: Scheers et al's algorithm after scanning by a GPR at optimised threshold=252. Note *SIMCA* algorithms improved performance on Glass targets; [C]: Vertical cross-sectional slice showing the Colombian guerrilla glass bottle mine.

	Burial depth of metallic M26 mine (cm)	Burial depth of glass bottle mine	Burial depth of metal plate
Ground truth	5.1	4.8	4.6
SIMCA	4.9	4.7	4.5
Scheers	4.7	4.6	4.4
Error in SIMCA	3.9%	2.1%	2.2%
Error in Scheers	7.8%	4.2%	4.3%

[A]

	Volume of metallic M26 mine (cm) <sup>3</sup>	Volume of glass bottle mine	Volume of metal plate	Processing time (s)
Ground truth	711	480	670	-
SIMCA	697	479	678	0.4
Scheers	551	49	482	1.9
Error in SIMCA	2.0%	0.2%	1.2%	-
Error in Scheers	22.5%	89.8%	28.1%	-

[B]



Table 4.4: [A]: Actual burial depth, depth obtained from the *SIMCA* method, depth obtained from the Scheers' method for each of the targets in centimetres for Figure 4.17. The table also gives the percentage errors for both the *SIMCA* and Scheers algorithms; [B]: Actual Volume, Volume of reconstructed target for *SIMCA* system, Volume of reconstructed target for Scheers' algorithm and processing time (CPU time) for Figure 4.17. The volumes are in cubic centimetres and the processing time is in seconds. The table also gives the percentage errors for both the *SIMCA* and Scheers algorithms.

#### 4.6.2.2 A Colombian guerrilla cast ironed mine, tree root and a metallic plate

Here a modified version of the OZM-4 antipersonnel mine along with a metal plate is buried amongst some tree roots to see if such clutter can deter the detection and rendering of the landmine. The researchers wanted to introduce such natural objects amongst the landmines to replicate the actual conditions in a real minefield. The fact that the mine has been emplaced in an oblique position is clearly seen in both the 3D isosurface in Figure 4.19[A] and from the vertical cross section in the same picture.

In spite of the burden placed by the root, the *SIMCA* algorithm is able to produce a much better reconstruction when compared to its Sheers' et al counterpart. Also the *SIMCA* algorithm is able to reconstruct the prongs that project on top of the mine. Such bounding mines when tripped launch the body of the mine 3-4 feet into the air and the main charge detonates and spray fragmentation is a major weapon that the UN wants cleared. Also the circular cross section of the mine is clearly shown in Figure 4.19[C] where the vertical slice shows the circular cross sectional shape of the mine.

From this setup it was found that mines made entirely of metal are easily detected by the GPR and accurate reconstructions of their shapes can be attained.



**Colombian guerrilla developed cast-ironed Antipersonnel mine**

This cylindrical mine is a bounding antipersonnel mine. The mine has a cast iron body and this is propelled into the air after the detonation of a small charge located at the base of the mine. A trip wire fuse is used for the detonation. The mine can shoot out to a radius of 15m. This mine is a modified form of the OZM-4 mine.

Construction information:

- Cylindrical
- Height = 67mm
- Diameter = 54mm
- Weight = 1 kg
- Cast iron case

Figure 4.18: Details of the targets buried in Figure 4.19.  
(Cameo Landmine clearance)

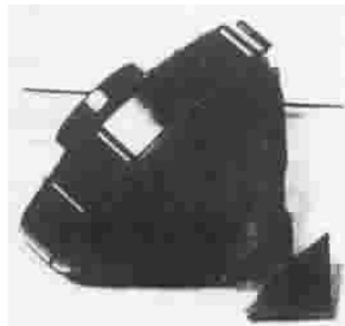


### 4.6.2.3 A plastic mine with a stone

A stone is buried along with a plastic AUS 15/50 antipersonnel mine. Often a stone is buried by opposition forces because some stones have a shape similar to a landmine and tend to confuse the opposition army. The stone can be considered as a mine like target<sup>3</sup> and is included to see how the algorithm performs when such objects are included and if they are able to detect the landmine. From the 3D isosurface in Figure 4.21 it is evident that one can deduce the shape of the stone and the plastic AUS 15/50 mine without any problems. This demonstrates that the *SIMCA* algorithm can produce accurate reconstructions.

The *SIMCA* algorithm is able to produce a better reconstruction of the plastic mine in comparison to the Scheers' algorithm. It is interesting to note *SIMCA* algorithm's ability to render the conical point of the landmine. Figure 4.21[C] also shows the cross section of the conical top of the landmine.

It is to be noted that a by-product of raising the GPR sensor above the surface as a safety measure causes substantial degradation in performance. This is because the target to background response decreases with elevation and the spatial resolution decreases with such elevation. It was found that elevations of 10cm or more causes a substantial decrease in detectability and total loss of target discrimination (Lopera, 2008).



**Plastic AUS 15/50 Antipersonnel mine**

A fragmentation mine. Upon application of pressure the mine fuse functions and detonates the charge. This results in the propelling motion of the fragments in a upward cone. The mine does not bound into the air.

Construction information:

- Conical
- Height = 100mm
- Diameter = 125mm
- Weight = 1.7 kg
- Plastic case
- Explosive type – Comp B

Figure 4.20: Details of the targets buried in Figure 4.21.  
(Cameo Landmine clearance)

<sup>3</sup>A mine like target can be defined as an object whose dimensions and shape are similar to a landmine.

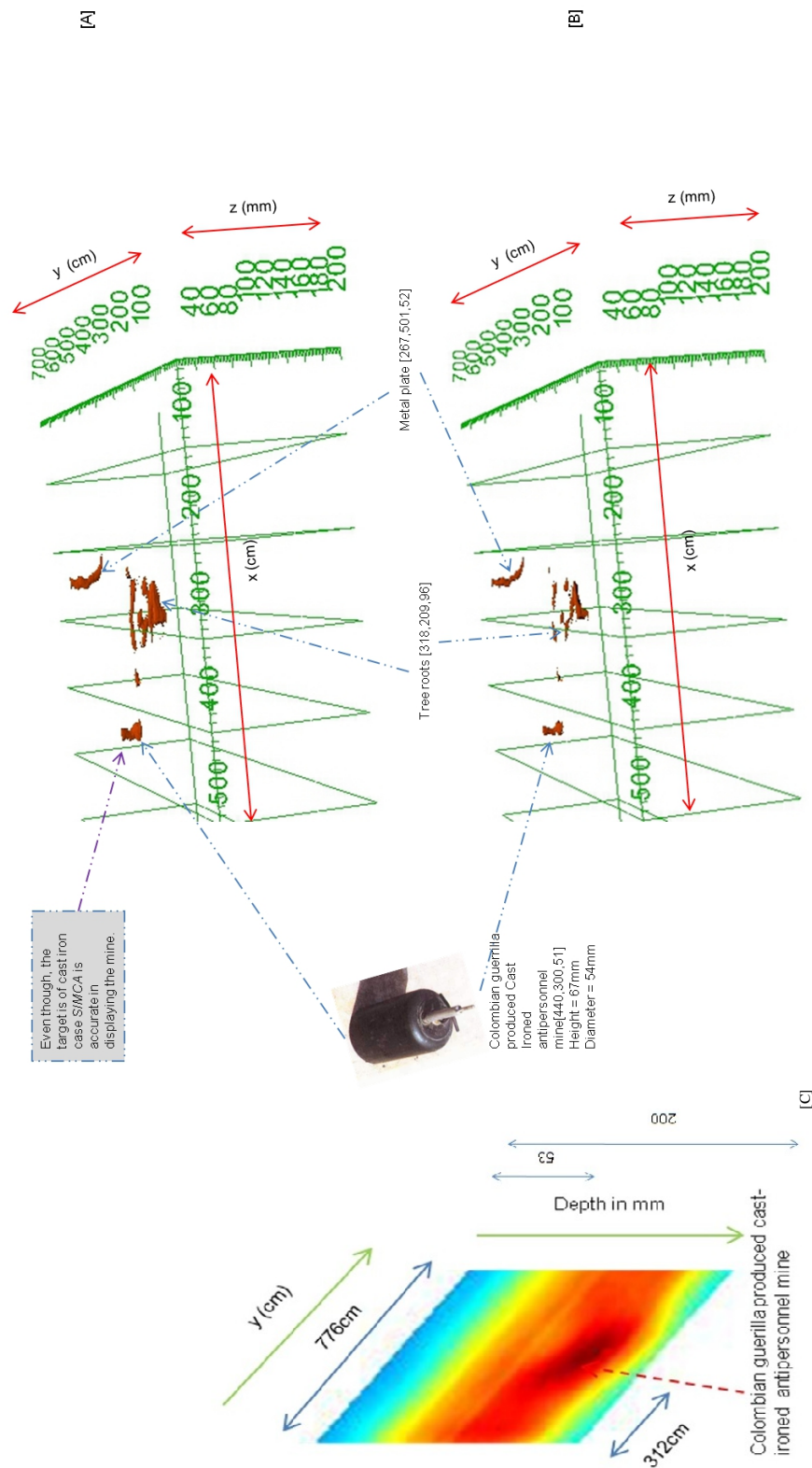


Figure 4.19: Reconstruction of volumes of real targets in a dry sandy soil using a GPR at optimised threshold = 230; [B]: Scheers et al's algorithm after scanning by a GPR at optimised threshold=252. Note even though there is a metallic mine Scheers' algorithm is not so accurate at displaying the mine; [C]: Vertical cross-sectional slice showing cast ironed OZM-45 mine.

	Burial depth of cast ironed mine (cm)	Burial depth of metal plate
Ground truth	5.1	5.2
SIMCA	5.3	5.1
Scheers	5.5	4.7
Error in SIMCA	3.9%	1.9%
Error in Scheers	7.8%	9.6%

[A]

	Volume of cast ironed mine (cm) <sup>3</sup>	Volume of metal plate	Processing time (s)
Ground truth	153	198	-
SIMCA	154	196	1.0
Scheers	108	164	2.3
Error in SIMCA	0.7%	1.0%	-
Error in Scheers	29.4%	17.2%	-

[B]



Table 4.5: [A]: Actual burial depth, depth obtained from the SIMCA method, depth obtained from the Scheers’s method for each of the targets in centimetres for Figure 4.19. The table also gives the percentage errors for both the SIMCA and Scheers algorithms; [B]: Actual Volume, Volume of reconstructed target for SIMCA system, Volume of reconstructed target for Scheers algorithm, and processing time (CPU time) for Figure 4.19. The volumes are in cubic centimetres and the processing time is in seconds.

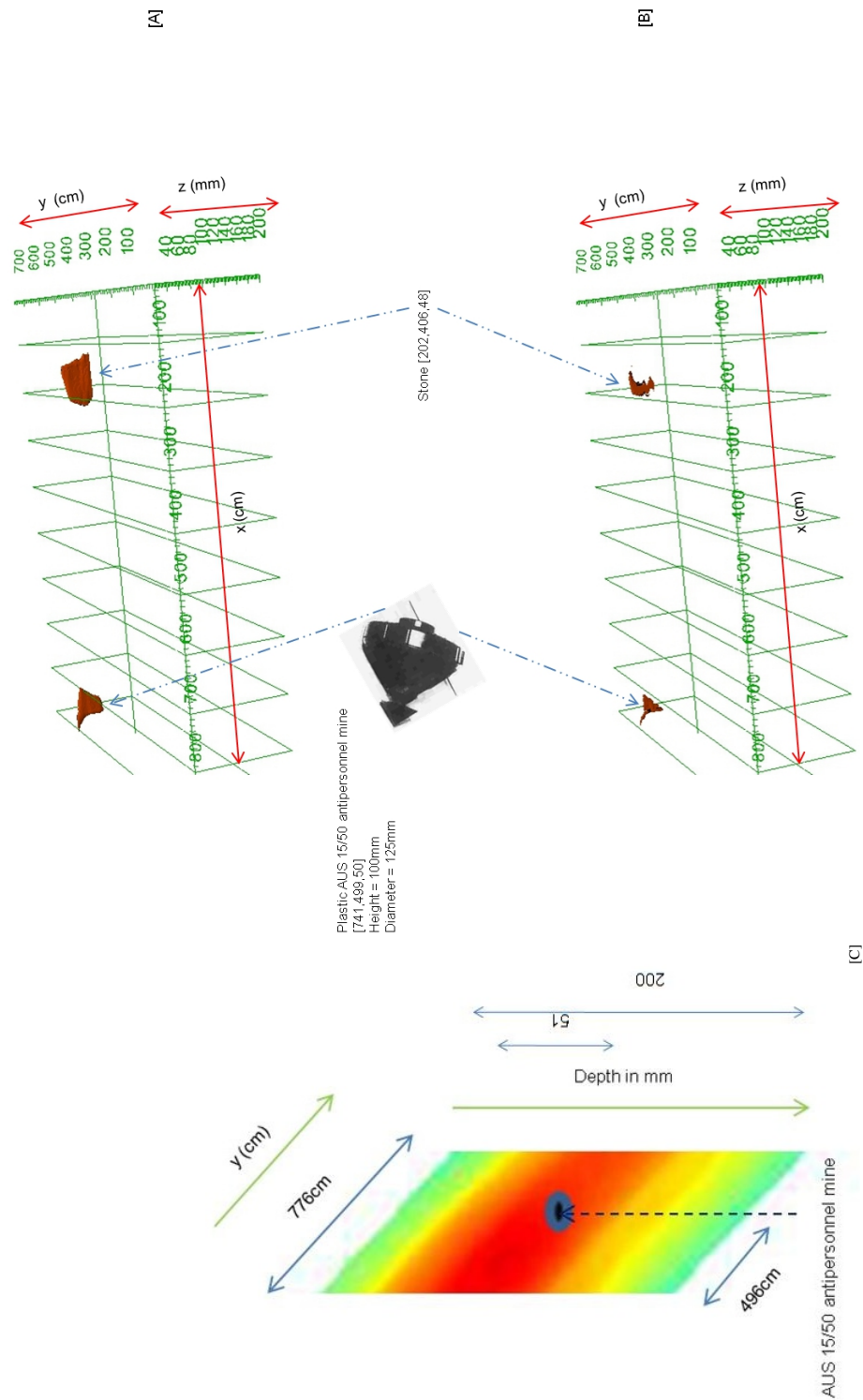


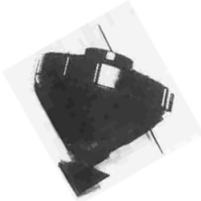
Figure 4.21: Reconstruction of volumes of real targets in a dry sandy soil using: [A]: *SIMCA* system after scanning by a GPR at optimised threshold = 230; [B]: Scheers et al's algorithm after scanning by a GPR at optimised threshold=252. Note plastic mines are rendered more accurately by the *SIMCA* algorithm; [C]: Vertical cross-sectional slice showing plastic AUS 15/50 mine.

	Burial depth of plastic AUS 15/50 mine (cm)		
Ground truth	5.0		
SIMCA	5.1		
Scheers	4.6		
Error in SIMCA	2.0%		
Error in Scheers	8.0%		

[A]

	Volume of plastic AUS 15/50 mine (cm) <sup>3</sup>	Processing time (s)
Ground truth	416	-
SIMCA	418	1.0
Scheers	201	2.4
Error in SIMCA	0.5%	-
Error in Scheers	51.7%	-

[B]



Plastic AUS 15/50 antipersonnel mine

[1]

Table 4.6: [A]: Actual burial depth, depth obtained from the SIMCA method, depth obtained from the Scheers’s method for each of the targets in centimetres for Figure 4.21. The table also gives the percentage errors for both the SIMCA and Scheers algorithms; [B]: Actual Volume, Volume of reconstructed target for SIMCA system, Volume of reconstructed target for Scheers algorithm, and processing time (CPU time) for Figure 4.21. The volumes are in cubic centimetres and the processing time is in seconds.

#### 4.6.2.4 A plastic mine, tree root and a metallic plate

The researchers buried a plastic APM 29 antipersonnel mine, a metal plate and tree roots in a dry sandy soil. The important and pleasing fact is that the *SIMCA* algorithm even reconstructs the open plates as shown in the isosurface reconstruction in Figure 4.23. The Scheers' method fails to accurately reconstruct the shape of this plastic landmine and this fact is also evident in the error rates as shown in Table 4.7. The *SIMCA* algorithm also runs in half the time compared to the Scheers method and this faster processing capability is important in a real demining situation.

Furthermore, the fact that one of the plates has been opened can be judged from the vertical cross section where there is a small interference pattern on the open plate with the surrounding soil.



**Plastic APM 29 Antipersonnel mine**

This mine is an directed fragmentation mine, The mine has two plates or wells on either side of the mine which can open. The mine stands on the ground using two pairs of scissor legs. A trip wire activates the mine. When activated the mines 923 steel ball fragments, each 5.6 mm in diameter are launched in a arc  $> 58^\circ$  away from the mine,

Construction information

- Rectangular
- Length = 265mm
- Width = 45mm
- Height = 120mm
- Weight = 2.9 kg
- Plastic case

Figure 4.22: Details of the targets buried in Figure 4.23.  
(Cameo Landmine clearance)

#### 4.6.2.5 A tiny plastic M14 antipersonnel mine, a plastic mine and a metallic plate

M14 mines are very difficult to detect because they are tiny antipersonnel mines and have a diameter of only 56mm and such low contrast conditions make the detection by GPR difficult and this calls for the software to successfully render the mine. For a typical antipersonnel mine, the internal structure is usually divided into four components: the casing, the explosives, the fuse and air. The explosives include the main charge which is triggered by a small amount of explosive known as



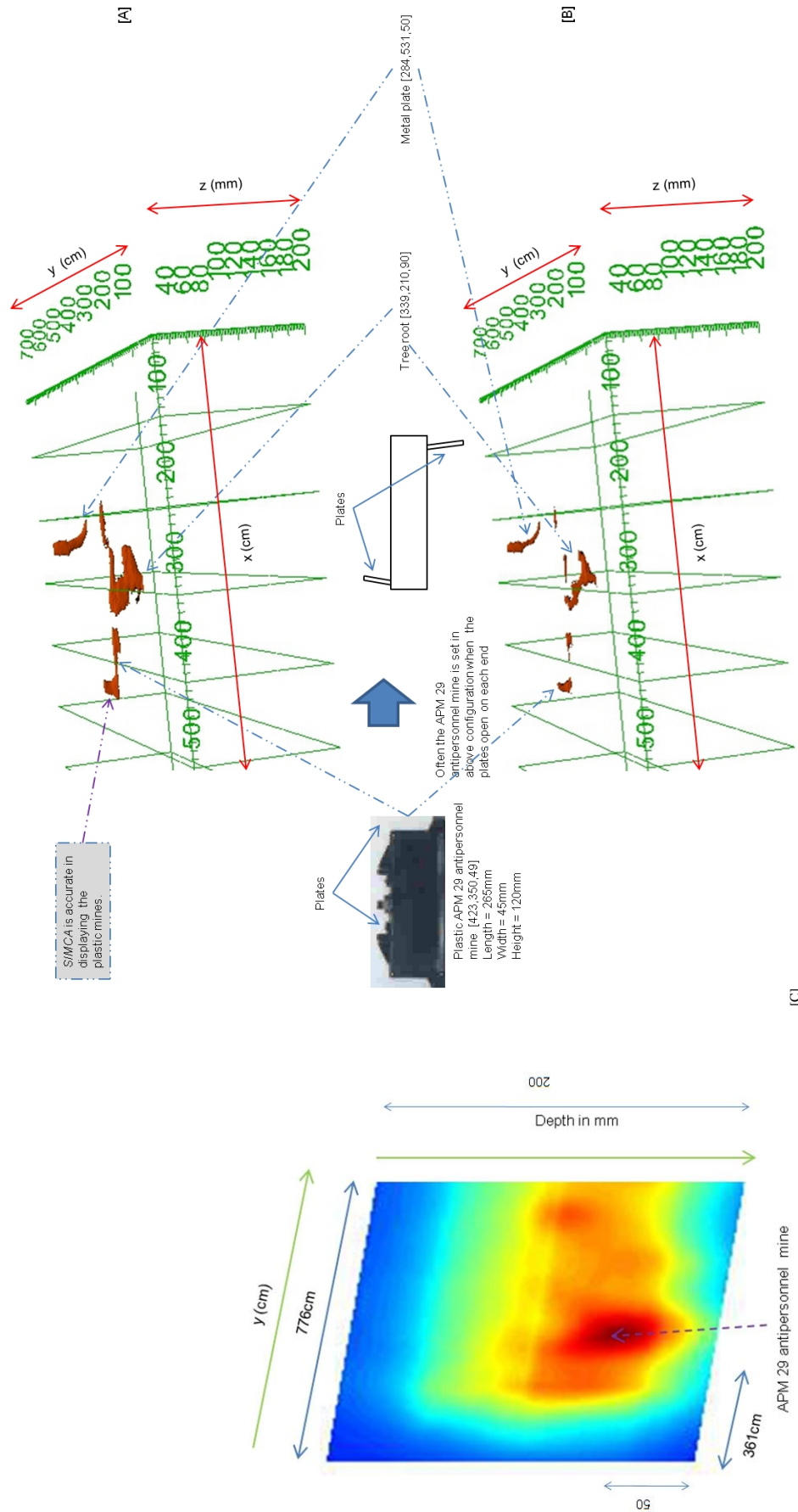


Figure 4.23: Reconstruction of volumes of real targets in a dry sandy soil using: [A]: *SIMCA* system after scanning by a GPR at optimised threshold = 230; [B]: Scheers et al's algorithm after scanning by a GPR at optimised threshold=252. Note *SIMCAs* natural ability at rendering plastic mines; [C]: Vertical cross-sectional slice showing plastic APM 29 mine.

	Burial depth of plastic APM 29 mine (cm)	Burial depth of metal plate
Ground truth	4.9	5.0
SIMCA	5.0	5.2
Scheers	4.4	5.4
Error in SIMCA	2.0%	4.0%
Error in Scheers	10.2%	8.0%

[A]

	Volume of plastic APM 29 mine (cm) <sup>3</sup>	Volume of metal plate	Processing time (s)
Ground truth	405	200	-
SIMCA	396	196	0.6
Scheers	238	164	1.1
Error in SIMCA	2.2%	2.0%	-
Error in Scheers	41.2%	18.0%	-

[B]



Table 4.7: [A]: Actual burial depth, depth obtained from the SIMCA method, depth obtained from the Scheers’s method for each of the targets in centimetres for Figure 4.23. The table also gives the percentage errors for both the SIMCA and Scheers algorithms; [B]: Actual Volume, Volume of reconstructed target for SIMCA system, Volume of reconstructed target for Scheers algorithm, and processing time (CPU time) for Figure 4.23. The volumes are in cubic centimetres and the processing time is in seconds.



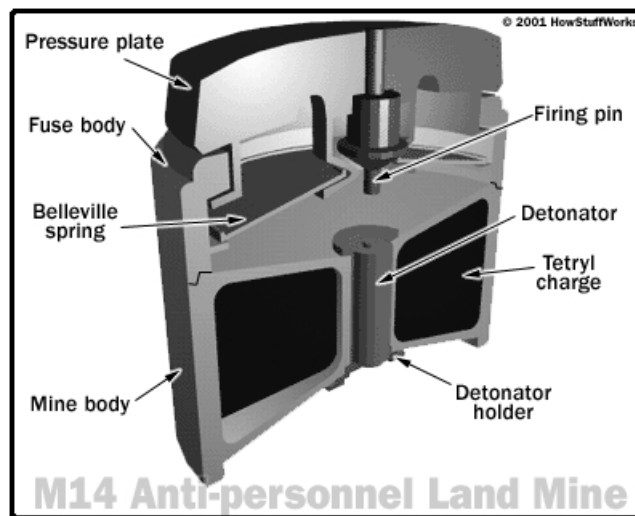


Figure 4.24: The internal structure of a M14 antipersonnel mine.  
(<http://science.howstuffworks.com>)

the detonator. A number of fuse mechanisms exist, such as the mechanical pressure fuse or the chemical pressure fuse. The fuse is usually the only component of a plastic cased landmine that has metallic parts. But the metallic content may be limited to no more than a small striker pin or firing pin. Figure 4.26 gives the reconstructed isosurface, whilst Figure 4.24 shows diagrammatically the internal structure of the M14 mine. In spite of the fact that the M14 mine is one of the most difficult mines to detect, the *SIMCA* algorithm successfully renders the volume of the landmine as shown in the isosurface reconstructions in Figure 4.26. Unfortunately the Scheers algorithm is not successful in rendering the plastic mine. In terms of the M14 mine the actual mine has some voids therefore it is subject to smaller burial losses in dry sand. This is advantageous for the detection as voids are included in the mine to allow movements behind the pressure plate (Anderson, 2002).

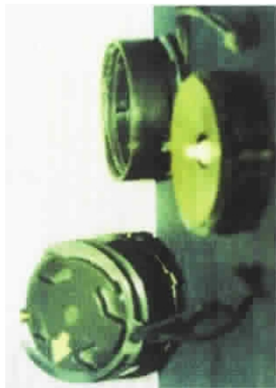
For the plastic PRB M409 mine, the only metallic parts are the firing pins and the two aluminium capers and it is evident that the Scheers' algorithm is only able to render these metallic parts. The circular cross sectional shape of the PRB M409 mine is also clearly shown in Figure 4.26. The poor rendering ability of the mines by the Scheers' algorithm is shown in Table 4.8. The circular nature of the PRB M409 mine is clearly seen in the vertical cross section produced using the *SIMCA* system.

#### 4.6.2.6 A metallic plate buried in a less compacted layer of sand

A metallic M2 antipersonnel mine is buried in a dry sandy soil. The researchers had not compacted the soil properly to test the effect on the detection of the landmine because often in field conditions the soil gets moved due to natural forces. This allowed the researchers to try and produce real conditions for the testing of algorithms. The fact that the soil has not been properly compacted is noticeable in the 3D isosurface as well as the vertical section where there is a distinct disturbance pattern.

The *SIMCA* algorithm when compared to the Scheers' method is able to successfully reconstruct

[A]



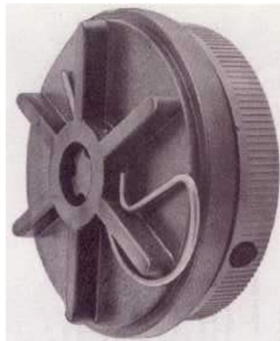
**Plastic M14 Antipersonnel mine**

This is a small plastic mine. The mine has 2 safety features and the pressure plate is rotated to a armed position to activate the mine. The lower part of the mine has 29g of tetryl. The only metallic part of the mine is the steel striker tip and the detonator. This mine is very difficult to detect.

Construction information:

- Cylindrical
- Height = 40mm
- Diameter = 56mm
- Weight = 0.099kg
- Plastic case
- Explosive type - Tetryl

[B]



**Plastic PRB M409 Antipersonnel mine**

A plastic bodied mine which is circular in shape. When a bolt is displaced the strikers of the mine are loosened and the caps detonate. The only metallic parts are the firing pins and two aluminium primer caps.

Construction information:

- Cylindrical
- Height = 28mm
- Diameter = 82mm
- Weight = 0.183kg
- Plastic case
- Explosive type - Triolene

Figure 4.25: Details of the targets buried in Figure 4.26.  
(Cameo Landmine clearance)

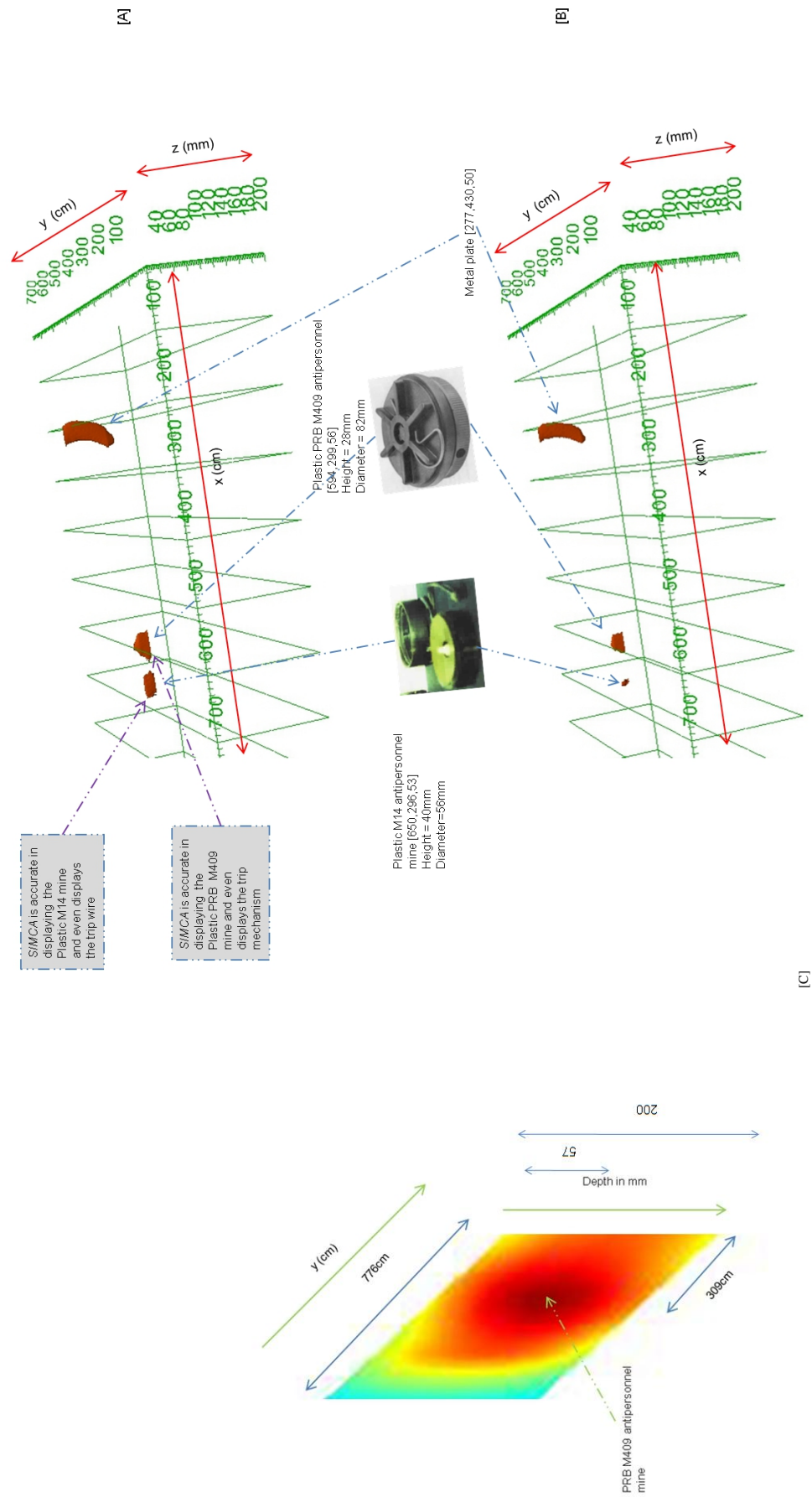


Figure 4.26: Reconstruction of volumes of real targets in a dry sandy soil using a GPR at optimised threshold = 230; [B]: Scheers et al's algorithm after scanning by a GPR at optimised threshold=252. Note *SIMCA* is more accurate in displaying plastic mines and their parts; [C]: Vertical cross-sectional slice showing plastic PRB M409.

	Burial depth of plastic M14 mine (cm)	Burial depth of plastic PRB M409 mine	Burial depth of metal plate
Ground truth	5.3	5.6	5.0
SIMCA	5.5	5.7	4.9
Scheers	5.7	5.1	5.4
Error in SIMCA	3.8%	1.8%	2.0%
Error in Scheers	7.5%	8.9%	8.0%

[A]

	Volume of plastic M14 mine (cm) <sup>3</sup>	Volume of plastic PRB M409 mine	Volume of metal plate	Processing time (s)
Ground truth	99	148	400	-
SIMCA	101	150	398	1.0
Scheers	30	131	333	1.8
Error in SIMCA	2.0%	1.4%	0.5%	-
Error in Scheers	69.7%	11.5%	16.8%	-

[B]



Table 4-8: [A]: Actual burial depth, depth obtained from the *SIMCA* method, depth obtained from the Scheers’s method for each of the targets in centimetres for Figure 4.26. The table also gives the percentage errors for both the *SIMCA* and Scheers algorithms; [B]: Actual Volume, Volume of reconstructed target for *SIMCA* system, Volume of reconstructed target for Scheers algorithm, and processing time (CPU time) for Figure 4.26. The volumes are in cubic centimetres and the processing time is in seconds.

the metallic mine with a better degree of accuracy. The Scheers method also renders the uncompacted sand layer and gives the impression to a deminer that there are 2 targets present which could be landmines. This is a hit and miss situation because the deminers might misjudge the presence of the M14 mine from the other 2 falsely derived targets. The vertical cross section from Figure 4.28[C] shows some interference patterns along the M2 antipersonnel mine.

Another important point to note is that inspite of the fact that the M2 mine is a relatively large mine with a volume of  $1767 \text{ cm}^3$  and hence there are strong electromagnetic contrasts between the sand and the metallic landmine and also low attenuation of the electromagnetic wave in sand; the Scheers' algorithm is not successful in rendering the shape of this mine.



**Metallic M2 Antipersonnel mine**

This is a bounding fragmentation mine. The fuse can function either by pressure or a trip wire. Upon triggering of the fuse, a charge at the bottom of the mine shoots up a 60mm mortar in a projectile. A delay element then ignites the main charge and the warhead bursts.

Construction information:

- Cylindrical
- Height = 244mm
- Diameter = 95mm
- Weight = 2.9 kg
- Metallic case
- Explosive type - TNT

Figure 4.27: Details of the targets buried in Figure 4.28.  
(Cameo Landmine clearance)

#### 4.6.2.7 A plastic and rubber cased mine, a plastic mine and a metal plate

The most important aspect of the APM detection is dependent on the actual character of the mines themselves (Capineri et al., 1998). Some mines such as the plastic and rubber cased PMA-3 mine used here have air spaces or voids and have a very small quantity of metal and the only metallic parts of the PMA-3 mine is the aluminium covering on the detonator cap.

The plastic VS-Mk2 mine receives a better reconstruction from the *SIMCA* algorithm and the cylindrical nature of this mine is also noticeable in terms of the reconstructions from the *SIMCA* method. The plastic and rubber cased PMA-3 mine is another small mine that has a height of only 36mm. The *SIMCA* method produces a better reconstruction in comparison to the Scheers' method.

Furthermore for the plastic and rubber cased mine the fuse mechanism has been also properly

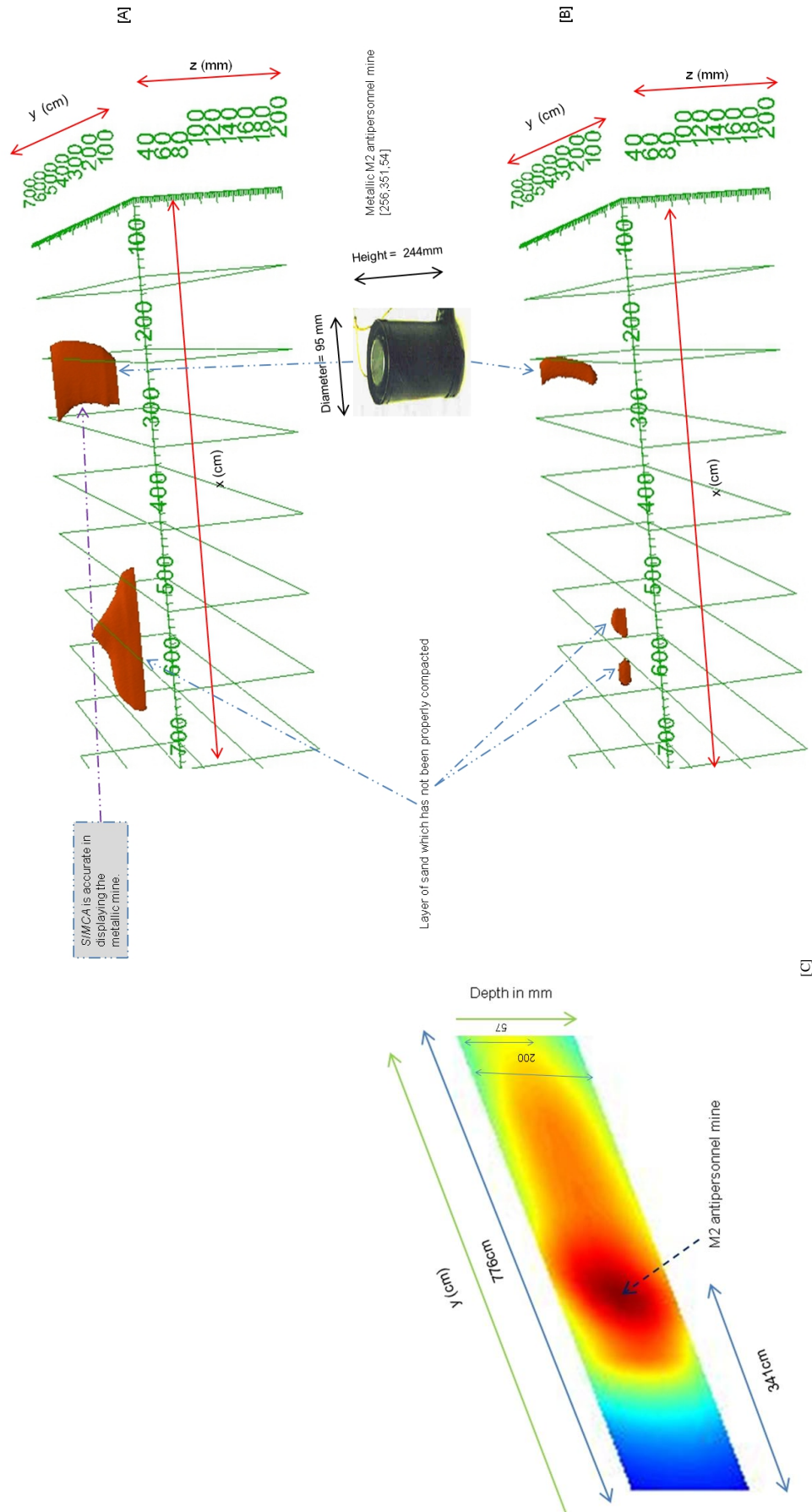


Figure 4.28: Reconstruction of volumes of real targets in a dry sandy soil using a GPR at optimised threshold = 230; [B]: Scheers et al's algorithm after scanning by a GPR at optimised threshold=252. Note *SIMCA* produces better reconstructions for metallic mines; [C]: Vertical cross-sectional slice showing metallic M2 mine.

	Burial depth of metallic M2 mine (cm)
Ground truth	5.4
SIMCA	5.7
Scheers	5.9
Error in SIMCA	5.6%
Error in Scheers	9.3%

[A]

	Volume of metallic M2 mine (cm) <sup>3</sup>	Processing time (s)
Ground truth	1767	-
SIMCA	1769	0.6
Scheers	817	1.2
Error in SIMCA	0.1%	-
Error in Scheers	53.8%	-

[B]



Metallic M2 antipersonnel mine

[1]

Table 4.9: [A]: Actual burial depth, depth obtained from the SIMCA method, depth obtained from the Scheers’s method for each of the targets in centimetres for Figure 4.28. The table also gives the percentage errors for both the SIMCA and Scheers algorithms; [B]: Actual Volume, Volume of reconstructed target for SIMCA system, Volume of reconstructed target for Scheers algorithm, and processing time (CPU time) for Figure 4.28. The volumes are in cubic centimetres and the processing time is in seconds.



rendered by the *SIMCA* method as is evident from Figure 4.31.

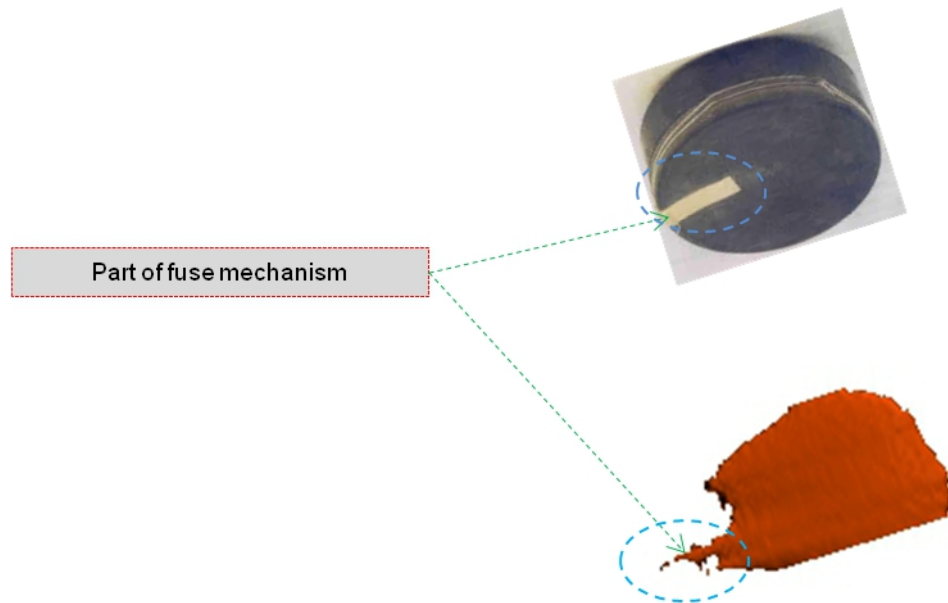


Figure 4.31: Figure showing wires in fuse mechanism.

#### 4.6.2.8 A steel bullet, a plastic mine and a metallic plate

The plastic PRM M409 mine is only buried at a depth of 5.5cm and here there is the direct impact of the air ground interface response. A large impedance contrast occurs everywhere and the PRB M409 mine responses are quite often hidden within the air ground interface response. The spatial differencing used by the *SIMCA* algorithm helps to extract the landmine response and hence an acceptable 3D reconstruction of the target is attained. Whether a simple difference detector or an imaging system with global background removal all carry out a spatial differencing operation (Caevic et al., 2008). Also what is pleasing to note from the reconstructions of the PRB M409 plastic landmine is that although the only metallic parts of the mine are the firing pins and the two aluminium primer caps, the *SIMCA* method can also accurately render the plastic parts. This is not the case with the Scheers' method which produces the reconstructions of the metallic parts of the plastic mine.

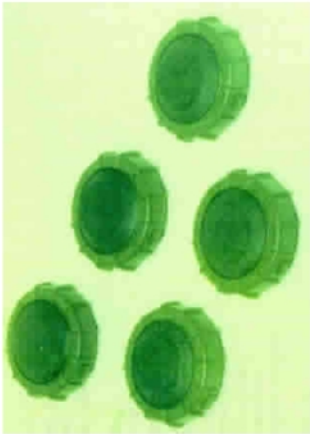
It is also important to note that the laying of the mines makes their cylinders' rotational axis almost vertical and this has an effect on the detection of the landmines. The steel bullet is a rotationally symmetric, strongly elongated object with a metal casing. But in spite of their metal casing and large size, the steel bullet has been accurately rendered by the *SIMCA* method. The Scheers' method has an error rate of 10.9% compared to the 0.9% produced by the *SIMCA* algorithm.

Also a factor to consider is that in a landmine detection scenario the target is located in the near field of the antenna system and this is unlike a typical radar situation where the target is situated in the far field of both the transmit and receive antennas (Jol, 1994).

In this setup it is also important to note that an Unexploded Ordnance (UXO) in the form of a steel bullet has been buried. A UXO is 'Military munitions that have been primed, fused, armed, or



[A]



**Plastic VS-Mk2 antipersonnel mine**

A small round and plastic mine. It was designed to be spread from helicopters but it is employed by hand. The mine is resistant to any blast like fuel or air explosives.

Construction information:

- Cylindrical
- Height = 33mm
- Diameter = 90mm
- Weight = 0.135 kg
- Plastic case
- Explosive type – Pressed RDX

[B]



**Plastic & rubber-cased PMA-3 antipersonnel mine**

Another small circular mine which consists of a flat cylindrical body and a base-mounted pressure fuse. The triggering of the mine occurs only upon rotation of an upper pressure plate which is within the lower assembly containing the fuse. The only metallic parts of the mine are the aluminium covering on the detonator cap. Since this mine is a minimum metallic mine, it is very difficult to detect. This mine is also very dangerous because of the low operating threshold.

Construction information:

- Cylindrical
- Height = 36mm
- Diameter = 103mm
- Weight = 0.183 kg
- Plastic & rubber case
- Explosive type – Pressed TNT

Figure 4.29: Details of the targets buried in Figure 4.30.  
(Cameo Landmine clearance)

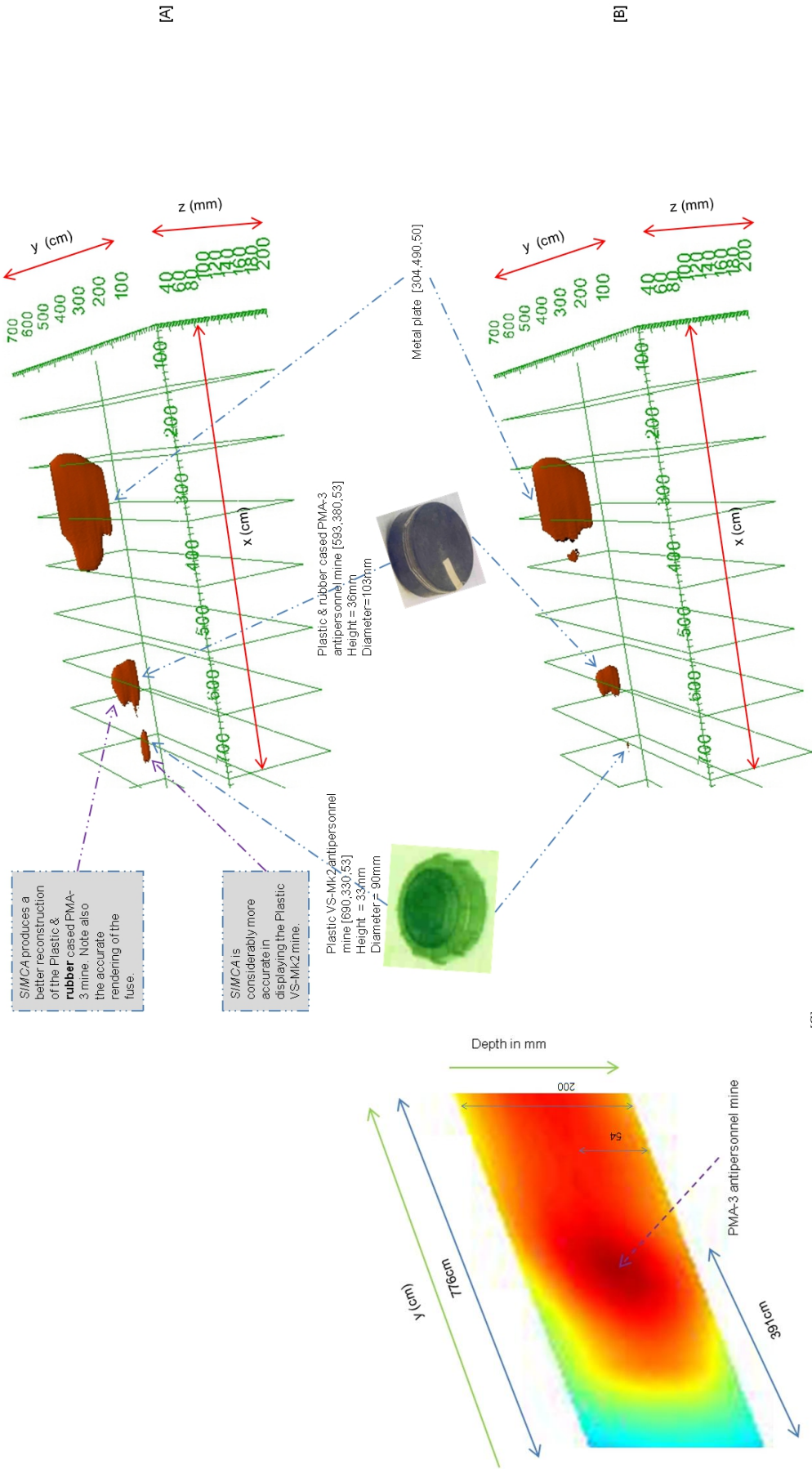


Figure 4.30: Reconstruction of volumes of real targets in a dry sandy soil using: [A]: SIMCA system after scanning by a GPR at optimised threshold = 252; [B]: Scheers et al's algorithm after scanning by a GPR at optimised threshold=252. Note plastic mines are rendered poorly by the Scheers' algorithm; [C]: Vertical cross-sectional slice showing plastic & rubber cased PMA-3 mine.

	Burial depth of plastic VS-Mk2 mine (cm)	Burial depth of plastic & rubber cased PMA-3 mine	Burial depth of metal plate
Ground truth	5.3	5.3	5.0
SIMCA	5.1	5.4	4.9
Scheers	5.8	4.9	5.4
Error in SIMCA	3.8%	1.9%	2.0%
Error in Scheers	9.4%	7.5%	8.0%

[A]

	Volume of plastic VS-Mk2 mine (cm) <sup>3</sup>	Volume of plastic & rubber cased PMA-3 mine	Volume of metal plate	Processing time (s)
Ground truth	210	306	2103	-
SIMCA	208	299	2113	1.0
Scheers	38	252	1623	1.5
Error in SIMCA	1.0%	2.3%	0.5%	-
Error in Scheers	81.9%	17.6%	22.8%	-

[B]



Plastic VS-Mk2 antipersonnel mine [1]



Plastic & rubber cased PMA-3 antipersonnel mine [2]



Metal plate [3]

Table 4.10: [A]: Actual burial depth, depth obtained from the *SIMCA* method, depth obtained from the Scheers's method for each of the targets in centimetres for Figure 4.30. The table also gives the percentage errors for both the *SIMCA* and Scheers algorithms; [B]: Actual Volume, Volume of reconstructed target for *SIMCA* system, Volume of reconstructed target for Scheers algorithm, and processing time (CPU time) for Figure 4.30. The volumes are in cubic centimetres and the processing time is in seconds.

otherwise prepared for action, and have been fired, dropped, launched, projected, or placed in such a manner as to constitute a hazard to operations, installation, personnel, or material, and remain unexploded either as a result of malfunction, design, or any other cause'. For this definition UXO is limited to items larger than 50 caliber<sup>4</sup>.

#### 4.6.2.9 A stone, steel cased mine and a metallic plate

Here a shallow water mine with a steel case is buried and a rock clutter is buried in a dry sandy soil condition. Both positions and geometry of the steel cased PLARM-1A landmine are well reconstructed. The integration of the *SIMCA* algorithm with existing statistical classification techniques can improve detection performance and this is a future study that can be undertaken beyond this PhD.

Besides its accuracy the fast processing speed and the simplicity of the algorithm are further advantages of the *SIMCA* algorithm when compared to the Scheers' et al method. For example it can be seen from Table 4.12 that the *SIMCA* algorithm runs in 0.9 seconds compared to 1.5 seconds by the Scheers' et al method.



**Steel cased PLARM-1A mine**

A very shallow water mine. The mine can be used in rivers to stop forces advancing in the water. It can be also used as a floating mine. Landing crafts are damaged by this type of mine.

Construction information:

- Steel case

Figure 4.33: Details of the targets buried in Figure 4.34.  
(Cameo Landmine clearance)

<sup>4</sup><http://www.uxoinfo.com>

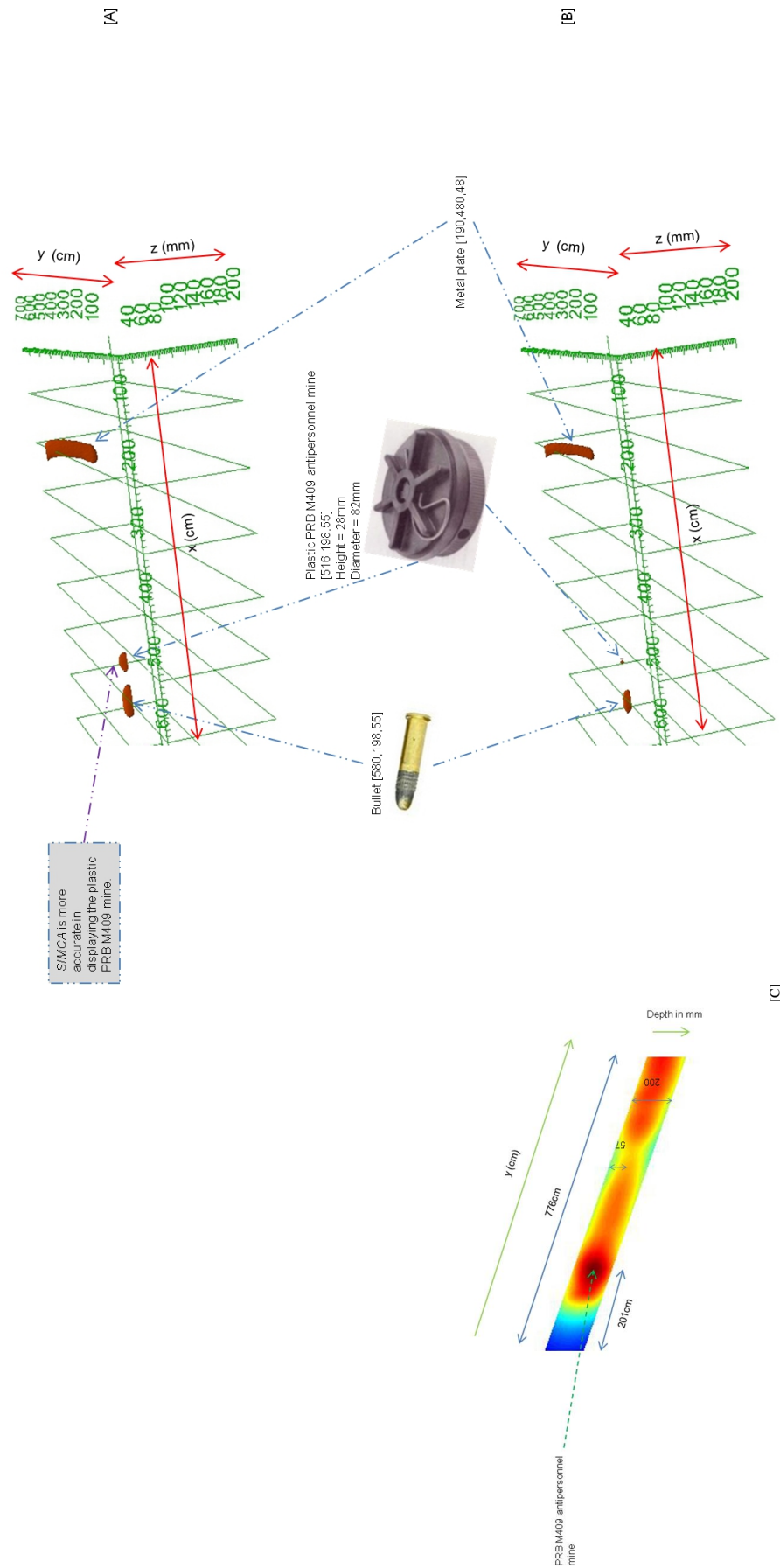


Figure 4.32: Reconstruction of volumes of real targets in a dry sandy soil using: [A]: *SIMCA* system after scanning by a GPR at optimised threshold = 230; [B]: Scheers et al's algorithm after scanning by a GPR at optimised threshold=252. Note *SIMCA* algorithm can reconstruct plastic mines more accurately; [C]: Vertical cross-sectional slice showing plastic PRB M409 mine.

	Burial depth of steel bullet (cm)	Burial depth of plastic PRB M409 mine	Burial depth of metal plate
Ground truth	5.5	5.5	4.8
SIMCA	5.4	5.7	4.9
Scheers	5.8	5.1	5.2
Error in SIMCA	1.8%	3.6%	2.1%
Error in Scheers	5.5%	7.3%	8.3%

[A]

	Volume of steel bullet (cm) <sup>3</sup>	Volume of plastic PRB M409 mine	Volume of metal plate	Processing time (s)
Ground truth	220	148	316	-
SIMCA	222	146	314	0.6
Scheers	196	13	257	1.3
Error in SIMCA	0.9%	1.4%	0.6%	-
Error in Scheers	10.9%	91.2%	18.7%	-

[B]

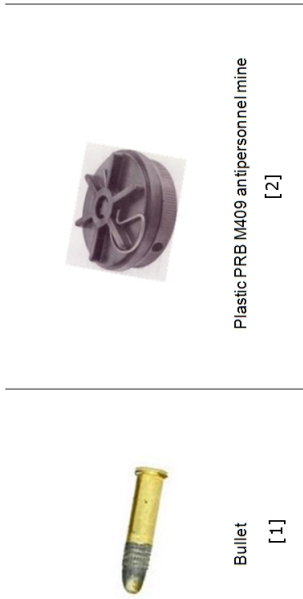


Table 4.11: [A]: Actual burial depth, depth obtained from the *SIMCA* method, depth obtained from the Scheers’s method for each of the targets in centimetres for Figure 4.32. The table also gives the percentage errors for both the *SIMCA* and Scheers algorithms; [B]: Actual Volume, Volume of reconstructed target for *SIMCA* system, Volume of reconstructed target for Scheers algorithm, and processing time (CPU time) for Figure 4.32. The volumes are in cubic centimetres and the processing time is in seconds.



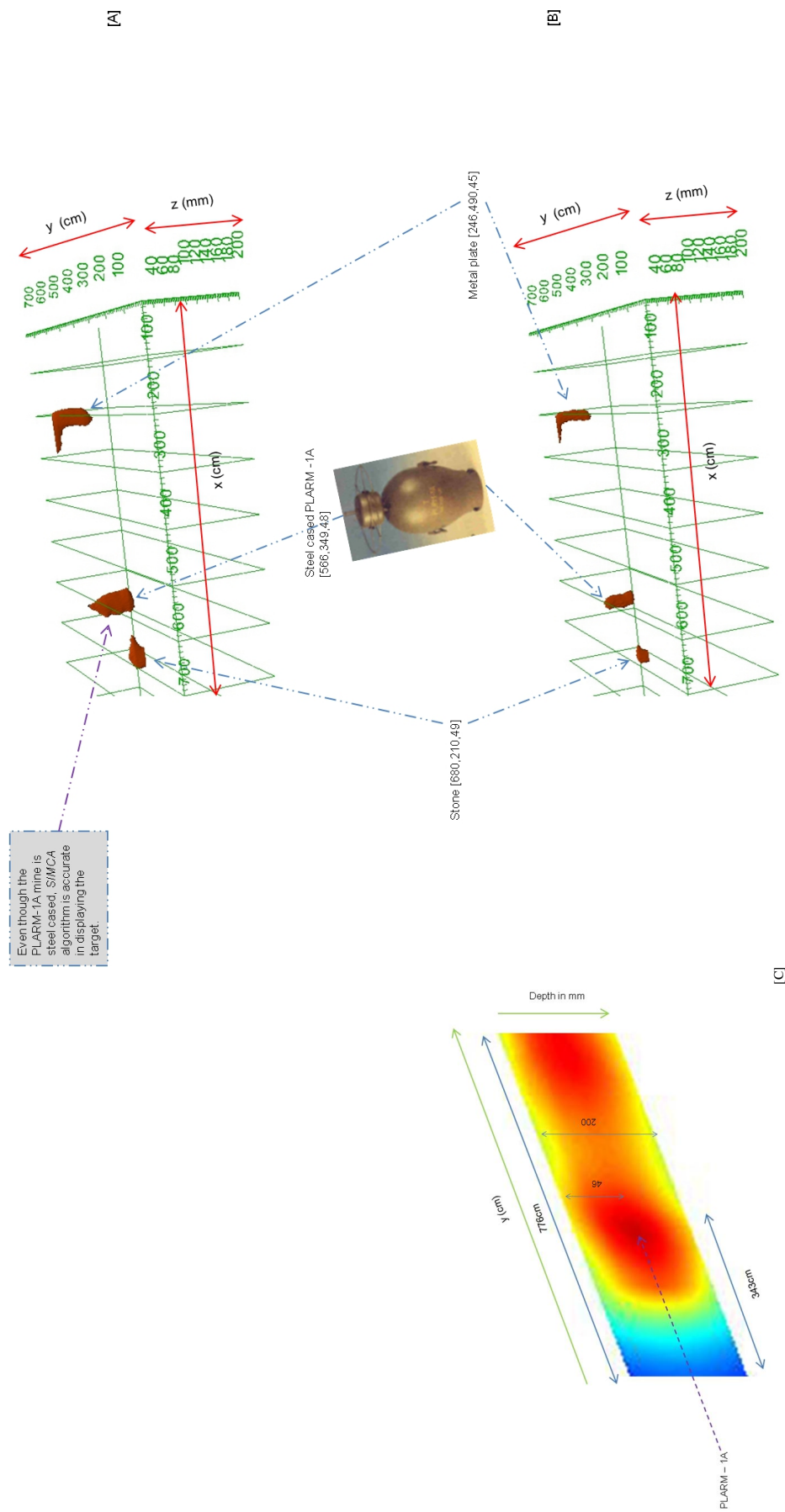


Figure 4.34: Reconstruction of volumes of real targets in a dry sandy soil using: [A]: SIMCA system after scanning by a GPR at optimised threshold = 230; [B]: Scheers et al's algorithm after scanning by a GPR at optimised threshold=252. Note steel cased mines are poorly reconstructed by the Scheers' algorithm.; [C]: Vertical cross-sectional slice showing steel cased PLARM-1A mine.

	Burial depth of steel cased PLARM-1A mine (cm)	Burial depth of metal plate
Ground truth	4.8	4.5
SIMCA	4.6	4.7
Scheers	5.1	4.1
Error in SIMCA	4.2%	4.4%
Error in Scheers	6.3%	8.9%

[A]

	Volume of steel cased PLARM-1A mine (cm) <sup>3</sup>	Volume of metal plate	Processing time (s)
Ground truth	600	280	-
SIMCA	602	274	0.9
Scheers	380	198	1.5
Error in SIMCA	0.3%	2.1%	-
Error in Scheers	36.7%	29.3%	-

[B]

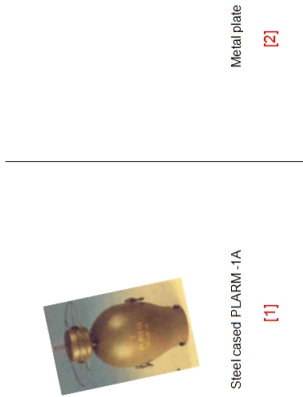


Table 4.12: [A]: Actual burial depth, depth obtained from the SIMCA method, depth obtained from the Scheers’s method for each of the targets in centimetres for Figure 4.34. The table also gives the percentage errors for both the SIMCA and Scheers algorithms; [B]: Actual Volume, Volume of reconstructed target for SIMCA system, Volume of reconstructed target for Scheers algorithm, and processing time (CPU time) for Figure 4.34. The volumes are in cubic centimetres and the processing time is in seconds.



### 4.6.3 Setup 3 - Wet clay conditions

The detection range of a GPR depends on the electrical conductivity in the ground and can be found using the following formulae (Jol, 1994):

$$\alpha = \frac{1.64 \cdot 10^3 \sigma}{\sqrt{K}} \quad (4.6.1)$$

where  $\sigma$  is the conductivity in mS/m and  $K$  is the permittivity. It is to be noted that the above equation does not include water relaxation losses which need to be added. The GPR signal travels with the least attenuation in signal amplitude in insulating materials (Lopera et al., 2005a). Clay soils as used in this setup are conductive and thus cause high attenuation of GPR signals. A compromise has to be reached between the penetration depth and the resolution when one selects a GPR system. As the water content increases and also the high frequency attenuation in wet materials increases, the penetration is reduced.

#### 4.6.3.1 A wooden cased mine, a plastic mine and a metallic plate

The wooden cased Model 43 mine is a rectangular shaped mine. The electromagnetic contrast between a mine and its environment is very important for an electromagnetic sensor such as the GPR. This electromagnetic contrast depends mainly on the soil in which the mine has been laid. In accordance with some studies (Redman et al., 2003), the largest reflectors in an APM are the detonators and the void. Also the circular cross sectional nature of the mine is seen in the vertical cross sectional slice.

The hinged box-type wooden cased Model 43 mine has been accurately reconstructed by the *SIMCA* algorithm and the fact that the mine is a hinged mine can be made out from the reconstruction. Again the small plastic M14 antipersonnel mine whose metallic parts are the steel striker tip and the detonator is accurately reproduced by the *SIMCA* algorithm. The circular contour of this mine is evident from the reconstruction.

### 4.6.4 Summary of the results

From the results it is quite evident that the *SIMCA* algorithm is able to reconstruct GPR images for a number of landmine targets and false targets such as metal plates. The results for the 3D visualization demonstrate that the algorithm is able to retrieve the geometry of the objects. For example from Figure 4.10, the *SIMCA* algorithm is considerably more accurate in displaying the plastic MAUS mine in comparison to the Scheers' method which is one of the main problems in landmine detection.

Furthermore in the same figure the *SIMCA* algorithm reproduces the wooden handle of the pistol much more accurately than the Scheers' algorithm. It was found from the researchers who buried this pistol that the pistol was not loaded with bullets and the Scheers' algorithm is only able to reconstruct the metallic spring of the magazine. Another example can be seen from Figure 4.17 where the glass bottle mine developed by the Colombian guerrillas is more accurately reconstructed

by the *SIMCA* algorithm when compared to the Scheers' algorithm.



**Wooden cased Model 43 Antipersonnel mine**

This is a hinged box-type mine which can be closed. The mine uses 200g block of TNT as its charge. Activation is accomplished by pressure on the lid, which causes a retaining pin in the fuse to be triggered.

Construction information:

- Rectangular
- Height = 40mm
- Width = 65mm
- Length = 190mm
- Weight = 0.42 kg
- Wooden case
- Explosive type – TNT

Figure 4.35: Details of the targets buried in Figure 4.36.  
(Cameo Landmine clearance)

The error rates for the volumes of the targets when compared to the actual volume of the targets for each of the *SIMCA* and Scheers et al method were given in tabular format. For example Tables 4.1 and 4.4 for two different soil conditions.

Furthermore, since in landmine detection the estimation of the depth is of concern, Tables 4.1 and 4.4 gave the actual burial depths, along with the depths found using the *ParaView* software for each of the two methods for two different soil conditions, the tables also outline the error rates for the burial depths. Again, the validation section of this paper discusses these error rates.

The CPU times for running the algorithms were given by tables. For example from Tables 4.1 and 4.4 it can also be noticed that the *SIMCA* algorithm runs quicker than the Scheers' method. It is noticed from Table 4.1 that the *SIMCA* algorithm runs in half the time compared to the Scheers' method for the wet sandy soil condition. Furthermore from Table 4.4 it can be seen that the *SIMCA* method runs at approximately 5 times faster than the Scheers' method for the dry sandy soil. This lower processing time is an important factor for an efficient and practical algorithm because time and hence battery power is a crucial factor using an GPR in an actual landmine clearance situation.

The visualization of a complete 3D data-cube requires powerful computing and fast graphics cards but the amount of data has been significantly reduced using isosurfaces and only considering the necessary data during correlation. Furthermore, the *SIMCA* algorithm only correlates between the intersecting parts of the kernel and the B scans as is shown in Algorithm 1; hence reducing the processing time. The order of magnitude of the algorithm is:

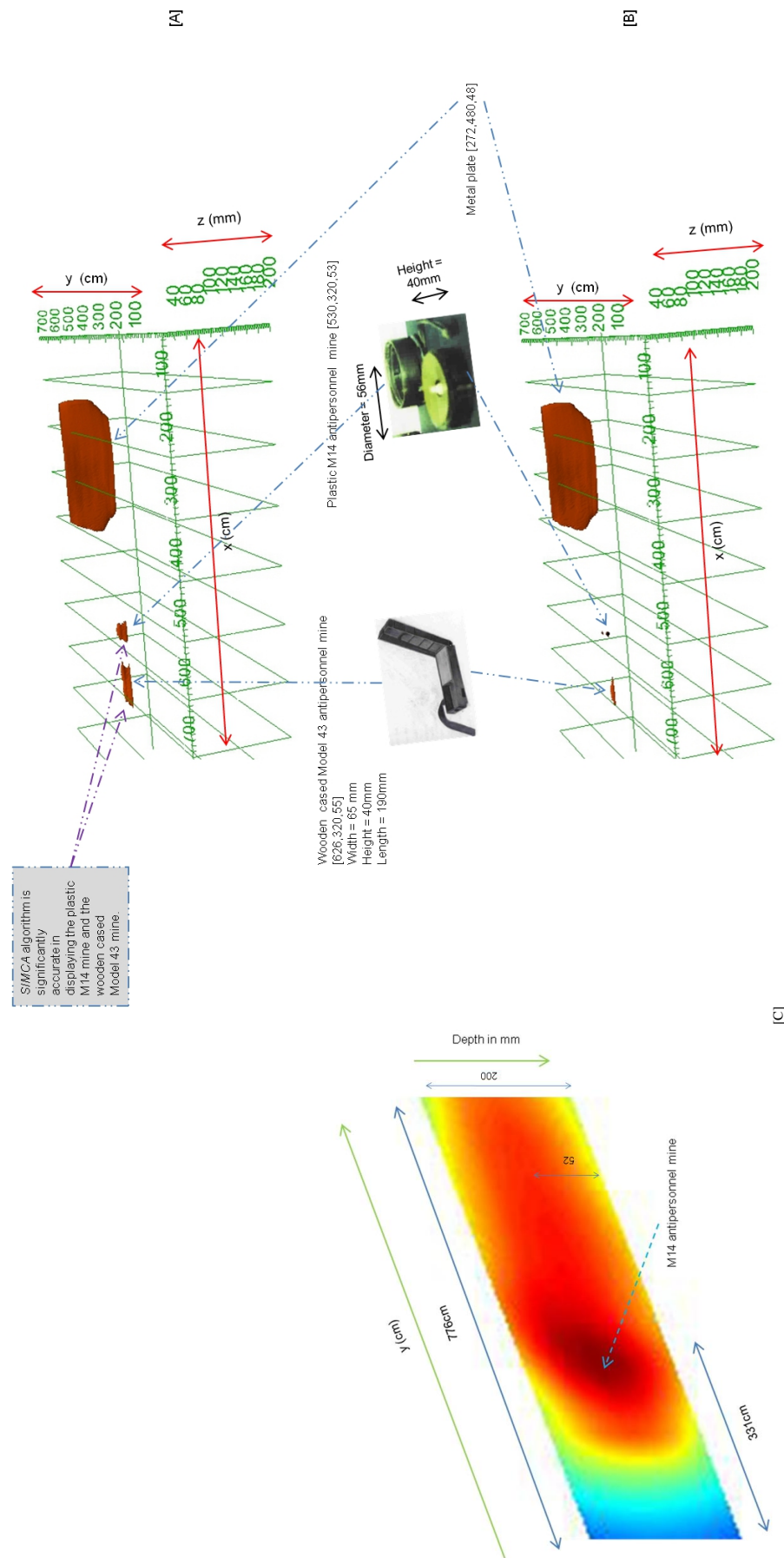


Figure 4.36: Reconstruction of volumes of real targets in a wet clay soil using: [A]: SIMCA system after scanning by a GPR at optimised threshold = 230; [B]: Scheers et al's algorithm after scanning by a GPR at optimised threshold=252. Note SIMCA algorithm can reconstruct plastic mines more accurately; [C]: Vertical cross-sectional slice showing plastic M14 mine.

	Burial depth of plastic M14 mine (cm)	Burial depth of wooden cased Model 43 mine	Burial depth of metal plate
Ground truth	5.3	5.5	4.8
SIMCA	5.2	5.7	4.6
Scheers	4.9	5.0	5.2
Error in SIMCA	1.9%	3.6%	4.2%
Error in Scheers	7.5%	9.1%	8.3%

[A]

	Volume of plastic M14 mine (cm) <sup>3</sup>	Volume of wooden cased Model 43 mine	Volume of metal plate	Processing time (s)
Ground truth	99	494	2300	-
SIMCA	96	489	2270	0.5
Scheers	17	244	2230	1.3
Error in SIMCA	3.0%	1.0%	1.3%	-
Error in Scheers	82.8%	50.6%	3.0%	-

[B]



Table 4.13: [A]: Actual burial depth, depth obtained from the *SIMCA* method, depth obtained from the Scheers’s method for each of the targets in centimetres for Figure 4.36. The table also gives the percentage errors for both the *SIMCA* and Scheers algorithms.; [B]: Actual Volume, Volume of reconstructed target for *SIMCA* system, Volume of reconstructed target for Scheers algorithm, and processing time (CPU time) for Figure 4.36. The volumes are in cubic centimetres and the processing time is in seconds.

$$(x \times y \times z) \times (m \times n \times o) \quad (4.6.2)$$

where  $x$ ,  $y$  and  $z$  are the dimensions of the B scan and  $m$ ,  $n$  and  $o$  are the dimensions of the kernel. The *SIMCA* algorithm collapses the hyperbolae to their diffraction peaks and uncovers the true 3D image reconstruction of the target and hence their dimensions. However the reconstructed images alone may not be enough to accurately classify between mines and clutters, but the geometry information will be very useful for improving the discrimination based on the features of the target.

There are many factors which affect the ability of a GPR to locate landmines. These include:

1. Type of landmine material and whether the mine is metallic or plastic.
2. The soil conditions and its texture and moisture.
3. The radar frequency.

Metallic landmines are easier to detect than plastic landmines but the *SIMCA* algorithm has demonstrated that it helps in the detection of plastic landmines. As also stated previously in the background and literature survey portion of this thesis in Chapter 2, increasing the soils' moisture content, regardless of the soil texture will ease the detection of plastic landmines and worsen the detection of metallic landmines. Also increasing the percentage clay in the soil will cause the same effect as the moisture content. The later statement is evident from the reconstruction in Figure 4.36 where for the plastic M14 antipersonnel mine in wet clay the reconstruction is much more accurate than the reconstruction in Figure 4.26 in a dry sandy soil.

Since the performance of a GPR is influenced mainly by the dielectric permittivity as it governs electromagnetic (EM) wave propagation, soil dielectric permittivity is an important factor which depends on the volumetric water content. The volumetric water content of the soil varies over time and since in field conditions some mines have been in soil over a long period of time, where the soil properties change; the ability to locate a landmine varies accordingly over time, depending on the property of the soil.

In order to test this, varying soil conditions have been used and the corresponding isosurfaces created. Figure 4.10 is in a wet sandy soil, whereas Figure 4.17 is in a dry sandy soil. It was found in Lopera and Milisavljevic (2007) that the ability of GPR to detect landmines depends to a great extent on the landmine type, water content of the host soil, utilized radar frequency, and soil texture. Increasing the soil's moisture content, regardless of soil texture, eases the detection of plastic landmines and exacerbates the detection of the metallic mines. This is evident in Figure 4.17 which is in a dry sandy soil, the metallic mine (M26) has a much better reconstruction and the circular top section of the mine is completely reconstructed; whereas in Figure 4.10 the M26 (metallic) mine in wet sandy conditions the whole circular top section of the mine is not completely reconstructed. This is because increasing the moisture content of the soil will decrease the dielectric contrast for metallic landmines and increase the dielectric constant for non-metallic landmines. Also because the diffraction from plastic landmines is mainly weaker than its metallic counterpart, the contrast between the image of the object and the background is relatively lower than in the metallic case (Song et al., 2006). Hence the type of the mine determines the accuracy of the reconstructions.

The glass bottle antipersonnel mine is a sophisticated mine, made in an artisan way and contains less metal, but the *SIMCA* algorithm can still show the shape of the target.

Although various targets are not landmines (such as the metal plate), the algorithm can generate meaningful isosurfaces which may allow human users to distinguish between mine and non-mine targets from the isosurfaces.

Another important thing to note is in Figures 4.10 and 4.17, the M26 antipersonnel mine has been buried in an oblique position (about  $60^\circ$ ); the isosurface shows the obliqueness of the mine.

Not only do the isosurfaces give enough depth resolution to distinguish the reflections on the targets from the air-ground reflections, but also give enough resolution in the lateral direction to give an idea of the shape of the target.

Furthermore, the landmines are usually placed within 10cm of the ground surface and are designed to explode upon encountering a triggering stimulus. But in this depth region the soil surface presents a severely cluttered environment to the GPR waveform and one can notice the accurate reconstruction of the glass bottle mine buried at only 4.8cm.

Often in field situations, one does not know exactly the soil electrical parameters or the burial depth of the target. Therefore the next section explores this phenomena and comes to a conclusion on the sensitivity of the *SIMCA 3D* technique to such factors.

## 4.7 Sensitivity of the algorithm to permittivity and depth changes

As a *priori* one does not know the depth of the buried object or the soil electrical parameters, therefore in order to test the effect of this on the reconstructions the following analysis has been carried out. Also please note that ways of having a library of kernels and in carrying out correlations based on these kernels is considered. The final concluding paragraph of this section also gives some light into this issue.

In order to test the sensitivity of the algorithm to permittivity and depth changes, the kernel is built using the GPR simulator at the correct depth of 5.1cm and using the correct properties of the soil. Then correct parameters are used but used depths of 6cm and 12cm respectively to build the kernel. Finally the correct simulated target depth is used but the wrong soil parameters. The next set of figures show the effects on the reconstructions on using the above parameters. For example from Figures 4.37 and 4.38.

Also shown for each soil setup is the resulting volumetric error rates compared to the ground truth error rates. For example Tables 4.14 and 4.15.

What is noticeable in the error rates is that the highest percentage errors are obtained when using the correct simulated target depth but the wrong soil parameters.

It can be seen and judged from the reconstructed isosurfaces that changing the depth at which the kernel is constructed does not affect the reconstruction of the objects and the same results are produced for the range of depths considered. This is further backed by the Tables underneath each of the reconstructed diagrams where the percentage errors for each of the reconstructions when compared to the ground truth are given.

From the tables it is evident that although acceptable the highest error rates are produced when using the correct simulated target depth but wrong soil parameters.

The maximum error rate is only 5.5% whilst the minimum error rate is 0.1%.

	[A]		[B]		[C]		[D]	
	1	2	1	2	1	2	1	2
Ground truth volume ( $cm^3$ )	405	200	405	200	405	200	405	200
Volume from <i>SIMCA</i> ( $cm^3$ )	396	196	399	195	394	193	426	210
Error (%)	2.2	2.0	1.5	2.5	2.7	3.5	5.2	5.0



Plastic APM 29 antipersonnel mine

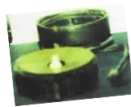
[1]

Metal plate

[2]

Table 4.19: Actual volume, volume from *SIMCA* reconstructed isosurface to test the sensitivity of *SIMCA* algorithm to depth and permittivity changes when building a kernel, Percentage error. For [A]: Simulated target depth at 5.1cm and using correct soil parameters; [B]: Simulated target depth at 6cm and using correct soil parameters; [C]: Simulated target depth at 12cm and using correct soil parameters; [D]: correct simulated target depth but wrong soil parameters for Figure 4.40. All volumes are in cubic centimetres.

	[A]			[B]			[C]			[D]		
	1	2	3	1	2	3	1	2	3	1	2	3
Ground truth volume ( $cm^3$ )	99	148	400	99	148	400	99	148	400	99	148	400
Volume from <i>SIMCA</i> ( $cm^3$ )	101	150	398	96	150	395	97	143	409	104	156	421
Error (%)	2.0	1.4	0.5	3.0	1.4	1.3	2.0	3.4	2.3	5.1	5.4	5.3



Plastic M14 antipersonnel mine

[1]



Plastic PRB M409 antipersonnel mine

[2]

Metal plate

[3]

Table 4.20: Actual volume, volume from *SIMCA* reconstructed isosurface to test the sensitivity of *SIMCA* algorithm to depth and permittivity changes when building a kernel, Percentage error. For [A]: Simulated target depth at 5.1cm and using correct soil parameters; [B]: Simulated target depth at 6cm and using correct soil parameters; [C]: Simulated target depth at 12cm and using correct soil parameters; [D]: correct simulated target depth but wrong soil parameters for Figure 4.42. All volumes are in cubic centimetres.





	[A]			[B]			[C]			[D]		
	1	2	3	1	2	3	1	2	3	1	2	3
Ground truth volume (cm) <sup>3</sup>	286	500	711	286	500	711	286	500	711	286	500	711
Volume from SIMCA (cm) <sup>3</sup>	280	491	698	276	486	696	273	480	683	301	524	741
Error (%)	2.1	1.8	1.8	3.5	2.8	2.1	4.5	4.0	3.9	5.2	4.8	4.2



Table 4.14: Actual volume, volume from SIMCA reconstructed isosurface to test the sensitivity of SIMCA algorithm to depth and permittivity changes when building a kernel, Percentage error. For [A]: Simulated target depth at 5.1cm and using correct soil parameters; [B]: Simulated target depth at 6cm and using correct soil parameters; [C]: Simulated target depth at 12cm and using correct soil parameters; [D]: correct simulated target depth but wrong soil parameters for Figure 4.37. All volumes are in cubic centimetres.

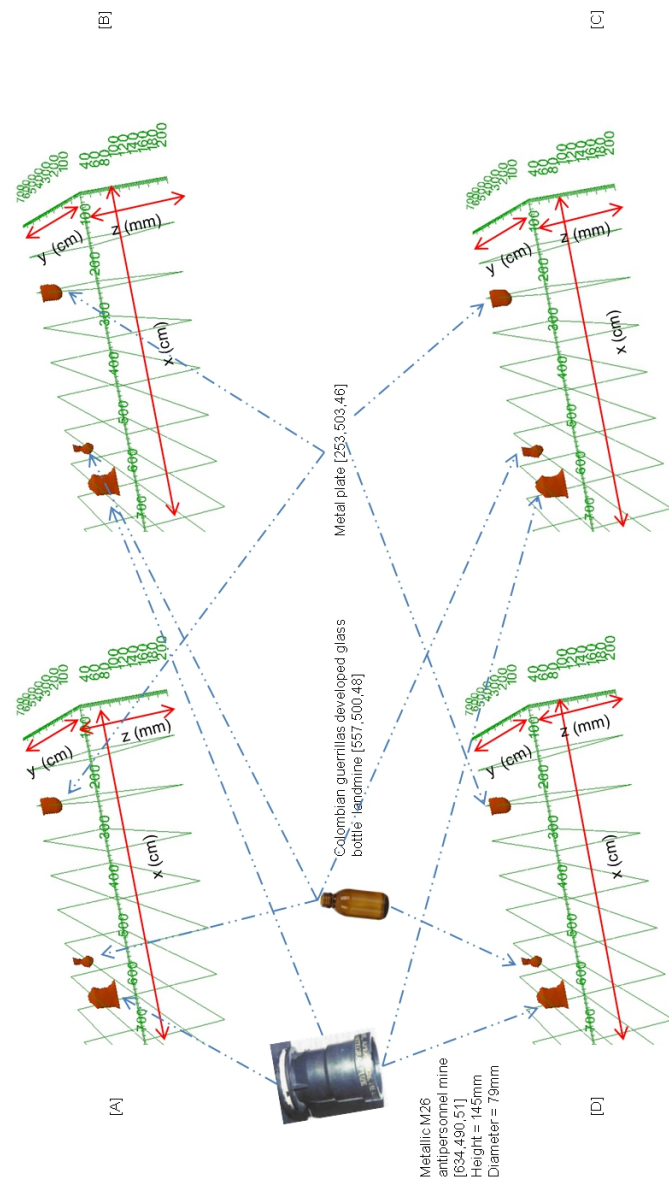
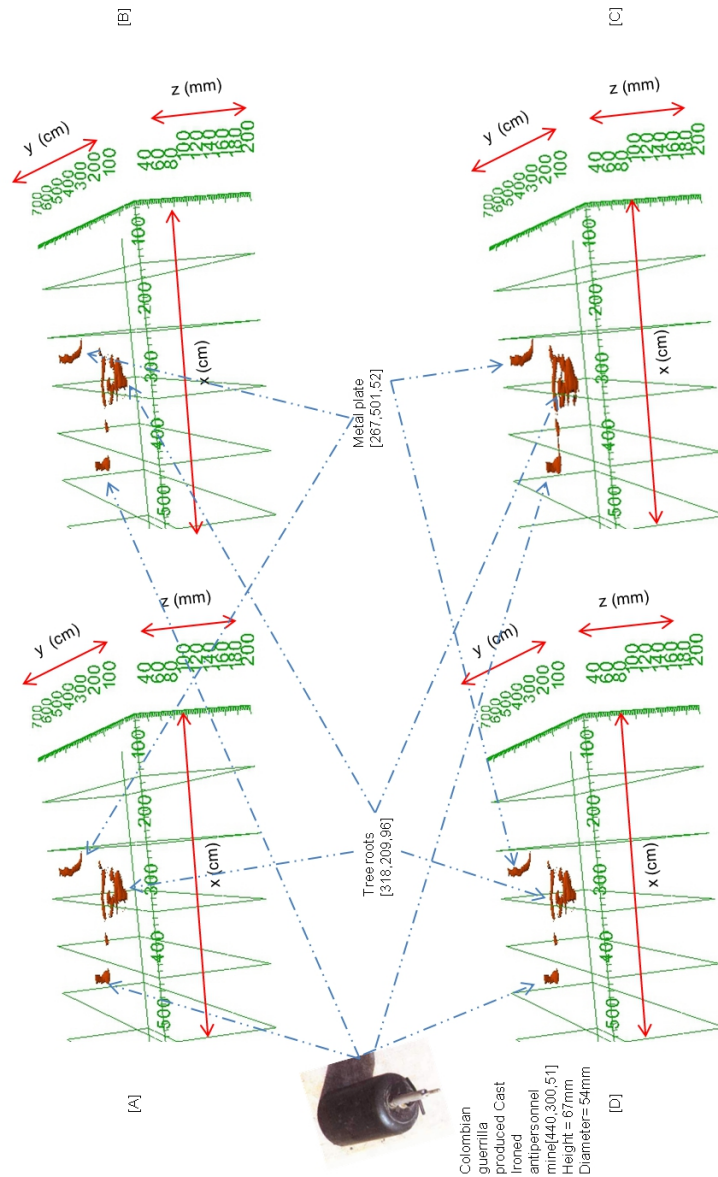


Figure 4.38: Sensitivity of *SIMCA* algorithm to depth and permittivity changes when building a kernel. Clockwise from left: [A]: Simulated target depth at 5.1cm and using correct soil parameters; [B]: Simulated target depth at 6cm and using correct soil parameters; [C]: Simulated target depth at 12cm and using correct soil parameters; [D]: correct simulated target depth but wrong soil parameters.

	[A]			[B]			[C]			[D]		
	1	2	3	1	2	3	1	2	3	1	2	3
Ground truth volume (cm) <sup>3</sup>	711	480	670	711	480	670	711	480	670	711	480	670
Volume from SIMCA (cm) <sup>3</sup>	697	479	678	695	475	682	689	470	686	746	500	700
Error (%)	2.0	0.2	1.2	2.3	1.0	1.8	3.1	2.1	2.4	4.9	4.2	4.5



Table 4.15: Actual volume, volume from SIMCA reconstructed isosurface to test the sensitivity of SIMCA algorithm to depth and permittivity changes when building a kernel, Percentage error. For [A]: Simulated target depth at 5.1cm and using correct soil parameters; [B]: Simulated target depth at 6cm and using correct soil parameters; [C]: Simulated target depth at 12cm and using correct soil parameters; [D]: correct simulated target depth but wrong soil parameters for Figure 4.38. All volumes are in cubic centimetres.



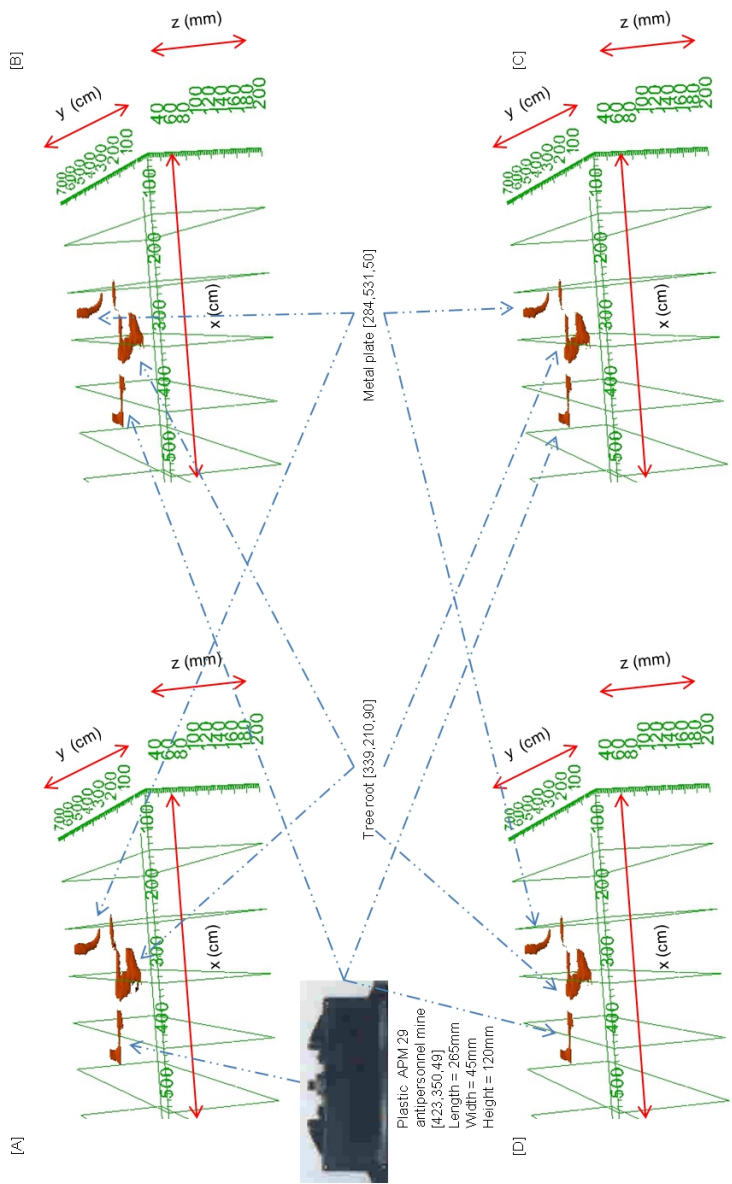


Figure 4.40: Sensitivity of *SIMCA* algorithm to depth and permittivity changes when building a kernel. Clockwise from left: [A]: Simulated target depth at 5.1cm and using correct soil parameters; [B]: Simulated target depth at 6cm and using correct soil parameters; [C]: Simulated target depth at 12cm and using correct soil parameters; [D]: correct simulated target depth but wrong soil parameters.

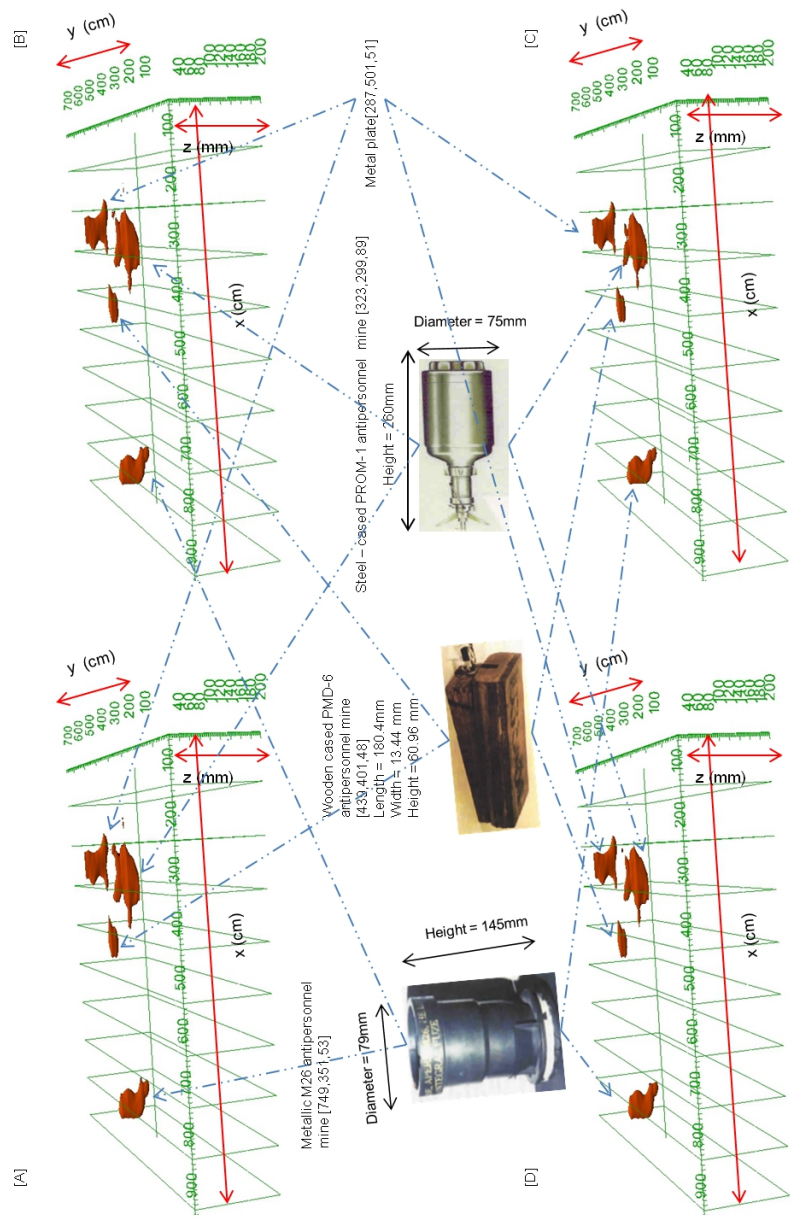


Figure 4.41: Sensitivity of *SIMCA* algorithm to depth and permittivity changes when building a kernel. Clockwise from left: [A]: Simulated target depth at 5.1cm and using correct soil parameters; [B]: Simulated target depth at 6cm and using correct soil parameters; [C]: Simulated target depth at 12cm and using correct soil parameters; [D]: correct simulated target depth but wrong soil parameters.

	[A]				[B]				[C]				[D]			
	1	2	3	4	1	2	3	4	1	2	3	4	1	2	3	4
Ground truth volume (cm) <sup>3</sup>	1149	143	711	830	1149	143	711	830	1149	143	711	830	1149	143	711	830
Volume from SIMCA (cm) <sup>3</sup>	1169	146	708	840	1141	147	715	841	1162	149	700	815	1173	150	731	849
Error (%)	1.7	2.1	0.4	1.2	0.7	2.8	0.6	1.3	1.1	4.2	1.5	1.8	2.1	4.9	2.8	2.3



Table 4.16: Actual volume, volume from SIMCA reconstructed isosurface to test the sensitivity of SIMCA algorithm to depth and permittivity changes when building a kernel, Percentage error. For [A]: Simulated target depth at 5.1cm and using correct soil parameters; [B]: Simulated target depth at 6cm and using correct soil parameters; [C]: Simulated target depth at 12cm and using correct soil parameters; [D]: correct simulated target depth but wrong soil parameters for Figure 4.41. All volumes are in cubic centimetres.



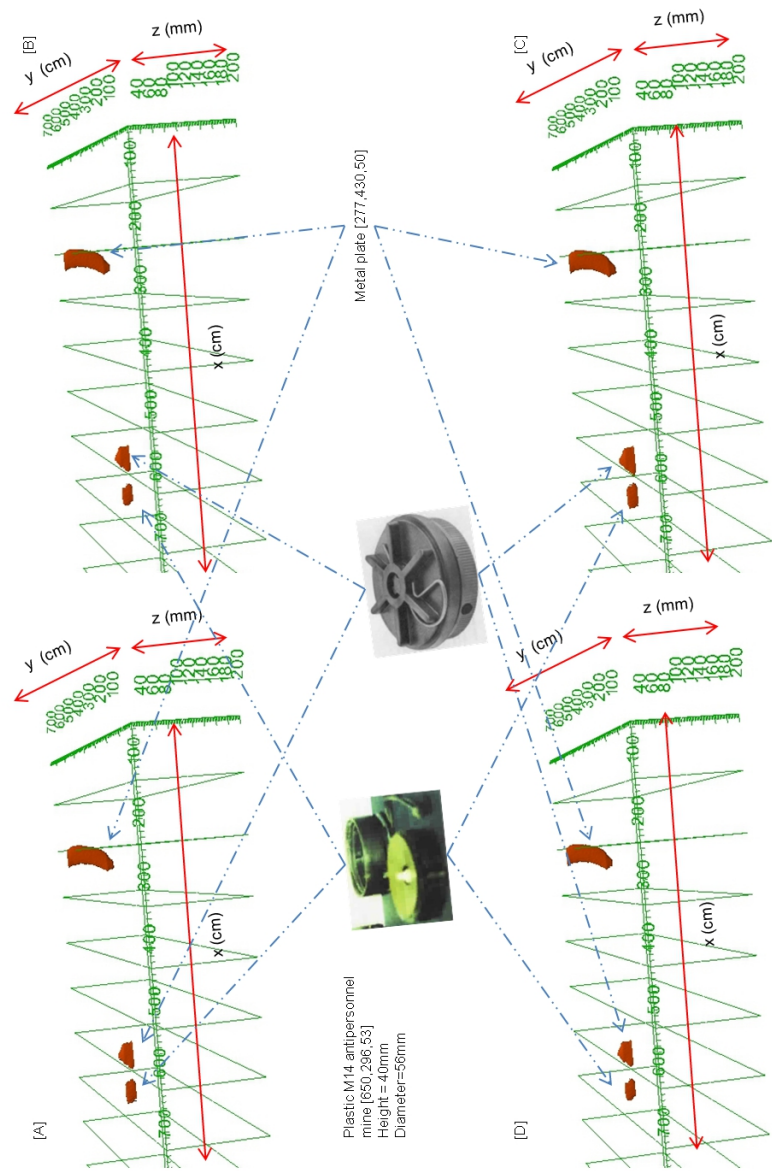


Figure 4.42: Sensitivity of SIMCA algorithm to depth and permittivity changes when building a kernel. Clockwise from left: [A]: Simulated target depth at 12cm and using correct soil parameters; [B]: Simulated target depth at 6cm and using correct soil parameters; [C]: Simulated target depth at 12cm and using wrong soil parameters; [D]: Simulated target depth at 6cm and using wrong soil parameters.



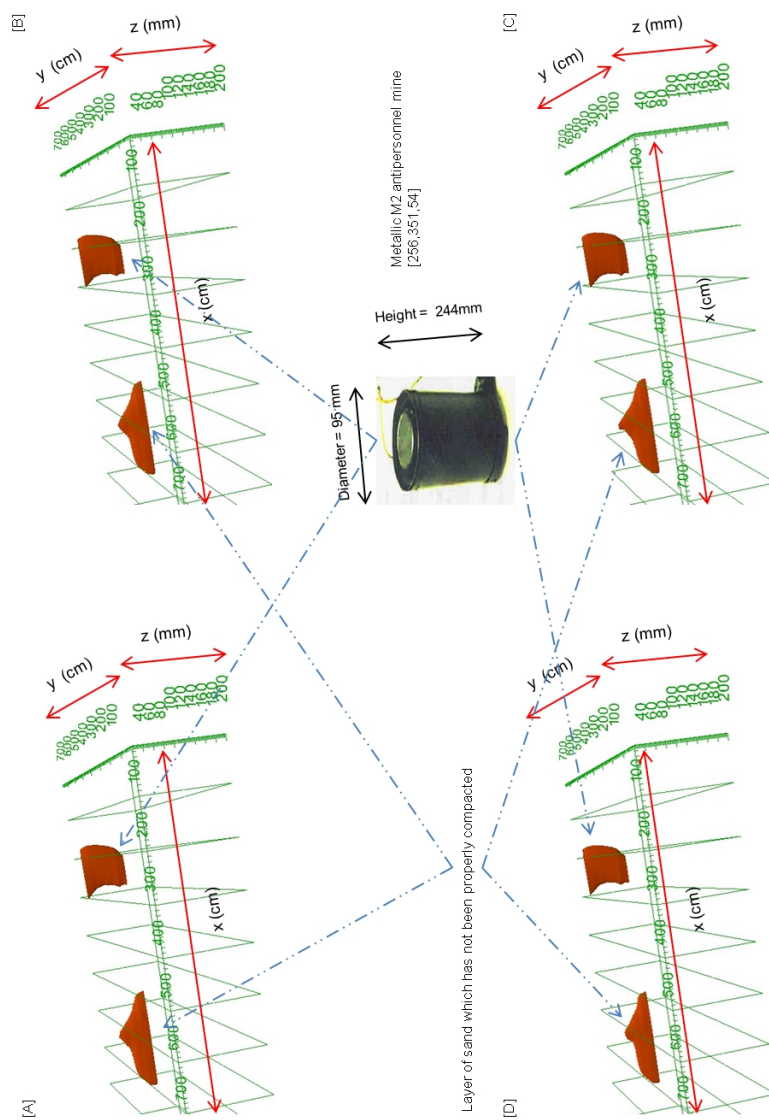


Figure 4.43: Sensitivity of *SIMCA* algorithm to depth and permittivity changes when building a kernel. Clockwise from left: [A]: Simulated target depth at 5.1cm and using correct soil parameters; [B]: Simulated target depth at 6cm and using correct soil parameters; [C]: Simulated target depth at 12cm and using correct soil parameters; [D]: correct simulated target depth but wrong soil parameters.

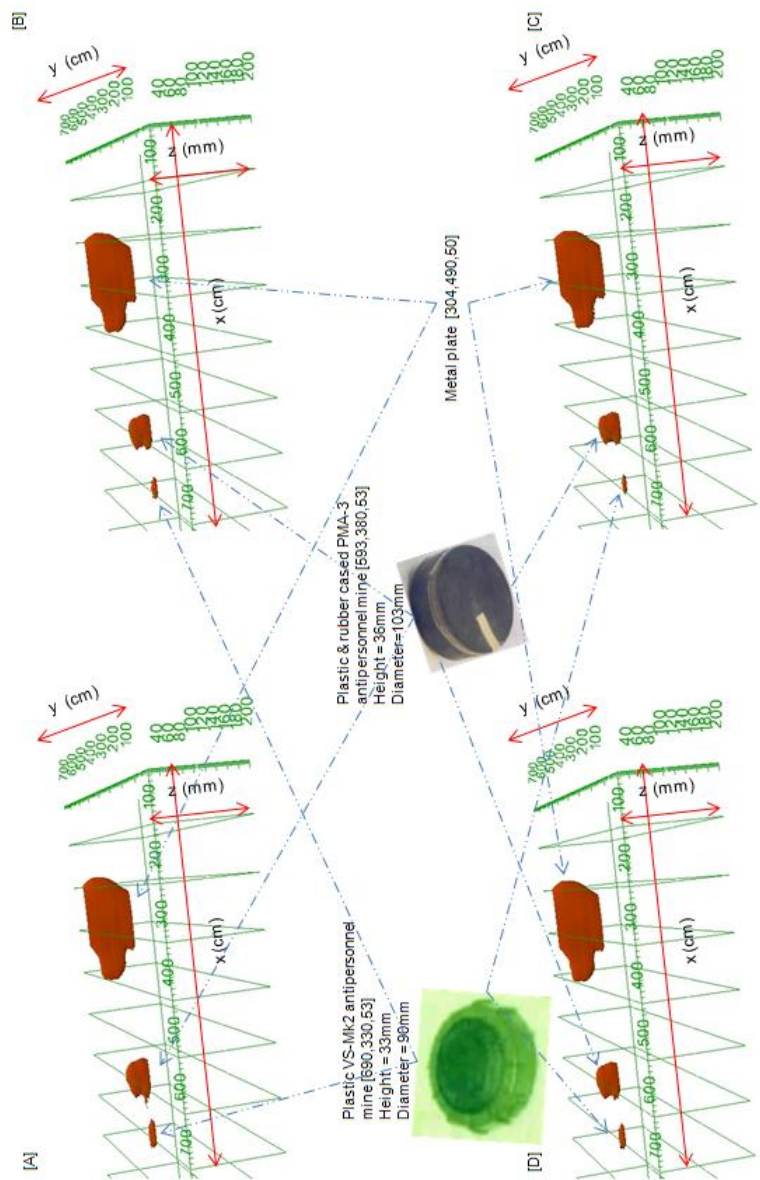


Figure 4.44: Sensitivity of *SIMCA* algorithm to depth and permittivity changes when building a kernel. Clockwise from left: [A]: Simulated target depth at 5.1cm and using correct soil parameters; [B]: Simulated target depth at 6cm and using correct soil parameters; [C]: Simulated target depth at 12cm and using correct soil parameters; [D]: correct simulated target depth but wrong soil parameters.

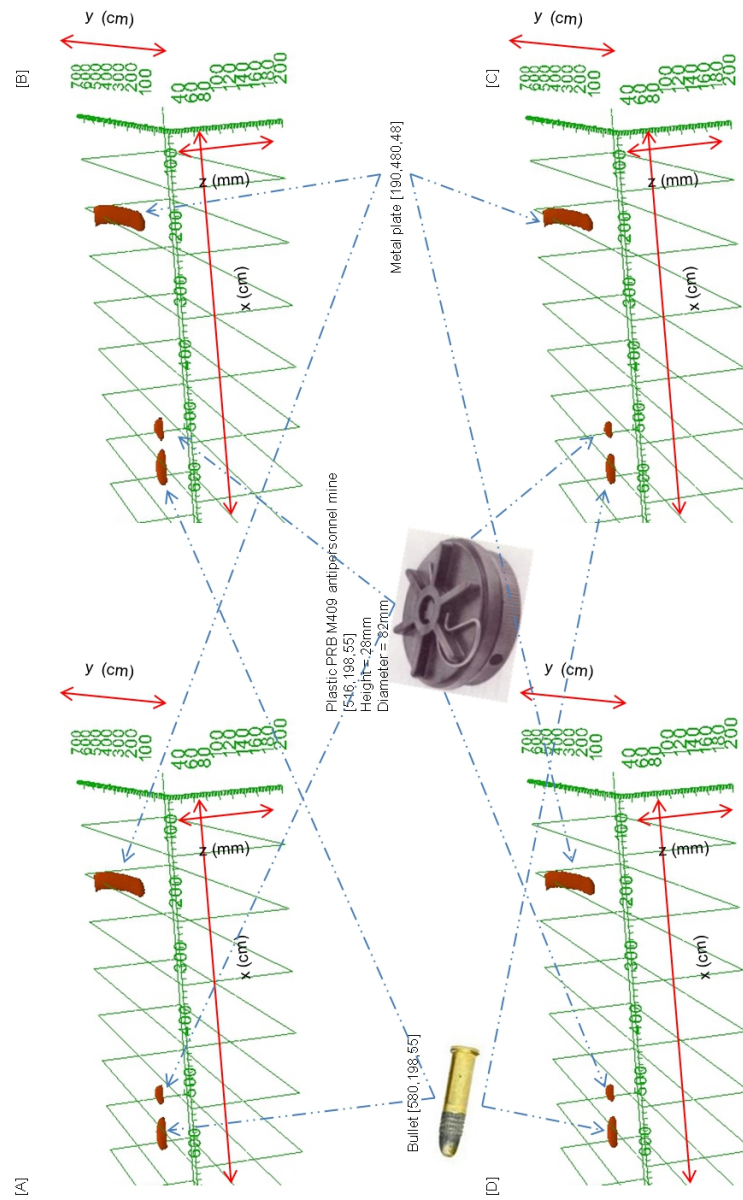


Figure 4.45: Sensitivity of *SIMCA* algorithm to depth and permittivity changes when building a kernel. Clockwise from left: [A]: Simulated target depth at 5.1cm and using correct soil parameters; [B]: Simulated target depth at 6cm and using correct soil parameters; [C]: Simulated target depth at 12cm and using correct soil parameters; [D]: correct simulated target depth but wrong soil parameters.

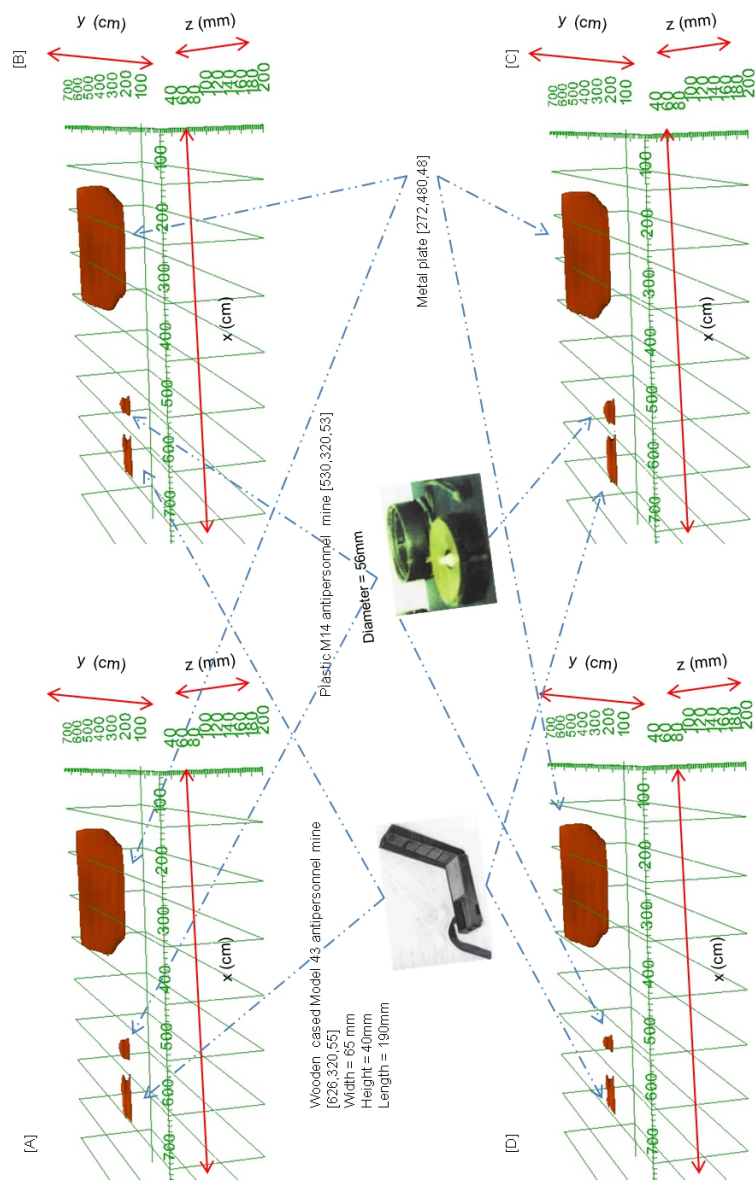


Figure 4.46: Sensitivity of *SIMCA* algorithm to depth and permittivity changes when building a kernel. Clockwise from left: [A]: Simulated target depth at 5.1cm and using correct soil parameters; [B]: Simulated target depth at 6cm and using correct soil parameters; [C]: Simulated target depth at 12cm and using correct soil parameters; [D]: correct simulated target depth but wrong soil parameters.

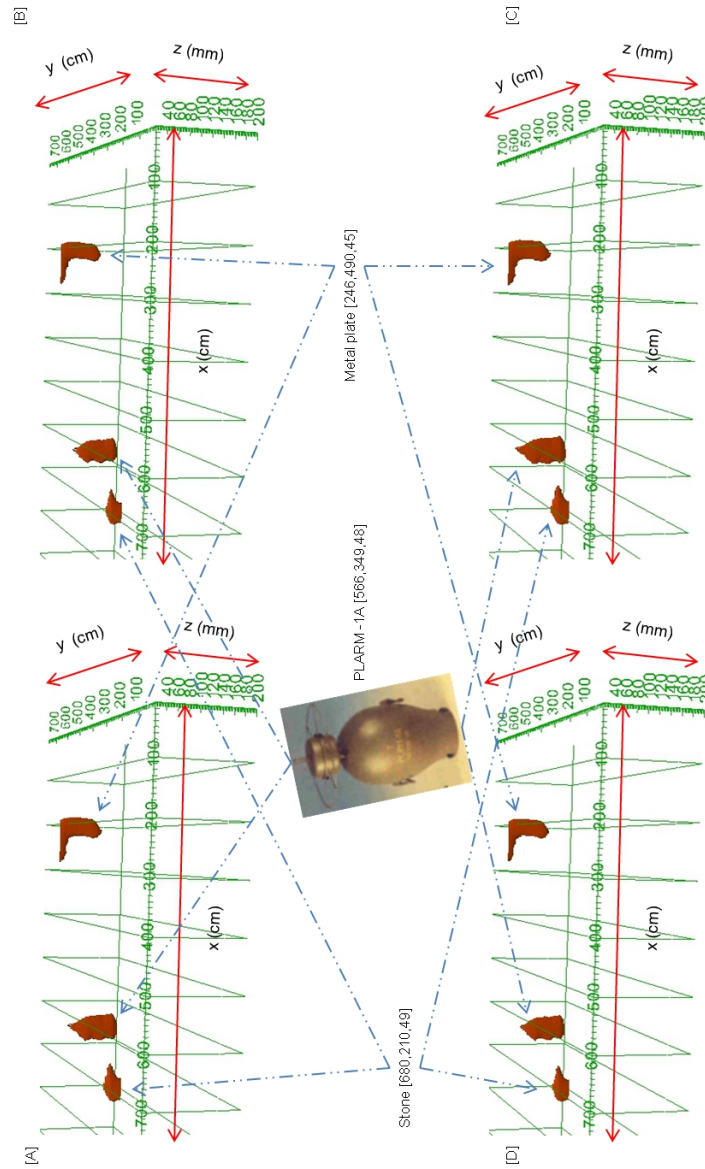


Figure 4.47: Sensitivity of *SIMCA* algorithm to depth and permittivity changes when building a kernel. Clockwise from left: [A]: Simulated target depth at 12cm and using correct soil parameters; [B]: Simulated target depth at 6cm and using correct soil parameters; [C]: Simulated target depth at 12cm and using wrong soil parameters; [D]: Simulated target depth at 6cm and using wrong soil parameters.



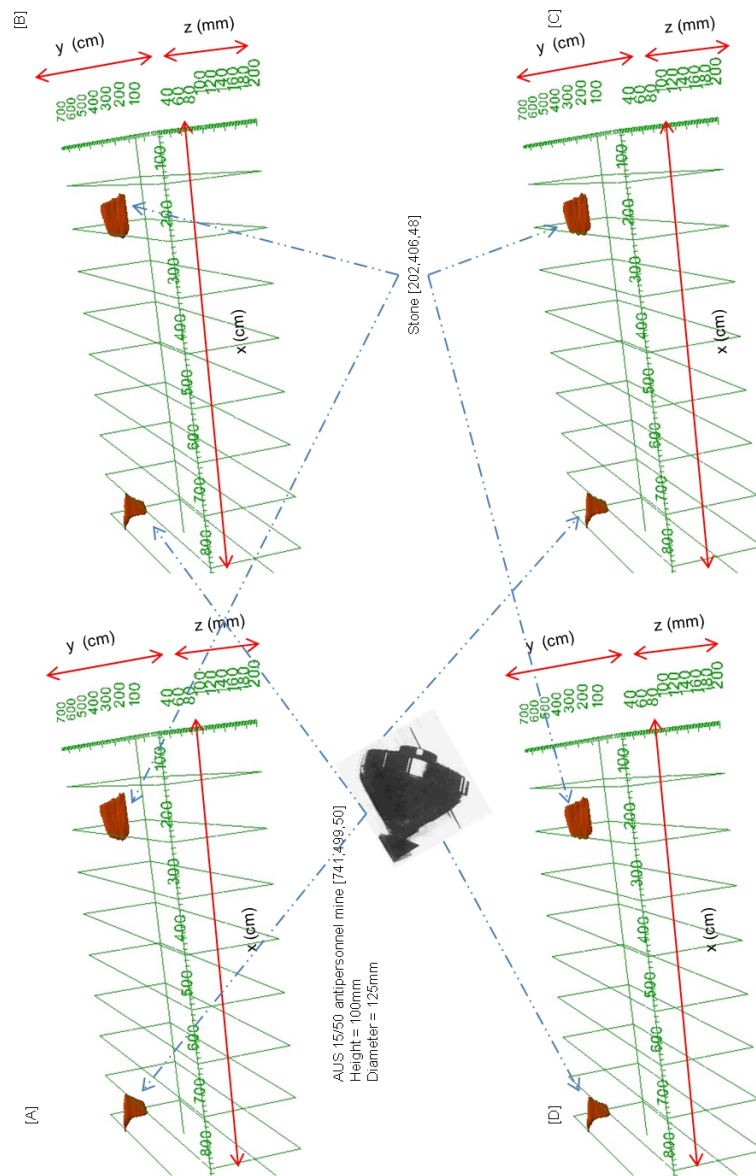


Figure 4.48: Sensitivity of *SIMCA* algorithm to depth and permittivity changes when building a kernel. Clockwise from left: [A]: Simulated target depth at 5.1cm and using correct soil parameters; [B]: Simulated target depth at 6cm and using correct soil parameters; [C]: Simulated target depth at 12cm and using correct soil parameters; [D]: correct simulated target depth but wrong soil parameters.

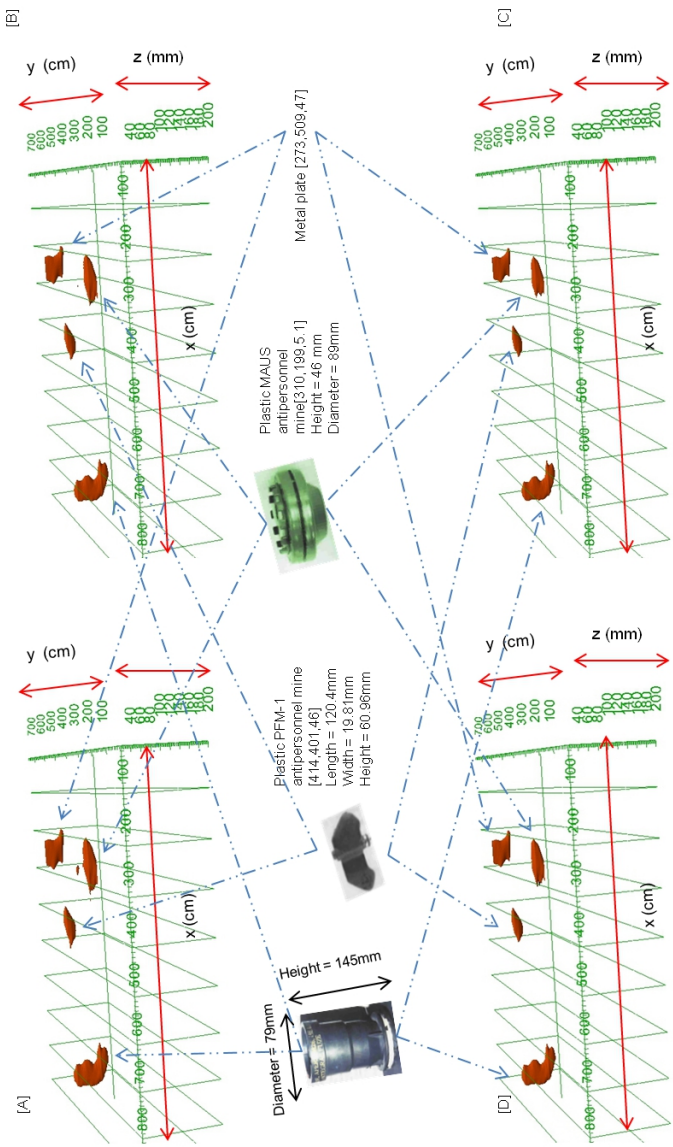


Figure 4.49: Sensitivity of SIMCA algorithm to depth and permittivity changes when building a kernel. Clockwise from left: [A]: Simulated target depth at 5.1cm and using correct soil parameters; [B]: Simulated target depth at 6cm and using correct soil parameters; [C]: Simulated target depth at 12cm and using correct soil parameters; [D]: correct simulated target depth but wrong soil parameters.

	[A]				[B]				[C]				[D]			
	1	2	3	4	1	2	3	4	1	2	3	4	1	2	3	4
Ground truth volume (cm) <sup>3</sup>	711	146	286	680	711	146	286	680	711	146	286	680	711	146	286	680
Volume from SIMCA (cm) <sup>3</sup>	708	144	288	671	720	148	290	669	730	143	280	700	740	154	300	710
Error (%)	0.4	1.4	0.7	1.3	1.3	1.4	1.4	1.6	2.7	2.1	2.1	2.9	4.1	5.5	4.9	4.4



Table 4.17: Actual volume, volume from *SIMCA* reconstructed isosurface to test the sensitivity of *SIMCA* algorithm to depth and permittivity changes when building a kernel, Percentage error. For [A]: Simulated target depth at 5.1cm and using correct soil parameters; [B]: Simulated target depth at 6cm and using correct soil parameters; [C]: Simulated target depth at 12cm and using correct soil parameters; [D]: correct simulated target depth but wrong soil parameters for Figure 4.49. All volumes are in cubic centimetres.



	[A]		[B]		[C]		[D]	
	1	2	1	2	1	2	1	2
Ground truth volume ( $cm^3$ )	153	198	153	198	153	198	153	198
Volume from <i>SIMCA</i> ( $cm^3$ )	154	196	151	194	149	192	161	208
Error (%)	0.7	1.0	1.3	2.0	2.6	3.0	5.2	5.1



Colombian guerrilla produced Cast Ironed antipersonnel

[1]

Metal plate

[2]

Table 4.18: Actual volume, volume from *SIMCA* reconstructed isosurface to test the sensitivity of *SIMCA* algorithm to depth and permittivity changes when building a kernel, Percentage error. For [A]: Simulated target depth at 5.1cm and using correct soil parameters; [B]: Simulated target depth at 6cm and using correct soil parameters; [C]: Simulated target depth at 12cm and using correct soil parameters; [D]: correct simulated target depth but wrong soil parameters for Figure 4.39. All volumes are in cubic centimetres.

	[A]	[B]	[C]	[D]
	1	1	1	1
Ground truth volume ( $cm^3$ )	1767	1767	1767	1767
Volume from <i>SIMCA</i> ( $cm^3$ )	1769	1739	1709	1860
Error (%)	0.1	1.6	3.3	5.2



Metallic M2 antipersonnel mine

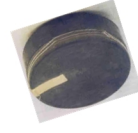
[1]

Table 4.21: Actual volume, volume from *SIMCA* reconstructed isosurface to test the sensitivity of *SIMCA* algorithm to depth and permittivity changes when building a kernel, Percentage error. For [A]: Simulated target depth at 5.1cm and using correct soil parameters; [B]: Simulated target depth at 6cm and using correct soil parameters; [C]: Simulated target depth at 12cm and using correct soil parameters; [D]: correct simulated target depth but wrong soil parameters for Figure 4.43. All volumes are in cubic centimetres.

	[A]			[B]			[C]			[D]		
	1	2	3	1	2	3	1	2	3	1	2	3
Ground truth volume ( $cm^3$ )	210	306	2103	210	306	2103	210	306	2103	210	306	2103
Volume from SIMCA ( $cm^3$ )	208	299	2113	214	310	2080	204	314	2169	221	320	2216
Error (%)	1.0	2.3	0.5	1.9	1.3	1.1	2.9	2.6	3.1	5.2	4.6	5.4

Plastic VS-Mk2  
antipersonnel mine

[1]

Plastic & rubber cased PMA-3  
antipersonnel mine

[2]

Metal plate

[3]

Table 4.22: Actual volume, volume from *SIMCA* reconstructed isosurface to test the sensitivity of *SIMCA* algorithm to depth and permittivity changes when building a kernel, Percentage error. For [A]: Simulated target depth at 5.1cm and using correct soil parameters; [B]: Simulated target depth at 6cm and using correct soil parameters; [C]: Simulated target depth at 12cm and using correct soil parameters; [D]: correct simulated target depth but wrong soil parameters for Figure 4.44. All volumes are in cubic centimetres.

	[A]			[B]			[C]			[D]		
	1	2	3	1	2	3	1	2	3	1	2	3
Ground truth volume ( $cm^3$ )	220	148	316	220	148	316	220	148	316	220	148	316
Volume from SIMCA ( $cm^3$ )	222	146	314	223	145	309	214	152	322	232	156	330
Error (%)	0.9	1.4	0.6	1.4	2.0	2.2	2.7	2.7	1.9	5.5	5.4	4.4



Bullet

[1]



Plastic PRB M409 antipersonnel mine

[2]

Metal plate

[3]

Table 4.23: Actual volume, volume from *SIMCA* reconstructed isosurface to test the sensitivity of *SIMCA* algorithm to depth and permittivity changes when building a kernel, Percentage error. For [A]: Simulated target depth at 5.1cm and using correct soil parameters; [B]: Simulated target depth at 6cm and using correct soil parameters; [C]: Simulated target depth at 12cm and using correct soil parameters; [D]: correct simulated target depth but wrong soil parameters for Figure 4.45 . All volumes are in cubic centimetres.

	[A]			[B]			[C]			[D]		
	1	2	3	1	2	3	1	2	3	1	2	3
Ground truth volume ( $cm$ ) <sup>3</sup>	99	494	2300	99	494	2300	99	494	2300	99	494	2300
Volume from SIMCA ( $cm$ ) <sup>3</sup>	96	489	2270	95	487	2268	94	510	2378	104	520	2420
Error (%)	3.0	1.0	1.3	4.0	1.4	1.4	5.1	3.2	3.4	5.1	5.3	5.2

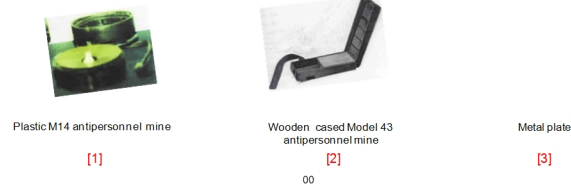


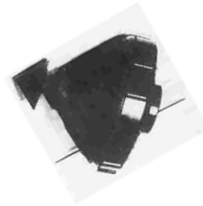
Table 4.24: Actual volume, volume from *SIMCA* reconstructed isosurface to test the sensitivity of *SIMCA* algorithm to depth and permittivity changes when building a kernel, Percentage error. For [A]: Simulated target depth at 5.1cm and using correct soil parameters; [B]: Simulated target depth at 6cm and using correct soil parameters; [C]: Simulated target depth at 12cm and using correct soil parameters; [D]: correct simulated target depth but wrong soil parameters for Figure 4.46. All volumes are in cubic centimetres.

	[A]		[B]		[C]		[D]	
	1	2	1	2	1	2	1	2
Ground truth volume ( $cm$ ) <sup>3</sup>	600	280	600	280	600	280	600	280
Volume from <i>SIMCA</i> ( $cm$ ) <sup>3</sup>	602	274	590	271	620	270	630	292
Error (%)	0.3	2.1	1.7	3.2	3.3	3.6	5.0	4.3



Table 4.25: Actual volume, volume from *SIMCA* reconstructed isosurface to test the sensitivity of *SIMCA* algorithm to depth and permittivity changes when building a kernel, Percentage error. For [A]: Simulated target depth at 5.1cm and using correct soil parameters; [B]: Simulated target depth at 6cm and using correct soil parameters; [C]: Simulated target depth at 12cm and using correct soil parameters; [D]: correct simulated target depth but wrong soil parameters for Figure 4.47. All volumes are in cubic centimetres.

	[A]	[B]	[C]	[D]
	1	1	1	1
Ground truth volume ( $cm^3$ )	416	416	416	416
Volume from <i>SIMCA</i> ( $cm^3$ )	418	419	430	435
Error (%)	0.5	0.7	3.4	4.6



PlasticAUS 15/50  
antipersonnel mine

[1]

Table 4.26: Actual volume, volume from *SIMCA* reconstructed isosurface to test the sensitivity of *SIMCA* algorithm to depth and permittivity changes when building a kernel, Percentage error. For [A]: Simulated target depth at 5.1cm and using correct soil parameters; [B]: Simulated target depth at 6cm and using correct soil parameters; [C]: Simulated target depth at 12cm and using correct soil parameters; [D]: correct simulated target depth but wrong soil parameters for Figure 4.48. All volumes are in cubic centimetres.

The shape of the hyperbola formed by a target is a function of the depth of the target. Thus it is not optimal to use the same kernel as one goes down performing the correlations. In principle one needs a set of kernels matched to the depth to obtain maximum horizontal resolution for targets deeper than the ones selected. Theoretically, building a kernel using the corresponding burial depth of the target and then generating the 3D reconstructions of the target using the *SIMCA* algorithm will produce a better result. But practically it can be seen that for the range of depths considered the reconstructions of the target are acceptable.

Also, using suboptimal soil parameters does not hugely affect the reconstruction. There is a slight but insignificant change for the plastic MAUS mine and the glass bottle mine when the incorrect parameters for the soil are used. This result is promising because in real situations the exact soil electrical parameters or the burial depth of the target is not known. The reason why using suboptimal soil parameters does not significantly affect the reconstructed volumes of targets is because correlation compensates for this inconsistency as stated in Section 4.4 of this chapter.

This illustrates that the *SIMCA* algorithm is robust and that the reconstructions are not affected by using suboptimal parameters for the soil.

The hyperbola that is formed is steeper at the top of the soil in comparison to the bottom of the soil surface and this was noted in the 2D *SIMCA* chapter of this thesis. For an example let us consider Figure 4.4[B] where a point target is at position  $x = 10cm$  and  $y = 10cm$ . Then the apparent depth,  $y_1$ , can be calculated using:

$$y1 = \left( \sqrt{(10^2 + 10^2)} \right) = 14.1cm$$

Now consider the case when the point target has moved to position (10, 40) then the apparent depth is:

$$y1 = \left( \sqrt{(10^2 + 40^2)} \right) = 41.2cm$$

Therefore the apparent depth increases with increase in depth.

For future work, kernels at different depths (e.g. 10cm, 20cm, 30cm etc) depending on the actual depth of burial of targets is generated and then using the *SIMCA* algorithm reconstructions of the 3D volumes is carried out using each of the above generated kernels. From these reconstructions the first slice (or B scan) from the first reconstruction is taken then the second slice from the second reconstruction and so on for the remainder of the reconstructions. Then the slices are merged into one complete reconstructed volume and this will be the final reconstructed image. Such an approach will give a better reconstructed 3D profile. Thus this will be an approach of using a library of kernels. The next sections present the summary graphs and statistics and compares the results of the *SIMCA 3D* technique and Scheers' algorithm.

## 4.8 Summary graphs and statistics

Tables 4.27 and 4.28 summarises the results for burial depth and computes some statistics for data. Tables 4.29 and 4.30 summarises the results for volume and computes some statistics for data. The tables indicate that the *SIMCA* algorithm is more accurate than the Scheers algorithm because of the lower values of the Root mean square of the differences between the estimated values from the algorithms and the ground truth. Figure 4.50 is a summary graph for depth of ground truth versus depth estimated. Figure 4.51 is a summary graph for volume of ground truth versus volume estimated. It can be concluded from the graphs that the *SIMCA* algorithm is more accurate than the Scheers algorithm because it is closer to the actual values of the parameters. In conclusion *SIMCA* results are more accurate than Scheers for chitests results.

## 4.9 Comparison with Scheers's algorithm

To compare the effectiveness of *SIMCA* algorithm with Scheers et al's algorithm, the same initial GPR data and same initial kernels were used with both algorithms to obtain 3D arrays of correlated and convolved data respectively. In each case the data was then visualised in *ParaView*. In order to obtain the best result for each algorithm independently optimised isosurface thresholds were obtained to minimise their volumetric error on the M26 landmine. The volumetric error is measured as:

$$error = \left( \log \left( \frac{v}{t} \right) \right)^2 \quad (4.9.1)$$

	Ground truth (cm)	SIMCA (cm)	Scheers (cm)	Difference_SIMCA	Difference_Scheers
1	5.1	5.0	4.8	-0.1	-0.3
1	8.9	9.2	9.5	0.3	0.6
1	5.2	5.4	4.7	0.2	-0.5
1	5.1	4.9	4.7	-0.2	-0.4
1	5.1	5.3	5.5	0.2	0.4
1	5.0	5.1	4.6	0.1	-0.4
1	4.9	5.0	4.4	0.1	-0.5
1	5.3	5.5	5.7	0.2	0.4
1	5.4	5.7	5.9	0.3	0.5
1	5.3	5.1	5.8	-0.2	0.5
1	5.5	5.4	5.8	-0.1	0.3
1	4.8	4.6	5.1	-0.2	0.3
1	5.3	5.2	4.9	-0.1	-0.4
2	4.9	4.7	4.5	-0.2	-0.4
2	4.8	5.0	5.2	0.2	0.4
2	4.6	4.4	5.0	-0.2	0.4
2	4.8	4.7	4.6	-0.1	-0.2
2	5.2	5.1	4.7	-0.1	-0.5
2	5.0	5.2	5.4	0.2	0.4
2	5.6	5.7	5.1	0.1	-0.5
2	5.3	5.4	4.9	0.1	-0.4
2	5.5	5.7	5.1	0.2	-0.4
2	4.5	4.7	4.1	0.2	-0.4
2	5.5	5.7	5.0	0.2	-0.5
3	4.9	4.8	4.6	-0.1	-0.3
3	5.3	5.4	5.7	0.1	0.4
3	9.0	9.3	8.4	0.3	-0.6
3	4.6	4.5	4.4	-0.1	-0.2

Table 4.27: Summary statistics for burial depth (1). All values in cm.

	Ground truth (cm)	SIMCA (cm)	Scheers (cm)	Difference_SIMCA	Difference_Scheers
3	5.0	4.9	5.4	-0.1	0.4
3	5.0	4.9	5.4	-0.1	0.4
3	4.8	4.9	5.2	0.1	0.4
3	4.8	4.6	5.2	-0.2	0.4
4	5.1	4.9	4.7	-0.2	-0.4
4	4.7	4.6	5.1	-0.1	0.4
Sum of differences <sup>2</sup>				1.03	5.95
Root_mean_square_difference_SIMCA				0.174	
Root_mean_square_difference_Scheers				0.418	
Correlation coefficient for SIMCA				0.989	
Correlation coefficient for Scheers				0.914	
Chi test for SIMCA				1.000	
Chi test for Scheers				0.900	

Table 4.28: Summary statistics for burial depth (2). All values in cm.

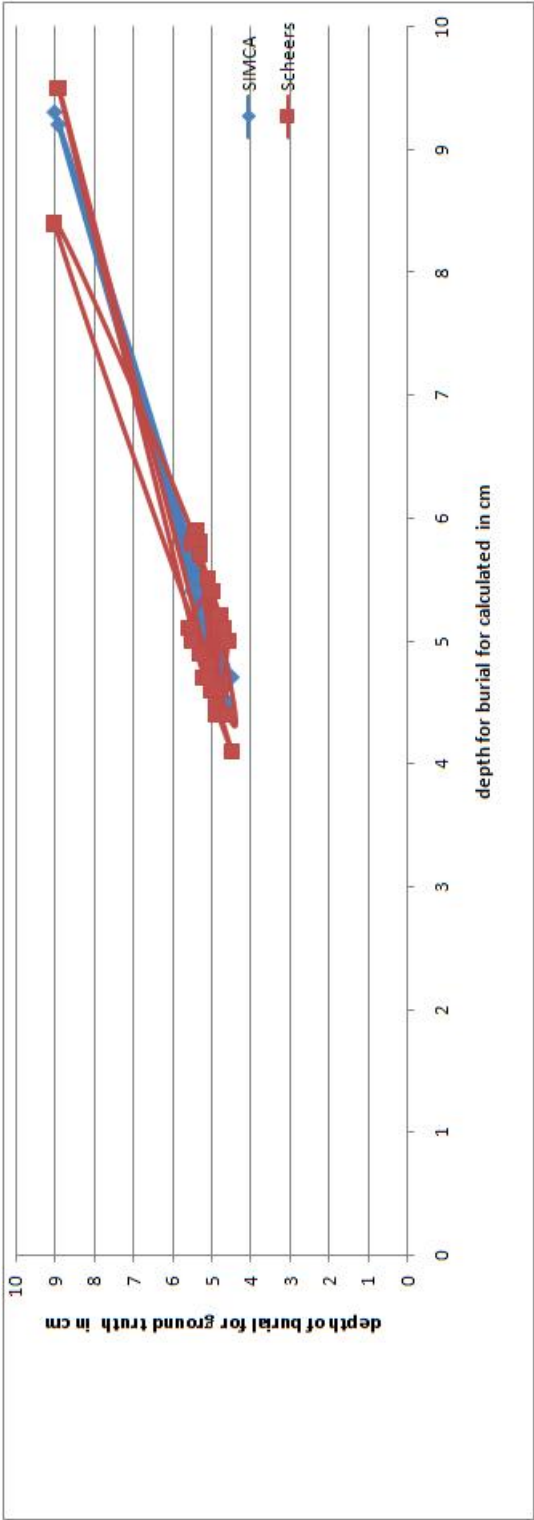


Figure 4.50: Summary graph for depth of ground truth versus depth estimated for Tables 4.27 and 4.28.



	Ground truth Ground truth ( $cm^3$ )	SIMCA Ground truth ( $cm^3$ )	Scheers Ground truth ( $cm^3$ )	Difference_SIMCA	Difference_Scheers
1	286.0	280.0	57.0	-6.0	-229.0
1	1149.0	1169.0	669.0	20.0	-480.0
1	711.0	708.0	271.0	-3.0	-440.0
1	711.0	697.0	551.0	-14.0	-160.0
1	153.0	154.0	108.0	1.0	-45.0
1	416.0	418.0	201.0	2.0	-215.0
1	405.0	396.0	238.0	-9.0	-167.0
1	99.0	101.0	30.0	2.0	-69.0
1	1767.0	1769.0	817.0	2.0	-950.0
1	210.0	208.0	38.0	-2.0	-172.0
1	220.0	222.0	196.0	2.0	-24.0
1	600.0	602.0	380.0	2.0	-220.0
1	99.0	96.0	17.0	-3.0	-82.0
2	500.0	491.0	380.0	-9.0	-120.0
2	143.0	146.0	25.0	3.0	-118.0
2	146.0	144.0	12.0	-2.0	-134.0
2	480.0	479.0	49.0	-1.0	-431.0
2	198.0	196.0	164.0	-2.0	-34.0
2	200.0	196.0	164.0	-4.0	-36.0
2	148.0	150.0	131.0	2.0	-17.0
2	306.0	299.0	252.0	-7.0	-54.0
2	148.0	146.0	13.0	-2.0	-135.0
2	280.0	274.0	198.0	-6.0	-82.0
2	494.0	489.0	244.0	-5.0	-250.0
3	711.0	698.0	590.0	-13.0	-121.0
3	7111.0	708.0	465.0	-6403.0	-6646.0
3	286.0	288.0	91.0	2.0	-195.0
3	670.0	678.0	482.0	8.0	-188.0

Table 4.29: Summary statistics for volume (1). All values in ( $cm^3$ ).

	Ground truth (cm <sup>3</sup> )	SIMCA Ground truth (cm <sup>3</sup> )	Scheers Ground truth (cm <sup>3</sup> )	Difference_SIMCA	Difference_Scheers
3	400.0	398.0	333.0	-2.0	-67.0
3	2103.0	2113.0	1623.0	10.0	-480.0
3	316.0	314.0	257.0	-2.0	-59.0
3	2300.0	2270.0	2230.0	-30.0	-70.0
4	830.0	840.0	459.0	10.0	-371.0
4	680.0	671.0	200.0	-9.0	-480.0
Sum of differences <sup>2</sup>					46764509.0
Root_mean_square_difference_SIMCA		1098.138			
Root_mean_square_difference_Scheers		1172.786			
Correlation coeeficient for SIMCA		0.477			
Correlation coeeficient for Scheers		0.445			
Chitest for SIMCA		0.000			
Chitest for Scheers		0.000			

Table 4.30: Summary statistics for volume (2). All values in (cm<sup>3</sup>).

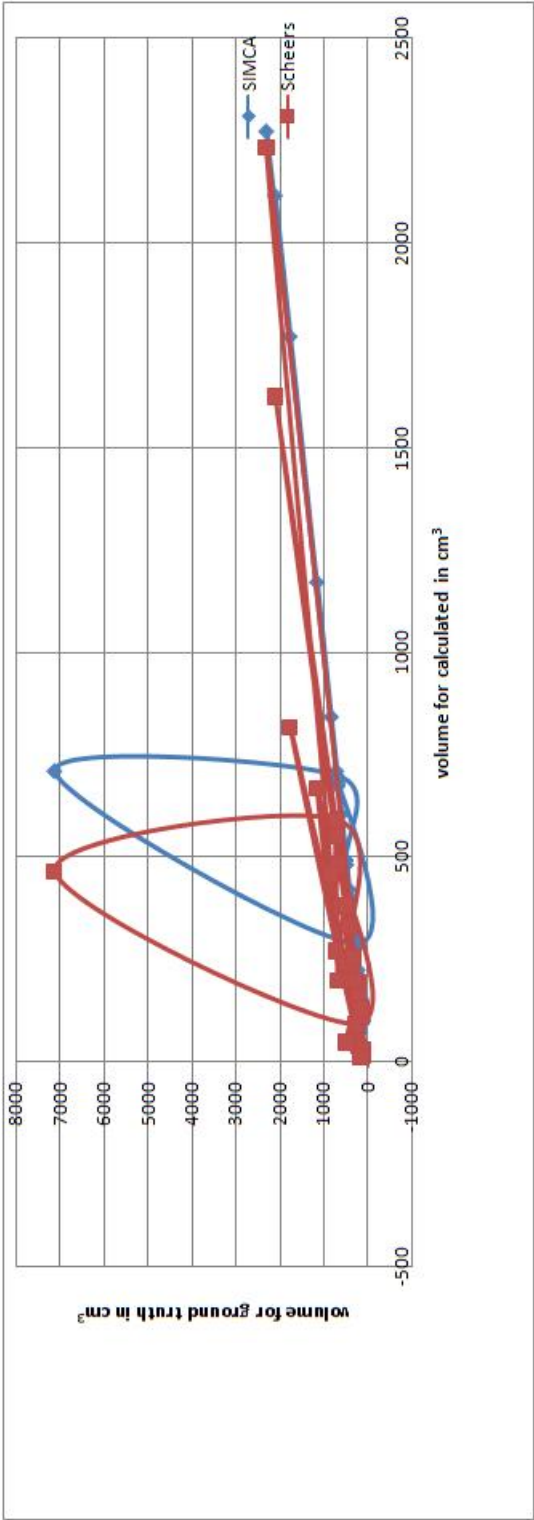


Figure 4.51: Summary graph for volume of ground truth versus volume estimated for Tables 4.29 and 4.30.

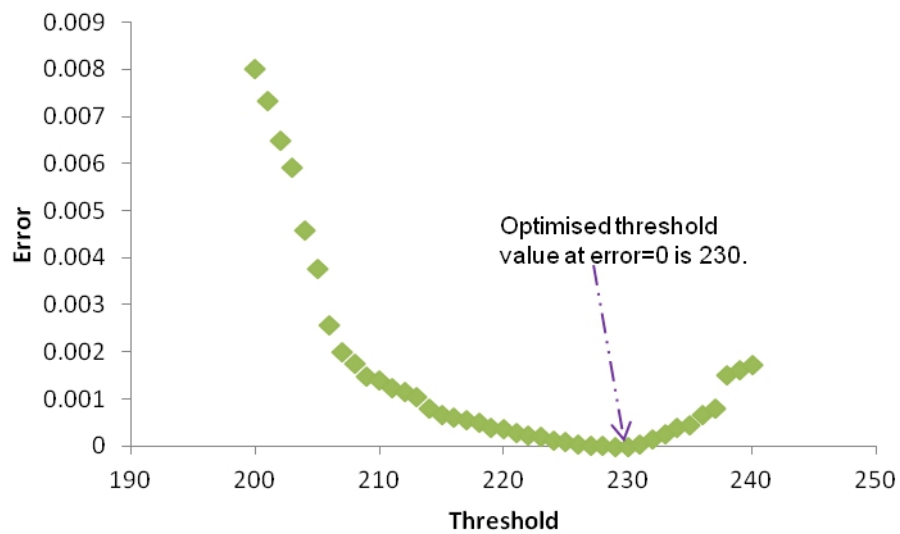


Figure 4.52: Graph of the error on estimating volume of a target as a function of isosurface threshold for *SIMCA* algorithm.

where  $v$  is the volume found at that threshold by using *vtkMassProperties* function class from the *ParaView* software and  $t$  is the true volume of the actual landmine. The *vtkMassProperties* is a function class and it estimates the volume of a 3D object. Alternatively, the volume of the 3D target can be found using the 'Process/Calculate Volume' command within the *ParaView* software.

Then graphs shown in Figures 4.52 and 4.53 were plotted with the error on the  $y$ -axis and the threshold level on the  $x$ -axis. The optimal threshold value was then determined by finding the value of the threshold when the error was equal to zero. From Figure 4.52 the optimal threshold for the *SIMCA* algorithm is 230 and from Figure 4.53 the optimal threshold for the Scheers method is 252.

The optimal thresholds for each method were used to obtain isosurface models of all the types of mines. Figure 4.10 shows the reconstructions of real targets in a wet sandy soil using the *SIMCA* method and Scheers' method. Figure 4.17 shows the reconstructions of real targets in a dry sandy soil using the *SIMCA* algorithm and Scheers et al's method for example.

As an objective validation process comparisons were made between the actual volumes of the landmines with the volumes found by using the *ParaView* software. For example Tables 4.1 and 4.4 show the actual volumes of the targets along with the respective volumes using both methods. Since the scattering behaviour of perfect electric conductors and dielectric objects is not similar, calculations of the error rates in determining the volume for the metal plate are also performed. Also the table shows the respective processing times (CPU Time) for each of the methods.

From Table 4.1 it can be seen that for the plastic MAUS mine Scheers et al algorithm does not produce a good reconstruction and the error rate is 80.1% compared to 2.1% error for the *SIMCA* algorithm. Likewise for the pistol the *SIMCA* method produces a better reconstruction and the error is only 1.8% compared to 24.0% for the Scheers's method. The same reconstruction problem can be noticed for the metallic M26 mine where the *SIMCA* method only produces an error rate of 1.8%.

From Table 4.4, for the glass bottle mine the Scheers et al's method again produces poor results

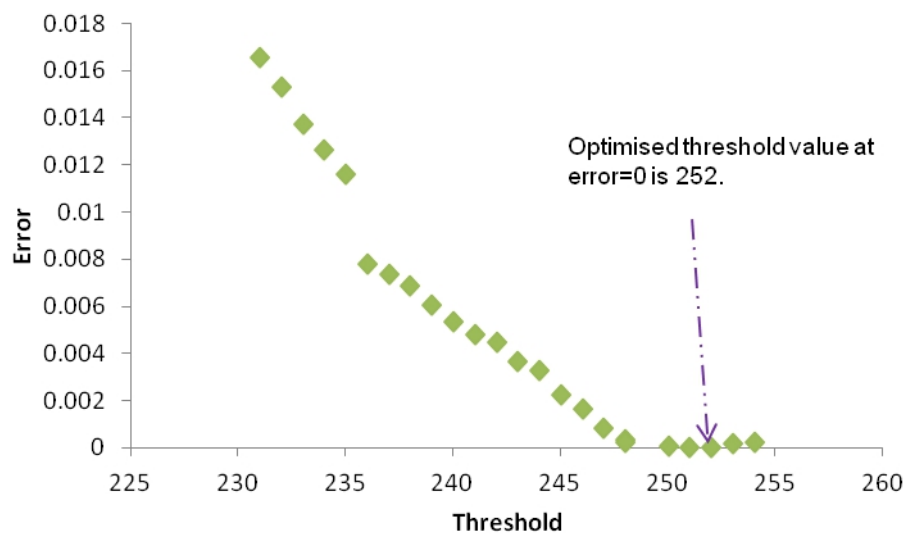


Figure 4.53: Graph of the error on estimating volume of a target as a function of isosurface threshold for Scheers algorithm.

with a volumetric error rate of 89.8% compared to only 0.2% produced by the *SIMCA* method. The same trend is noticeable for the M26 mine and the metal plate where the Scheers' algorithm produces error rates of 22.5% and 28.1% compared to 2.0% and 1.2% respectively for the *SIMCA* method. A similar trend is noticed for the remainder of the mines in Table 4.2 where for the wooden cased PMD-6 mine the percentage error for the *SIMCA* method is only 2.1% compared to the 82.5% for the Scheers' algorithm. For the plastic PFM-1 mine and MAUS mines, Table 4.3 illustrates that the *SIMCA* method has a percentage error of 1.4% and 0.7% compared to 91.8% and 68.2% respectively.

Table 4.6 gives the same indication for the plastic AUS 15/50 mine with an error rate of 0.5% for the *SIMCA* method and 51.7% for the Scheers et al's method. Table 4.7 illustrates the same worrying trend for the plastic APM 29 mine and error rates of 2.2% are produced for the *SIMCA* method in comparison to the 41.2% by the Scheers' method. For the plastic M14 and PRB M409 mines Table 4.8 shows that the *SIMCA* method is able to reconstruct the targets with percentage errors of 2.0% and 1.4% for the mines in comparison to 69.7% and 11.5% for the same mines.

In Table 4.10 the *SIMCA* method gives acceptable error rates of 1.0% and 2.3% for the plastic VS-Mk2 and plastic and rubber cased PMA-3 mine in comparison to worrying rates of error of 81.9% and 17.6% for the Scheers method. Finally the percentage errors for the wooden cased Model 43 mine and the plastic M14 mine are 1.0% and 3.0% for the *SIMCA* method compared to 50.6% and 82.8% for the Scheers' method as indicated by Table 4.13.

Tables 4.1 and 4.4 for example show the actual burial depth of the targets along with the burial depths obtained by the two methods. It can be seen that the *SIMCA* method is more accurate in estimating the depth. Results indicated a promise for the algorithm using laboratory controlled experiments, but it would be necessary to test the algorithm in actual field conditions. The same

trend is noticed across the board for the other target burial depths.

It was mentioned that the *SIMCA 3D* technique carries out correlation between the intersecting parts of the kernel and the data using interpolation. The next section investigates whether such an interpolation degrades the 3D reconstructions.

## 4.10 Effect on using interpolation

Section 4.4 stated often in the acquiring of 3D data using GPR, the separation between A scans that make up a B scan is typically smaller than, and not always an integer multiple of the spatial separation between the B scans that make up a C scan. This constraint was overcome by the *SIMCA* algorithm by using interpolation. Because interpolation is used, it would be necessary to see if the reconstructions get degraded as a result of using interpolation.

In order to investigate this a typical C scan data that had a number of slices is used and then starting at slice 1 and all slices are used but at a spacing of 2cm (that is every second slice), then at a spacing of 3cm. The remainder of the slices were filled using interpolation. Then starting at slice 2 and repeating the above at spacing's of 2cm, 3cm and 4cm respectively. Finally starting at slice 3 and repeating the above at spacing's of 2cm, 3cm and 4cm respectively. Figure 4.54 shows the respective 3D reconstructions obtained from the *SIMCA 3D* algorithm for each of the above situations.

Table 4.31 shows the actual volume of the M2 metallic antipersonnel mine along with the volumes calculated for each of the scenarios detailed above. The table also gives the percentage error for these volumes when compared to the ground truth and also the percentage error for the volumes of the individual scenarios when compared to the isosurface created without leaving any of the slices out.

From the table it is evident that interpolation does not significantly affect the reconstructions and that accurate reconstructions are still obtained by using interpolation. In summary the highest percentage error is only 0.3% and the lowest percentage error is 0%.

The next section then gives the problem of using the *MATLAB* processing environment for displaying of the isosurfaces for the landmine data.

## 4.11 Isosurfaces in *MATLAB*

Creation of isosurfaces for the landmine data using the *MATLAB* environment was conducted but the main problem in using *MATLAB* was the slow rendering of the 3D isosurfaces when the threshold value of the isosurface was changed. This is a major problem in a real landmine clearance situation because the deminers require fast response times. However to demonstrate that the same isosurfaces can be re-created in *MATLAB* for the car park data isosurfaces are created using *MATLAB* in Appendix B. The next section details the reason of why an image is used as opposed to an audible signal.

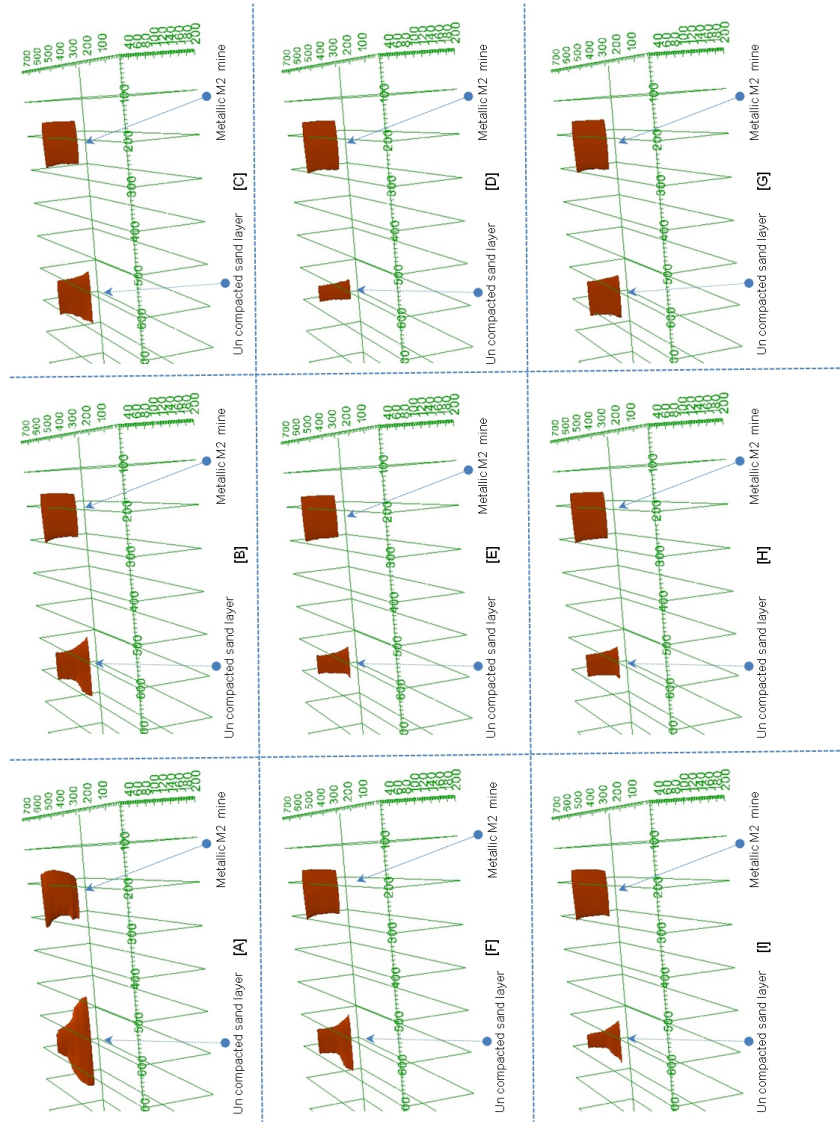


Figure 4.54: Various isosurfaces created to test the effect of interpolation. The isosurfaces have been created with various slices left out and the rest of the slices calculated using interpolation. [A]: The isosurface created without leaving any slices out; [B]: starting at the 1st slice and using all slices but at a spacing of 2cm; [C]: starting at the 1st slice and using all slices but at a spacing of 4cm; [D]: starting at the 2nd slice and using all slices but at a spacing of 2cm; [E]: starting at the 2nd slice and using all slices but at a spacing of 3cm; [F]: starting at the 2nd slice and using all slices but at a spacing of 4cm; [G]: starting at the 3rd slice and using all slices but at a spacing of 2cm; [H]: starting at the 3rd slice and using all slices but at a spacing of 3cm; [I]: starting at the 3rd slice and using all slices but at a spacing of 4cm.

	[A]	[B]	[C]	[D]	[E]	[F]	[G]	[H]	[I]
	M2 mine	M2 mine	M2 mine	M2 mine	M2 mine	M2 mine	M2 mine	M2 mine	M2 mine
Ground truth volume (cm) <sup>3</sup>	1767	1767	1767	1767	1767	1767	1767	1767	1767
Volume from SIMCA (cm) <sup>3</sup>	1769	1770	1768	1771	1772	1766	1766	1769	1769
Error when compared to ground truth (%)	0.1	0.2	0.1	0.2	0.3	0.1	0.1	0.1	0.1
Error when compared to the volume obtained by not leaving any slices (%)	0	0.1	0.1	0.1	0.2	0.2	0.2	0	0



Metallic M2 antipersonnel mine

[1]

Table 4.31: Actual volume, volume from the SIMCA reconstructions for leaving slices as detailed from Figure 4.54 and percentage errors. All volumes are in cubic centimetres.



## 4.12 The use of an image as opposed to an audible signal

The developers of the *ALIS* system presented in Chapter 2, conducted a number of field tests with human deminers and came to the conclusion that a system which can output images like the *SIMCA* system makes interpretation simple compared to an audible signal which alerts the position of the landmine. They also conclude that the produced images can be stored and used for further processing when compared to an audible output.

The typical operating environment for a deminer is often in a rugged harsh and hot climate such as Iraq or Afghanistan, and the deminer can get particularly tired and over-worked. For example, a BBC Panorama programme (“A Very British Hero”) found that the reason behind the death of Sergeant O Schmid was because of fatigue and over-work. In such harsh environments the soldier/deminer has to be presented with a tool that removes guesswork and increases the chances of detecting landmines. Furthermore, there is an English saying “A picture tells a 1000 words” and one can argue that the same can be applicable here and a clear 3D reconstruction from the *SIMCA* 3D algorithm can make it simpler for personnel involved in landmine clearance activities to clear the landmine with no expert knowledge. On the other hand, a tired deminer might misinterpret or miss an audible signal and this could have serious consequences. The next section details as to why the validation of the *SIMCA* algorithm was carried out using human users rather than an automated testing mechanism.

## 4.13 Why was validation carried out for the *SIMCA* using human users rather than an automated testing mechanism?

In Chapter 3, human users (an expert and 4 other general users) were used to validate the correlated images raised to a power of 3 (produced by the 2D *SIMCA* algorithm as opposed to using an automated validation suite) because a study by Sato et al. (2005) revealed some of the following points. Landmine clearance personnel on an Emirates flight from Glasgow to Dubai on his way to Afghanistan affirmed that using humans to validate the algorithm was a really good idea and stated that automated programs do not work well in all situations because they cannot cover all possible situations. Also input from several experts in the area of landmine detection met at radar conferences is summarised below:

- Often in real landmine detection scenarios in a field covered with landmines, the human operators are used to locate and clear the landmines. Therefore the benefits of using a human early on in the decision process can bring significant advantages.
- The automatic image classification is easy for human beings and human beings have a natural tendency to recognize patterns and images and to identify targets more accurately when compared to an automated program.
- The use of humans in a loop can bring higher detection rates.

Having said this, validation of the data was done using humans in the chain for only part of the data, because it is rather difficult to get a lot of users to test the whole test scenario. As was shown in Chapter 3 (for the 2D case) and in Chapter 4 (for the 3D case), a quantitative approach was used to validate the algorithm. For the 2D case, a *qualitative* approach was used to compare the images produced by different approaches with the images produced by the *SIMCA* algorithm. Although the *SIMCA* algorithm has been tested on hand held and robot scanned systems, the testing and integration with vehicle-based-systems would need to be carried out. The following section recommends a system for a landmine detection case and a non landmine case.

#### **4.14 Recommended system for a landmine detection scenario and a non landmine detection scenario**

Here the options of using a vehicle based forward looking multi array for landmine detection and use of a hand held system for a non landmine application are given.

##### **4.14.1 Vehicle based solution for landmine detection**

Researchers at Delft University of Technology, The Netherlands (Kovalenko et al., 2004) claim that the mounting of GPRs on a re-locatable scanner provides sub-millimetre accurate positioning on the 2D measurement grid. Use of a vehicle based multi array system integrated with the *SIMCA* algorithm which can provide an image which is easy to interpret is required. Therefore a vehicle mounted system for the detection of buried ordnance that combines a multiple GPR device with algorithms including *SIMCA* to provide 3D visualization of the subsurface environment is required. For a vehicle based scanner with multiple channels, voxel based volumetric rendering techniques could also be used. As was stated in Chapter 3, the algorithm was validated using both expert and non expert users as this will be the scenario in actual conditions. The users of the system were able to locate the targets with a good degree of accuracy when compared with current research (Abujarad, 2007). A point to note is that the use of a positioning table alleviates the use of a multi array system.

A forward looking vehicle based system which uses a positioning table system that allows the moving of the GPR to any location on the  $x, y$  grid whilst adjusting the height manually is proposed. The whole setup can be controlled by a computer program which transmits commands via a serial connection the position of the  $x, y$  scanner. Therefore the cartesian gantry system used in the laboratory can be replicated on a vehicle based system in the front of the vehicle. A schematic diagram of the proposed vehicle based system is shown in Figure 4.55, where the cartesian gantry system used in the laboratory is replicated towards the front of the vehicle thus having a forward looking mode. Also to be noted are the wheels on the gantry to allow for the forward movement and the stereo vision camera which can be used to allow for the automation in the scanning and to get the positional information.

One point to note is the use of a complete cartesian grid structure whereby the array of antennas scan the ground in a manner similar to that used by a dot matrix printer (i.e. scan from one end to

the other and progress to the next line and repeat the scanning pattern). A scan and go mechanism is employed here. This is because if a complete cartesian grid is not used in certain cases, the target might lie in the edges of the cartesian grid and therefore a complete hyperbolic kernel cannot be applied to these and only half of the hyperbolae is used by the *SIMCA* algorithm. A test carried out revealed that accurate reconstructions of the target geometry is not possible when using half a hyperbola for the kernel. The 3D reconstruction using a half a hyperbola for the kernel is shown in Figure 4.56 along with the reconstruction using a full hyperbola for the kernel.

#### 4.14.2 Hand held system for a non landmine application

In the case of a non landmine application area such as the location of foundations in the demolished building a hand held GPR integrated with the *SIMCA* algorithm is proposed. Also using encoder wheels for precise positioning and for acquiring equal spaced data is proposed. Also using a grid drawn on a sheet lay on the ground to maintain accurate scanning and to ensure correct spacing's is suggested. A comparison of the vehicle based and hand held systems is required.

#### 4.14.3 Comparison of the vehicle based and hand held systems

The use of a forward looking multi array system has advantages when compared to a downward looking system because overpass capability is not required for a forward looking system. But the disadvantage of the vehicle based system in comparison to its hand held counterpart is that the effective range of the radar head is restricted. The effective range being dependent on the speed of the vehicle (Ishikawa et al., 2005). The disadvantage of a hand held system is the slow acquiring of data in comparison to a vehicle based system. The hand held system is however flexible, but cannot acquire uniformly gridded data and interpolation has to be used to get uniform gridded data. The next section summarises this chapter.

### 4.15 Summary and Discussions

The main goal of this chapter was to present the *SIMCA* 3D algorithm and to use it for landmine visualisation using GPR. The chapter also pointed out that such 3D techniques have advantages over the 2D technique developed in the previous chapter. Such advantages included the accurate derivation of the dimensions of the target and the fact that such volumetric displays allow the deminer to visualize the data volume in its entirety using a single volume.

It was shown that the *SIMCA* algorithm produces much better reconstructions of the real targets and is computationally less intensive than a Scheers method.

Also the *SIMCA* method was more accurate in determining the burial depth of targets.

The algorithm was validated using an objective validation process which compared the actual volume of the targets to the volume at that threshold as calculated using *ParaView* software.

Results obtained to date indicate promise for the algorithm using laboratory controlled experiments, but the next step necessary would be to test the algorithm in a number of actual field conditions.

Stereo vision camera to allow for automation of scanning and to attain positional information.

Cartesian gantry system used in the lab employed on a forward looking multi-array vehicle based system. Note the wheels on the gantry to allow for movement.



Figure 4.55: Proposed vehicle based system using the cartesian gantry employed in the laboratory and in a forward looking mode. The system also has a stereo vision camera to allow for automatic scanning and to attain positional information. (Sato et al., 2004)

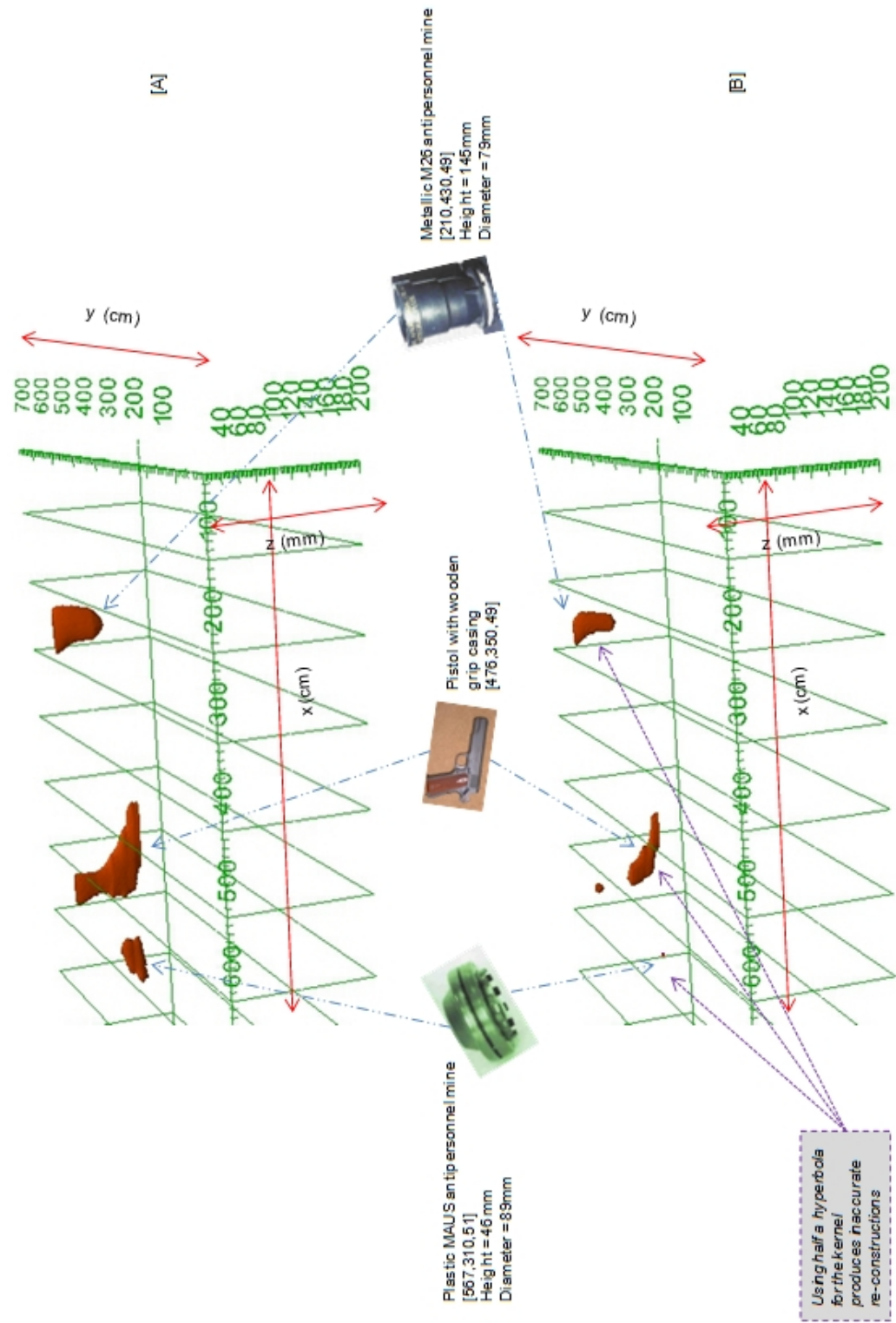


Figure 4.56: 3D reconstruction using the SIMCA algorithm - [A]: Using a full hyperbola for the kernel and [B]: Using half a hyperbola for the kernel.

In spite of the accurate 3D reconstructions produced by the *SIMCA* algorithm some form of spatial positioning is required and simple differencing can be made to depend only on the operator's position. But in reality sophisticated image processing such as the *SIMCA* algorithm and advanced analysis requires positioning information as part of the data stream to allow for data processing. Therefore advanced systems will need an added complexity of spatial positioning technology and this is discussed in some detail in the next chapter (Chapter 5) of this thesis. Furthermore it was stated in Chapter 3 that a system that produces images over a system that produces an audio output has advantages. This paves the way for the *SIMCA* algorithms to be used as practical software integrated into GPR.

The chapter then considered the reason as to why an image as opposed to an audible output has advantages. These included the ability of a tired soldier involved in landmine clearance to miss or wrongly interpret an audible signal. Next the chapter presented the reason as to why a human user was used for the validation of the data and concluded that a human user has better pattern matching ability when compared to an automated test suite.

Finally the chapter proposed a forward looking multi array cartesian gantry system like used in the laboratory integrated with the *SIMCA* algorithm for the detection of landmines and a hand held device integrated with the *SIMCA* algorithm for the non landmine application area. The chapter finally compared the hand held and vehicle based system and pointed out the advantages and disadvantages of both approaches. It was stated that the hand held is flexible but cannot attain uniform gridded data. But the vehicle based system can acquire data at a fast rate but the range of the radar head is restricted in comparison to the flexible hand held.

The next chapter will draw conclusions from this research project and give suggestions as how to improve and extend this work.

## Chapter 5

# Conclusions and Future Work

*This chapter serves to summarise the research conducted in this thesis and indicate the significance of this work in light of the current literature. The chapter then revisits the hypothesis along with the research questions and the objectives and concludes how the hypothesis along with their objectives were addressed. The chapter also summarises the contributions made by this thesis to current literature. Finally the chapter concludes with potential directions for future work in which this thesis initiated.*

### 5.1 Introduction

In accordance with the United Nations there are 70 million landmines that have been planted in a third of the world's nations and there is a global casualty rate as high as 20,000/year (Anderson, 2002). Thus this calls for the development of advanced algorithms such as the proposed *SIMCA* algorithm that was discussed in this thesis. Anti-personnel mines can vary in size, ranging from 5 to 15 cm and they can be metal, plastic or wood. Such APMs are normally buried at shallow depth and triggered by very low pressure. They have severe consequences on civilians and can kill or maim people. Typical anti-personnel mines as discussed in this thesis were PMN2, M14 and Type 72. The construction details of these landmines along with the details of other landmines were already given in Chapters 3 and 4.

An effective landmine detector should locate the landmine with a very high probability of detection and with a very low false alarm rate (Deiana, 2008). Due to landmines being encountered in a range of sizes and materials (such as plastic and metal) and being buried in various types of soil and in various depths reliable detection is very difficult for the landmine detector. Most sensors have their advantages and disadvantages and some detectors are better able to locate the landmines than others. It was already pointed out that the GPR is the most successful of these sensors and it particularly an important sensor because it is able to produce images of the subsurface.

In summary the *SIMCA* algorithm compares the trace that would be returned by an ideal point reflector in the soil conditions at the site and the actual clutter removed trace. From this it works back to the collection of objects that might have generated the observed traces. Further details are given in Section 5.3 of this chapter (Chapter 5).

The *SIMCA* algorithm was tested using landmine data obtained in a laboratory robotic controlled gantry setup containing a sandbox and also using car park data which located foundations in a demolished building. Comparisons of the accuracy of the *SIMCA* system with Scheers et al. (2000) the best alternative system reported in the open literature were performed. The techniques were used to image a variety of landmines using GPR scans. The types of mines included plastic, wooden and glass ones. In all cases clear images were obtained with *SIMCA*. In contrast Scheers' algorithm, the present state-of-the-art system, failed to provide clear images of non metallic landmines. A number of other procedures were used to validate the algorithm both in 2D (using B scans) and 3D reconstructions of real targets after scanning by a GPR (using C scans). A summary of the methods used is summarised in the following sections.

## 5.2 Aim of PhD Research

The aim of this PhD research was developing a 2D and 3D visualization system that was able to clean the clutter from a raw GPR radargram and to produce a clean B scan and a 3D isosurface for detecting landmines. Such images help deminers to locate and remove landmines and mine clearing personnel do not require prior information about GPRs.

## 5.3 Hypothesis, Research Questions and Objectives Revisited

The following hypothesis was established:

*This thesis argues that if the system aspects of the radar as well as the physics of waveguides and the soil properties are taken into consideration, and a kernel<sup>1</sup> developed from these using GPR simulation, then by correlating the kernel against the clutter removed GPR data will produce a much clearer image of the landmines and IEDs than can be obtained by existing techniques.*

The above was further refined into a number of questions which had an additional number of objectives as follows:

### Research Question 1

A clutter removal technique has to be developed which removes various unwanted signals such as cross talk, initial ground reflection and antenna ringing.

Therefore how do we remove the clutter which exists in the raw GPR trace?

#### • Objective 1

Identify the various clutter removal techniques. This is because GPR signals contain not only the response from a potential target, but also undesirable effects from antenna coupling, system ringing and soil reflections.

---

<sup>1</sup> A kernel is an array of coefficients used in filtering. The kernel is set prior to correlation so as to enhance a particular feature in an image.



To back up the assertion that by generating a kernel that included the system aspects of the radar as well as the physics of wave propagation and the soil properties and then correlating the kernel against the clutter removed GPR B scan will produce a much clearer image of the landmines and IEDs than existing techniques, the following was performed.

Objective 1 was addressed in Chapter 2 where the various techniques that are available to reduce the clutter in raw GPR images and thus to identify the buried object signal and thus the buried object was considered. This was because a GPR signal contains not only the response from a potential target, but also undesirable effects from antenna coupling, system ringing and soil reflections, which obscure the target response (Daniels et al., 2004). These effects have to be filtered out from the signal to enhance landmine detection.

For the *SIMCA* algorithm after comparing the various clutter removal techniques use of the technique discussed by Daniels (2004) was made in Chapters 3 and 4. The clutter removal technique reduced clutter by calculating averaged values over an ensemble of A scans and subtracting this from each of the A scans (Daniels, 2004) (Equation adapted from Daniels (2004)):

$$a'_{n,a}(t) = a_{n,a}(t) - \frac{1}{Na} \sum_{a=1}^{Na} a_{n,a}(t) \quad (5.3.1)$$

where  $n = 1$  to  $N$  and  $N$  is the number of samples;  $a = 1$  to  $Na$  and  $Na$  is the number of A scan waveforms.  $a_{n,a}(t)$  is the unprocessed A scan and  $a'_{n,a}(t)$  is the processed A scan.

### Research Question 2

What technique can be used to re-focus the reflection footmarks in the recorded data back to their true positions?

#### • Objective 2

Identify the different techniques that are available to correct the beam pattern of the antenna which is widely spread and cause degradation of the spatial resolution of the image.

Objective 2 was addressed in Chapters 2, 3 and 4. The *SIMCA* algorithm in essence re-focuses the reflection footmarks in the recorded data back to their true positions. The *SIMCA* ('*SIM*ulated *Correlation* Algorithm') is a technique based on an area correlation between the trace that would be returned by an ideal point reflector in the soil conditions at the site and the actual trace. During an initialization phase, *SIMCA* carries out radar simulation using the design parameters of the radar and the soil properties (this is the ideal trace). The trace which would be returned by a target under these conditions is then used to form a correlation kernel using a GPR. The details of this GPR simulation is detailed in Objective 3 of this section. Then *SIMCA* takes the raw data as the radar is scanned over the ground and uses a clutter removal technique to remove various unwanted signals such as cross talk, initial ground reflection and antenna ringing (this is the actual trace).

In Chapter 3, the 2D technique using B scans was presented and it compared the trace that would be returned by an ideal point reflector in the soil conditions at the site and the actual clutter removed trace. From this it works back to the collection of objects that might have generated the observed

traces. This resulted in a correlated image which is brightest at points most similar to the canonical target. Raising the image to an odd power  $>2$  enhances the target/background separation.

Whilst in Chapter 4, the equivalent 3D kernel was formed by rotating the 2D kernel along the polar co-ordinates, whilst the 3D data was formed by stacking 2D slices. The *SIMCA* algorithm carries out correlation between the intersecting parts of the kernel and the data using the Pearson's correlation coefficient, resulting in a correlated image which is brightest at points most similar to the canonical target. The algorithm then uses the *ParaView* software to create isosurfaces of the slices raised to an odd power  $>2$  to enhance the target/background separation.

### Research Question 3

What technique can be used to derive the ideal point reflector trace for a GPR?

#### • Objective 3

Establish how to derive the kernel which has the system aspects of the radar and the characteristics of the ground and how these features can be matched in the clutter removed GPR data.

Objective 3 was addressed in Chapters 2, 3 and 4. The trace that would be generated by the ideal point reflector was obtained using *GprMAX2D v1.5* developed by Giannopoulos (2005); an electromagnetic simulator for ground probing radar. The simulation solves Maxwell's equations using the finite-difference-time-domain method. The simulation takes as input a data file describing soil conditions, domain size, discretization step, time window, details of the buried object, details of radar and the location of the transmitter and receiver. This allowed the derivation of a mathematical model of the response of a point reflector and then to build a deconvolution system.

### Research Question 4

What 2D technique can be used to produce clearer 2D scans or B scans and also correct the issue identified by Research Question 2?

#### • Objective 4

Establish how the techniques identified in Objectives 2 and 3 can be used to present clearer images to the demining personnel when applied to B scans. Also establish how these results can be validated to ensure that clearer images are produced.

Objective 4 was partly addressed by Objective 2 and the other part of Objective 4 was addressed in Chapter 3. For the part addressed by Objective 2, please refer to the above. The other part of Objective 4, which states 'how to validate the algorithm and ensure that clearer 2D images are produced' is detailed now. In order to validate the *SIMCA 2D* algorithm, *qualitative evidence* was used where comparisons of the B scans produced by the *SIMCA* algorithm with some techniques which are the best alternative systems reported in the open literature was performed. It was found from this that the *SIMCA* algorithm clearly produces clearer B scans in comparison to the other

techniques. Next *quantitative evidence* was used to validate the *SIMCA* algorithm and demonstrate that it produced clear images. Use of two methods to undertake this *quantitative evidence* was performed. In the first method an expert GPR user and 4 other general users were used to predict the location of landmines and validate the *SIMCA 2D* algorithm. It was found from this study that the expert user is able to locate the landmines and the highest percentage error for the burial depth is only 16%, whilst for the position in the  $x$  direction it is 25% and these results are not bad for initial results when compared with current research (Kovalenko, 2006). It was also shown in Chapter 3 by using a chart which plotted the estimated depth versus the actual depth for the general users, that the users were able to predict the location of landmines to acceptable degrees of accuracy as indicated by the closeness of the predicted and the actual depths.

For the second *quantitative evidence* method, *AMIRA*<sup>2</sup> software was used to obtain values of the burial depth and position of the target in the  $x$  direction and hence validate the *SIMCA 2D* algorithm. Then the absolute error values for the burial depth along with the absolute error values for the position in the  $x$  direction obtained from the *SIMCA* algorithm and the Scheers et al. (2001) algorithm when compared to the corresponding ground truth values were calculated. In all cases the *SIMCA* algorithm was considerably more accurate than the Scheers et al. (2001) and thus produced clearer images. This was also the case for plastic landmines, which are one of the problems in landmine detection.

Furthermore for the car park data, where foundations were located in demolished buildings it was evident from the B scans that the *SIMCA* algorithm produced clearer B scans that would allow the operator to easily interpret the images when compared to the commercial *REFLEXW* software and to the Scheers et al. (2001) method.

### Research Question 5

What 3D technique can be used to produce clearer 3D reconstructions and also correct the issue identified by Research Question 2?

#### • Objective 5

Establish how the identified techniques in Objectives 2 and 3 can be used to present clearer 3D reconstructions of the targets after scanning by a GPR. Also establish what validation procedure can be used to validate these results and to ensure that clearer images are produced.

Finally Objective 5 is partly addressed by Objective 2 and the other part of Objective 5 was addressed in Chapter 4. For the part not yet addressed herewith is outlined the method. For the part of Objective 5, which states 'how to validate the algorithm and ensure that clearer 3D reconstructions are produced' the following is outlined. The *SIMCA 3D* technique and the Scheers et al. (2001) algorithm (the best alternative system reported in the open literature) technique were used to image a variety of landmines using GPR scans. The types of mines included plastic, wooden and glass ones. In all cases clear images were obtained with *SIMCA*. In contrast Scheers' algorithm, the present state-of-the-art system, failed to provide clear images of non metallic landmines. Also for

<sup>2</sup>*AMIRA* is a visualization system and allows visualization of GPR data sets.

the car park the *SIMCA 3D* algorithm produced more accurate results when comparing the absolute error values for the position in the  $x$  and  $y$  directions and the burial depth for the foundation in the demolished building in comparison to the Scheers et al. (2001) method and to the commercial *REFLEXW* software.

Since these objectives have been met, it can be concluded that this thesis has demonstrated its research hypothesis to hold.

## 5.4 Contributions to Research

The contributions of this thesis were as follows:

- The *SIMCA* algorithm uses correlation based on template matching where a '*template*' or a '*kernel*' derived from actual GPR simulations is matched against the clutter removed GPR image. But the techniques reported in the literature use convolution such as the Scheers et al. (2001) method. Sengodan et al. (2012) carried out a study which revealed that correlation is better because it compensated for differences in gain and black level between the kernel and the area of the image being matched. This was further illustrated in Chapters 3 and 4. Furthermore by using a kernel developed by using a point target buried in the same soil conditions using a GPR simulator, the complete GPR signature (antenna pattern) was obtained rather than part of the signature and this is really important as was shown in Chapter 4, Section 4.14.1 where using only half a hyperbola produced inaccurate reconstructions. It was also pointed out in Chapter 3, Section 3.8.1 that using a complete hyperbolic signature produced better localisations in the targets.
- Often the spatial separation between A scans that make up a B scan is typically smaller than, and not always an integer multiple of, the spatial separation between the B scans that make up a C scan. This is particularly significant in a C scan and the *SIMCA 3D* technique takes this into consideration. The reason as to why this spatial separation difference is significant was outlined in Chapter 4, Section 4.4.
- When considering the CPU times, it was stated in Chapter 4 that the *SIMCA 3D* algorithm only correlates between the intersecting parts of the kernel and the data. Thus the amount of data to be correlated was reduced because the correlation is carried out between the relevant sections. Therefore the *SIMCA* algorithm runs much faster than the Scheers et al. (2001) method. This is particularly important because field based GPR equipment is restricted in terms of processing capacity and battery life.
- By using the rendering mechanisms available in the open-source *ParaView* software, the *SIMCA* system is able to provide to the user a flexible approach of rotating the isosurfaces and to obtain slices along a number of planes. A further point to note is that because the *SIMCA* system uses open-source software the cost of the *SIMCA* system can be reduced for the end user.

- It was demonstrated in Chapter 4 that the *SIMCA 3D* technique is able to obtain an accurate volume of the rendered mine; existing techniques do not calculate the volume of targets. Furthermore the burial depth and the position in the  $x$  direction values by the *SIMCA* technique is more accurate than that produced by Scheers et al. (2001).
- The *SIMCA* algorithm also produces clearer images both in 2D and in 3D and a number of criteria were used to access this as outlined in Chapter 3 for the *SIMCA 2D* algorithm and in Chapter 4 for the *SIMCA 3D* algorithm.
- Although raising the brightness to an odd power  $>2$  to enhance the target/background separation is not new in image processing, none of the GPR techniques make use of this concept.
- Finally none of the techniques reported in the literature report using human users or *qualitative evidence* to validate their algorithms.

## 5.5 Future Work

This work provided an initial investigation in the area of detecting targets and foundations in a demolished building using GPRs. The development of a reliable, robust, cheap and field usable single array and multi array GPR is long. There is still much of Research and Development to be carried out, but the topics of possible future work are potentially inexhaustible. A number of studies required to enhance the current *SIMCA* system is provided:

- Due to the lack of funds to acquire a hand held GPR, it was not possible for the author to collect data in a real field situation. In the laboratory conditions all the conditions are well controlled and the air ground interface is flat. However in reality this is not true and the air ground interface can be very rough and this introduces further clutter, which may interfere with the reflections on the target. Furthermore in field conditions the problems of the patchy vegetation can cause a problem to target detection. Also the ground may not be homogeneous and due to rain and storms the soil conditions will be different. It is also possible that the landmines might have been displaced by natural conditions and are now tilted. It would be important to test the *SIMCA* algorithm under these conditions to test its performance in such conditions.
  - Accurate positioning of the GPR data is one of the most important aspects to consider during the data collection process. Data that does not have correct referencing is not useful and the production of accurate images of the subsurface requires knowledge of the precise position of the antenna. An outline of the various methods available to obtain the positional information is outlined. Therefore for future work positioning can be done by the following methods:
1. Using encoders that control the sampling interval. Encoders can be installed on vehicle wheels or on distance measuring apparatus. These encoders can measure rotation angles for the sweeping system with sensors on poles that can rotate. For example Radzevicius and

Daniels (2000) use a *SIR2000* radar system which is equipped with an encoder wheel for precise positioning and to acquire equally spaced data. They use a 2.54 cm grid drawn on plywood to ensure that consistent and accurate spacing is obtained between the GPR profiles. Another advantage of using the plywood surface was that it enabled a smooth consistent surface for the encoder wheel. They claim that the 0.6 cm thick sheet of plywood did not degrade the image quality.

2. Adding markers to the GPR data at known reference points, also known as Fiduciary markers. Markers can be inserted in the data at known reference points such as access road intersections, culverts and bridge joints.
3. Use of a GPS technique as detailed in Chapter 2. The GPS technology increases the accuracy of the positioning. With a standard differential GPR system, an accuracy of  $\pm 0.01\text{m}$  can be gained, while with the latest virtual reference system (VRS) using a GPS and Glonass satellites cm precision accuracy gained. GLONASS stands for the Global Navigation Satellite System and is based on a constellation of active satellites which continuously transmit coded signals in two frequency bands, which can be received by users anywhere on the Earth's surface to identify their position and velocity in real time based on ranging measurements' (<http://www.spaceandtech.com>). The GPS accuracy will improve with the completion of the Galileo satellite network. Other methods of using GPS technology were stated in Chapter 2, Section 2.6. The Mala range of GPR equipment have a GPS system on a USB which can be integrated into their GPR equipment and the positional information can be tied into the GPR data. Some technologies also use Real Time Kinematic (RTK) as a positional technology. RTK satellite navigation is based on the use of a carrier phase measurement of the GPS signal and where a single reference station can provide the real-time corrections, and this provides up to centimetre-level accuracy (Jol, 1994).
4. Digital video linkage to GPR scan numbers also helps in obtaining positional information and to allow for a non randomised scan pattern.
5. Inertial measurement units (IMUs) can also provide rotation angles for sweeping systems and provide cm precision accuracy.
6. Use of laser technology. Some systems use an auto-tracking laser theodolite or a rotary laser to get positional information and some studies have claimed to get cm precision. For example, Herman (1997) describes a robotic subsurface mapper which is composed of a robotic manipulator, a GPR, a 2D scanning laser rangefinder, and a large rectangular soil container used for the burial of objects. The surface mapper made up of the 2D laser rangefinder and elevation map allows the measurement of the height of the ground in a very fine grid and to obtain positional information. The laser scanner is made up of a 2D Perceptron laser scanner which is able to produce a range image with a range resolution of 1cm within the maximum range of 40cm. The GPR output can be tagged with the antenna position. The elevation map generator then computes an elevation map based on these range data. The elevation map is

then used by the excavation planner and the subsurface mapper. The elevation map is used by the excavation planner to plan the automated excavation. Figure 5.1 shows such a 2D laser rangefinder used by the author.

The best method is to use a combination of the above methods to improve accuracy.

Other methods of positioning that can be used include:

A wooden frame system could be constructed to support an antenna cart which allows for survey lines to be taken in two orthogonal directions. A conquest grid placed on the ground surface will allow positioning information to be found, whilst measuring the GPR data. Figure 5.2 shows such a view of the survey grid used for obtaining the position information. A problem to note in the system detailed in Figure 5.2 is that for a landmine detection scenario, the contact of the plywood with the ground could trigger the landmine and is dangerous in this situation. However, the use of the plywood can be adapted for an archaeological scenario.

In such a system the survey involves moving the sensor over a pre-defined grid of parallel and perpendicular lines in both of the directions. As is illustrated in the figure, a clear plastic sheet laid on the surface provides a guide for positioning the GPR system. Positioning information is attained by using an odometer wheel at the back of the unit. The odometer measures positions along a line. The odometer can also be placed on the wheels of the cart. The traces can be acquired using a trigger pulse generated by the odometer wheel.

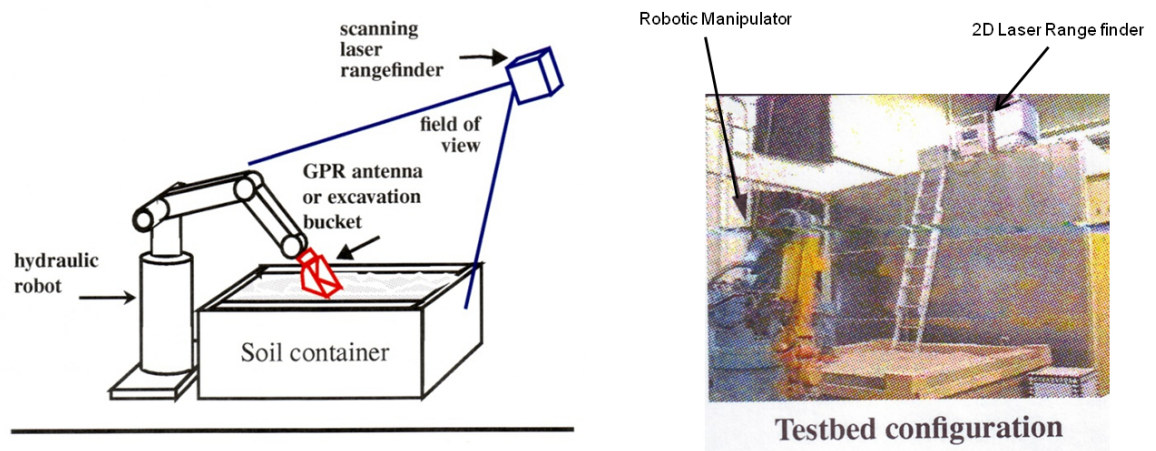
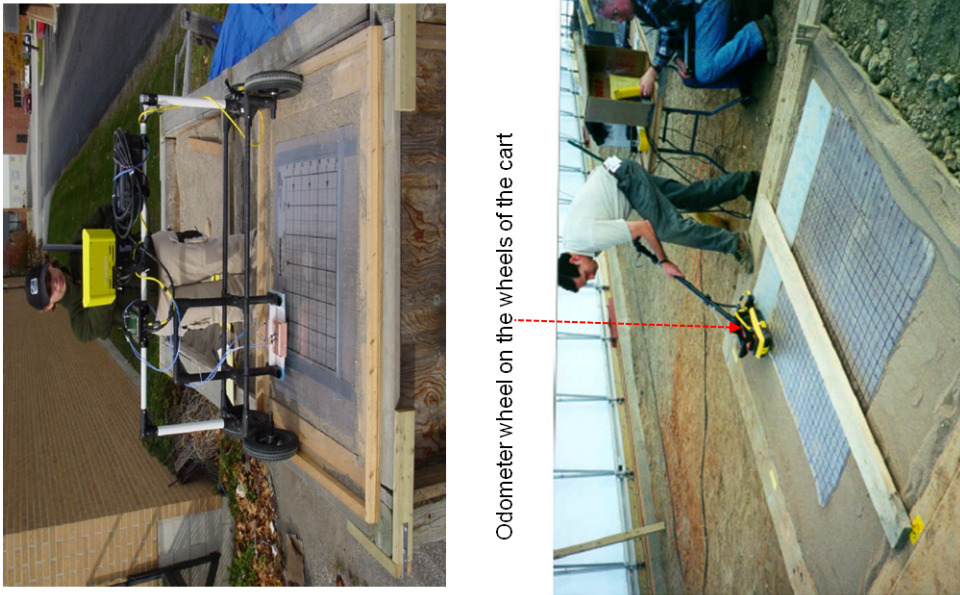


Figure 5.1: 2D Laser rangefinder used to attain positional information.

(Herman, 1997)

A positioning table as shown in Figure 5.3 can allow for moving the GPR system to any desired  $x, y$  location on a grid. The height of the radar head can be adjusted manually. Such a table system can allow for the acquiring of very closely spaced GPR data, that have very accurate and repeatable positioning and mm positioning accuracy can result. The device can be controlled with stepper motors which allow the GPR head to be accurately positioned at any point on the grid, using software programs. The whole setup is controlled by a computer, which transmits commands via a serial connection the position of the  $xy$ -scanner. The same  $xy$ -scanner can be mounted on the



Odometer wheel on the wheels of the cart

Figure 5.2: Views of the SSI test cell, antenna cart and survey grid.  
(SSI)





Figure 5.3: A positioning table.  
(SSI)

vehicle based system.

In terms of the laboratory system used to acquire landmine data, the precise moving of the sensor can be achieved by a cartesian gantry system. It has two motorized axes ( $X, Y$ ) whilst the height of the antenna is manually adjusted. The control of the displacement is achieved via a 486 PC which is used as an interface to the specified measuring system. Using stepped motors for the motorization is a viable option. A computer program (written in Visual Basic) controls the movement of the sensor on the gantry.

In a hand held device the operator would need to move the sensor. A requirement of signal processing is accurate relative spatial information. A robotic arm mounted onto a vehicle can provide a stable platform for deploying the sensor as well as integrating spatial information, improving the data quality. Sato et al. (2005) have extended the ALIS system described in Chapter 2, Section 2.5.1.3. In their system, upon allocation of a measurement position by the sensor, a signal is triggered to a vector network analyzer (VNA) controller. The controller then controls the data acquisition by the VNA sensor. Thus the quality of the data will be stable and the sensor can be scanned automatically resulting in the ability to obtain positional data. But a minor problem would be because of the narrow operation area of the robotic arm, a scanning area is limited, unlike the freedom of scanning a hand-held device has.

In Chapter 2, Section 2.5.1.3, an ALIS hand held dual sensor was described which had a charge coupled device (CCD) camera attached to the GPR head. Upon acquiring the data, the position of the sensor can be computed from the CCD picture. By placing a black cloth and two white references on the ground and this superimposed with the CCD camera picture helps the deminer scan the area in a regular gridded pattern. A sensor tracking algorithm has been developed by Sato et al. (2005).

Furthermore, by using cameras on a tripod and a set of markers on an antenna will allow the positional information to be attained. In Chapter 2, Section 2.5.2, a system developed by Fukushima et al. (2005) was given which accomplishes the automatic topographical mapping generation and

scanning by the use of stereo-vision cameras mounted on the manipulator link. This enables automation of the scanning process, thereby removes the positional accuracy problems attached with the manual scanning by a human operator. Also the proximity sensor integrated into the sensor is a simple solution for the automatic adjustment of the vertical head to the terrain. They presented the following sensors:

- Active stereo vision - This is expensive but is very accurate and the acquisition speed is fast.
- Passive stereo vision - This is not so expensive and the accuracy is not as good as the active stereo vision.
- 1D Laser range finder - Is accurate but is slow because a laser range finder attached to the scanner would need to be driven back and forth to get sufficient topographical points.
- 2D/3D laser scanner is expensive but very accurate and is fast in the acquisition speed.

But the authors use a passive stereo vision system for its acceptable cost/performance ratio and for its ease of use. They use a stereo vision camera with a resolution of 1024x768. They state that the camera is pre-calibrated and has a library of disparity calculations and depth map extractions.

Researchers at the Demining Technology Centre (DETEC) of the Swiss Federal Institute of Technology have come up with a hand held device called *DETEC-1* which has two main parts: a mobile and a static unit. They then re-designed the DETEC-1 system which is dependent on a mechanical design rather than on a sophisticated electronic position tracking sensor for moving the antenna head more accurately and to acquire positional information. They called this new system the *DETEC-2* system (van Kempen, 2006). The static unit which primarily is the sensor has the antenna, a position tracking bar and a box that has the radar interface electronics, a radio modem and a battery. The static unit on the other hand is the computing and display device with a computer, a digital signal processor, an LCD screen, a light throughput radio, a modem and an accumulator. The mobile and static units are connected through a wireless transmitter.

To produce images, the system's requirement is to know the precise position of the antenna moved by the operator. This is accomplished by the position tracking bar and a small display shows the area been scanned. Furthermore since the operator cannot follow a precise scan pattern, traces can be obtained in a pseudo-random manner. Therefore during data processing, it is necessary to move each acquired trace to points on a fixed grid by linear interpolation. Figure 5.4 illustrates such a position tracking system. As can be seen in the diagram a polar arm with rotation point is installed at the back of the enclosure whilst the supporting point carrying the radar head is at the front. The angular movement is undertaken by the deminer, whilst the linear motion is controlled by the system. An "automobile jack" like system using a trigger actuated by the deminer, moves the antenna forward. A 1042 steps optical encoder provides the angular co-ordinate of the arm. The linear co-ordinate is measured by a multi-turn 100 steps encoder. The antenna position in the vertical direction is adjusted via a system based on springs holding the antenna in the upward position.

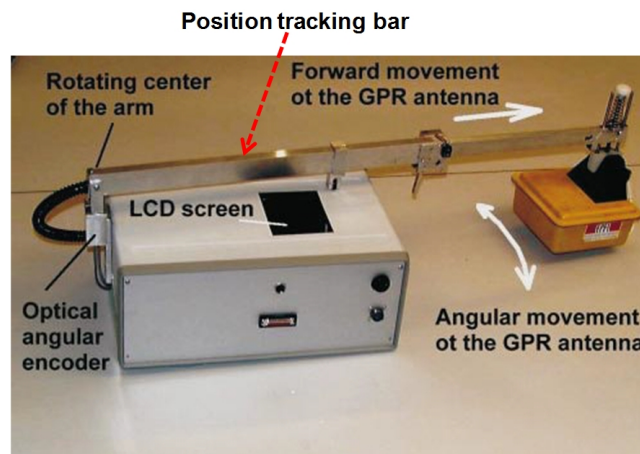


Figure 5.4: The *DETEC-2* system with the position-tracking bar.  
(*DETEC-2*)

Whilst GPR can detect landmines without using positioning systems, position information will increase the target detection capability. By including position information, the ability to perform spatial filtering and the application of processing algorithms which helps detection is possible. It also ensures the complete coverage of the search area and can allow the presentation of a map image to the deminer.

Versatility is required for a practical positioning technology. The method must be easy to use and maintain accuracy. Another method would be for the operator to establish a coordinate system on the survey area and for the operator to follow a specific protocol to position the sensor at the desired spatial position. This would require some prior planning by a skilled operator and data acquisition is not fast. An advantage of such an approach is the minimal technical complexity and also is a cheaper option. Such a system like the positioning table described earlier, establishes the sensor position. The system gives an indication of the sensor position, but the actual positioning is done by another operation.

- Data fusion, considering the features extracted by GPR in this thesis and other features from different sensors such as Metal Detector (MD), should be included in future research. The output of the GPR system will be analysed for enhancement, target recognition and multi-sensor data fusion. Different sensor data can be obtained using metal detector array (MMD) based on electromagnetic induction (EMI), an infrared imager (IR), ground penetrating radar (GPR), and a confirmatory sensor which requires the system to be stationary and near a target of interest, consisting of a thermal neutron analysis (TNA) detector. Each of the sensors can provide information concerning the presence (or absence) of physical properties that accompany the presence of landmines. For example, infrared imager provides a measure of thermal anomalies, electromagnetic induction reports anomalies in electrical conductivity, GPR detects anomalies in dielectric and other electromagnetic properties, and the thermal neutron analysis provides a measure of nitrogen content. A data fusion system will require each of the sensors to provide a position estimate and a measure of the confidence that the

respective property, detectable by that sensor, is present in a local patch of ground about the reported position. *Mala ProEx* for example has two auxiliary data ports which are able to incorporate and log data from other sensors. Mala just need to configure the ports to accept the data string (MALA, 2012).

As a result, sensor fusion will optimise each sensor and complement one another's strengths. For example studies in:

1. 'Infrared' ((Carin et al., 2008); (Ruffell and Donnelly, 2009))
  2. Multi Sensor ((Kabakchiev et al., 2009))
  3. Multispectral imagery (Huang et al., 2010)
  4. Ultrasound (Lopera, 2008).
- It was pointed out in Chapter 1 that the scope of this thesis was restricted to the detection stage. However in a future study it would be possible to include the actual identification process. For example, Roth (2004) performed the identification of landmines from GPR data by including practical models that related the measured target response to the main response. Therefore Roth (2004) represented the measured target response via a convolutional model that described the sequences of "radiation, propagation, target scattering and receiving" and then using deconvolution estimated the target impulse response. This was accomplished by including target characteristics such as its outer dimension, contrast and internal structure. Therefore a development of a novel technique to help in the identification stage would add a complete perspective to the *SIMCA* algorithm. The integration of the *SIMCA* algorithm with existing statistical classification techniques can improve detection performance and this is a future study that can be undertaken beyond this PhD. Other studies that have performed the identification process of landmine detection include (Strifors et al. (1998); Caelli et al. (1999)).
  - It was also pointed out in Chapter 4, Section 4.12 that using an image as opposed to an audible signal has its advantages. But to produce a complete solution integrating an audible signal output to the *SIMCA* system is preferable. For this to be accomplished it may be possible to use *neural networks* to help convert a radar signal to an audio signal. The training process available in *neural networks* can play an important role in utilizing GPR data after being transformed into a pattern that represents special features such as when a target is present and convert it to an audio signal. Some studies using neural networks include (Yang and Bose (2005); Maier and Brooks (1996)).
  - For future work, kernels at different depths (e.g. 10cm, 20cm, 30cm etc) depending on the actual depth of burial of targets is generated and then using the *SIMCA* algorithm reconstructions of the 3D volumes is carried out using each of the above generated kernels. From these reconstructions the first slice (or B scan) from the first reconstruction is taken then the second slice from the second reconstruction and so on for the remainder of the reconstructions. Then

the slices is merged into one complete reconstructed volume and this will be the final reconstructed image. Such an approach will give a better reconstructed 3D profile. Thus this will be an approach of using a library of kernels.

- In the current research the opportunity to develop the actual GPR equipment was not possible. For example as part of a future study being involved with also the development of a hand held and vehicle based system integrated with the *SIMCA* algorithm is advantageous. It was hoped when submitting the *SIMCA* algorithm to the Thales Scottish Technology Prize 2010 that with the help of Thales a vehicle based system integrated with the *SIMCA* algorithm was produced. But due to the fact that the Thales facility here in Glasgow that was running the competition was specialized with Optronics and Laser technologies the proposal could not be taken further. It would also be beneficial to study Ultra-Wideband Ground Penetrating Radar (UWB) because some studies state that the UWB radar gives better depth resolution and the back scattered signal has more frequency information on the object ((Scheers et al., 2001); (Yarovoy et al., 2007b); (Yarovoy et al., 2007a)). Furthermore integration of the *SIMCA* algorithm into equipment can be investigated and include:
  1. Integration of the *SIMCA 2D* algorithm developed in Chapter 3 and the *SIMCA 3D* algorithm developed in Chapter 4 into either a hand held or vehicle based system depending on the application area (landmine or non landmine scenario) is necessary as further future work.
- The Utility detection market amongst the other applications areas such as in breast cancer research would benefit from the *SIMCA* algorithm. A group of scientists and medical professionals at Bristol University for example have come up with a GPR system that is able to screen breast cancer patients and provide images of the breast from which the cancerous tissues can be identified. Furthermore, with the large number of pipes and cables being constantly upgraded to the network, it would be important for engineers to be able to make sure that they do not dig existing utilities and cause dangerous explosions. It would be particularly useful to collaborate with such engineers (utility detection) and researchers (cancer research) to test the *SIMCA* algorithm.
- Finally collaboration with the UK Ministry of Defence (MOD) or military companies such as BAE systems or QinetiQ to further test the *SIMCA* algorithm and to get feedback and to improve the algorithm so that it can be used by the troops in Afghanistan to help save lives is useful. The author is passionate about saving lives and hopes to act as a volunteer for organizations such as HALO Trust and to provide them the *SIMCA* technology. Furthermore association with the Time Team a group of archaeologists who produce TV programs and carry out investigations in areas of Archaeological significance would bring real benefit to the improvement of the *SIMCA* algorithm and to make it a field tested system.

## 5.6 Summary & Conclusions

This dissertation has presented the *SIMCA* algorithm that is a technique based on area or volume correlation between the trace that would be returned by an ideal point reflector in the soil conditions at the site and the actual trace. During an initialization phase, *SIMCA* carries out radar simulation using the design parameters of the radar and the soil properties. The trace which would be returned by a target under these conditions is then used to form a kernel. The system correlates the kernel with the data and produces 3D images of the surface of subterranean objects detected. Comparisons of the accuracy of the *SIMCA* system with Scheers et al. (2001), the best alternative system reported in the open literature was completed. The *SIMCA* and Scheers' algorithms were used to image a variety of landmines using GPR scans. The types of mines included plastic, wooden and glass ones. In all cases clear images were obtained with *SIMCA*. In contrast Scheers' algorithm, the present state-of-the-art system, failed to provide clear images of non metallic landmines.

The *SIMCA 2D* algorithm on the other hand produces clearer B scans in comparison to existing techniques such as the Scheers et al. (2001) technique. Using *qualitative evidence* and *quantitative evidence* the *SIMCA 2D* algorithm produced more accurate results than existing systems. The *SIMCA 2D* technique was able to also better locate the foundations in demolished buildings when compared to the Scheers et al. (2001) method and to the commercial *REFLEXW* software. Furthermore the *SIMCA 3D* technique produced more accurate reconstructions of the foundations in comparison to the other two methods (Scheers et al., 2001) and the *REFLEXW* commercial software. It was also shown that it was practical to transfer the laboratory based system into a field based system but the necessity of a positioning system to be integrated with the GPR system was also prioritised.

## Appendix A

### Algorithm listing for *SIMCA* Algorithm

This appendix shows the list of algorithms used by the *SIMCA 3D* algorithm. The algorithm can also be found online by going to the following URL: <https://sites.google.com/site/3dsimcaalgorithm/>. The algorithm listing here is used by the *SIMCA 3D* algorithm outlined in Chapter 4 of this thesis:

1. Algorithm 2 lists the first sub listing of the main *SIMCA 3D* algorithm.
2. Algorithm 3 lists the second sub listing of the main *SIMCA 3D* correlation algorithm.
3. Algorithm 4 lists the third sub listing of the main *SIMCA 3D* algorithm.
4. Algorithm 5 lists the '*meshgrid*' MATLAB function used by the *SIMCA 3D* correlation algorithm. After loading the 3D matrix variable which contains the data, co-ordinate assignment is made using the *meshgrid* routine.
5. Algorithm 6 lists how MATLAB uses the '*interp3*' MATLAB function to carry out trilinear interpolation.
6. Algorithm 7 lists how *SIMCA 3D* handles correlation.

---

**Algorithm 2** *SIMCA* 3D Algorithm to consider spacing in x,y and z directions.

---

The conventions used for variables in this algorithm are: Roman bold capitals are used for Matrices, Roman bold lowercase are used for Vectors and Roman italics lowercase for scalar.

{ Specifying kernel steps. Kernel Steps are specified in centimetres:  $sk1$  is kernel step in x direction,  $sk2$  is kernel step in y direction and  $sk3$  is kernel step in z direction }

{ Specifying data steps. Data Steps are specified in centimetres:  $sd1$  is data step in x direction,  $sd2$  is data step in y direction and  $sd3$  is data step in z direction }

{ Specifying decimation:  $zks$  is decimation of kernel,  $x_{dm}$  is decimation in scan in x direction,  $y_{dm}$  is decimation in scan in y direction and  $z_{dm}$  is decimation in scan in z direction }

{ Calculate Array sizes: **KG** is the kernel and **DQ** is the data }

{ The shape function finds the dimensions of a matrix }

$[ksy\ ksx\ ksz] = \text{shape}(\mathbf{KG})$

$[dsx\ dsy\ dsz] = \text{shape}(\mathbf{DQ})$

{ Calculate Kernel co-ordinate arrays: **xk1** is x co-ordinates of kernel co-ordinate array, **yk1** is y co-ordinates of kernel co-ordinate array and **zk1** is z co-ordinates of kernel co-ordinate array }

{ In the next 3 steps, the algorithm gets vectors of x,y,z offsets of the kernel data in centimetres }

$\mathbf{xk1} = ((-ksx+1)/2:1:(ksx-1)/2)*sk2$

$\mathbf{yk1} = ((-ksy+1)/2:1:(ksy-1)/2)*sk1$

$\mathbf{zk1} = ((-ksz+1)/2:1:(ksz-1)/2)*sk3$

{ Transform 1D array into 3D array }

{ In order to transform 1D array into 3D array: 3 matrices are created - a matrix containing replicated rows of the array, replicated columns of the array and replicated n dimensional values are created. Hence the rows of the output array X are copies of the vector x; columns of the output array Y are copies of the vector y and array Z are a combination of copies of the rows and columns in z }

{ Please see Algorithm 5 that specifies algorithm for meshgrid }

$[\mathbf{XK}, \mathbf{YK}, \mathbf{ZK}] = \text{meshgrid}(\mathbf{xk1}, \mathbf{yk1}, \mathbf{zk1})$

{ Calculate Data co-ordinate arrays: **xd1** is x co-ordinates of data co-ordinate array, **yd1** is y co-ordinates of data co-ordinate array and **zd1** is z co-ordinates of data co-ordinate array }

$\mathbf{xd1} = (0:1:(dsx-1))*sd2$

$\mathbf{yd1} = (0:1:(dsy-1))*sd1$

$\mathbf{zd1} = (0:1:(dsz-1))*sd3$

---



---

**Algorithm 3** *SIMCA* 3D Algorithm to consider spacing in x,y and z directions continued from above.

---

The conventions used for variables in this algorithm are: Roman bold capitals are used for Matrices, Roman bold lowercase are used for Vectors and Roman italics lowercase for scalar.

{Transform 1D array into 3D array}

{In order to transform 1D array into 3D array: 3 matrices are created - a matrix containing replicated rows of the array, replicated columns of the array and replicated n dimensional values are created. Hence the rows of the output array **X** are copies of the vector **x**; columns of the output array **Y** are copies of the vector **y** and array **Z** are a combination of copies of the rows and columns in **z**}

[**XD**, **YD**, **ZD**] = meshgrid(**xd1**, **yd1**, **zd1**)

{Apply decimation to data to allow for kernel to scan data correctly: **xca** is data in x-direction after applying decimation, **yca** is data in y-direction after applying decimation and **zca** is data in z-direction after applying decimation}

**xca** = 1:*xm*:dsx

**yca** = 1:*ydm*:dsy

**zca** = 1:*zdm*:dsz

{Scan kernel along data: **XKT** is shifting kernel 3d array value in scan procedure in x direction, **YKT** is shifting kernel 3d array value in scan procedure in y direction and **ZKT** is shifting kernel 3d array value in scan procedure in z direction}

For all **xc=xca**

**XKT** = **XK** + (xc-1)\**sd2*

For all **yc=yca**

**YKT** = **YK** + (yc-1)\**sd1*

For all **zc=zca**

**ZKT** = **ZK** + (zc-1)\**sd3*

{(**XD**, **YD**, **ZD**) specifies data and its position in space, whereas (**XKT**, **YKT**, **ZKT**) specifies current kernel position}. {Size of **XKT**, **YKT** and **ZKT** are the same size as that of the kernel}.

{**KDT** uses MATLAB's *interp3* to find 3D data interpolation. **VI** = *interp3*(**X**,**Y**,**Z**,**V**,**XI**,**YI**,**ZI**) interpolates to find **VI**, the values of the underlying three-dimensional function **V** at the points in arrays **XI**, **YI** and **ZI**. **XI**, **YI**, **ZI** must be arrays of the same size, or vectors. Vector arguments that are not the same size, and have mixed orientations (i.e. with both row and column vectors) are passed through meshgrid to create the **Y1**, **Y2**, **Y3** arrays. Arrays **X**, **Y**, and **Z** specify the points at which the data **V** is given. Out of range values are returned as NaN.}

{Linear interpolation is carried out}

{Please see Algorithm 6 which specifies how *interp3* is calculated}

---

---

**Algorithm 4** *SIMCA* 3D Algorithm to consider spacing in x,y and z directions continued from above.

---

The conventions used for variables in this algorithm are: Roman bold capitals are used for Matrices, Roman bold lowercase are used for Vectors and Roman italics lowercase for scalar.

**KDT** is Linear interpolation between **XD**, **YD**, **ZD**, **XKT**,  
**YKT** & **ZKT**

{returns 'NaN' for places where kernel and data do not intersect}. {The definition of intersection is that in order to intersect the point of intersection of the kernel should lie within the upper and lower limits of the slice concerned}.

{**KDTJ** then finds the column vector of **KDT**}

**KDTJ**=**KDT**(:)

{**IND** refers to the corresponding column number of the column vector that does not have 'NaN' as a value}

**IND** = find(~isnan(**KDTJ**))

{**INJ** finds the elements of **KDTJ** that are not 'NaN'. So, **KDTJ** contains all values including 'NaN'; **IND** finds the corresponding column number of column vector that does not have 'NaN' as a value and finally **INJ** is the resulting values corresponding to the column numbers of **KDTJ** that are not 'NaN'.}

**INJ** =**KDTJ**(**IND**)

{Now find corresponding 1D vector(or column vector) of kernel}. {end is used in an indexing expression in the next line}

**KG1**=**KG**(: , : , 1:zks:end)

**KG2**=**KG1**(:)

{Carry out correlation between intersecting parts of data and kernel, here Pearson's correlation coefficient is calculated using '*corrcoef*' in MATLAB}

**R**=corrcoef(**INJ**,**KG2**)

{Please see Algorithm 7 which specifies how correlation is carried out}

{**R** is 2x2 matrix with R correlation values and we need R(1,2) because that gives the correlation of first array with second array}

**R1**(yc,xc,zc)=**R**(1,2)

end for

end for

end for

Draw isosurface of correlated result with isosurface level. For this the value of the 3d array(**R2**) and the co-ordinates of the 3d arrays(**XD1**, **YD1** and **ZD1**) are calculated.

**R2**=**R1**(yca,xca,zca)

**XD1**=**XD**(yca,xca,zca)

**YD1**=**YD**(yca,xca,zca)

**ZD1**=**ZD**(yca,xca,zca)

isosurface(**XD1**,**YD1**,**ZD1**,**R2**,isosurface level)

---

---

**Algorithm 5** Algorithm to specify meshgrid function.

---

The conventions used for variables in this algorithm are: Roman bold capitals are used for Matrices, Roman bold lowercase are used for Vectors and Roman italics lowercase for scalar.

Let  $\mathbf{xk} = \begin{bmatrix} -2.5000 & +2.5000 \end{bmatrix}$

Let  $\mathbf{yk} = \begin{bmatrix} -2.5000 & +2.5000 \end{bmatrix}$

Let  $\mathbf{zk} = \begin{bmatrix} -2.5000 & +2.5000 \end{bmatrix}$

Then  $\begin{bmatrix} XK & YK & ZK \end{bmatrix} = \text{meshgrid}(\mathbf{xk}, \mathbf{yk}, \mathbf{zk})$  produces

$XK$  which is a 2x2x2 matrix with :

$$XK(:, :, 1) = \begin{bmatrix} -2.5000 & +2.5000 \\ -2.5000 & +2.5000 \end{bmatrix}$$

$$XK(:, :, 2) = \begin{bmatrix} -2.5000 & +2.5000 \\ -2.5000 & +2.5000 \end{bmatrix}$$

$YK$  which is a 2x2x2 matrix with :

$$YK(:, :, 1) = \begin{bmatrix} -2.5000 & -2.5000 \\ +2.5000 & +2.5000 \end{bmatrix}$$

$$YK(:, :, 2) = \begin{bmatrix} -2.5000 & -2.5000 \\ +2.5000 & +2.5000 \end{bmatrix}$$

$ZK$  which is a 2x2x2 matrix with :

$$ZK(:, :, 1) = \begin{bmatrix} -2.5000 & -2.5000 \\ -2.5000 & -2.5000 \end{bmatrix}$$

$$ZK(:, :, 2) = \begin{bmatrix} +2.5000 & +2.5000 \\ +2.5000 & +2.5000 \end{bmatrix}$$


---

---

**Algorithm 6** Algorithm to specify interpolation function.

---

The conventions used for variables in this algorithm are: Roman bold capitals are used for Matrices, Roman bold lowercase are used for Vectors and Roman italics lowercase for scalar. [Algorithm adopted from MATLAB](#).

{*MATLAB* uses Trilinear interpolation and is an extension of linear interpolation. It works on a 3-dimensional regular grid and is a method of multivariate interpolation. It calculates an approximate value of an intermediate point  $x, y, z$  in a local axial rectangular prism in a linear way}

Taking a periodic and cubic lattice with a spacing 1, let  $x_x, y_y,$  and  $z_z$  be the differences between each of  $x, y, z$  and the smaller coordinate related:

$$x_x = x - x_0$$

$$y_y = y - y_0$$

$$z_z = z - z_0$$

And:

$x_0$  is the lattice point underneath  $x$  and  $x_1$  is the lattice point above  $x$

$y_0$  is the lattice point underneath  $y$  and  $y_1$  is the lattice point above  $y$

$z_0$  is the lattice point underneath  $z$  and  $z_1$  is the lattice point above  $z$

The method interpolates along  $z$  and results in:

$$i_1 = \text{Volume}[x_0, y_0, z_0](1 - z_z) + \text{Volume}[x_0, y_0, z_1]z_z$$

$$i_2 = \text{Volume}[x_0, y_1, z_0](1 - z_z) + \text{Volume}[x_0, y_1, z_1]z_z$$

$$j_1 = \text{Volume}[x_1, y_0, z_0](1 - z_z) + \text{Volume}[x_1, y_0, z_1]z_z$$

$$j_2 = \text{Volume}[x_1, y_1, z_0](1 - z_z) + \text{Volume}[x_1, y_1, z_1]z_z$$

The algorithm then interpolates these values along  $y$  and results in:

$$w_1 = i_1(1 - y_y) + i_2y_y$$

$$w_2 = j_1(1 - y_y) + j_2y_y$$

Finally the algorithm interpolates these values along  $x$

$$\text{INTERPOLATION}_{final} = w_1(1 - x_x) + w_2x_x$$

This gives the predicted value for the point and hence *MATLAB* uses this to carry out 3D interpolation using *interp3* function.

---

---

**Algorithm 7** Algorithm specifying how correlation is carried out.

---

The conventions used for variables in this algorithm are: Roman bold capitals are used for Matrices, Roman bold lowercase are used for Vectors and Roman italics lowercase for scalar.

Pearson's correlation coefficient between two variables is used by *MATLAB's* *corrcoef* and is defined as the covariance between two variables which is defined as the covariance of the two variables divided by the product of their standard deviations:

$$\rho_{X,Y} = \frac{\text{cov}(X,Y)}{\sigma_X \sigma_Y}$$

Replacing estimates of the covariance's and variances based on a sample gives the *sample correlation coefficient*, commonly denoted *r*:

$$r = \frac{1}{n-1} \sum_{i=1}^n \frac{X_i - X}{S_X} \cdot \frac{Y_i - Y}{S_Y}$$

Where:

$$\frac{X_i - X}{S_X}$$

and  $X$  and  $S_X$  are the standard score, sample mean, and standard deviation respectively.

---

## Appendix B

### Car park case study

*This appendix details the car park study and commences by outlining the data acquisition procedure used by the author and a colleague to obtain data in the car park to facilitate the testing of the SIMCA algorithm to locate foundations in demolished buildings. The data was acquired by the author and his colleague at the Department of Archaeology at the University of Glasgow. The author's colleague was sponsored by the Natural Environment Research Council (NERC) and had access to GPR equipment provided by NERC. The appendix also summarises the results obtained using B scans and the 3D reconstructions as produced by the SIMCA 2D and SIMCA 3D algorithms respectively.*

#### **B.1 Data acquisition procedure used to obtain data for locating foundations in demolished buildings**

An area of 47.75 square metres was surveyed in the NE of the car park, with the aim of detecting a possible wall foundation suggested by the tarmac surface. Figure B.1[A] is a map showing the plan of the surveyed car park as attained from Google maps whilst Figure B.1[B] is the satellite map of the car park. The figure also indicates the grid of the actual surveyed area.

The GPR system used for this investigation was a pulseEKKO 1000 manufactured by Sensors and Software<sup>1</sup>. The system was equipped with a shielded high frequency antenna of 450 MHz. Since the tops of structures were expected to be fairly shallow (c.1m or less from the surface), a high frequency antenna was selected in order to balance resolution and depth of penetration requirements. The actual components of the pulseEKKO system comprising of the control unit, the laptop integrated with the software for data display and for the full control over data acquisition and the battery source are shown in Figure B.3, whilst the actual GPR head is shown in Figure B.2.

The survey mode was common offset reflection mode with an antennae separation of 0.25m. This step mode allowed for maintaining a constant separation distance and a beep sound alerted when the GPR head had to be moved to the next position. The acquisition was set to continuous mode. A reference tape measure was located along each GPR profile and further parameters were

---

<sup>1</sup><http://www.sensoft.ca/Products/pulseEKKO-PRO/Overview.aspx>

selected in order to ensure correct antennae positioning. Figure B.2 shows the use of the reference tape measure to allow for accurate antenna positioning. Please note that in this photograph the survey is shown being carried out in the adjoining car park and not in the section of the car park where results are shown in section B.5 for *SIMCA 2D* and in section B.8 for *SIMCA 3D*. Since the target features were expected to be fairly large (wall/foundations) the line spacing used was 0.5m with an in line spacing of 0.05m. This spacing resolution is enough to resolve the requirement of less than a quarter wavelength grid spacing to avoid spatial aliasing and efficient data acquisition for the antenna frequency used.

The profiles were recorded in parallel and not in zigzag to avoid coupling loss problems as changes in antennae orientation with respect to the ground can potentially cause variation in the data which can be confused with anomalies. The orientation of the GPR profiles was N-S in order to survey in cross-section the target structures. The tarmac surface of the car park was fairly flat, apart from the regular variations due to the underlying structures. This flat surface provided a good contact between the antennae and the ground. Energy loss due to antennae coupling problems was thus avoided. Since the variations on the surface were fairly subtle, no topographic correction was needed.

The next section details the results.

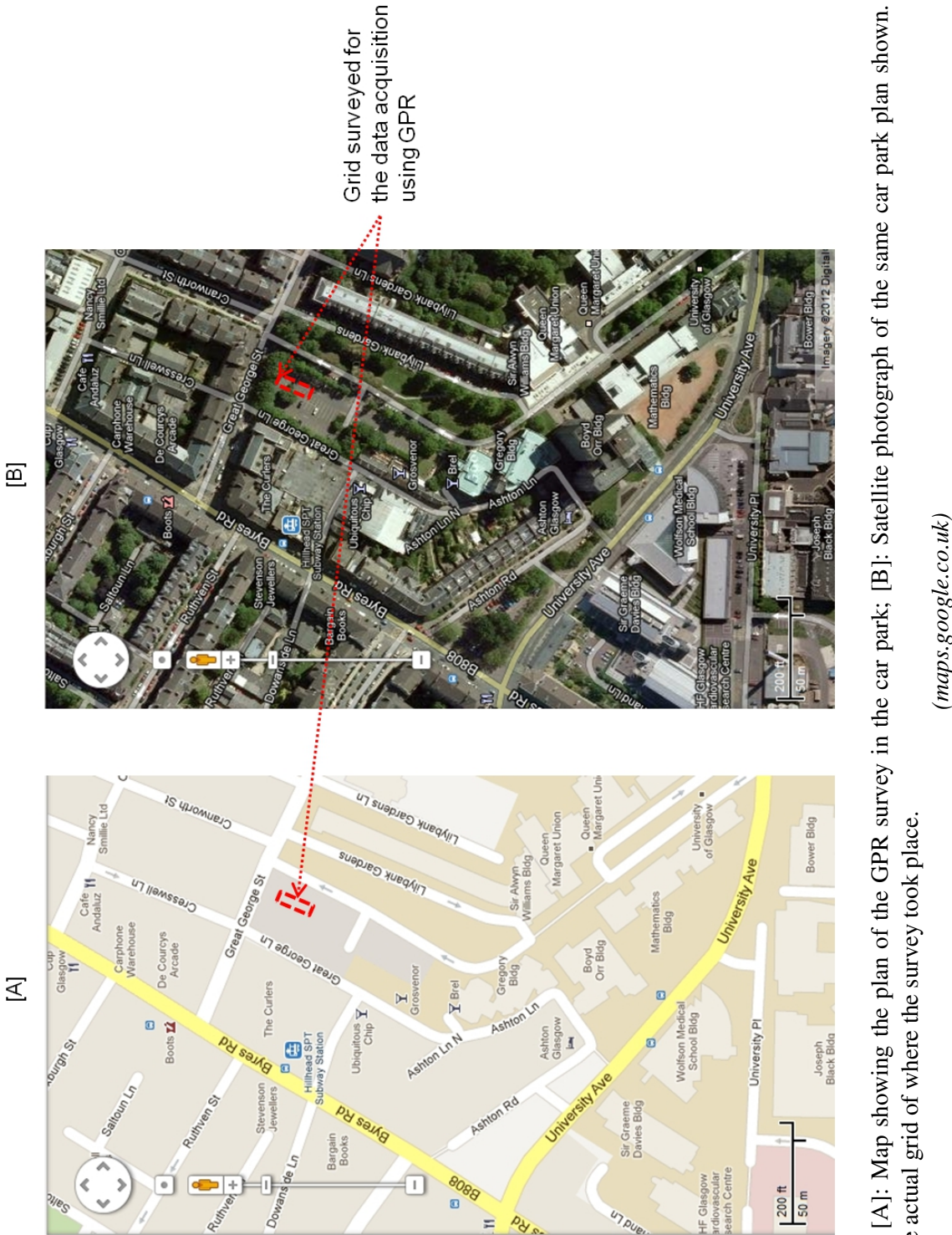
## **B.2 Processing of GPR data using *SIMCA 2D* and its use in locating foundations in demolished buildings**

### **B.3 Introduction**

Having validated and tested the *SIMCA* algorithm on the location of landmines in a laboratory environment and having obtained exceptional results, the *SIMCA* algorithm was then tested on locating foundations in demolished buildings. The data acquisition procedure for acquiring the data required to test the algorithm in the location of foundations in demolished buildings was already given.

The west end of Glasgow where the university is located went through a lot of development due to the expansion of the university. A large number of buildings were also demolished and on the area where the survey was conducted, a car park was developed. The car park in Lilybank Gardens is located on a steep hill in the West End of Glasgow (Figure B.4[B]). The car park occupies the former site of a row of 19th century terraced houses (Figure B.4[A]). During the 20th century the university acquired these properties and in the 1960/70s they were demolished to build the new Business Studies building. The university plans changed and the gap left at the site is currently used as a public car park.

The car park surface is covered in tarmac and shows regular areas of slight bumps and irregular subsidence of the tarmac. This damage to the surface of the car park appears to be caused by the structural remains of the demolished terraced houses that were present at the site prior to the car park construction. Hence, the remains of walls, foundations and other features of the former





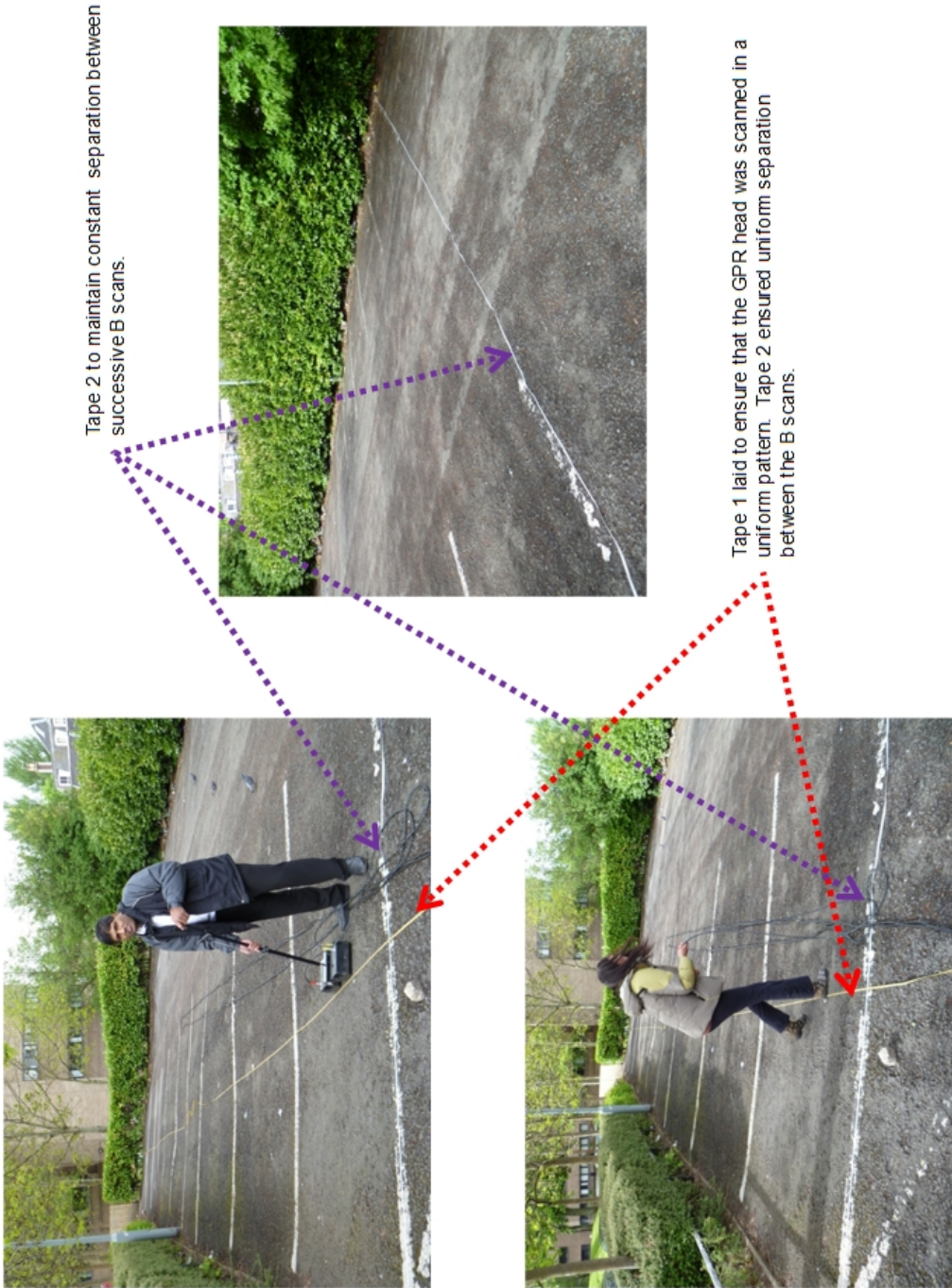


Figure B.2: Photographs showing the method used in the acquisition of data in the car park. Note the tape measures which have been laid out to allow for accurate positioning of the data. Also please note that the above photographs show the survey conducted in the adjoining car park and not in that part of the car park where the results are shown for *SIMCA 2D* and *SIMCA 3D*.



Figure B.3: Photograph showing the pulseEKKO 100 control unit, the laptop with the software and the battery source to power the system.

<i>Processing steps</i>	
<i>1</i>	Static correction
<i>2</i>	Subtract-mean (dewow)
<i>3</i>	Gain (energy decay)
<i>4</i>	Background removal
<i>5</i>	Time cut

Table B.1: The processing steps used in the REFLEXW software.

terraced houses can be subtly perceived on the car park surface.

Since the car park allows identifying known buried structures, this site represented an excellent opportunity to test the *SIMCA* algorithm. The aim of the survey was to test the result of this *SIMCA* algorithm with known buried structures.

To go further the *SIMCA* algorithm was tested against data gathered using a GPR and then validated using the Scheers algorithm and the *REFLEXW* commercial program. Furthermore photographs of the demolished buildings before they were demolished, construction plans from Glasgow City Council, photographs of the cracks in the car park and B scans of the correlated results from the *SIMCA* algorithm were used to provide further validation of the *SIMCA* algorithm. The next section presents the *REFLEXW* software used to obtain results.

## B.4 REFLEXW software

It was mentioned in Chapter 2 Section 2.10.2 that the *REFLEXW* offline package written by Sandmeier (1996) is of seismic processing origin. It was stated that the software had modules for data analysis, display of B scans, 1D/2D filters, migration, data interpretation such as viewing of several profiles, time slice computation and 3D visualization.

The GPR data was also processed with the *REFLEXW* package, so as to compare the results with the *SIMCA* algorithm and the Scheers algorithm. A fairly standard processing flow was applied to the data and consisted of *Dewow Jol* (1994) and background removal, time zero correction and the addition of time based gain. Figure B.6[B] shows the B scans produced by the *REFLEXW* software.

A three-dimensional block was constructed from the parallel profiles and time slices extracted from this. Table B.1 illustrates the processing steps used to process the data using the *REFLEXW* software. Attenuation in the ground is compensated by a time-varying gain in the receiver part of the system. These time slices were also built with the *REFLEXW* processing package. These time slices are used for the 3D processing and are presented in section B.8.2.

The next section illustrates the B scans produced by the *SIMCA 2D* algorithm and the Scheers algorithms.

## B.5 Results

Figure B.6 shows the results from the *SIMCA* algorithm (Figures B.6[C] and B.6[E]), Scheers algorithm (Figure B.6[F]) and the *REFLEXW* software (Figure B.6[B]). It is evident from the B scans





Figure B.4: Photographs showing [A]: Location of the original 19th Century terraced houses; [B]: The existing car park after the houses were demolished and the car park built over the location of the demolished buildings.  
(The photograph of the original 19th Century terraced houses were obtained courteous of T. R. Annan and Sons)

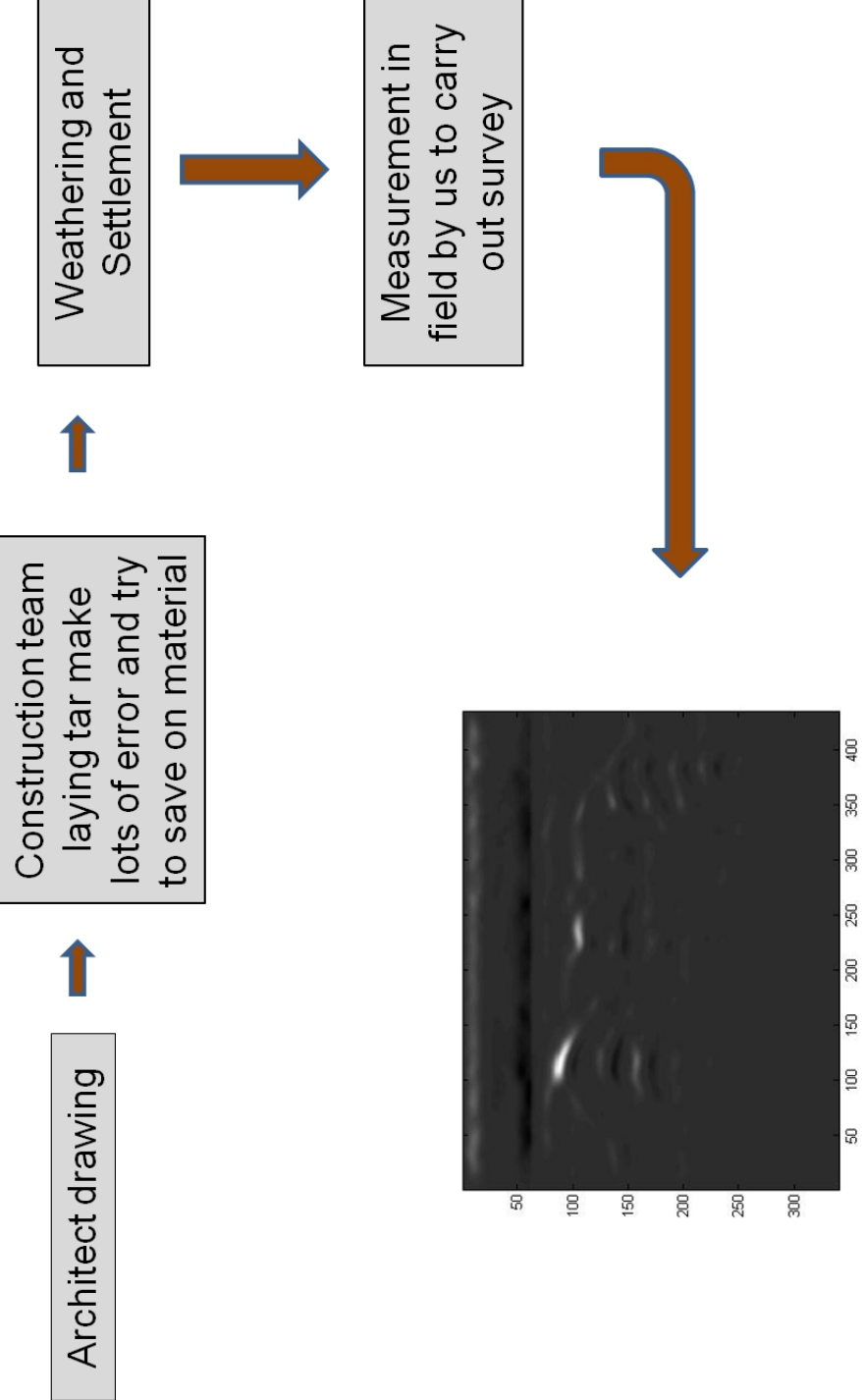
that the *SIMCA* algorithm produces clearer B scans that would allow the operator to easily interpret the images. Figure B.6[C] also shows the mesh generated by the *SIMCA* algorithm using *MATLAB* and from this figure the peak shows the location of the foundations.

Figure B.7 shows photographs taken of the degrading car park and construction plans (Architect drawings) from Glasgow city council revealed that the *SIMCA* algorithm was able to locate the foundations and that the location obtained using the *SIMCA* algorithm correlated well with the construction plans. It is to be noted however that an accurate location of the actual foundations can only be obtained and then the results compared with the construction plans by excavating the car park and locating the foundations. This is not feasible and only a rough estimate can be attained for these circumstances. Also whilst comparing the values of the position in the  $x$  direction and the burial depth from the Architect drawings it can be noted from Figure B.5 that an accurate estimate of the above values cannot be attained from the Architect drawings because:

1. During the laying of the tar the construction team made lots of errors in laying the actual foundations and the values of the burial depth and the position in the  $x$  direction is not achieved in reality. It also happens in some cases that to economise the cost of the project the construction teams save on concrete and thus the above values are also not achieved.
2. The actual foundation could have weathered and settlement of the foundations might have occurred over time and this will cause errors in the values of the parameters.
3. Some of the foundations might have been removed to make way for the car park.
4. Some discrepancies in the measurement campaign by our survey.

All the above errors accumulate and thus the final value of the burial depth and the position in the  $x$  direction obtained from the Architect drawings are not accurate. Thus it is not possible to calibrate the *SIMCA* algorithm and to validate the values of the above parameters and to estimate the error of the algorithm. Therefore a discrepancy will exist between the readings obtained from the *SIMCA* algorithm and an accurate estimate can only be attained by excavating the car park and looking for the foundations.

Table B.2 compares the absolute errors when comparing the depth and the position in the  $x$  direction obtained from the *SIMCA* algorithm, Scheers algorithm and from the *REFLEXW* software. It can be concluded that the *SIMCA* method is more accurate in predicting the location of the foundations and the absolute error for the position in the  $x$  direction is 40.3% compared to 48.2% and 50.4% for the Scheers method and *REFLEXW* software. Likewise for the depth the absolute error for the *SIMCA* algorithm is 20.4% and 23.1% and 21.3% for the Scheers method and the *REFLEXW* software respectively. The absolute errors are high but this can be explained by the fact that an accurate estimate of the depth and the position in the  $x$  direction can only be attained by excavating the car park and actually locating the foundations. More accurate estimation could be attained using C scans and this is going to be demonstrated.



Accumulation of error from other sources results in discrepancy between values of depth and position obtained from the *SIMCA* algorithm when compared to the corresponding values from the Architect drawings

Figure B.5: The sources of error in the values of the position in the  $x$  direction and the burial depth as obtained from the Architect's drawings.

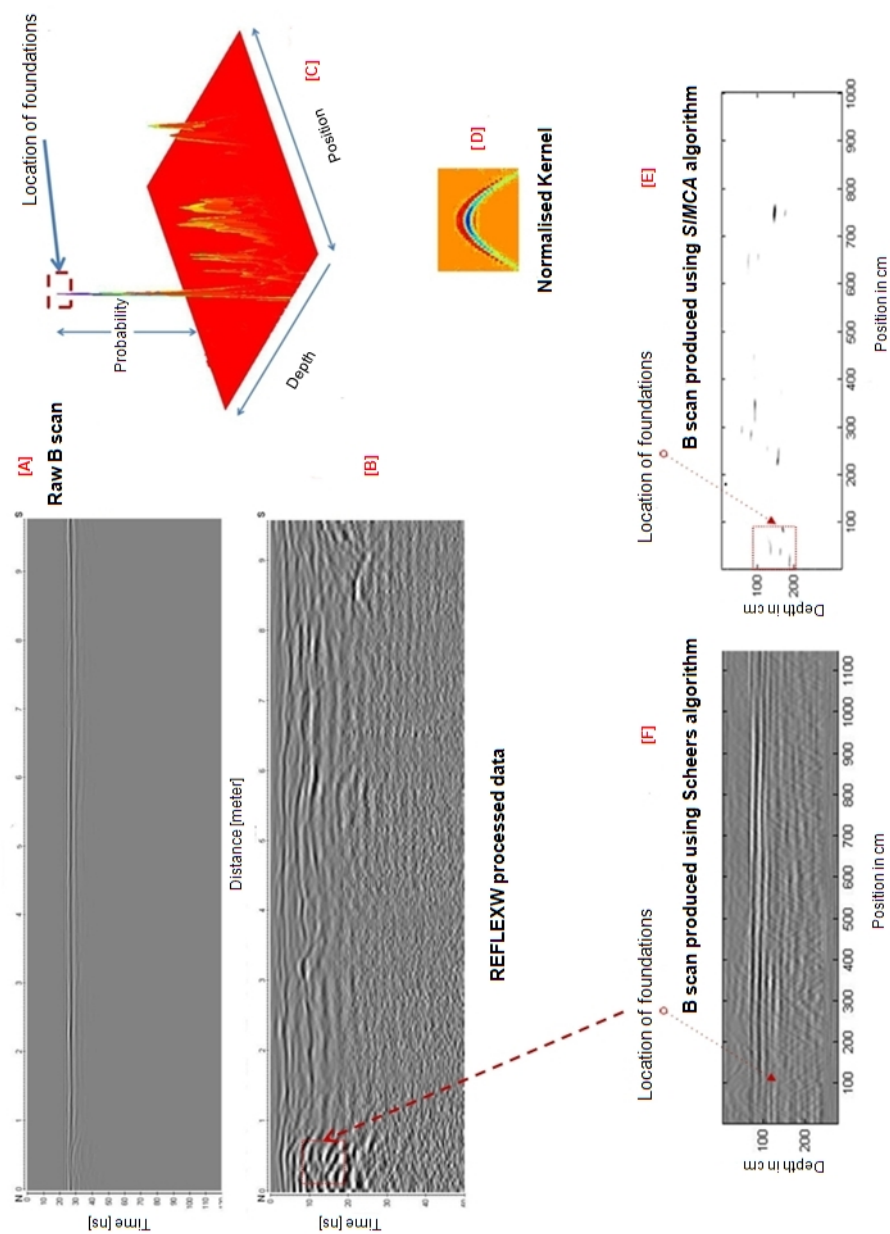


Figure B.6: Results from [A]: Unprocessed B scan; [B]: *REFLEXW* processed B scan; [C]: 3D plot showing probability of occurrence of objects with respect to depth and position on the scan line; [D]: Normalised Kernel; [E]: B scan produced using *SIMCA* algorithm; [F]: B scan produced using Scheers algorithm.



Cracks in the existing car park where the GPR survey was conducted.  
This confirms the location of the foundations

Further cracks in the existing car park beyond the  
boundary of the survey. Also can be seen is the  
bumps in the car park.



Figure B.7: Photographs showing the cracks in the existing car park [A]: Within the boundary of the survey; [B]: Beyond the boundary of the survey.



	<i>x</i> -position (cm)	depth (cm)	% error in <i>x</i>	% error in depth
Values from Architect drawing	139	108	-	-
<i>SIMCA</i> algorithm	83	130	40.3%	20.4%
Scheers algorithm	72	133	48.2%	23.1%
REFLEXW software	69	131	50.4%	21.3%

Table B.2: Position in the *x*-direction from the Architect drawings, Burial depth from Architect drawings and corresponding values produced by the *SIMCA* algorithm, Scheers algorithm and the *REFLEXW* commercial software. The table also gives the percentage error for the three methods when compared to the ground truth. The dimensions are in centimetres for the position in the *x* direction and centimetres for the depth.

## B.6 The processing of GPR data using the *SIMCA* 3D algorithm and its use in locating foundations in demolished buildings

The next section then uses the car park data to process the GPR data using the *SIMCA* 3D technique and to locate the foundations in demolished buildings. The results of the study based on the results from the *SIMCA* 3D technique, the Scheers algorithm and the results from the *REFLEXW* commercial software are given and a comparison is carried out.

## B.7 Introduction

The basic aim of the study was to acquire data from a car park which was built on the former site of a row of 19th century terraced houses. The University of Glasgow acquired the above property and in the 70s the plan was to demolish the houses and build a new Business studies building. But the university changed its plans and the vacant land was used as a public car park. It was pointed out that since the foundations were not completely removed the car park shows bumps, cracking and irregular subsidence of the tarmac. The pictures of the actual terraced buildings were given and pictures of the car park as it is now shows the deterioration of the car park as a result of the unremoved foundations. It is to be noted that the 3D processing of the data is done using the same *SIMCA* 3D outlined in Section 4.4.

It is the aim of this appendix to present the 3D reconstructed isosurface as produced by the *SIMCA* algorithm and compare them to 3D results obtained using the *REFLEXW* software. Also the same data is going to be processed using the Scheers algorithm. Details about the *REFLEXW* software were given in the literature review chapter (Chapter 2) and also the *SIMCA* 2D Chapter (Chapter 3). Calculations of the percentage error for the depth and the position in the *x* and *y* directions as was approximately obtained from original construction drawings of the buildings are provided. Accurate values cannot be obtained as some of the foundations might have been demolished and without excavating it is difficult to get the above parameters.

## B.8 3D Isosurfaces produced by the *SIMCA 3D* algorithm

It was mentioned in Section 4.11 that the isosurfaces for this part of the data will be presented using the *MATLAB* processing environment.

In archaeological surveys rather than show the changes in the reflected energies along a vertical B scan slice of the ground, they tend to map horizontal changes of reflected energy along the vertical B scan slice of the ground. For example the vertical slices of the landmines in Section 4.6 Figure 4.10. These are also referred to as time slices and can be defined as the 'mapping of reflection anomalies horizontally across a site at various depths' Goodman (1994).

Figure B.8 shows the 3D reconstructions obtained using the *SIMCA 3D* algorithm.

The next section displays the isosurface created using the Scheers method.

### B.8.1 3D Isosurfaces produced by the Scheers method.

Figure B.9 shows isosurfaces reconstructed using the Scheers' method.

The next section displays the isosurface created using the *REFLEXW* commercial software.

### B.8.2 Results using the *REFLEXW* commercial software.

Figure B.10 shows the 3D isosurface reconstructed using the *REFLEXW* commercial software whilst Figure B.11 shows time slices obtained using the same software.

Having produced the isosurfaces using the *SIMCA 3D* algorithm, Scheers algorithm and the commercial *REFLEXW* commercial software, the next section compares these results.

### B.8.3 Comparison of Results

From the 3D isosurfaces reconstructed using the *SIMCA 3D* algorithm (Figure B.8), the Scheers' method (Figure B.9) and the *REFLEXW* software (Figure B.10) it is evident that the *SIMCA* algorithm is able to produce a less cluttered representation and it would be easy for a GPR practitioner to locate the foundations from the *SIMCA 3D* generated isosurface.

Table B.3 gives the values for the  $x$ -position,  $y$ -position and the burial depth for the ground truth and those from the three methods. The percentage errors indicate that the *SIMCA* algorithm is slightly better than the *REFLEXW* software and that the Scheers' algorithm again is not accurate. This shows that the *SIMCA* algorithm is accurate in reconstructing targets. The absolute errors for the  $x$ -position and the burial depth for the *SIMCA 3D*, Scheers algorithm and the *REFLEXW* software are better than the corresponding results obtained using the 2D methods, but overall the *SIMCA 3D* algorithm produces better results in comparison to the other two techniques.

The values of the percentage errors for the values obtained in the table below for the *SIMCA* algorithm are really good when considering the various error sources which cause the value of the above parameters attained from Architect drawings to be not accurate. This was discussed in detail in Section B.5.

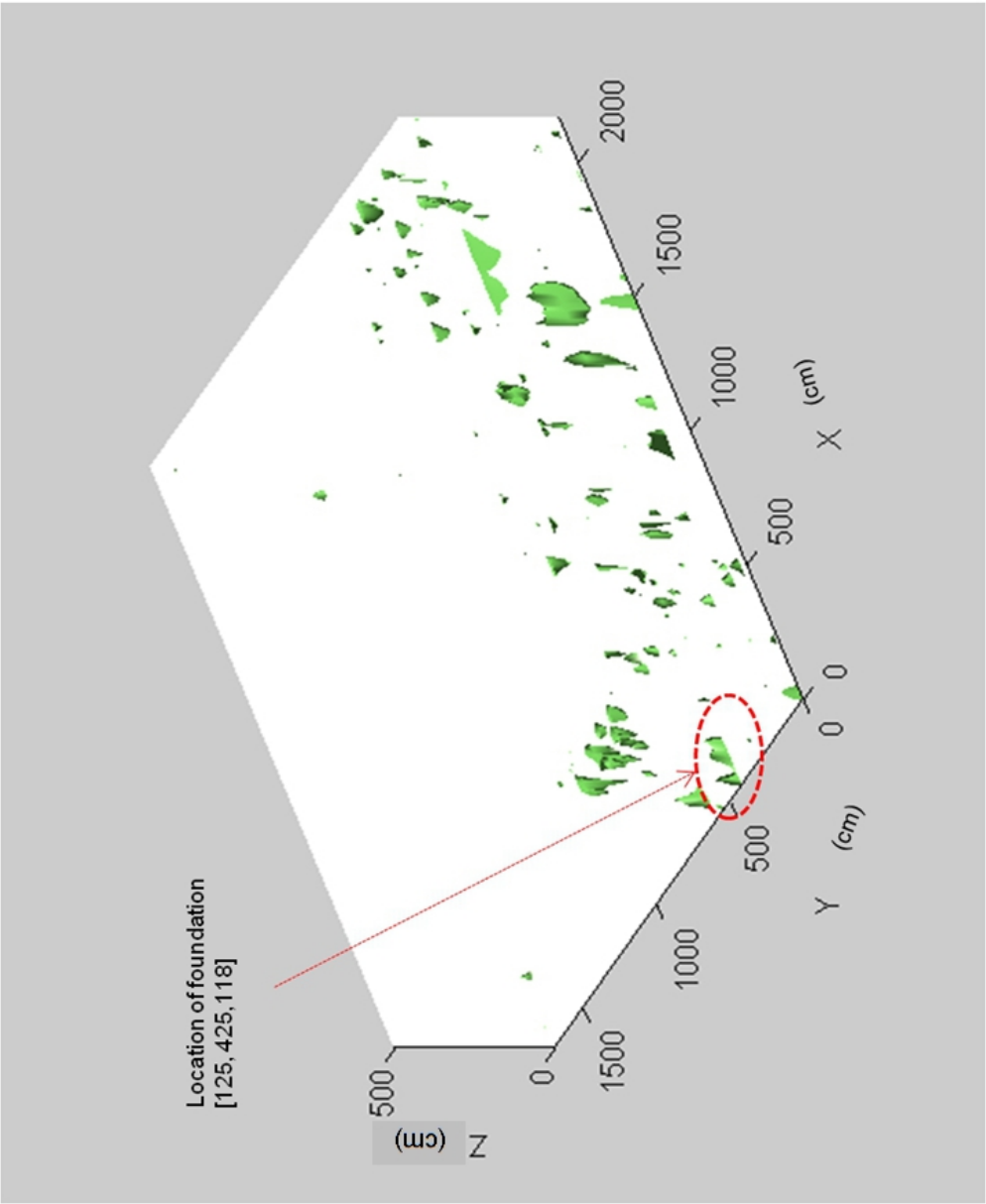


Figure B.8: 3D isosurface produced using the SIMCA method. Isosurface level = 0.02.

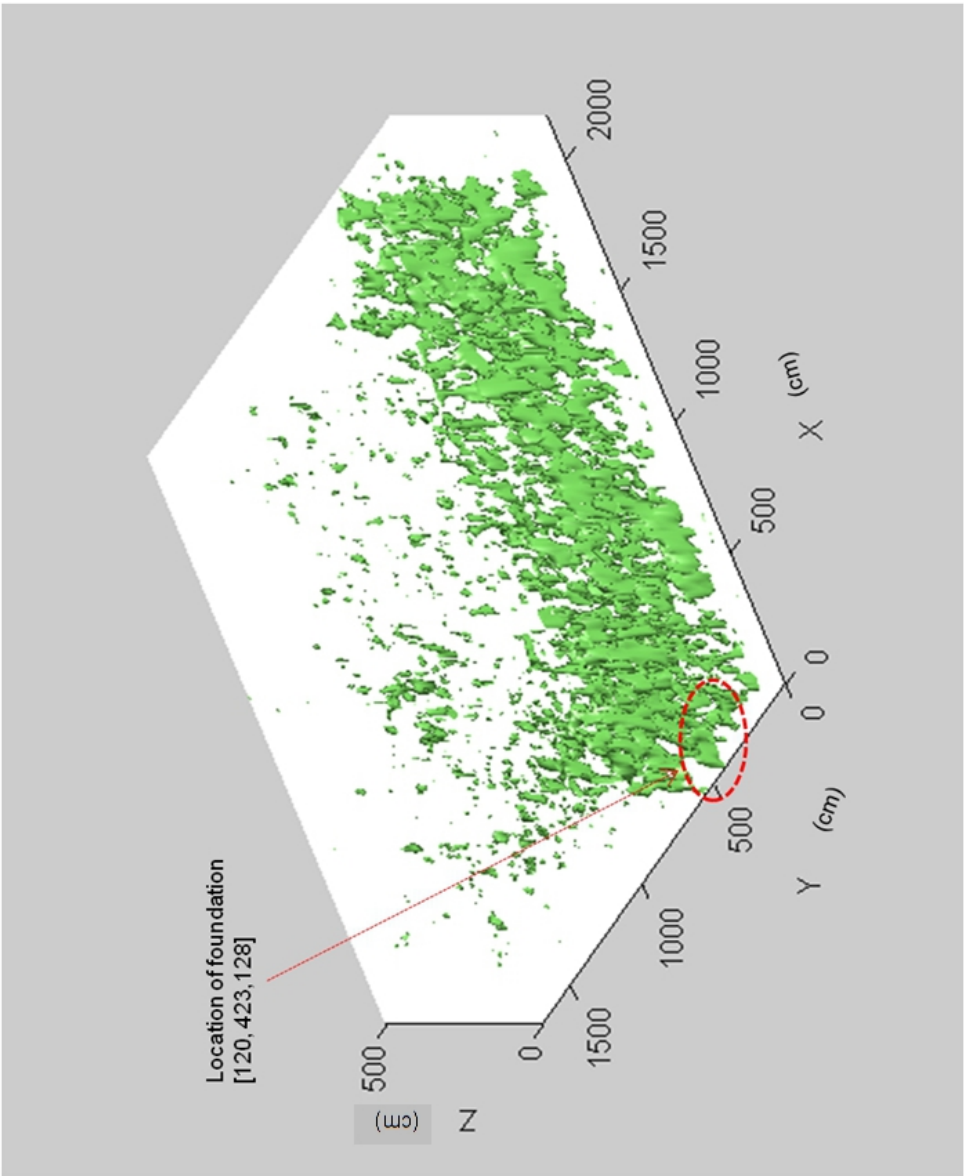


Figure B.9: 3D isosurface produced using the Scheers' method. Isosurface produced at isosurface level =  $1e3$ .

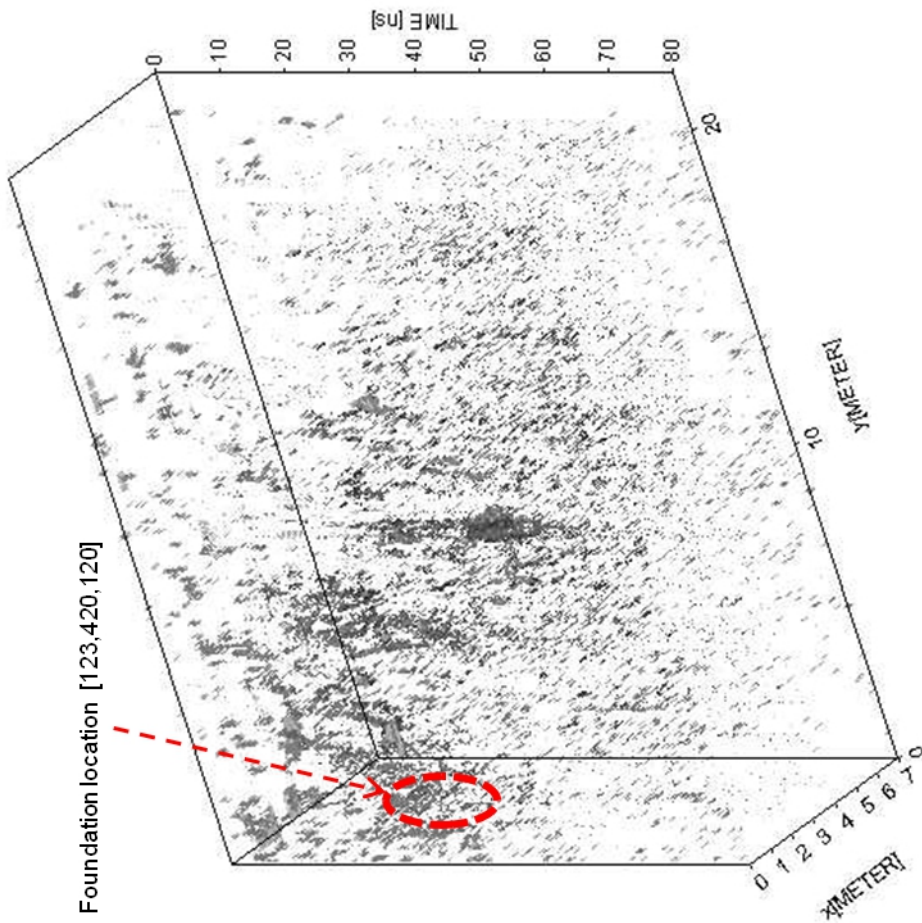


Figure B.10: Isosurface generated using *REFLEXW* commercial software at threshold of 247.

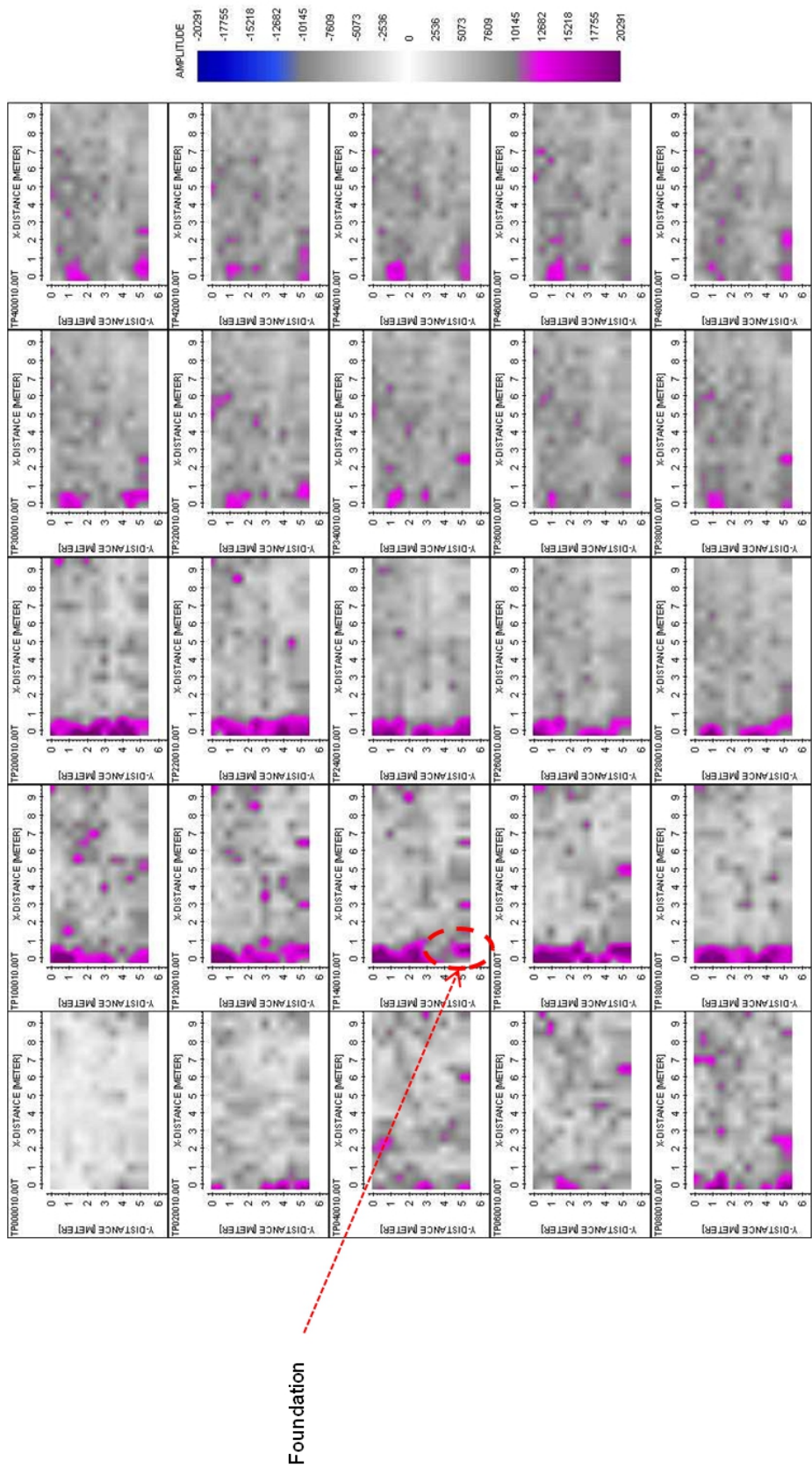


Figure B.11: Time slices obtained using REFLEXW software. It is to be noted that the foundation is clearly visible in some of the time slices.

	<i>x</i> -position (cm)	<i>y</i> -position (cm)	depth (cm)	% error in <i>x</i>	% error in <i>y</i>	% error in depth
Ground truth	139	440	108	-	-	-
<i>SIMCA</i> algorithm	125	425	118	10.1	3.5	9.5
Scheers algorithm	120	423	128	13.7	3.9	18.5
REFLEXW software	123	420	120	11.5	4.5	11.1

Table B.3: Actual position in the *x*-direction, actual position in the *y*-direction, actual burial depth and corresponding values produced by the *SIMCA* algorithm, Scheers algorithm and the *REFLEXW* commercial software. The table also gives the Percentage error for the three methods when compared to the ground truth. The positions in the *x* and *y* directions are in centimetres and the depth is in centimetres.

## B.9 Summary and Discussions

It was shown in this appendix for the location of foundations that the *SIMCA* algorithm was an improvement over the Scheers algorithm. Furthermore the results from the *SIMCA* algorithm correlate well with the corresponding values obtained from the Glasgow City Council plans of the car park, when compared to the same results using the Scheers algorithm and from the *REFLEXW* software.

The appendix also used the *SIMCA 3D* technique to locate the foundations of a demolished building. It was shown that the *SIMCA 3D* technique produced accurate reconstructions when compared to the Scheers' algorithm and the commercial *REFLEXW* software.

# Bibliography

- Abrahamsson, R., E. G. Larsson, J. Li, J. Habersat, G. Maksymenko, and M. Bradley: 2001, 'Elimination of leakage and ground-bounce effects in ground-penetrating radar data'. In: *in Proc. IEEE Workshop on Statistics Signal Processing*. Singapore. 2.8.1
- Abujarad, F.: 2007, 'Ground Penetrating Radar signal processing for landmine detection'. PhD dissertation, Otto-von-Guericke-Universitat Magdeburg, Magdeburg, Germany. 1.1, 1.2, 3.11.2.1, 4.14.1
- Ackenhusen, J., A. Quentin, C. King, and J. Wright: 2001, *Detection of mines and minefields*. Ann Arbor, MI., 2001: Technical Report 440000-217-T, Infrared Information Analysis Center. 1.2, 2.3
- Al-Nuaimy, W., Y. Huang, M. Nakhkash, M. Fang, V. Nguyen, and A. Eriksen: 2000, 'Automatic detection of buried utilities and solid objects with GPR using neural networks and pattern recognition'. *Journal of Applied Geophysics* **43**, 157–165. 3.11.1.1
- Ambrose, S.: 1990, *Handbook on German Military Forces*. Elsevier Science. 2.2.1, 2.2.2, 2.4
- Anderson, S.: 2002, 'Landmine detection research pushes forward despite challenges'. *IEEE Intelligent Systems Magazine*. 4.6.2.5, 5.1
- Andrews, H. and B. Hunt: 1977, *Digital Image Restoration*. New Jersey: Prentice Hall. 2.8.1, 2.9.2.6
- Annan, A.: 1993, *Practical processing of GPR data*. Proceedings of the Second Government Workshop on Ground-Penetrating Radar, Columbus, Ohio. 1.2, 3.1
- Annan, A. and S. Cosway: 1992, 'Ground penetrating radar survey design'. *Annual Meeting of SAGEEP*. 2.1
- Arbel, E. and L. B. Felsen: 1963, *Theory of radiation from sources in anisotropic media, Part 1: General sources in stratified media, Electromagnetic Theory and Antennas, Part 1*. New York: Macmillan. 4.1
- Baum, C., E.: 1993, *The SEM representation of scattering from perfectly conducting targets in simple lossy media*. Philips Laboratory Note 492. 2.5.2, 4.6.1.1



- Berkhout, A. J.: 1981, 'Wave field extrapolation techniques in seismic migration-A tutorial'. *Geophysics* **46**, 1638–1656. 2.9, 2.9.2, 4.2
- Berkhout, A. J.: 1982, *Seismic Migration-Imaging of Acoustic Energy by Wave Field Extrapolation-A. Theoretical Aspects*. New York: Elsevier. 2.9.2, 4.2
- Binningsbo, J., E. Eide, and J. Hjelmstad: 2000, '3D migration of GPR array-antenna data'. *Proc. Eight Int. Conf. on Ground Penetrating Radar (GPR2000)*. 2.9.2
- Bradley, M., T. Witten, R. McCummins, and M. Duncan: 2002, 'Mine detection with ground penetrating radar synthetic aperture radar'. *Proc. SPIE-Int. Soc. Opt. Eng.*, **4742**, 248–258. 2.5.2, 2.5.2
- Brooks, J.: 2000, 'The detection of buried non-metallic anti-personnel land mines'. PhD dissertation, University of Alabama, Alabama, Huntsville, USA. 2.8.1, 2.8.1, 2.8.1, 2.8.1, 3.1, 3.11.2.1, 4.1, 4.6.1.2
- Brunzell, H.: 1998, 'Signal processing techniques for detection of buried landmines using ground penetrating radar'. PhD dissertation, Department of Signals and Systems, Chalmers University of Technology. 2.3.2
- Bruschini, C., B. Gros, F. Guerne, P. Pice, and O. Carmona: 1998, 'Ground penetrating radar and imaging metal detector for antipersonnel mine detection'. *Journal of Applied Geophysics*. 1.2
- Caelli, T., D. Carevic, and I. Chant: 1999, 'Feature extraction and classification of mine like targets from GPR data using Gaussian mixture models'. *Proc. Information, Decision and Control Conf., Adelaide, Australia*. 5.5
- Caevic, D., M. Craig, and I. Chant: 2008, 'Modelling GPR echoes from landmines using linear combination of exponentially damped sinusoids'. in *Proc. SPIE-Detection Remediation Technol. Mines Mine-Like Targets II* **3079**, 1022–1032. 3.1, 4.6.2.8
- Capineri, L., P. Grande, and J. Temple: 1998, 'Advanced image processing techniques for real time interpretation of Ground Penetrating Radar images'. *IEEE Transactions* **9**, pp. 51–59. 2.8.1.1, 4.6.2.7
- Carevic, D.: 1999a, 'Clutter reduction and target detection in ground penetrating radar data using wavelets'. in *SPIE Conf. Detection Remediation Technologies Mines, Minelike Targets IV* pp. 973–978. 2.8.1
- Carevic, D.: 1999b, *Clutter reduction and target detection in Ground Penetrating Radar data using wavelets*. in *SPIE, Detection and Remediation Technologies for Mines and Minelike Targets IV*, pp. 973–978, Orlando, FL., 4.1
- Carin, L., N. Geng, M. McClure, Y. Dong, Z. Liu, J. He, J. Sichina, M. Ressler, L. Nguyen, and A. Sullivan: 2002, 'Wide-area detection of land mines and unexploded ordnance',. *Inv. Probl.* **18**, pages 575–609. 2.9

- Carin, L., N. Geng, M. McClure, J. Sichina, and L. Nguyen: 1999, 'Ultrawide band synthetic-aperture radar for mine-field detection'. *IEEE Antennas and Propagation Magazine*. 1.2, 1.2, 4.1
- Carin, L., K. Ho, J. Wilson, and P. Gader: 2008, 'An Investigation of Using the Spectral Characteristics From Ground Penetrating Radar for Landmine Clutter Discrimination'. *IEEE Trans. Geosci. Remote Sens.* 1
- Chen, C. and L. Peters: 1997, 'Design and Development of Enhanced Ground Penetrating Radar Systems for the Detection and Classification of Unexploded Ordnances and Land Mines'. *Joint Technical report* (733346-1,733946-1,730181-3). 3.7
- Chen, C., K. Rao, and R. Lee: 2001, 'A tapered-permittivity rod antenna for ground penetrating radar applications'. *Journal of Applied Geophysics*. 1.2
- Chen, C.-C., B. Higgins, M., K. O'Neill, and R. Detsch: 2000, 'Tyndall AFB Measurement Results of UXO Characterization Using Full-Polarimetric Ultra-Wide Bandwidth (UWB) GPR','. *Proc. UXO/Countermines Forum, Anaheim, California* . 1.2, 2.5.2, 2.12
- Chen, C. C., F. Paynter, J. Young, and J. Peters: 1994, 'Use of ground penetrating radar (GPR) for detection of unexploded ordnance'. *Tech. Rep. 727 388-2, ElectroSci. Lab., The Ohio State Univ., Columbus, OH*, . 3.7
- Ciochetto, G., S. Delbo, P. Gamba, and D. Roccatto: 1999, 'Fuzzy shell clustering and pipe detection in ground penetrating radar data'. *IGARSS'99, 1999* 5, 2575–2577. 3.13
- Clement, A., R. Wu, J. Li, E. G. Larsson, M. Bradley, J. Habersat, and G. Maksymenko: 2001, 'Adaptive ground bounce removal'. *Electron. Lett.* 37(20), 1250–1252. 2.8.1
- Collins, L. M., P. Gao, and L. Carin: 1999, 'An improved Bayesian decision theoretic approach for land mine detection'. *IEEE Trans. Geosci. Remote Sens.* 4.1
- Conyers, L. and J. Lucius: 1996, 'Velocity analysis in archaeological ground penetrating radar studies'. *Archaeological Prospection* 3, 25–38. 3.2
- Daniels, D.: 1996, *Surface Penetrating Radar*. The Inst. Electrical Engineers, London. 2.3, 2.5, 2.8.1, 2.24, 3.2, 3.3
- Daniels, D.: 2006, 'An assessment of the fundamental performance of GPR against buried landmines'. *Detection and Remediation Technologies for Mines and Minelike Targets XII, SPIE 2007* (Paper 6553-16). 3.10, 4.6.1.1
- Daniels, D. and R. Allan: 2009, 'Multi-channel landmine detection radar signal processing using blind deconvolution'. *Proceedings of the 6th European Radar Conference*. 3.11.1.3

- Daniels, D., P. Curtis, R. Amin, and J. Dittmer: 2004, 'An affordable humanitarian mine detector, in'. *SPIE, Detection and Remediation Technologies for Mines and Minelike Targets IX* pp. pages 1185–1193. 2.8.1, 2.8.1, 5.3
- Daniels, D. J.: 1985, 'Location of underground services by ground probing radar'. *NODIG 85 Int. Conf.* pp. 5.1.1, 6. 3.13
- Daniels, D. J.: 1988, 'Detection of pipes using circular polarisation'. *Tunnelling Systems Symposium, Brussels, Belgium.* 3.13
- Daniels, D. J.: 2004, *Ground Penetrating Radar, Second Edition*. London, UK: The Institution of Electrical Engineers. 1.2, 2, 1.2, 1.2, 1, 2.5, 2.8.1, 2.8.1, 2.8.1, 2.8.1, 3.1, 3.4.1, 4.1, 4.2, 5.3
- Daniels, D. J. and D. Schmidt: 1995, 'The use of ground probing radar technology for the non-destructive testing of pipes and their surroundings'. *Int. Symposium on NDT in civil engineering, Berlin, Germany* pp. 162–165. 3.13
- Daniels, J., D. Grumman, and M. Vendl: 1997, 'Vertical Incident Three Dimensional GPR:'. *Jour. Env. Eng. Geoph.* **2**(2), pp. 1–9. 2.5
- Das, B., J. Hendrickx, and B. Borchers: 2001, 'Modelling transient water distributions around landmines in bare soils',. *Journal of Soil Science* **166**, pages 163–173. 2.7
- Deiana, D.: 2008, 'A Texture analysis of 3D GPR Images'. MSc dissertation, Delft University of Technology, TU Delft. 5.1
- der Kruk, v., J. Wapenaar, and v. der Berg: 2003, 'Three-dimensional imaging of multi-component ground penetrating radar data",. *Geophysics* **57**, pages 1241–1254. 2.7
- der Merwe, A., G. I.J., and P. L. Jr.: 1999, 'A Clutter Reduction Technique for GPR Data from Mine Like Targets'. *Proc. SPIE 3710, 1094.* 2.8.1, 2.8.1, 2.8.1, 2.8.1, 2.8.1
- Dietrich, M.: 1991, *Theory of dielectric optical waveguides.* 3.4.1
- Dobson, M., F. Ulaby, M. Hallikainen, and M. El-Rayes: 1985, 'Microwave dielectric behaviours of wet soil - Part II: Dielectric mixing models",. *IEEE Transactions on Geoscience and Remote Sensing* **23**, pages 35–46. 2.7, 2.7, 2.7
- Eblagh, K.: 1996, 'Practical Problems in Demining and Their Solutions",. *Proc. EUREL Conf. on the Detection of Hidden Land Mines, Edinburgh, UK,* pp. pages 1–5. 1.2
- Ekstein, R.: 1997, 'Anti-Personal Mine Detection - Signal Processing and Detection Principles'. PhD dissertation, Vrije Universiteit, Faculteit Toegepaste Wetenschappen, Brussels. 3.11.2.1
- erl email: 2012, 'Details of Experimental setup'. 3.6
- Extracted from Enclosure 5 to NVESD Memorandum: 1995, 'Subject: Minutes of the 18-19 Jan 95'. *Humanitarian Demining and Military Operations Other Than War (OOTW) Workshop.* 2.4

- Farhang-Boroujeny, B.: 1998, *Adaptive Filters: Theory and Applications*. Chichester, UK: John Wiley and Sons. 2.8.1
- Farina, A. and A. Protopa: 1998, 'New results on linear prediction for clutter cancellation'. *IEEE Trans. Aerosp. Electron. Syst.* **24**(3), 275–285. 3.1
- Feng, X. and M. Sato: 2004, 'Pre-stack migration applied to GPR for landmine detection'. *Inverse problems* **20**, pages S99–S115. 2.9.2.2
- Feng, X. and M. Sato: 2005, 'Landmine imaging by a Hand-held GPR and metal detector sensor (ALIS)'. *Proc. of the 2005 IEEE International Geoscience and Remote Sensing Symposium (IGARSS '05)* pp. 379–382. 1.2, 2.5, 2.5.1.3, 2.11
- Fischer, C., J. Fortuny, and W. W.: 2000, '3-D imaging for near-range ground-penetrating radar based on w-k migration'. *Proc.EUSAR 2000, 3rd European Conf. on Synthetic Aperture Radar*. 2.9.2
- Fisher, C., R. Stewart, and H. Jol: 1994, 'Processing ground penetrating radar data'. *Proceedings of the 5th international conference on Ground Penetrating Radar GPR'94, Canada* pp. pages 661–675. 2.9.2
- Fisher, E., G. McMechan, A. Annan, and S. Cosway: 1992, 'Examples of reverse-time migration of single-channel, ground penetrating radar profiles'. *Geophysics* **57**(4), pages 577–586. 2.9.2
- Fortuny-Guasch, J.: 2002, 'A Novel 3-D Subsurface Radar Imaging Technique'. *IEEE Trans. Geosci. Remote Sens.* **40**(2), 443–452. 2.5
- Fritze, M.: 1995, 'Detection of buried landmines using ground penetrating radar'. *SPIE proceeding* **2496**, pages 100–108. 2.7, 2.8.1, 4.1
- Fruwirth, R. and R. Schmoller: 1996, 'Some aspects on the estimation of electromagnetic wave velocities'. *GPR'96: International conference on Ground Penetrating Radar, Sendai, Japan* pp. 135–138. 3.2
- Fukushima, E., P. Debenest, Y. Tojo, K. Takita, M. Freese, H. Radrich, and S. Hirose: 2005, 'Tele-operated Buggy Vehicle and Weight Balanced Arm for Mechanization of Mine Detection and Clearance Tasks'. *International workshop on Robotics and Mechanical Assistance in Humanitarian demining (HUDEM 2005)* pp. pp. 58–63. 2.5.2.1, 2.17, 5.5
- Fung, P., W. Lee, and I. King: 1996, 'Randomized Generalized Hough Transform for 2-D Grayscale Object Detection'. *Proceedings of the 13th International Conference on Pattern Recognition* **2**, 511–515. 2.8.1.1
- Gader, P. D., J. M. Keller, and B. Nelson: 2001a, 'Recognition technology for the detection of buried landmines'. *IEEE Trans. Fuzzy Syst.* **9**(1), 31–43. 1.2, 2.8.1.1

- Gader, P. D., M. Mystkowski, and Y. Zhao: 2001b, 'Landmine detection with Ground penetrating radar using hidden Markov models'. *IEEE Trans. Geosci. Remote Sens.* **39**(6), 1237–1244. 4.1
- Gamba, P. and S. Lossani: 2000, 'Neural detection of pipe signatures in ground penetrating radar images'. *IEEE Trans. Geosci. Remote Sens.* **38**(2), 790–797. 3.13
- Gazdag, J.: 1978, 'Wave equation migration with the phase-shift method'. *Geophysics* pp. pages 1342–1351. 2.9, 2.9.2.5
- Gazdag, J.: 2005, 'Wave equation migration with the phase shift method'. *Geophysics*. 4.2
- Gazdag, J. and P. Sguazzero: 1978, 'Migration of seismic data'. *Proc. IEEE*. 4.2
- Gazdag, J. and P. Sguazzero: 1984, 'Migration of Seismic Data'. *Proceedings of the IEEE* **72**(10), pages 1302–1315. 2.9
- Giannopoulos, A.: 1997, 'The investigation of transmission-line matrix and Finite-Difference Time-Domain methods for the forward problem of Ground probing radar'. PhD dissertation, Department of Electronics, University of York, UK. 2.8.1.1, 2.8.2
- Giannopoulos, A.: 2005, 'GprMax software and manual'. <http://www.gprmax.org>. 3.4, 3.4.1, 4.3, 5.3
- Goodman, D.: 1994, 'Ground penetrating radar simulation in engineering and archaeology'. *Geophysics* **59**, 224–232. B.8
- Groenenboom, J. and A. G. Yarovoy: 2002, 'Data processing and imaging in GPR system dedicated for landmine detection'. *Subsurf. Sens. Technol. Appl.* **3**(4), 387–402. 2.11, 3.1, 3.11.1.4, 3.11.2.1
- Gu, K., G. Wang, and J. Li: 2004, 'Migration based SAR imaging for ground penetrating radar systems'. *IEE Proc. - Radar Sonar Navig.* **151**(5), 317–325. 2.5.2, 2.9.2.5
- Gunatilaka, A. H. and B. A. Baertlein: 2000, 'A subspace decomposition technique to improve GPR imaging of anti-personnel mines'. *Proc. SPIE* **4038**, 1008–1018. 4.1
- Gunton, D. J. and H. F. Scott: 1987, 'Radar detection of buried pipes and cables'. *The Institution of Gas Engineers, Presented at 53rd Autumn Meeting, London*. 3.13
- Gupta, I., A. van der Merwe, and C. C. Chen: 1998, 'Extraction of complex resonances associated with buried targets'. *Proc. SPIE* **3392**, pages 1022–1032. 2.8.1, 3.1
- Guyon, I., J. Makhoul, R. Schwartz, and V. Vapnik: 1995, 'What size test set gives good error rate estimates?'. *AT&T Bell Labs memorandum, submitted to PAMI* (BL0115540-95120607). 3.11.2.1, 3.11.2.1
- Hagedoorn, J., G.: 1954, 'A process of seismic reflection interpretation'. *Geophys. Prospect.*, **2**, pages 85–127. 2.9

- Herman, H.: 1997, 'Robotic subsurface mapping using ground penetrating radar'. PhD dissertation, The Robotics Institute, Carnegie Mellon University. 2.9.2.1, 6, 5.1
- Ho, K. and P. Gader: 2002, 'A linear prediction land mine detection algorithm for hand held ground penetrating radar'. *IEEE Trans. Geosci. Remote Sens.* **40**(6), 1374–1384. 3.1
- Hoekstra, P. and A. Delaney: 1974, 'Dielectric properties of soils at UHF and microwave frequencies'. *J. of Geophysics Res.* **79**, 1699–1708. 2.7
- Hoggar, S.: 2006, *Mathematics of digital images*. Cambridge University Press. 2.8.1
- Holzrichter, M. and G. Sleefe: 2000, 'Resolution enhancement of landmines in ground penetrating radar images', *Proc. SPIE*, **4038**, pages 1160–1170. 2.9
- Hough, P. V. C.: 1962, *Methods and means for recognizing complex patterns*. U.S. Patent 3,069,654. 2.8.1.1
- Hsia, T.: 1976, *System Identification*. Lexington, MA, Lexington Books. 2.8.1
- Huang, Y., Q. Liu, and Z. J.: 2010, 'Improved 3-d GPR detection by NUFFT combined with MPD method', *Progress In Electromagnetics Research*. 3
- Hughes, I. and T. P. A. Hase: 2010, *Measurements and Their Uncertainties: A Practical Guide to Modern Error Analysis*. Oxford University Press. 3.11.2.1, 3.12
- Idi, B. Y. and M. N. Kamarudin: 2012, 'Interpretation of Ground Penetrating Radar Image Using Digital Wavelet Transform'. *Asian Journal of Applied Sciences*. 4.1
- IIT email: 2012, 'Details of Experimental setup'. 4.5
- International Campaign: 2011, 'International campaign to ban landmines'. 1.1, 2.4
- Ishikawa, J., M. Kiyota, and K. Furuta: 2005, 'Experimental design for test and evaluation of anti-personnel landmine detection based on vehicle-mounted GPR systems'. in *Proc. Detection and Remediation Technologies for Mines and Minelike Targets X, Orland, FL, USA, Proc. of SPIE* **5794**, 929–940. 4.14.3
- Johnson, P., G. and P. Howard: 1999, 'Performance results of the EG and G vehicle mine detector'. *Proc. SPIE* **3710**, pages 1149–1159. 2.7
- Jol, H. M.: 1994, *Ground Penetrating Radar: Theory and Applications*. Elsevier Science. 1.2, 1.2, 2.6, 2.7, 2.8, 2.19, 2.8.1, 2.21, 2.9.2, 2.11, 3.4.2, 4.6.2.8, 4.6.3, 3, B.4
- Jury, W., A. and W. Garener: 1991, *Soil Physics*. Wiley, New York. 2.7
- Kabakchiev, C., V. Behar, B. Vassileva, D. Angelova, K. Aleksiev, V. Kyovtorov, I. Garavanov, L. Doukovska, and P. Daskalov: 2009, 'UXO Signal Multi Sensor Detection and Estimation'. *Springer*. 2

- Kabourek, V. and P. Cerny: 2010, 'SAR and Stolt Migration Processing for Plastic Landmine Detection'. *20th International Conference Radioelektronika*. 2.9.2.4
- Kaiser., G.: 2009, *A Friendly Guide To Wavelets*. Birkhauser, Boston. 2.8.1
- Karlsen, B., J. Larsen, H. Sorensen, and K. Jakobsen: 2001, 'Comparison of pca and ica based clutter reduction in gpr systems for anti-personnel landmine detection'. in *Proceedings of the 11th IEEE Signal Processing Workshop on Statistical Signal Processing* pp. 146–149. 1.2
- Kerner, D., J. Deni, J. Grubb, H. C., R. Johnson, and T. Kincaid: 1999, 'Anti-Personnel Landmine (APL) Detection Technology Survey and Assessment'. 2.4
- Kovalenko, V.: 2006, 'Advanced GPR Data Processing Algorithms for Detection of Anti-Personnel Landmines'. MSc dissertation, Karazin Kharkiv National University, Oekraine. 2.7, 3.11.2.1, 5.3
- Kovalenko, V., A. Yarovoy, and L. Ligthart: 2004, 'Reduction of Clutter in Data of Mine-Detecting GPR'. *accepted for publication in the book of Proc. of EuroEM 2004*. 4.14.1
- Lee, S., G. McMechan, and C. Aiken: 1987, 'Phase-field imaging: The electromagnetic equivalent of seismic migration'. *Geophysics* **52**, 678–693. 4.2
- Leonard, L.: 1951, *Advanced theory of waveguides*. Wireless Engineer. 3.4.1
- Lertniphonphun, W. and J. McClellan: 2000, 'Migration of underground targets in UWB-SAR systems'. *Proc. Int. Conf. on Image Processing* **1**, 713–716. 2.9.2
- Lester, J. and L. E. Bernold: 2007, 'Innovative process to characterize buried utilities using Ground Penetrating Radar'. *ELSEVIER Automation in Construction* **16**, 546–555. 3.13
- Leuschen, C. and R. Plumb: 2000, 'A matched-filter approach to wave migration'. *Journal of Applied Geophysics* **43**, pages 271–280. 2.9.2, 4.2
- Ligthart, E., A. Yarovoy, F. Roth, and L. Ligthart: 2004, 'Landmine detection in high resolution 3D GPR images'. *Proceedings, MIKON'04* pp. 423–426. 2.11
- Lipson, S. G., H. Lipson, and D. S. Tannhauser: 1998, *Optical physics*. Cambridge, UK: Cambridge University Press. 4.3
- Loewenthal, D., L. Lu, R. Roberson, and J. Sherwood: 1976, 'The wave equation applied to migration'. *Geophysical Prospecting* **24**(2), pages 380–399. 2.8.1.1
- Lopera, O.: 2008, 'An Integrated Detection and Identification Methodology Applied to Ground-Penetrating Radar Data for Humanitarian Demining Applications'. PhD dissertation, Universite catholique de Louvain, Louvain-la-Neuve, Belgium. 2.5, 4.6.2.3, 4
- Lopera, O., B. Macq, N. Milisavljevic, and B. Scheers: 2005a, 'Denoising and migration techniques for landmine identification from Ground-Penetrating Radar 2D data'. in *GRETSI 2005*. 3.1, 4.6.3

- Lopera, O., B. Macq, N. Milsavljevic, and B. Scheers: 2005b, 'Denoising and migration techniques for landmine identification from ground-penetrating radar 2d data', . In: *UCL-FSA (Ed.), eProceedings of GRETSI 2005, Louvain-la-neuve, Belgium* p. p. on CD. 2.8.1.1, 2.9.2.5, 3.10
- Lopera, O. and N. Milisavljevic: 2007, 'Prediction of the effects of soil and target properties on the antipersonnel landmine detection performance of ground-penetrating radar: a Colombian case study'. *Journal of Applied Geophysics*. 2.7, 2.7, 3.10, 4.6.4
- Lopera, O., N. Milisavljevic, B. Macq, I. van den Bosch, S. Lambot, and A. Gauthier: 2004, 'Analysis of segmentation techniques for landmine signature extraction from Ground Penetrating Radar 2D data'. in *eProceedings of the II International IEEE Andean Region Conference*. 2.9.2.5
- Lu, R.: 1998, 'Finite-impulse-response reduction-to-the-pole filter'. *Geophysics*. 3.4.3
- MacDonald, J. and J. R. Lockwood: 2003, *Alternatives for Landmine Detection*. New York: RAND. 1.2, 2.3, 2.3.1, 2.3.3, 4.1, 4.11
- MacDonald, J., J. Lockwood, T. Altshuler, T. Broach, L. Carin, R. Harmon, C. Rappaport, W. Scott, and R. Weaver: 2003a, 'Alternatives for Landmine detection'. *RAND, Santa Monica, CA*. 2.8.1
- MacDonald, J. A., J. R. Lockwood, and J. McFee: 2003b, 'Research plan for multi-sensor landmine detector'. in *Proc. EUDEM2-SCOT-2003, International Conference on Requirements and Technologies for the Detection, Removal and Neutralization of Landmines and UXO, Brussels, Belgium* pp. 625–632. 2.3, 2.5
- Maier, M. and J. W. Brooks: 1996, 'Application of system identification and neural networks to classification of land mines'. *EUREL Int. Conf. on The detection of abandoned land mines: a humanitarian imperative seeking a technical solution*. 5.5
- MALA: 2012, 'Mala Professional Explorer (ProEX) System Manual'. <http://www.malags.com>. 5.5
- Martel: 2001, 'Modelling and design of antennas for GPR systems'. PhD dissertation, School of Electronics, Department of Electrical Engineering, University of Surrey, Guildford, Surrey. 3
- Meats, C.: 1996, 'An appraisal of the problems involved in three-dimensional ground penetrating radar imaging of archaeological features". *Archaeometry* **38**(2), pages 359–379. 2.9.2
- Milisavljevic, N.: 2001, 'Analysis and fusion using belief functions theory of multisensor data for close-range humanitarian mine detection'. PhD dissertation, Royal Military Academy, Belgium, Ecole Nationale Supérieure des Telecommunications, France. 2.8.1, 2.8.1.1
- Moran, M., S. Archone, A. Delaney, and R. Greenfield: 1998, 'Pre-stack migration applied to GPR for landmine detection". *Proceedings of the 7th International Conference on Ground Penetrating Radar GPR'98, USA* pp. pages 225–231. 2.9.2



- Norwegian Aid: 2008, 'Landmine database of the Norwegian peoples aid mine actions in Angola'. 1.1
- Ordata: 1998, 'Version 1.0 (cd-rom)'. *Naval Explosive Ordnance Disposal Technology Division, Indian Head, MD.*,. 3.10
- Özdoğan Yilmaz: 1987, *Seismic data processing*. Tulsa, USA: Society of Exploration Geophysicists. 2.9
- Paik, J., C. Lee, A. Mongi, and A. Abidi: 2002, 'Image Processing-Based Mine Detection Techniques: A Review'. *Subsurface Sensing Technologies and Application: An International Journal*. 2.8.1
- Pavlidis, T.: 1982, *Algorithms for graphics and image processing*. 3.10
- Peplinski, N., F. Ulaby, and D. M.: 1995, 'Dielectric properties of soils in the 0-3-1.3 GHz range"', *IEEE Transactions on Geoscience and Remote Sensing* **33**, pages 803–807. 2.7, 2.7, 2.7, 2.7
- Pizurica, A., W. Philips, I. Lemahieu, and M. Acheroy: 1999, 'Speckle Noise reduction in GPR Images'. *Proc. of the International Symposium on Pattern Recognition, In Memoriam Pierre Devijver, Brussels, Belgium* pp. 162–165. 3.8
- Potin, D., E. Duflos, and P. Vanheeghe: 2006a, 'Landmines Ground-Penetrating Radar Signal Enhancement by Digital Filtering'. *IEEE Trans. Geosci. Remote Sens.* 3.11.1.2
- Potin, D., P. Vanheeghe, E. Duflos, and M. Davy: 2006b, 'An abrupt change detection algorithm for buried landmines localization'. *IEEE Trans. Geosci. Remote Sens.* 2.8.1.1
- Powers, M. H.: 1995, 'Dispersive ground penetrating radar modelling in 2D'. PhD dissertation, Colorado School of Mines, CO, USA. 2.8.2
- Radzevicius, S. J., B. T. Clark, and T. T. Webster: 2005, 'Processing ground penetrating radar data from curvilinear interfaces'. In: R. N. Trebits and J. L. Kurtz (eds.): *Proc. SPIE, Radar Sensor Technology IX*, Vol. 5788. pp. 86–96. 4.2
- Radzevivius, S. and J. Daniels: 2000, 'Ground penetrating radar polarization and scattering from cylinders'. *Journal of Applied Geophysics* pp. 111–125. 3.4.1, 1
- Rahman, M. and K.-B. Yu: 1987, 'Total least squares approach for frequency estimation using linear prediction'. *IEEE Trans. Acoust., Speech, Signal Processing* **ASSP-35**, pages 1440–1545. 2.8.1
- Redman, J., A. Annan, and Y. Das: 2003, 'GPR for anti-personnel landmine detection: results of experimental and theoretical studies.'. *Proceedings SPIE* **5089(I)**, 358–374. 4.6.1.2, 4.6.3.1
- Rees, W.: 2003, *Physical principles of remote sensing*. Cambridge University Press, Cambridge, UK. 3.4.3

- Rhebergen, J., H. Lensen, R. van Wijk, J. Hendrickx, L. van Dam, and B. Bouchers: 2004, 'Prediction of soil effects on GPR signatures, ', in *Defence and Security Symposium, edited by SPIE* (0). 2.7
- Rhebergen, J. B., H. A. Lensen, R. V. W. A, and J. M. H. Hendrickx: 2005, 'Prediction of soil effects on GPR signatures'. 2.7
- Robinson, E., A. and S. Treitel: 1980a, *Geophysical signal analysis*. Prentice-Hall. 2.9, 4.1
- Robinson, E. and S. Treitel: 1980b, *Geophysical signal analysis*. Prentice-Hall. 2.8.1
- Roth, F.: 2004, 'Convolution models for landmine detection with ground penetrating radar'. PhD dissertation, Delft University of Technology, Delft, The Netherlands. 1.2, 2.7, 2.8.1, 2.8.1.1, 3.8, 5.5
- Ruffell, A. and C. Donnelly: 2009, 'Location and Assessment of an Historic Old Mass Grave Using Geographic and Ground Penetrating Radar'. *Journal of Forensic Sciences*. 1
- Russ, J.: 1992, *The image processing handbook*. CRC Press, Boca Raton, Florida. 3.4.3, 3.10
- Ruthenberg, I.: 1998, 'Curve fitting and migration of gpr data for the detection of pipes and cables'. PhD dissertation, Department of Computer Science and Electrical Engineering, University of Queensland. 2.8.1.1
- Saito., N.: 1994, *Local Feature Extraction And Its Applications Using A Library of Bases*. PhD. Thesis, Yale University. 2.8.1
- Sandmeier, K.: 1996, 'REFLEXW software'. B.4
- Sato, M., J. Fujiwara, F. X., and T. Kobayashi: 2005, 'Dual sensor ALIS evaluation test in Afghanistan'. *IEEE Geosci. Remote Sensing Society Newslett.* pp. 22–27. 4.13, 5.5
- Sato, M., Y. Hamada, X. Feng, F.-N. Kong, Z. Zeng, and G. Fang: 2004, 'GPR using an array antenna for landmine detection'. *Near Surface Geophys.* 4.55
- Scheers, B.: 2001, 'Ultra-Wideband Ground Penetrating Radar with application to the detection of anti personnel landmines'. PhD dissertation, Laboratoire d' hyperfréquences and Department of Electrical Engineering and Telecommunication, Université Catholique de Louvain and Royal Military Academy. 2, 2.9.2.6, 2.9.2.6, 2.25, 2.9.2.6, 2.26, 2.9.2.6, 2.9.2.6, 3.11.2.1, 4.1
- Scheers, B., M. Acheroy, and A. Vorst: 2001, *Migration technique based on the time-domain model of the Ground Penetrating Radar*. SPIE. 1.4, 2.9.2.1, 2.9.2.2, 2.9.2.4, 2.9.2.6, 2.11, 3.3, 3.4.1, 3.8.1, 3.11.2.1, 4.2, 4.2, 4.4, 5.3, 5.4, 5.5, 5.6
- Scheers, B., M. Acheroy, and V. Vorst.: 2000, 'Time domain modelling of UWB GPR and its application on landmine detection'. *Proc. SPIE* **4038**, pages 1452–1460. 1.4, 2.7, 2.22, 2.11, 5.1

- Schneider, W.: 1978, 'Integral formulation for migration in two and three dimensions"', *Geophysics* **43**, pages 49–76. 2.9, 2.9.2.2, 4.2
- Sengodan, A. and W. P. Cockshott: 2012a, 'A 2D processing algorithm for detecting landmines using Ground Penetrating Radar data, Warsaw, Poland'. *IRIS 2012*. 1.4.1
- Sengodan, A. and W. P. Cockshott: 2012b, 'The *SIMCA* algorithm for processing Ground Penetrating Radar data and its use in landmine detection, Montreal, Canada'. *ISSPA 2012*. 1.4.1
- Sengodan, A., W. P. Cockshott, and C. Cuenca-Garcia: 2011, 'The *SIMCA* algorithm for processing Ground Penetrating Radar data and its use in locating foundations in demolished buildings'. *2011 IEEE RadarCon conference, Kansas City, USA*. 1.4.1
- Sengodan, A., W. P. Cockshott, and C. Cuenca-Garcia: 2013, 'A 3D reconstruction algorithm for the location of foundations in demolished buildings'. *EUCAP 2013, Gothenburg, Sweden*. 1.4.1
- Sengodan, A., W. P. Cockshott, and J. P. Siebert: 2012, 'An algorithm for 3D reconstruction from Ground-Penetrating Radar'. *IEEE Trans. Geosci. Remote Sens. (submitted under review)*. 1.4, 1.4.2, 4.2, 5.4
- Sengodan, A. and A. Javadi: 2005, 'Landmine detection using masks on Ground Penetrating Radar images'. In: *IRIS*. 1.4.1, 3.4, 3.4.2, 4.2
- Siebert, P. J. and C. Boguslaw: 2008, *An introduction to 3D computer vision techniques and algorithms*. John Wiley and Sons Inc. 3.4.3, 4.4
- Song, J., Q. H. Liu, P. Torriane, and L. Collins: 2006, 'Two-Dimensional and Three-Dimensional NUFFT Migration Method for Landmine Detection Using Ground-Penetrating Radar'. *IEEE Trans. Geosci. Remote Sens.* **44**(6), 1462–1469. 2.9.2, 2.23, 4.6.1.2, 4.6.4
- Song, L. and Q. H. Liu: 2005, 'Ground-penetrating radar land mine imaging: Two-dimensional seismic migration and three-dimensional inverse scattering in layered media'. *Radio Sci.* **no. RS1S90**. 4.2
- Squillacote, A.: 2008, *The Paraview Guide, Version 3*. Kitware, Inc. 7, 4.2
- Stern, W.: 1930, 'Methodik und bisherige Ergebnisse elektrodynamischer Dickenmessung von Gletscherei.'. *Zeitschrift f r Gletscherkunde, f r Eiszeitforschung und Geschichte des Klimas*. 1.2
- Stolt, R.: 1978a, 'Migration by Fourier Transform"', *Geophysics* **43**(1), pages 23–48. 2.9.2.4, 4.2
- Stolt, R. H.: 1978b, 'Migration by Fourier transform'. *Geophysics*. 4.2
- Strifors, H. C., A. Gustafsson, S. Abrahamson, and G. C. Gaunard: 1998, 'Fuzzy-cluster representation of time-frequency signatures as a means for automatic classification of buried mine-like targets'. *Proc. IEEE-SP Int. Time-Frequency and Time-Scale Analysis Symposium, 1998* pp. 597–600. 5.5

- Sun, W., Q. Xu, and G. Xie: 2011, 'Application of Ground Penetrating Radar with GPS in Underwater Topographic Survey'. *2nd International Conference on Artificial Intelligence, Management Science and Electronic Commerce (AIMSEC)* pp. 1946–1949. 2.6
- The Mathworks Inc, 2009a: 2009, 'Matlab Image Processing Toolbox Guide'. *Natick, MA*. 4.4
- Topp, G. C., J. L. Davis, and A. P. Annan: 1980, 'Electromagnetic determination of soil water content: Measurements in coaxial transmission lines'. *Water Resources Research* **16**(3), 574–582. 2.7
- Torrione, P. A., C. Throckmorton, and L. M. Collins: 2006, 'Performance of an Adaptive Feature-Based Processor for a Wideband Ground Penetrating Radar System'. *IEEE Trans. Aerospace, Elect. Syst.* **42**(2), 644–658. 2.5.2, 2.14
- Trang, A., H.: 1996, 'Simulation of mine detection over dry soil, snow, ice, and water'. *SPIE* **2765**, pages 430–440. 2.7
- United Nations: 1997, *International Mine Action Standards (standard section 5, paragraph 10)*. United Nations. 1.1, 1.2, 2.4
- United Nations: 2011, 'The Convention on Certain Conventional Weapons'. 1.1
- van den, B.: 2006, 'Accurate Modeling of Ground-penetrating Radar for Detection and Signature Extraction of Mine-like Targets Buried in Stratified Media'. PhD dissertation, Faculte de Sciences Appliquees, Universite Catholique de Louvain, Faculte Polytechnique, Ecole Royal Militaire, Belgium. 3
- van der Merwe, A. and I. J. Gupta: 2000, 'A novel signal processing technique for clutter reduction in GPR measurements of small, shallow land mines'. *IEEE Trans. Geosci. Remote Sens.* 1.2, 3.1, 4.1
- Van Gestel, J. and P. Stofa: 2000, 'Migration using multi-configuration data". *Proceedings of the 8th International Conference on Ground Penetrating Radar GPR 2000, Australia* pp. pages 448–452. 2.9.2
- van Kempen and L. Sahli, H: 2001, 'Signal processing techniques for clutter parameters estimation and clutter removal in GPR data for landmine detection'. *Statistical Signal Processing, Proceedings of the 11th IEEE Signal Processing Workshop on* pp. pages 158–161. 1.2, 2.8.1, 2.8.1
- van Kempen, L.: 2006, 'Ground penetrating radar for anti-personnel landmine detection'. PhD dissertation, Vrije Universiteit Brussel, Belgium. 3, 5.5
- van Kempen, L., A. Katqrtzis, V. Pzurica, J. Cornelis, and H. Sahli: 1999, 'Digital Signal/Image Processing For Mine Detection'. *Euroconference on: Sensor systems and signal processing techniques applied to the detection of mines and unexploded ordnance (Mine'99)*. 1.6

- van Kempen, L., H. Sahli, E. Nyssen, and J. Cornelis: 1998, 'Signal Processing and Pattern Recognition Methods For Radar Application Mine Detection and Identification'. *IEE Second International Conference on the Detection of Abandoned Landmines (MD '98)*, Edinburgh, UK pp. pages 81–85. 2.8.1
- Ware, C.: 2004, *Information Visualization: Perception for design*. Elsevier. 3.10
- Yang, C. and N. K. Bose: 2005, 'Landmine detection and classification with complex-valued hybrid neural network using scattering parameters dataset'. *IEEE Transactions on Neural Networks* **16**, 743–753. 5.5
- Yarovoy, A. G., F. Roth, V. Kovalenko, and L. P. Ligthart: 2007a, 'Application of UWB bear-field polarimetry to classification of GPR targets'. in *Sabath, F. Mokole, E.L., Schnek, U. and Nitsch, D. (eds), Ultra-wideband, Short-pulse Electromagnetics 7*, New York Springer Science + Business Media LLC. 5.5
- Yarovoy, A. G., T. G. Savelyev, P. J. Aubry, P. E. Lys, and L. P. Ligthart: 2007b, 'UWB array-based sensor for near-field imaging'. *IEEE Trans. on Microwave Theory and Tech.* 5.5
- Yee, K. S.: 1966, 'Numerical Solution of Initial Boundary Value Problems Involving Maxwell's Equations in Isotropic Media',. *IEEE Transactions on Antennas and Propagation* **14**, pages 302–307. 2.8.2, 2.20
- Yilmaz, O.: 2001, 'Seismic Data Analysis: Processing, Inversion, and Interpretation of Seismic'. *Tulsa, OK: Soc. Explor. Geophys.* 4.2
- Yu, H., X. Ying, and Y. Shi: 1996, 'The use of FK techniques in GPR processing'. *Proceedings of the 6th International Conference on Ground Penetrating Radar GPR'96, Japan* **20**, pages 595–600. 2.9.2
- Zhang, A., J. Yansheng, W. Wenbing, and W. Cheng: 2000, 'Experimental studies on GPR velocity estimation and imaging method using migration in frequency-wavenumber domain",'. *Proceeding of the 5th International Symposium on Antennas, Propagation and EM Theory* pp. pages 468–473. 2.9.1, 2.22
- Zhu, Q. and L. M. Collins: 2005, 'Application of feature extraction methods for landmine detection using the Wichmann/Niitek ground penetrating radar'. *IEEE Trans. Geosci. Remote Sens.* **43**(1), 81–85. 2.8.1.1
- Zoubir, A. M., I. J. Chant, C. L. Brown, B. Barkat, and C. Abeynayake: 2002, 'Signal Processing Techniques for Landmine Detection Using Impulse Ground Penetrating Radar'. *IEEE Sensors Journal*. 4.1